Study Of Polymer Composites Containing Nano- And Micro-particles For Materials Engineering Applications

Ahssad A. Fiaz

Thesis submitted in partial fulfilment of the requirements for the degree of

Doctor of Philosophy

The University of Sheffield

Department of Materials Science and Engineering

2018

Abstract

The research conducted in this report is broad; however, it demonstrates innovative approaches for several potential applications. The projects advocate the use of composite scaffolds to enhance or improve the roles of standard polymer-based materials. Two techniques have been utilised to create the structures, poly-high internal phase emulsions, templated using two immiscible liquids, and the continuous phase containing the monomer material. Also, hydrogel synthesis, a hydrophilic monomer cured to form a highly swellable polymeric gel. The three subject areas are polymeric hydrogels – as potential sensors; microcarriers for bone and tissue engineering, and poly-high internal phase emulsions (poly-HIPEs) as thermal insulators; all three are briefly outlined below in chronological order of their chapter allocation:

The production of polymeric sensors is the application considered in the following chapter using the environmentally sensitive polymer – poly-isopropyl acrylamide. Initially started using the poly-HIPE route, but the attention was focused on hydrogels as a more suitable alternative. Due to the improved mechanical nature and ability to retain structural integrity in water, the properties were enhanced using magnetically responsive nano- and micro-particles. The project utilises ferrogels are hydrogels loaded with magnetite that were synthesised via a co-precipitation and solvothermal route, creating particle sizes of 1 – 10 nm and around 250 nm, respectively. Additionally, the use of Maxwell-inductance Bridge demonstrates a low, but detectable response for in-situ samples. Although results for the Microparticle containing gels are unclear, they possess significant volume transition responses compared to in situ ferrogels; and with some modification of the inductance bridge, there is potential for the transition of micro-ferrogels to be detectable with the chosen sensing method.

Microcarriers are highly porous materials that provide a surface suitable for cellular adhesion. In this case, emulsion templating was utilised to create porous beads with embedded carbonyl-iron particles to provide a magnetic response. By applying an external magnetic field, a novel method is used to create fluid shear stress in order to encourage osteogenic differentiation. Common osteo-indicators such as alkaline phosphatase activity, collagen and calcium were used as a measure for an osteogenic response.

I

In the last section, a case for Poly-HIPEs as thermal insulation materials is proposed. Due to their controllable nature, they have characteristics similar to those found in insulation materials, small pores, a highly porous and hydrophobic structure are key factors in quality insulators. Porosity was controlled by increasing the volume of water, which formed the internal phase; samples with 60% to 90% were manufactured. The conductivity of the material was similar to conventional insulators; however, they were less insulating with increasing porosity. Addition of wood fibre improved the insulation properties of the 90% porous sample but had the opposite effect on the sample with low porosity.

Table of Contents

Acknowledgements

I want to thank my supervisors Dr Frederik Claeyssens and Professor Dan Allwood, firstly, for giving me the opportunity and then supporting me throughout. Furthermore, they gave me the freedom to explore and experiment with different avenues of interest. The meaningful participation from Dr René Dost, who helped and assisted with the magnetic and electrical side of the project, and was always readily available to explain concepts. Dr Kerry Abrams and Quan Wan, for contributing with SEM images and Dr Ian Ross for TEM support, due to the nature of the material. Darren and Lejla for their cell culture 101 tutorials. The position then occupied by Hossein, whom I worked with closely, he aided and supported the microcarrier project by putting in hours to help me prepare scaffolds, troubleshoot and culture. Colin, for his poly-HIPE insight and willingness to collaborate. Mohammed Uddin, Marwah and Sarina for being there when I required help using particular techniques.

In addition, I extend my appreciation to the technical staff, who helped greatly — additionally, the EPSRC for funding me for 3-years.

I want to thank other friends and colleagues I met during my time at Kroto. Together they created an environment where the exchange of ideas allowed me to learn about new fields of study. Also, to the numerous students that I had been tasked with, particularly the earlier ones in my PhD - I did genuinely feel sorry for you. You indirectly improved my ability to communicate ideas and my understanding; it was partly a case of the blind leading the blind, but we got there in the end.

A special thanks to the family, for the rides and lunches - obviously.

Finally, to good company, I want to thank my friends both distant and near, especially from the "Zombs/Cod/Poker/Mahjong" group - an aspiring bunch that motivated me to finish this PhD.

List of abbreviations

2,2′-Azobis(2-methylpropionitrile)	AIBN
2-Ethylhexyl acrylate	EHA
Acrylamide	AAm
Alkaline phosphatase	ALP
Ammonium persulphate	APS
Benzoyl peroxide	BPO
Bone marrow mesenchymal stem cells	BMSCs
Bone morphogenetic proteins	BMPs
Carbon Dioxide	CO_2
Dexamethasone	DEX
Dynamic Light Scattering	DLS
Extracellular matrix	ECM
Fetal bovine/calf serum	FBS/FCS
Fibroblast growth factor	FGF
Fluid Shear Stress	FSS
Giant Magnetoresistance	GMR
Human embryonic stem cell-derived mesenchymal progenitors	hES-MPs
Human Mesenchymal Stem Cells	hMSCs
Hydrophile-lipophile balance	HLB
Interpenetrating polymer network	IPN
Isobornyl acrylate	IBOA
Lower critical solution temperature	LCST
Maghemite	$\gamma\text{-}Fe_2O_3$

Magnesium Chloride	$MgCl_2$
Magnetite	Fe_3O_4
Molecular weight	MW
Tetramethylethylenediamine	TEMED
N,N′-methylenebis(acrylamide)	BIS
Oil-in-water	O/W
Optimal cutting temperature compound	OCT Media
Phosphate buffered saline	PBS
poly(ethylene glycol) diacrylate	PEGDA
Poly-Acrylic Acid	AAc
Poly-high internal phase emulsions	Poly-HIPE
Poly-Isopropylacrylamide	Poly-NIPAAm
Poly-Methyl methacrylate	Poly-MMA
Potassium persulphate	KPS
Rotations per minute	RPM
Scanning Electron Microscopy	SEM
Sodium acetate	NaAc
Sodium dodecyl sulfate	SDS
Sodium Hydroxide	NaOH
Tetramethylammonium hydroxide	TMAOH
Thermogravimetric analysis	TGA
Three dimensional	3D
Transmission Electron Microscopy	TEM
TRIS hydrochloride	TRIS-HCl
Upper critical solution temperatures	UCST

Water-in-Oil	W/O
X-ray diffraction	XRD
Zinc Chloride	$ZnCl_2$

Units

% weight per weight	% w/w
Angstrom	$\dot{A}$
Hertz	Hz
Hour	hr
kilo Ampere/meter	kA/m
Meter	m
Micro litres	µl
Micrometre	µm
Micromolar	µM
Millihenry	mH
Millimole	mmol
Millilitre	ml
Millimolar	mM
Minute	Min
Molar	M
Nanogram	Ng
Nanometer	nm
Nanometer	nm
Picomol	pmol
Tesla	T
Volts	V
Volume %	Vol%
Watts/ (meter Kelvin)	$W\ m^{-1}\ K^{-1}$

Weight per cent   Wt%

Weight/volume %   w/vol %

Thesis Introduction

Over time, the role of nano-, micro-particles, or nanostructures nanoparticles has increased, and they have become much more influential. If their surface properties are tailored to complement an emulsion, it can lead to increase stability; the addition can also provide a supplementary response to the bulk material. Furthermore, they can act as cross-linking centres for various physiochemical interactions [1].

By embedding nano-, or micro-particles into polymeric structures, it is possible to not only improve their mechanical properties but in doing so, enhance their characteristics for the desired applications; and take advantage of a synergistic effect. A few different examples highlight this: Carbon black was added as a method to improve thermal insulation properties of aerogels [2]; Iron oxide nanoparticles have been used to remove carcinogenic chromium (VI) ions, these provide adsorption surfaces, it also makes them easier to remove, thanks to their magnetic properties [3].

In some cases, they are combined with environmentally responsive polymers and can benefit from the innate response determined by the moieties within the polymer structure [4]. The compounding effect can provide opportunities to benefit existing problems like improving the efficiency of drug delivery [5], cancer treatment [6], glucose monitoring [7], oil/water separation [8]. These novel combinations demonstrate how valuable polymer composites can be.

The work compiled in this thesis continues with the same theme. The objective of this work is to investigate several polymer composites with the addition of inorganic and organic particles. Plus, to further test them within their chosen applications, in the hope of providing a novel way to tackle existing problems.

In chapter one magnetic particles are loaded into thermally responsive hydrogels for sensing applications. Chapter 2 looks into using polymer beads incorporated with magnetic particles to enhance the role of microcarrier cell culture from traditional static culture to dynamic supports. Finally, thermal insulation potential of poly-high internal phase foams with the addition of wood fibre is investigated in chapter 3.

Chapter 1| Investigating Magnetic & Thermally Responsive Hydrogels for Sensing

1. Aims and Objectives

The aim of this chapter is to manufacture a thermally responsive hydrogel loaded with magnetic particles. Then to test within a Maxwell bridge setup to determine its feasibility as a sensor and a sensing method. The following steps will contribute to the objectives:

1. Manufacture Poly(N-isopropylacrylamide) hydrogels loaded with magnetic particles that undergo a significant volume change.
2. Characterise magnetic particles to ensure the formation of magnetite and no other variations.
3. Test swollen gel and the collapsed version within the Maxwell inductance setup to determine the change in magnetic permeability.

2. Introduction

Hydrogels are hydrophilic, cross-linked polymers, which can absorb water within their structure and typically can swell up to 10-fold in volume when in contact with water [9]. This swelling behaviour is thermodynamically driven and can be influenced by the internal structure and functionality of the polymer [10]

Under the right environmental conditions, either physical or chemical these gelatinous materials often undergo transitions dramatically, changing volume by either expansion or contraction [11]. Hydrogels containing charged (acidic or basic) groups within their structure can undergo a collapse upon pH change [12]. While tuning the hydrophilic-hydrophobic nature of acrylamide-based polymers can invoke a temperature response at different temperatures (e.g. (N-Isopropylacrylamide-co-Acrylic acid) [13].

Recent literature is mostly focused on the use of these environmentally responsive hydrogels as targeted drug delivery vehicles. These gels act as both a vehicle and barrier to protect a drug, or cargo that is only released when a particular stimulus instigates the material to undertake a transition in phase volume. The contraction once triggered changes the hydrophilic nature of the material to more hydrophobic, in doing so it expels water and any loaded drugs along with it. The benefit of this method is that the drug retains most of its healing potential when released around the treatment site, thus enhancing the efficiency of treatment. Other potential applications that have been investigated using responsive hydrogels are water treatment [14], biological devices

to sense glucose, specific analytes [15] - and chemical analysis and microfluidics [15] to name but a few.

There have been multiple references to the suitability of environmentally responsive hydrogels for sensing applications. However, exploration of hydrogels as sensors in itself is a relatively embryonic area, and few reports have investigated making responsive hydrogels incorporating a sensing element. Achieving built-in sensor-like capabilities within hydrogels requires a method to change a physical response, in this case, the volume transition to an electrical output, which is both detectable and measurable. For example, the natural tendency of the hydrogel to swell and contract causes a shift in transparency, shifting from an opaque-white in its collapsed state, to translucent in its swollen state – this optical change is a measurable property [17]. Another investigated the fluorescent detection of changing glucose concentration, the intensity of which increased proportionally with concentration [18]. A technique, which we explore in this chapter, revolves around the addition of ferric oxide particles, as they exhibit magnetic response. We aimed to detect the change in magnetic response of these hydrogels before and after collapse using a Maxwell-inductance bridge [15,19].

3. Literature Review

3.1. Hydrogels

Hydrogels are a 3-dimensional network of cross-linked monomer units, and once cross-linked the hydrophilic groups within the polymer matrix hold the water within the gel [20]. In its purest state, a hydrophilic monomer would dissolve in water; however, as a cross-linked monolith structure, it becomes insoluble due to the interconnected bonds [21]. Another visible change they undergo during shrinking/swelling is the reversible change in transparency due to the variation of the refractive index that shifts the appearance from either a cloudy nature to transparent.

Nonetheless, the volume phase transition is regarded as a slow process for sensor technology. The method used to counteract this is to reduce the size of the hydrogel, but this compromises the mechanical properties and thus results in structures incapable of withstanding repeated handling and the stress/strain required for most applications [22,23].

3.2. Stimuli-responsive Polymers

Environmentally responsive polymers can be manipulated due to their inherent ability to respond to external stimuli, by reversibly swelling or contracting. The stimulus triggers the hydrogel volume phase transitions due to various mechanisms: Van der Waals' forces, hydrogen bonding, hydrophobic and electrostatic forces [24].

Temperature and pH are the most commonly studied methods, though there are numerous other ways to instigate a response from a smart polymer, i.e. mechanical force, light [25], chemo-responsive [4], ion strength [26], redox [27]. Figure 1 below highlights the stimuli and some of the groups, or compounds that are associated with the responses.
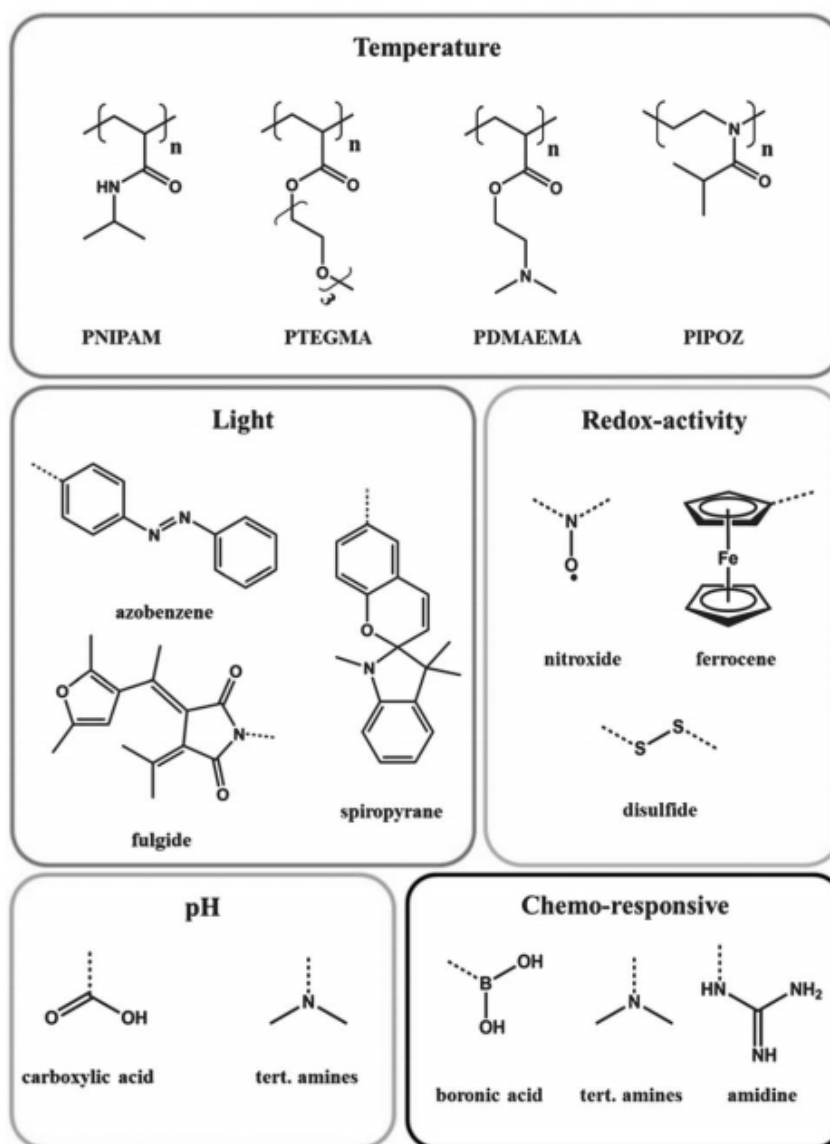
Figure 1: Summary of the most common stimuli and the compounds that give them this ability. Reproduced from Ref. [4] *with permission from The Royal Society of Chemistry.*

Poly(N-isopropylacrylamide)(Poly-NIPAAM) is the polymer of focus in this chapter, a prototypical temperature-responsive polymer. The structure of the polymer is given in Figure 2, also highlighted is the common cross-linker used in conjunction, N,N′-Methylenebis(acrylamide). Isopropylacrylamide is often used within biomedical applications, as the lower critical solution temperature phase transition from a swollen water state to a dehydrated state occurs at around body temperature (32ºC), it is also biocompatible. Hence it is often used in biomaterials studies [28].

As Poly-NIPAAM contracts around body temperature it is commonly used in research that involves drug release vehicles; in one particular example up to 93.1 mg/g beads of the anti-inflammatory drug, indomethacin was loaded into the hydrogel vehicles

based on the same nature. Release studies showed up to 82% of the drug was released at 37ºC [29]. Furthermore, biomaterial applications have also been investigated, as the surface properties changing from hydrophilic to –phobic is also advantageous for the detachment of cells [30]. In a study by Zhang et al., Poly-NIPAAM was grafted onto microcarrier surfaces to encourage cellular attachment below 32ºC as the gels swell and detachment above this point [31]. It has also shown promise in sensor-like applications; by combining a poly-NIPAAM hydrogel with gold nanocrystals, the fluorescence intensity decreased with increasing temperature from 25 - 43ºC [32]. Similarly, a visible detection concept was applied by Islam et al. but using the same polyNIPAAM as a humidity sensor [33].
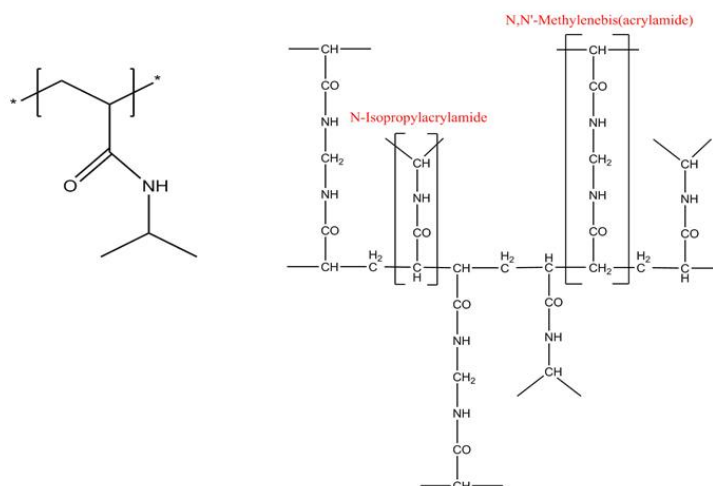
Figure 2: Chemical structures of N-Isopropylacrylamide (Left) and a segment of its polymeric chain when cross-linked using N,N'-Methylenebis(acrylamide).

3.3. Temperature responsive polymers

Lower critical solution temperature (LCST) and upper critical solution temperatures (UCST) define the limits at which point thermoresponsive polymers react to their surroundings. LCST polymers undergo an inverse volume change above a critical point, shrinking and separating from the solution as temperature increases [13]. Polymers that are the reverse of this separate below a critical point (UCST), proportionally changing volume with temperature [34]. Once cross-linked into a hydrogel form, the LCST/UCST is referred to as the volume phase transition temperature (VPTT) [28].

The isopropyl group of the monomer (see Figure 2) is hydrophobic, and below the LCST the water molecules surrounding this part of the monomer are highly ordered. The arrangement allows for strong hydrogen bonds in between the water molecules to occur which is enthalpically favoured, but comes with an entropic cost because of the increase of the order of water molecules. Above the LCST the entropic contribution dominates, breaking the ordering around the isopropyl group and causing the water and the polymer phase to separate and the polymer to shrink in a hydrophobic collapse [35]. Various other thermos-responsive polymers that display LCST and UCST are listed in Table 1. The LCST polymers will collapse from hydrated to dehydrated state above a given temperature, while UCST polymers exhibit the opposite behaviour.

Table 1: Brief list of some thermoresponsive polymers with either LCSTs or UCSTs [36–39].

Polymer	Phase Transition Temperature
LCST	
Poly(N,N-diethylacrylamide)	37ºC
N,N-dimethylacrylamide	33ºC
Poly(methyl vinyl ether)	30 – 50ºC
Poly(N-vinylcaprolactam)	20 – 85ºC
poly(ethylene glycol)	85ºC
UCST	
N-methylacrylamide	57ºC
Polyacrylamide and polyacrylic acid	20 – 40ºC
poly(acrylamide-co-butyl methacrylate)	10 – 30ºC

LCST is a tuneable property and can be varied by branching on hydrophobic or hydrophilic groups by producing copolymers. Hydrophilic groups raise the transition temperature, whereas hydrophobic groups lower it [40]. Lue et al. added various concentrations of the co-monomer acrylic acid (AAc) and found an AAc/NIPAAm ratio of 0.9 – 2.7% could alter the LCST from 32ºC to 35 – 44ºC [13]. Poly-NIPAAm co-polymerised with HEMA-acrylate and cysteamine both showed alterations from the standard LCST temperature of NIPAM, though former decreased to around 29ºC and the latter was higher much close the natural range (27 - 30ºC) [41]. Copolymerization with hydrophobic monomer polystyrene also shifted the LSCT below 30ºC with increased content of the copolymer. However, after the addition of 75 wt% of styrene, the volume transition became unnoticeable [42].

3.4. pH-responsive hydrogels

Figure 1 suggests several functional groups can respond to changes in pH of the solution, for example, weak acidic groups such as carboxyl groups are protonated at pH values below their pK_a while they ionise above their pK_a. The charged side chains cause a charge build-up within the polymer. To maintain charge neutrality within the polymer counter charges diffuse into the network. In turn, this causes an increase in osmotic pressure, triggering the gel to swell [43]. On the other hand, basic side chains such as amines swell in below the pKa of the amine as they are in ionic form due to the protonation of the amines within the polymer structure and positive charge accumulation [44].

Like temperature response polymers, pH response materials are also exploited as drug delivery vehicles, and it can be argued that these more suited due to the variations of pH around the body, which vary from 1 – 8 and are more suitable for targeting more localised areas [45]. The limitation of pH-gels lies in the fact that the volume transition point cannot be tailored, unlike their temperature responsive counterparts.

Poly-acrylic acid (Poly-AAc) is the most predominant anionic polymer. Its coil-to-globule transition occurs around pH 5; the structure is in a partially collapsed state with some water solubility, in a more alkaline environment; however, an open structure is observed [46,47]. Poly-methacrylic acid (PMAA) and PEG methacrylate were combined with the different ratio of each monomer for controlled on-off microgels. The PK_A of which is similar to Poly-AAc, below pH 5 all ratios were in a moderately collapsed state, however, between pH 5 - 6 the equal concentration of both monomers showed an increased weight-swelling ratio above 6 [48].

Cationic variations swell under acidic conditions; poly(4-vinylpyridine) is a commonly studied variation, it observes a volume transition from pH 6.8 to 4.1. The change in environmental conditions leads to three times the increase in size [49]. Chitosan, a naturally occurring polysaccharide dissolves below pH of 6.5 [12]. Risbud et al. formulated chitosan-polyvinyl pyrrolidone gels showed increased swelling from pH 3 to pH 1. Under acidic conditions, this leads to an increase in drug release (up to 70%) [50]. Poly((2-dimethylamino) ethyl methacrylate), was alleged to have a transition

9

around pH 8; microgels plateaued from a diameter of 470 nm to 150 nm at between pH 7 and pH 9.5 [51].

3.5. Magnetically responsive hydrogels

Magnetically responsive polymer structures have also increased in popularity. However, these composite hydrogels are not known for their physiochemical volume-phase transitions, but more the way they can be manipulated from a distance using generated magnetic fields [52]. Controlled and pulsatile release of drug-loaded ferrogels was possible using an on-off mechanism by magnetic compression. The controlled release and frequency were controlled using motorised piston heads, mounted with neodymium magnets acting on the gels causing the temporary compressive deformation [53]. Fuhrer et al. demonstrated their use as soft actuators by fixing one side of a magnetic hydrogel monolith to a permanent magnet. Quick and reversible actuation was possible using a generated magnetic field, causing the gel to elongate to 123% of its original length [54]. The properties are also highly useful for fast and effective separation. Ma et al. created magnetically responsive micro-composites using PMAA-shell and magnetite core. Up to 53% of magnetic material was loaded into the gels, enough for rapid separation. The recovery of magnetic hydrogels for water treatment showed 98% recovery in a short space of time; this was consistent for the 20 cycles tested [55]. The ability to control magnetically loaded-gels externally presents a novel method of targeted and controlled drug delivery using an external magnetic field. Once injected they can be brought to a targeted location for effective delivery of the drug [56].

Although volume phase transitions can be triggered, it only occurs when magnetic nanoparticles are combined within a thermo-responsive polymer matrix; and then exposed to an alternating magnetic field. Alternating the field causes superparamagnetic nanoparticles to generate heat, which dissipates into the matrix causing contraction feedback in the hydrogel [57,58]. Bruvera et al. and Satarkar et al. both used the temperature responsive polymer Poly-NIPAAM in this way. A remote pulsatile release was possible, furthermore, by controlling the duration of the field, it was possible to regulate the quantity of drug released [5,59].

3.6. Analyte Response

More interestingly and probably more practical to real applications is the detection of specific analytes. As the volume phase transition is reported to be a result of osmotic pressure, attracting specific analytes to trigger a change in osmotic pressure and in turn a change in volume is feasible [60]. For example, this was used to make a hydrogel-based sensor for mercury ions in seawater. The hydrogel incorporated N,N′-cystamine bisacrylamide molecules, this functionality selectively binds with Mercury (Hg^{2+}) ions via forming S-Hg-S bonds. The polymer was formed in a 3D photonic crystal that allowed the structure to have a different UV-VIS spectrum upon binding with Mercury. The amount of binding was correlated with the colour change of the hydrogel [60].

Sensors for other heavy metals such as Pb^{2+} ions have been constructed via incorporating ligands that selectively bind this ion, for example, acrylamide hydrogels incorporating the monomer di(acryloylaminobenzo)-18- crown-6 [61]. These hydrogels swelled after exposure to a $Pb(NO_3)_2$ solution (because of charge build up within the hydrogel), and this swelling was concentration dependent. By producing a diffraction grating of the hydrogel and measuring the wavelength of the diffracted light the Pb^{2+} concentration within the solution can be measured. By utilising 8-hydroxyquinoline sites and polyacrylamide-based hydrogel cations such as Cu^{2+}, Co^{2+}, and Zn^{2+} were selectively bound [62].

Besides, more biologically targeted molecules have been used as analytes as stimuli for hydrogel sensors. A very popular biological analyte is glucose, efficient detection of glucose within a hydrogel could yield the next generation of implantable sensors measuring glucose levels in diabetic patients. Introducing glucose response within hydrogels is typically done via incorporating phenylboronic acid within its structure, this group interacts selectively and reversibly with glucose molecules [62]. The principle was used to make a fluorescent subcutaneous hydrogel that worked as a glucose sensor when implanted in a murine model, under the skin of the mouse's ear [63]

Interaction of biological molecules can be introduced into the polymeric network using three different methods according to Rein et al. The first involves integrating small biomolecules that have an affinity for larger macromolecules; the second is similar,

11

once the protein binds to the enzyme sensitive substrate a chemical reaction is involved in breaking the bonds. The third involves converting the biomolecules by entrapped enzymes, which then results in response either by swelling or contracting [64]. An imprinting technique was used on a hydrogel containing methacrylic acid to sense the complementary protein bovine serum albumin selectively, this was detected by the shift in higher wavelength due to photonic components, proportional to the concentration [65]. Miyata et al. created a reversibly responsive gel; the volume transition mechanism was antigen specific. The network was formed up of an immobilised antigen and antibody; which shrunk in the absence of free antigen molecules [66]. Plunkett et al. created acrylamide-based gels that were able to selectively undergo dissolution within 20 minutes when the digestive enzyme Chymotrypsin at 0.5 mg L^{-1} was present in solution [67].

Though most of the reports use a hydrogel-based scaffold, in some cases Poly-HIPE materials have also been noted to have the potential application as sensors. Biosensors were able to detect hydrogen peroxide concentrations to 10^{-7} M; the conducting nature was due to graphite particles [68]. C.liu et al. used the foam-like material for selective fluorescent sensing of the organic compound, λ-Cyhalothrin [69].

3.7.   Multi-responsive hydrogels

Combining different functional groups within the hydrogels to achieve multiple responsive polymers is also feasible. For example, Si et al. and Efthimiadou et al. both co-polymerised acrylic acid with NIPAAM to produce both temperature and pH-responsive microspheres [70,71]. The former group concluded that increasing the concentration of acrylic acid content within the polymer also increases the mesopores/micropores within the structure. Triple and quadruple-stimuli responsive polymers are also achievable, by including more functional groups within the polymer network; this also increases the complexity of the polymer. Garcia et al. synthesised a hydrogel that exhibited light, temperature and pH response via incorporating spiropyran and amine groups within the poly-NIPAAM network [72]. This strategy was further used to include the previous functional groups, and also to include an additional metal ion response via incorporating 2-acrylamido-2-methylpropane sulfonic acid within the polymer network [73].

Addition of specific functional groups not only adds a new stimuli reactive group to the polymer, but it can also alter the response of the base polymer. Acrylic acid when combing with Poly-NIPAAM not only provides an additional pH-responsive group (i.e. the –COOH group), but because of the hydrophilicity it also increases the phase transition temperature from 31^0 to 45^0 at pH 7 – this is because the acrylic acid functionality is inherently more hydrophilic than NIPAAM [40].

3.8. Improving response and mechanical properties

There is controversy in using this material as a sensor, for example, Mou et al. claim that the time response of the material to its dynamic environment is too slow for any practical use as a sensor [74]. Additionally, although cross-linking is essential for making a hydrogel the degree of crosslinking has an essential effect on the mechanical properties of the hydrogel and the degree of swelling as well as on the appearance of the hydrogel [75]. Lower crosslinking allows high volume retention, but poor mechanical properties. Whereas, high cross-linking increases its stiffness, but reduces the swelling potential [76]. Increasing the amount of cross-linker also decreases the spacing in between the cross-links within the 3-dimensional polymer network; this makes the gel brittle with a cloudy appearance at conditions below its LCST [20].

A more conventional approach to resolving this issue is to assess various other chemical crosslinkers. Low and high molecular weights of poly(ethylene glycol) diacrylate (PEGDA) have been used to do this. It was found that due to the longer chain length a more significant difference in shrinking and swelling was observed with a higher molecular weight (MW) PEGDA, than for both BIS and low MW PEGDA components. Furthermore, the LCST temperatures were found to be tunable with different MW of PEGDA [35]. Lee & Lin compared the swelling behaviour of poly-NIPAAM using several crosslinkers; BIS, tetraethylene glycol diacrylate (TEGDA), and poly(ethylene glycol) dimethacrylate (EGDMA). TEGDA showed the highest swelling ratio, up to 3 times greater due to more hydrogen bonding opportunities and a more substantial chain length, but this was also reported to have 94% lower gel modulus compared to the other two [77]. Cross-linker interaction with water is key, and it depends on it hydrophilic properties At 5 mol% MBAM, the more hydrophilic of the three cross-linkers tested continued to show a high swelling ratio, whereas the same concentration of EGDMA and 3,9-Divinyl-2,4,8,10-tetraoxaspiro[5.5]undecane resulted in a dramatic decrease by approximately 27% [78].

The addition of ionic copolymers can also improve swelling ability; 1 – 10% acrylic acid for example proportionally increased the swelling ability of NIPAAM gels [20,79]. The trend with acrylic acid was also noted by Korotych et al., homogenous NIPAAM gel showed the lowest degree of swelling of 6 wet g /g of dry state, which increased as the ratio of acrylic acid did from 0 – 75% [80]. 50:50 blend of NIPAAM and poly(ethylene glycol) methylether acrylate (PEGMEA) showed increased swelling and

faster deswelling ability compared to ratios of 70:30 and 90:10. Up to 30 g/g was possible, and this decreased to ~22 g/g for the highest ratio of NIPAAM [77].

Increasing the surface area results in a quicker response by creating porous hydrogels through emulsion templating, for example, but this deteriorates the mechanical properties further [81].

Introduction of nanoparticles has been used from various sources such as laponite (i.e. clay nanoparticles) [82], nanogels (i.e. hydrogel nanoparticles) [75], carbon nanotubes [83], giving rise to improved performance. Nanocomposite materials can influence a variety of properties such as mechanical, thermal and barrier properties [82]. Nanomaterials can act as cross-linking agents, so that doping with nanoparticles often requires a lower amount of cross-linker [84].

Clay has been used frequently, Haraguchi used as a multifunctional crosslinking agent, instead of the typical crosslinker (BIS), which is regularly utilised in combination with N-isopropyl acrylamide [85]. These research studies report that the elasticity of the gel increased with the addition of clay compared to BIS cross-linked gel. Notably, the gels were able to withstand elongation up to a 1000% strain before fracture. A self-gelating hydrogel with silica nanoparticles showed increased compressive strength with 5 wt% of silicon nanoparticle addition. Though the LCST temperature of the hydrogel remained unaffected between 5 – 15 wt% of silica [22]. In another report, the same group reported the ability to elongate the materials to 50 times compared to conventional chemical cross-linked gels, as well as the ability to withstand high levels of deformation [86]. Swelling properties of PEG–diacrylate hydrogels with up to 5 wt% nanoparticles allowed swelling to increase more than 500% times its original weight. It also had a positive effect on mechanical properties, for both tensile and compressive test – having retained their elastic properties after being stretched to 1500% their original length, compared to ~1500%, without nanoparticles [87].

Another interesting approach was taken by Xia et al., who used poly(N-isopropylacrylamide) nanostructures as an integral part of a Poly-NIPAAM hydrogel architecture [75]. By controlling the reaction time of the nanogels and the concentration in the monolith, they were able to show increased mechanical properties – the gel stretched 12 times its initial length, and contracted to over 80% its initial volume. Furthermore, an improved response time of the hydrogel was observed. The

addition of microgels also further improved the tensile stress by up to 50% by laponite containing hydrogels [82]. Self-healing Gar gum enhanced hydrogels showed significant improvement in comparison to microgels that used just conventional cross-linking. After being cut into multiple segments, they were able to form the original structure [88].

On the contrary, in some cases, there is often a trade-off between the concentrations of particles introduced, as an excess amount can lead to loss of function and poor mechanical properties [54]. Although as reported above 5 wt% of silica improved Poly-NIPAAM based hydrogels properties, the silica content when increased beyond this point showed opposing effects. Adding over 5% of silica to the poly-NIPAAM decreased swelling and deswelling ratios additionally lowered the compressive ability as well with higher weight % [22].

For the application in mind, fundamental characteristics will be a fast response and robust mechanical properties that can undergo swelling and collapse numerous times. Though hydrogels often struggle with the final point hence their limited introduction to real life applications [81].

3.9. Magnetism

Generating a magnetic field has various responses on a material, which is determined by the movement of electrons. The alignment of a material's magnetic poles determines its strength or suitability as a magnet. This natural response within an applied field can be highlighted by the dimensionless quantity, susceptibility, which determines the magnitude to which they can be magnetised in an applied field [89].

Most known covalently bound and ionic materials are classed as diamagnetic; they have no or little response in a magnetic field due to their electron being paired in closed shell configurations. In paramagnetic materials, the atoms do possess a permanent magnetic dipole, because of unpaired electrons within their structure, but the orientation of the magnetic poles are disordered and have no net alignment [90,91]. Only in an applied magnetic field, the dipoles align, and induced magnetism is observed, which disappears when the magnetic field is removed. However, when a ferromagnetic material is placed in a magnetic field, the domains align such that a significant net magnetic moment is produced. Even upon removal of this generated field, metals like iron, nickel, cobalt and their alloys retain some residual magnetism [92]. Ferrimagnetic materials are usually ferrites such as magnetite and maghemite; they behave similarly to ferromagnets under an applied field. However, unlike their Ferro- counterparts, the alignment is unequal, but there is a net magnetic moment. Ferro- and Ferrimagnets magnetise relatively quickly and to a higher degree through the application of a smaller applied field [93]. Paramagnetic materials like magnesium and lithium on the other hand when placed in a magnetic field start to align, but weakly, and commence to lose their magnetism once the field has been removed [93].

Magnets are further divided into two categories, hard magnets, which remain saturated after the field has been removed and have broader magnetisation curves. They are commonly found in electric motors, generators and actuators. On the contrary, soft magnets have a narrower loop and generally, lose their magnetic ability immediately after the field is removed. They find their use in applications where an on-off mechanism is necessary, for example, an electromagnet used to separate, or a transformer [94].

3.9.1. Magnetism in micro vs nano-sized particles

The size of a magnetic material is essential to its magnetic properties; when a ferromagnet is below a critical point, it becomes a single domain structure [19]. Nanoparticles around 10 nm and below with single domain structure have an affinity to magnetic fields, but retain no residual magnetism, once the field is removed. The amount of permanent magnetisation is called remanence [95]. A critical limit is observable for such particles where they start to demonstrate single domain characteristics. The size dependence of nanoparticles on coercivity, the magnetic field required to zero magnetisation after saturation can be seen in Figure 3 below.
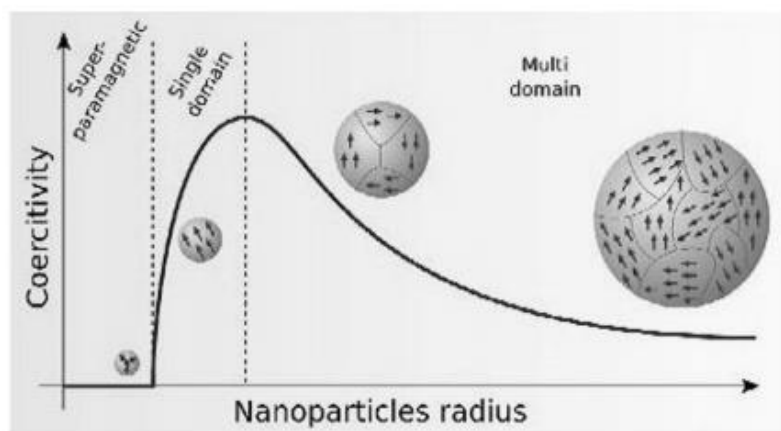
Figure 3: Image adapted from Akbarzadeh et al., depicting the relationship between ferromagnetic nanoparticle size and domain structure; where D_C and D_S represent the critical size and superparamagnetism limit [96].

A typical magnetisation curve for a ferromagnet is illustrated below. The shape is such because once the applied field is removed all domains do not have the same orientation of which they started. Hence, a remanent magnetisation at a zero applied field [97]. However, ferromagnetic nanoparticles below a certain size do not result in such a defined curve, as the coercivity tends to zero with decreasing size (Figure 4). Work was done on magnetic particles of various sizes between $10 - 40$ nm and shown to increase in susceptibility with an increase in size [98]. Due to their lower susceptibility, they require higher applied fields to achieve magnetic saturation [98].
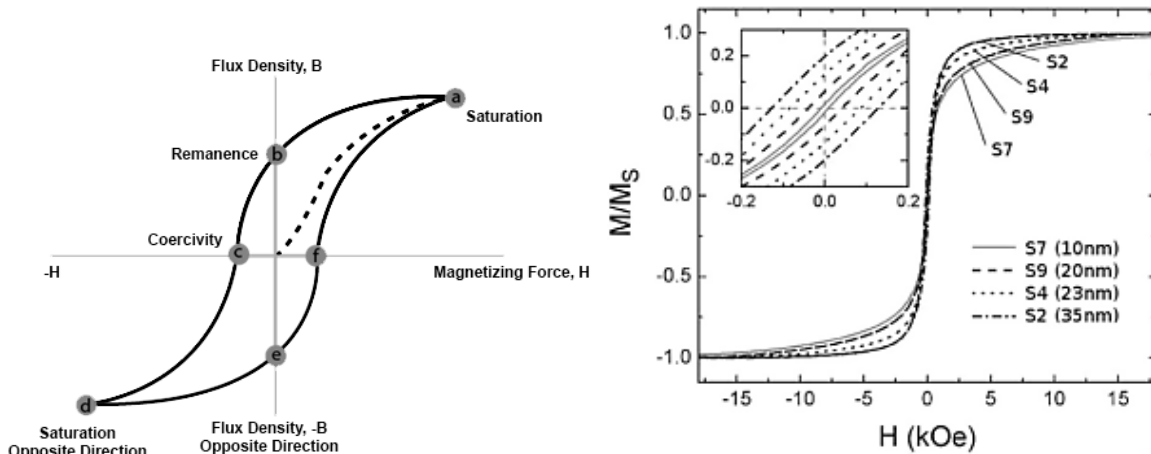
Figure 4: A typical hysteresis loop (Left), highlighting the key points. Moreover, curves of four different particle sizes of magnetite nanoparticles (Right), showing the effects of broadening as the diameter increases, adapted from [98].

3.10. Magnetite

The critical component of this project revolves around the formation of magnetic particles that will be effective for sensing based applications. A large number of techniques exist to synthesise iron oxide mainly of the magnetite (Fe_3O_4) and Maghemite (γ-Fe_2O_3) variation.

The precedence of a particular oxidation state over the other can negatively influence the magnetisation properties; such is the case with magnetite and maghemite. The former contains two oxidations states Fe^{2+} and Fe^{3+}, and the latter exists as Fe^{3+} [98]. Magnetite displays the strongest magnetism of any transition metal-based oxide [97].

3.10.1. Co-precipitation Method

The co-precipitation method is the most common and straightforward technique used to synthesise magnetite nanoparticles. By mixing Fe^{3+} and Fe^{2+} ions in a 2:1 ratio, then precipitation of Fe_3O_4 nanoparticles occurs by adding sodium or ammonium hydroxide, dropwise. The reaction is often carried out in the presence of nitrogen to ensure the precipitate is of homogenous quality. An oxygen-free environment is highly advised to produce a homogenous slurry of magnetite; without it, other oxidation states such as Maghemite (Fe_2O_3) can form. What remains is a black colloidal suspension of nanoparticles that respond to an external magnetic field – often given the term ferrofluid.

$$2FeCl_3 + FeCl_2 + 8\boldsymbol{B}OH \rightarrow Fe_3O_4 + 4H_2O + 8\boldsymbol{B}Cl$$
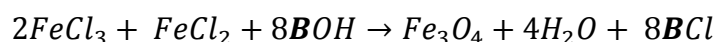
Equation 1: Chemical equation for co-precipitation of magnetite. Where $\boldsymbol{B} = Na^+$, K^+ or $(C_2H_5)_4N^+$.

Nucleation and growth phase are the occurrences that regulate the size and the homogenous nature of the final product [99]. Although the reaction can be complete within a minute, according to Fang et al. these two phases should remain independent; to achieve a narrow distribution, it is advised the nuclei are created at the same time. A study by the same group demonstrated rapid mixing led to better control of the nucleation phase, and this resulted in the smaller and narrow distribution of particles; evident from the differences in standard deviation, 134 nm^2 for rapid mixing and 522 nm^2 for slow mixing [100,101]. Formation of initial primary nanocrystals is followed by agglomeration through processes like Oswald ripening and diffusion forming larger particles [99].

Careful iron salts selection for example oxalates, nitrates and sulphates, or the addition of modifiers can also determine shape, size, composition and magnetic properties. The ratios of both ferric and ferrous sources are also factors to consider [102,103]. Typical modifiers are; sodium acrylate, acrylic acid, ethylene glycol, Diethylene glycol, TMAOH, sodium citrate, oleic acid, SDS which are added pre- or post-synthesis [103–107]. A study presented by Shen et al. demonstrated that more control could be implemented using the co-precipitation method by varying the concentration of sodium dodecyl sulphate (SDS) and irradiation time of visible light, they managed to control the shape, and size of the nanoparticles, respectively. Varying the ratio of citrate ions to iron ions (Between 0 and 1.2) showed a decrease in particle size from 10.5 nm to 4.4 nm with an increase in concentration. The standard deviation of particles also reduced from 4.2 to 1.0 nm showing a more monodisperse size distribution [108].

Size control can be regulated by pH, at constant pH however, the base concentration determines size. Though, at a constant hydroxide concentration this is inversely dependent, and results in smaller particles at high pH [109]. Similarly shown by Ramadan et al. - pH of 8 up to 12.5 showed an insignificant decrease in particle size with increase in pH. However, an increase, beyond pH 11 was observed [110]. A comparable dip and increase was observed, but at a higher pH - at pH 12.15 particle size decreased to 10.6 from its initial value of 17.7 nm, then returned to its original value [111]. Ramadan et al. concluded that pH is more influential controlling the phase, rather than size [110].

Temperature is a factor that can control grain growth, Fang et al. demonstrated an increase resulted in a proportionate change in size from 4 nm at 0°C to 10.5 nm above 90°C [112]. Post-synthesis heat treatment has shown to affect the uniformity of the particles still, though their sizes were not significantly affected [113].

The appeal of co-precipitation is its simplicity and ability to produce large quantities, but it is difficult to control the size distribution. Furthermore, the product of this technique often displays poor crystallinity, which results in lower magnetic properties; and it requires an oxygen-free environment for the homogenous production of Fe_3O_4 [102].

3.10.2. Solvothermal synthesis

The hydrothermal or solvothermal synthesis route is also relatively straightforward; however, it requires high temperature (200- 300°C) and a high-pressure autoclave. The advantage of this is the narrow size distribution and production of good crystallinity while maintaining its composition [114,115]. The process involves a one-pot synthesis method mixing a source of Fe^{3+}, ethylene glycol/ diethylene glycol, which act as strong reducing agents; and the addition of sodium acetate (NaAc), which aids the reduction of $FeCl_3$ to Fe_3O_4. Without NaAc and under the same reaction conditions the formation of Fe_3O_4 did not occur [116]. In the presence of urea, which was used as an alternative alkali source, iron oxide particles were found to be porous with a hollow structure. Replacing this with sodium acetate and ammonium hydroxide formed solid structures, but the latter produced particles that were magnetically weak [117].

Refining the conditions of the solvothermal method can dictate sizes within the nano- and micron range depending on the precursors. Deng et al. found that altering precursor concentration and reaction time could affect the diameters of Fe_3O_4 microparticles [116]. While keeping the concentrations constant and only altering the reaction time of; 8, 28 and 72 hours the range approximate diameters increased from 200, 400 and 800 nm, respectively. A similar trend was also noticed when increasing initial concentrations. Polyethylene glycol and sodium dodecyl sulphate were found to be more effective at maintaining a narrow size distribution and a mean size of 80 nm. Whereas, when they were used individually, it resulted in larger particles and in the case of Polyethylene glycol, this also meant heterogeneous sizes [118].

21

3.10.3. Other Methods

Organometallic precursors such as – iron (III) oleate, iron oxyhydroxide, or iron pentacarbonyl form the basis of thermal decomposition reactions and are typically used in iron oxide synthesis [119]. Along with high boiling point solvents and stabilisers, which can alter surface energies for shape control, or oxidation strength for phase control [120]. The stabilisers cap the end surface groups and provide stability to the particles. In a thermal decomposition reaction, iron oxide crystal size is usually delimited/restricted by the boiling temperature of the solvent [121].

The same authors suggest that the precursor also determines the size range, for requirements less than 10 nm iron pentacarbonyl is more suitable. Whereas, sizes between 10 – 30 nm can be fabricated with either iron oleate or oxyhydroxide. Thermal decomposition of Iron(III) acetylacetonate at different temperature and time showed variation in size. Higher reaction time from 30 minutes to 24 hr showed a dependent increase in average diameter from ~ 6 to 11 nm. Increasing temperature from 300 to 330 °C for up to 4 hours showed a similar trend, and an increase from ~ 7 to 10 nm was observed [121].

Reverse Microemulsion

Using a water-in-oil emulsion to contain the reaction in droplets, and through the addition of surfactants (bis(2-ethylhexyl) sulfosuccinate, sodium dodecyl sulphate, cetyltrimethylammonium bromide (CTAB), and PVP) the co-precipitation method is modified [114]. This method provides a higher degree of control as the reaction proceeds in each droplet reactor [122]. The size can be controlled by the droplet phase, concentration of iron precursors and surfactants [122].

3.11. Manufacturing Magnetic Particle Embedded polymers

A basic understanding of combining magnetic particles with a polymer scaffold is another consideration which is mandatory to this the success of the project.

Firstly, simple mixing of the monomer form with iron oxide before polymerisation is the classic and most straightforward way of achieving a magnetically responsive composite. Often for this to occur, the surface characteristics of the nanoparticles should ideally permit them to be highly dispersible, homogenous, and stable in solution for an optimum period. And it is often more of a concern if the thermal curing route is taken, which tends to take longer than photo-induced polymerisation. This method can

lead to reduced mechanical properties, and the non-anchored particles can often leach out as Fuhrer et al. discovered. 20 wt% of unfunctionalised particles were lost due to frequent elongation and contraction [54].

In-situ co-precipitation is a technique, which utilises the hydrophilic nature of some polymers, allowing them to swell in Fe^{3+}/Fe^{2+} solution, which is then exposed to a reducing agent; this allows the deposition of metal oxides into the structure. Hernandez et al., repeated the oxidation process up to three times to increase the presence of iron oxide within an Interpenetrating Polymer Network based polymer matrix [123]. The water uptake increased by approximately 20% after precipitation during the first cycle and did not change much with cycle 2 or 3. In another case, cycle loading of a gelatin matrix almost doubled the swelling degree to 1500% more than their dry weight, but after that cycles of 3 and 6 reduced its swelling weight % to ~ 500% and then 125%, respectively [124,125].

During this process the polymer is either immersed within the Ferro-solutions for a short duration, studies were done for 30 mins to 2 hours [123,126], or more extended soaking periods (12 – 48 hours) have also been investigated [125,127].

In normal in-situ precipitation, the particle-matrix interaction does not occur, and the nanoparticles directly precipitate within the small cavities of the structure – that could limit their abilities to swell and contract. In other studies the metal cations are bound via, interaction with polymeric groups such as carbonyl, amine and anionic groups of gelatin molecules, for example [124]. Polymeric substances like chitosan chelate with metallic ions, before precipitation is carried out conventionally. Chelating due to hydroxyl groups of poly(vinyl alcohol) have also been found to homogenously fix ferrous ions actively to the polymer matrix [128]. Poly(2-acrylamido-2-methyl-1-propanesulfonic acid) was also used due to its strong ion exchange capability, resulting in strong binding of a metallic cation on the sulfonyl groups within the polymer [127].

Integrating particles into the matrix can be accomplished by coating the surfaces with molecules that can ionically interact with the surfaces, but also, contain moieties that all them to covalently bind themselves in the polymer backbone during polymerisation [129]. Particle surfaces must then be functionalised accordingly and bound to a polymeric compound, which contains reactive double bonds in order for free-radical

polymerisation to occur [130]. Iron oxide particles were functionalised with maleic anhydride-polyethylene glycol polymer and then reacted with acrylamide via free radical polymerisation [130]. Poly-acrylic acid gels were also cross-linked using acrylic acid-coated iron oxide nanoparticles similarly. The oxygen groups of the acrylic acid directed themselves towards the positive charge of the iron oxide surface, leaving the double bond inclined to react with the rest of the polymeric chain. Crosslinking with cobalt nanoparticles was carried out using a 4-vinyl-biphenyl, via hydrophobic interactions. This molecule cross-links the cobalt nanoparticle surface with the polymer matrix, the vinyl groups in this molecule cross-link to a 2-hydroxy-ethyl-methacrylate based hydrogel. Up to 60 wt% was loaded into the gel, even with such high loading the gel remained highly elastic, with stretching up to 123% its initial length [54]. Methyl methacrylate (MMA) and styrene-based polymers were cross-linked with iron oxide by an exchange reaction. The nanoparticles were initially oleate-capped and in the initial part of the formulation methacrylate units replaced the oleate groups. Increasing the concentration of nanoparticles within a poly-MMA matrix resulted in a brittle structure due to the limited movement of the bonds. The glass transition temperature was also affected by this increase; loading between 0 – 6 wt% resulted in a rise from 99.59 to 118.98 °C. An increase also occurred for polystyrene, which changed from 72.12 to 74.30 °C [131].

A significant benefit with complex iron oxide formation is the homogenous control of particle distribution throughout the matrix by varying the length of the functional groups that act as binding sites [125]. Acrylamide (AAm) was introduced as a co-monomer by changing the ratio of the two constituents; this led to a decrease in iron content due to less binding sites being available [127]. The size in some cases can similarly be tailored by limiting the space between the active sites [132]. In a study by Feldgitscher et al. it was proposed that by controlling the hydrophilic ratio of poly(ethylene oxides) and –phobic polymer regions the growth of nanoparticles was limited to approximately 8 nm [133]. Hydrophilic moieties acted as an anchor point for Fe^{2+} ions, and the density of the polymer limited the growth phase of the particles.

3.12. Surface Functionalisation

A problem that is often experienced with particles in the nano- and micron range is that they tend to agglomerate quickly. The primary cause of their coagulation is due to Van der Waals forces acting to minimise interfacial energy; as a result, nanoparticles gather and form larger micron-sized aggregates [99]. Due to their surface-to-volume ratio, they are highly vulnerable to oxidation; hence a shielding layer is necessary for chemical stability, this layer can also help in the homogenous distribution in different mediums [105].

Particles are usually suspended in an aqueous solution, for this purpose, their ability to remain dispersed and in suspension will be key, not only for application but also for successful characterisation. Additional stabilisers can be added during, or post-synthesis, but the advantage with methods like coprecipitation and solvothermal synthesis is that they are usually one-pot synthesis methods. In this report, hydrophilic surface functionalisation moieties will be considered; however, there are also numerous compounds that be can be utilised for hydrophobic environments with hydrophobic moieties such as oleic acid [119] and various organo-silanes; like (3-Aminopropyl)triethoxysilane (APTES) or (3-Mercaptopropyl) trimethoxysilane (MPTMS), which are common capping agents [134].

Polar functional groups such as carboxylic groups (-COOH), amine groups (-NH_2), and hydroxyl groups (-OH) bind to the surface of iron oxides and have an intrinsic affinity to water due to hydrogen bonding [114]. Str et al. used 25 % citric acid, even with this coating, the particle size increased rapidly from 0.4 µm after 20 seconds, because of the formation of nanoparticle aggregates, eventually stabilising at approximately 1-1.2 µm [135]. In another case, the addition of ascorbic acid during the solvothermal process acted as a reducing agent, but the oxidised product - dehydroascorbic acid turns interestingly into an effective stabiliser, producing a Fe_3O_4 suspension which was stable for several months [136].
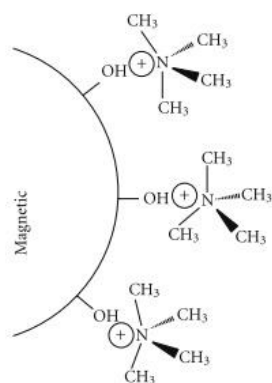
Figure 5: interaction of tetramethylammonium ions with the surface of hydroxyl ion coated magnetic nanoparticle. The cationic species ionically bind with negative hydroxyl groups, an image adapted from Andrade et al. [105].

Tetramethylammonium hydroxide (TMAOH) is often used as an effective peptising agent – this acts as a surfactant leading to improved dispersion and colloidal stability [137,138]. The interaction occurs via their -OH groups, and the tetramethylammonium ions surrounding the particles provide a cationic repulsion layer (Figure 5) [112]. Andrade et al. studied the effects of TMAOH addition as an alkalization reagent and a peptizing agent; this was in place of conventional NaOH and NH_4OH or base required to initiate precipitation of iron oxide. It was found that as an alkalization reagent in place of ammonium hydroxide resulted in larger agglomerated particle sizes [105]. Whereas, when utilised as a peptizing agent - added post-synthesis, the nanoparticles had improved dispersion and narrower distribution.

Sodium citrate coated nanoparticles showed high stability (~ 1 month in suspension), it was found to be effective due to the charge of the citrate ions, each bound citrate group consisting of three carboxyl groups which improve its affinity to water [139]. Polymer functionalisation can provide multiple functional groups, which also increase the time nanoparticles stay in suspension, as well as improve homogeneity by steric stabilisation. Wu et al. utilised sodium citrate, sodium citrate plus poly-vinylpyrrolidone (PVP) and the amino acid asparagine, all three remained stable for up to 6 months, due to the polar groups [140]. PVP is an amphiphilic polymer dispersible in a range of solvents, but also capable of forming stable colloids in water [140,141]. However, Wu et al. established that PVP had poor water solubility when used individually. Sodium citrate was also used in combination with sodium polyacrylate to form a highly-dispersed colloidal solution [117]. Polyethylene glycol is one such polymer which can control both structures as well act as a necessary stabilising agent [142].

In a review, Boyer et al. mentioned the use of Dextran, Poly(oligoethylene oxide), Poly(imine), Poly(N,N-dimethyl ethylamino acrylate) [143]. Numerous other functionalisation options have also been considered: Benzyl Alcohol [144], 2-pyrolidone [145], mPEG acid [146]. Boyer et al. reviewed numerous methods to stabilise nanoparticles using polymers [143]. It is suggested that Dopamine, Amine, Cysteine, phosphonic acid, carboxylic acid and trimethoxy silanes are all capable of reacting with iron oxide surfaces for stabilisation, but they also allow the opportunity to react further with polymers.

In some cases, the surface coating can lead to direct coupling into the polymeric chain, which provides altered mechanical properties and improved distribution [143]. Magnetite surfaces were firstly positively charged then treated with acrylic to expose the double bond of the vinyl group, suitable for further reaction. By doing so, this enabled cross-linkage of the particles into a polyacrylamide matrix [147]. Berkum et al. also proposed an alternative route, by using a ligand exchange method of oleic and acrylic acid, similarly carried out by Vo et al. Oleic acid coating on TiO_2 nanorods was replaced with short-chain carboxylic groups (acrylic acid and methacrylic acid), the outward facing vinyl groups could be used to cross-link polymer structures covalently [144,145]. Oktay et al. introduced Allyl-groups by first reacting thiodiglycolic acid, which acted as a stabiliser; the addition of allylamine provided the double bonds required for covalently cross-linking with PEG-diacrylate and PCL-diurethane acrylate [148]. Polyacrylamide gels have also been cross-linked with cobalt ferrite particles treated with Methacryloxypropyltrimethoxysilane [149]. Finally, PVA was used to cross-link iron oxide particles, by utilising amino- silica precursors [150].

To conclude, instability is unavoidable when nanoscale particles concerned, high surface energy is inherent with such solutions, unless, the surface charges have been minimised with some form of coating [114,151]. In order to preserve the magnetic properties inhibiting phase change from natural oxidation will be the biggest challenge [99]. A further benefit is colloidal stabilisation, as this will result in the homogenous distribution of particles within the hydrogel matrix, once polymerisation is complete.

3.13. Polymeric Sensors

Sensing capabilities have been conceptualised by taking advantage of the volume phase transition of environmentally sensitive polymers to produce quantitative results.

These changes are often measured from changes in volume, optical appearance, change in mass, even electrical and magnetic properties.

Visible changes are often sensed using photonic gels; they rely on the diffraction of light from the polymerised crystal colloidal (PCC) arrays as an environmentally sensitive gel undergoes a phase transition [7]. Bragg's law of diffraction is used to describe the colour change of PCC arrays in the visible spectrum as the spacing between the periodic planes determines the wavelength of light reflected [152]. Hence, photonic-based gels present a relatively straightforward method of detecting a change, as the trigger can often result in the visible change in colour from red at 660 nm to violet at 420 nm [7]. As was the case with pH and ionic strength sensitive gels based on acrylamide, the high refractive index of the embedded Fe_3O_4 nanoparticles meant that any structural change was visible by a change in colour [153]. A similar sensing device was proposed by Holtz & Asher, where crystalline colloidal arrays were able to detect Pb^{2+}, Ba^{2+} and K^+ by reflecting an intense colour [154]. Several other authors have demonstrated a similar method to detect various analytes: mercury ions [60], Fe^{3+} [155], glucose [7]. Protein sensing of bovine serum albumin was possible by combining photonic crystals and molecular imprinting [65].

The electrical property resistivity was measured for a humidity sensor, centred on a ferrite incorporated polyacrylamide-based hydrogel [156]. Change in resistivity was also notable in polyaniline containing hydrogel, which is naturally electrically conductive. The stress applied resulted in a linear decrease in resistivity as compressive stress was applied [157]. A similar concept was reported by Naficy et al. where the electrical resistance increased in the swollen state, and high conductivity in the shrunken state [158]. In another case, a piezoresistive pressure sensor was used to convert the physical pressure exerted into an electrical output signal to measure the volume change of a pH-sensitive hydrogel [159]. Similarly, Lei et al. used the pressure exerted by the swelling of the hydrogel in a micro-capacitor, which was remotely detected using a resonant circuit by picking up the frequency generated [160].

Volume change subjected by their environment also influences the mass, and alternative approaches have capitalised on this. A cantilever-based sensor was designed by coating with a gel, which had active groups to absorb metallic ions. Stress generated by the change in weight was converted to a resistance measurement by a

piezoresistive effect; the resultant change in voltage was amplified using a Wheatstone bridge circuit [161]. Micro-cantilevers can detect minute changes in bending or vibrational frequency; hence the sample sizes are proportionally smaller. Polymer brushes were applied to one side, instead of a thin film altering the surface stress. A micro-cantilever system coated with an N-isopropylacrylamide layer changed the amount of deflection during its hydrated and collapsed forms; this changed by up to 75 nm [162]. In the same report, a pH-responsive polymer also resulted in a measurable change between pH 4 – 6, altering the deflection by 121 nm/pH unit. In another study, a mass–sensitive magnetoelastic sensor platform was coupled with a pH-responsive gel. Resonant frequency decreased as the pH of the solution containing the acrylic acid-centred hydrogel was altered periodically between 4.03 and 7.02 [163].

3.13.1.   Methods of Detection

A brief overview has been delivered on the numerous methods available for detecting changes in polymers, that all have various stimuli. However, the focus in this section will be more towards detection methods that take advantage of the changing magnetic properties of a material.
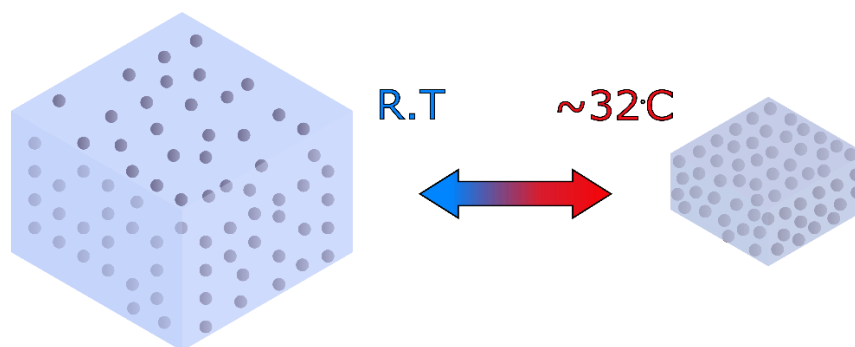
Figure 6: An illustration to show how during the volume transition in a typical PNIPAAM hydrogel additives move closer during shrinking when the temperature reaches approximately 32 °C, and further apart during cooling until room temperature (21°C).

The concept revolves around the change in distance between each particle within the hydrogel during the volume phase transition (Figure 6) changing the magnetic permeability of the material. There is an increase in the concentration of nanocomposite particles due to shrinkage that is often a detectable change. Magnetic permeability is the capacity of a material to form internal magnetic fields, often compared relatively to the permeability of free space. Song et al. used this principle to measure the change in magnetic permeability of pH-responsive ferrogel, which was

done wirelessly by monitoring the change in inductance using an impedance analyser [15].

Another material property that is often measured is the inductance – which is defined as the force generated when there is a change in current through a coil. Inductance sensors are based on a non-contact technique, thus require little maintenance and can operate in harsh conditions [164]. A Maxwell inductance bridge is a modification of a Wheatstone bridge, which can convert a small change in resistance to a much more significant change in potential difference (Figure 7) [92]. In addition to inductance, with the right modifications the standard bridge can be used to measure other quantities such as; capacitance (Maxwell-Wien Bridge) and impedance. The principle relies on an imbalance caused by entering a magnetic material into a coil. As the magnetic permeability changes the inductance, from this a voltage difference is detectable [165].
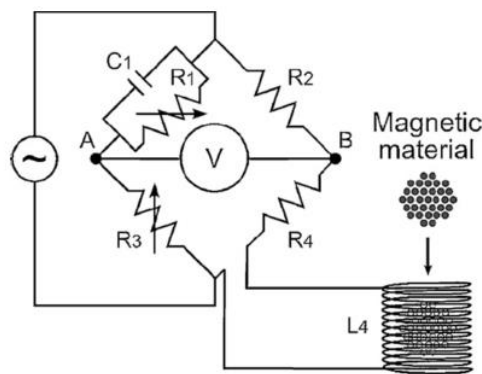
Figure 7: An illustration of a Maxwell bridge variation, which uses an inductance coil to detect the change in permeability, adapted from Tamanaha, Mulvaney, et al., (2008)*.*

An alternative sensor mechanism is a Giant Magnetoresistance (GMR) sensors measure the change in resistance due to a magnetic field. The distance of the particles either grows or move closer to each other, thereby changing the resistance of the GMR element [166]. They are preferred in small spaces and for the detection of low magnetic fields, hence their suitability in bio-related applications as biosensors. The ability to detect fields of single domain nanoparticles used as molecular markers makes them ideal for "lab on a chip" devices" [167]. Kim et al. demonstrated this by using magneto-nanosensors to detect protein biomarkers with high sensitivity [168,169]. The concept was also demonstrated by Park et al. who used a GMR sensor to detect the volume change due to the pH of an implantable hydrogel wirelessly [170].

Materials & Method

3.14. The Setup

Equipment: SR830 Lock-In Amplifier, Keithley 2000 Multimeter, TG1000 - Function Generator, Kepco power supply BOP 20-5M, EL302R - Bench Power Supply.

The inductance bridge provided the input signal for the lock-in amplifier – used to detect small changes in voltage. The amplifier was capable of generating up to 5 V, hence the addition of both power supplies and the function generator allowed up to 15 V, in order to increase the generated field strength. Keithley multimeter was used to determine changes in resistance.

From Figure 8, R1 is the arm of the bridge, which includes the empty inductance coil in which magnetic hydrogels/ ferrogels were inserted. R4 is also an identical inductance coil but used as a reference coil for balancing the bridge.
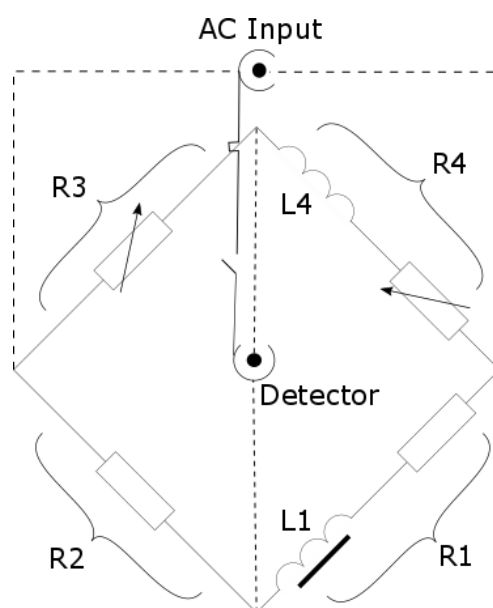
Figure 8: Diagram of the Maxwell inductance bridge, indicating the coil in which the ferrogel will be inserted (L1) and R3, the variable resistor which will be adjusted to compensate for any voltage change as the magnetic material is inserted.

3.15. NIPAAM Hydrogels:

N-Isopropylacrylamide (NIPAAM), Acrylic Acid (AAc), *N,N'*-Methylene bisacrylamide (BIS), sodium dodecyl sulfate (SDS), Iron (II) Chloride, Iron (III) Chloride, Sodium Hydroxide (NaOH), N,N,N′,N′-Tetramethylethylenediamine (TEMED), Potassium persulphate (KPS), Ethylene Glycol, Sodium acetate (NaAc), Tetramethylammonium hydroxide (TMAOH). All chemicals purchased from Sigma-Aldrich, unless stated otherwise.

3.16. Synthesis of Poly(N-isopropylacrylamide) nanogels

The method utilised was carried out previously by Xia et al., the authors in this paper optimised the synthesis, and in this synthesis protocol, we adopted the most suitable protocol provided in this paper [75]. 50 ml of distilled water was bubbled through with N_2 for 5 min in a round bottom flask. The following chemicals were then subsequently added: NIPAAM (1.13 g), BIS (0.0616 g) and KPS (0.027 g) and stirred until total dissolution had occurred. 0.27 g of SDS was added to the same solution and dissolved before the flask was sealed up, the atmosphere within was pumped with N_2 for 5 min. The temperature was raised to 60°C for 20 mins, and thereafter it was immediately sealed and transferred into an ice bath to stop the reaction. Once cooled, the solution was transferred to a sealable glass jar and used when required.

3.17. Synthesis of Poly(N-isopropylacrylamide) hydrogel with nanogels

Hydrogel monoliths were synthesised continuing from the method by Xia et al. [75]. 2.5 ml of distilled water, and previously prepared nano-gel solution were added together and bubbled through with N_2 for several minutes. The following were then added: NIPAAM (0.8 g), KPS (0.013 g). Once the ingredients had dissolved, and a clear solution was observed 40 µl of TEMED was added to initiate the reaction. It was left in a mould at room temperature for approximately 24 hours to allow a translucent gel-like material to form. They were removed, washed repeatedly and stored in distilled water.

3.18. In-situ preparation of Fe_3O_4 Poly(N-isopropylacrylamide) hydrogel

Synthesis of Fe_3O_4 nanoparticles was carried out in-situ. The gels were soaked in a Fe^{3+}/Fe^{2+} solution for 24 hours – 200 ml distilled water, 5.8 g $FeCl_3$, 2.1 g $FeCl_2$, which was then decanted. The now yellow hydrogels were transferred to a 0.5 M sodium hydroxide solution, which was bubbled through with N_2 for 5 minutes beforehand and left for a further 24 hours. The solution was decanted, and the hydrogels were washed with distilled water briefly and then replaced with degassed distilled water for storage in sealed test tubes.

3.19. Synthesis of Fe_3O_4 microspheres

40 ml of ethylene glycol, 0.81 g of FeCl$_3$ (5 mmol), 3.59 g of NaAc (43.8 mmol) were added into a beaker stirred vigorously using a homogeniser. After stirring for 30 min, the obtained yellow solution was transferred into an autoclave for 10 hours, at 200°C. The black precipitate obtained was separated by decanting the solution using a strong magnet. It was then repeatedly washed using ethanol and water. This method was adapted from the work done by Qiufeng et al. [171].

3.20. Surface coating Fe$_3$O$_4$ microspheres

The above microparticles were washed and centrifuged down into a thick slurry. The particles were transferred to a small flask, and 0.4 ml of TMAOH was added per millilitre of the slurry. The mixture was stirred using a magnetic stirrer under vacuum for 30 minutes, if the solution started bubbling the pressure was increased, by adding more holes into the Suba-Seal.

The particles were again washed numerous times with ethanol and water, using a magnet to decant the supernatant. In order to separate the stirrer bar, a weighing boat was placed blew a strong magnet, neodymium in this case and edged closer until the bar was attached. The strength of the magnet allowed the particles to attach to the weighing boat leaving the relatively bar clean.

3.21. Hydrogel preparation of pre-mixed magnetic particles

Surface coated particles from section 3.20 were mixed with the monomer-nanogel solution made in section 3.17, at different concentrations of: 0.2 mg/ml, 14 mg/ml and 100 mg/ml and cured as instructed in the same section.

3.22. Maxwell-inductance Bridge method

The initial resistance of R3 and its corresponding voltage were noted as a reference for an empty coil. The magnetic hydrogel was inserted into the coil, any change in the voltage was noted, and R3 was adjusted or referred to as trimmed from here on - to match the voltage of the empty coil. As a result of this, a new resistance was recorded, and then the process was repeated for other samples. For reference, the magnetic field strength created at each voltage tested was measured using a Gaussmeter, Table 2.

Table 2: Corresponding field strengths at the different voltages, acquired from a Gaussmeter.

Voltage	Corresponding Field Strength
1 V (0.47 Vpp)	52 A/m
5 V (2.37 Vpp)	475 A/m
15 V (7.13 Vpp)	1.59 kA/m

4. Results

4.1.1. Poly-NIPAAM Nanogels

The starting point of this project was to manufacture a robust temperature responsive hydrogel capable of significant volume changes. The inclusion of nano-fabricated gels as opposed to a standard hydrogel, improves the swelling and mechanical properties greatly, as concluded by Xia et al., [75]. The research group experimented with different reaction times and the introduction of various concentrations of nanogels, which was regarded as the best – in terms of mechanical properties was adapted further in this report.

Due to the 20-minute reaction time, the FT-IR spectra (Figure 9) is expected to contain unsaturated bonds around the 981 cm^{-1} peak. The nearest matching peak in Figure 9 is located at 991 cm^{-1} [75]. Haider et al. studied Poly-NIPAAM microgels and found the C-N peak to be in the range of 1100 – 1200 cm^{-1}, and the N-H peak between 3300 and 3500 cm^{-1}. Peaks assigned to the propyl group were located at 1381 and 1408 cm^{-1} [172]. The amide group was responsible for the peak at 1640 cm^{-1}, but in this spectra, it could be represented by either the peaks at 1654 or 1624 cm^{-1} [172]. All key features have indicated that unsaturated bonds and important features of Poly-NIPAAM are present according to literature.

SDS is used as an emulsifying agent to hinder the nucleation step and create nanogels < 100nm [75,173]. The presence of SDS in the spectra (Figure 9) will be evident, as dialysis was not used to remove unreacted precursors for analysis. Typircal features in the SDS structure are the S=O bonds and S-O. Both characteristics peaks are present at 1220 and 991 cm^{-1}, hence confirming the presence of SDS [174].
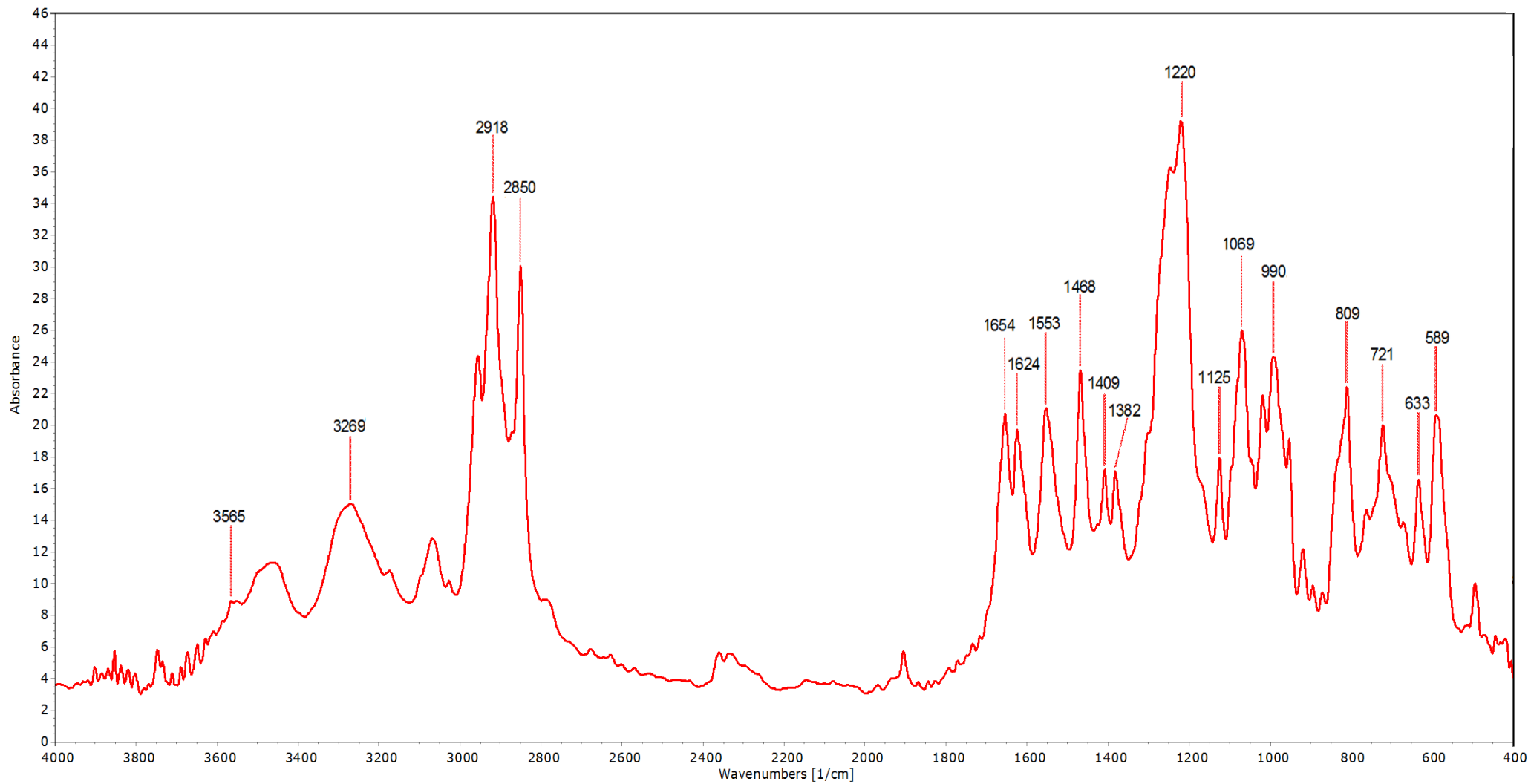
Figure 9: Spectra of freeze-dried poly-NIPAAM nanogels, which form the nanocomposites in the hydrogel, highlighting main peaks of Poly-NIPAAM and confirming the presence of SDS.

4.2. Nanoparticle Characterisation

The first method of introducing magnetic particles into the material required a dipping process, first in a solution of $FeCl_2$ and $FeCl_3$. Then proceeding to soak in NaOH solution to allow in-situ co-precipitation to occur. The following are the characterisation techniques undertaken to determine specific parameters of the nanoparticles in the polymer, the same ratio of $FeCl_2$ and $FeCl_3$ solution was mixed dropwise into NaOH to precipitate a ferrofluid solution in order to make characterisation more straightforward. The techniques where this method was applied was where the sole focus was to establish more information about the nanoparticles, i.e. oxidation state, size. For other techniques, the ferrogel structure was used, i.e. SEM, thermogravimetric analysis, and magnetic characterisation.

4.2.1. Dynamic Light Scattering (DLS)

DLS measurements are dependent on concentration, 1 and 10 µl solution of ferrofluid was diluted into a 1 ml cuvette and filled with deionised water. Both samples were sonicated for 5 minutes before analysis. The data below demonstrates the dependence on concentration. After diluting the original solution 5x, the lowest value of 79 nm was obtained, with a low PDI. Whereas adding a small quantity of the original solution had no real effect, the average diameters suggest severe agglomeration; complimented with a high PDI often associated with hetrogenous colloidal solutions.

*Table 3: Dilution of ferrofluid and the average diameter obtained using DLS, for a refractive index of 2.32. * After diluting the original solution 5x times.*

Sample	Average Diameter (nm)	PDI
1 µL	2045	0.97
10 µL	2588	0.46
1 µL*	79	0.23

4.2.2. X-ray diffraction (XRD)

XRD results below compared to the COD database suggests the state Fe_3O_4 is present. Furthermore, by using the Scherrer equation, $D_N = \frac{k\lambda}{\beta cos\theta}$, it was possible to estimate the crystalline size. Where k, the shape function value is 0.94, λ is the wavelength of the radiation, 1.54 Å; β, is the full width at half maximum and θ, is the angle corresponding to that. D_N is the crystal size, averaged from several intense peaks (311), (440), (511), it was calculated to be around 12.9 nm.
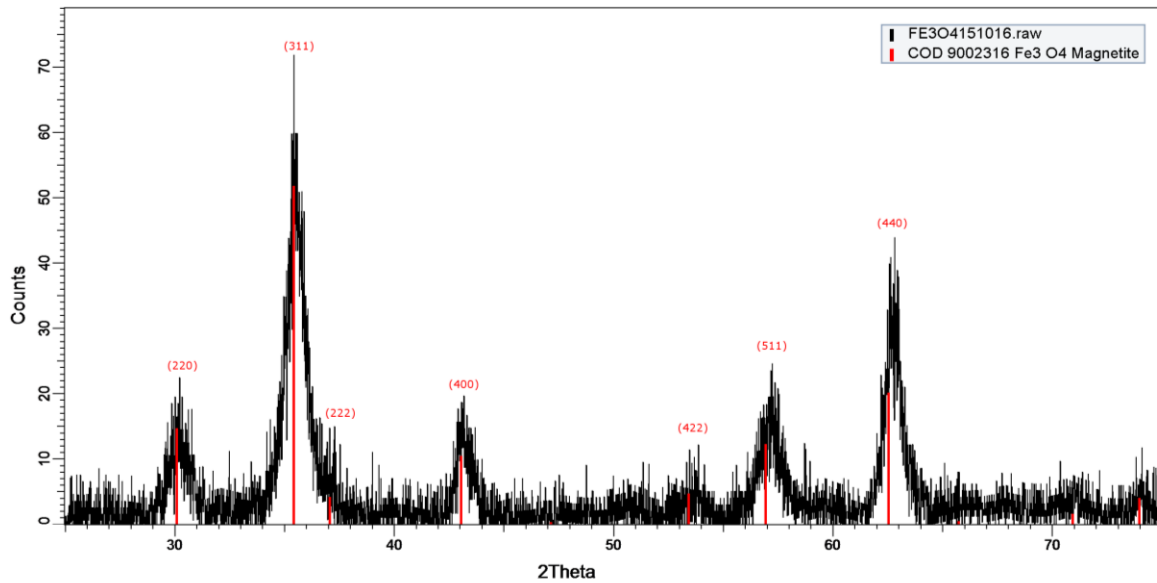
Figure 10: XRD of magnetic nanoparticles.

4.2.3. Transmission Electron Microscopy (TEM)

TEM was used to get a more accurate idea of the size, but by using selected area diffraction and high-resolution electron microscopy; it was further confirm the phase of iron oxide.

The ring pattern is indicative of a polycrystalline structure, which was analysed as standard to obtain the d-spacing, and lattice constant (Figure 11). By converting the pixel ratio to angstroms the actual diameters were determined. Standard values for both common iron oxides states, magnetite, and maghemite have been listed below for comparison.
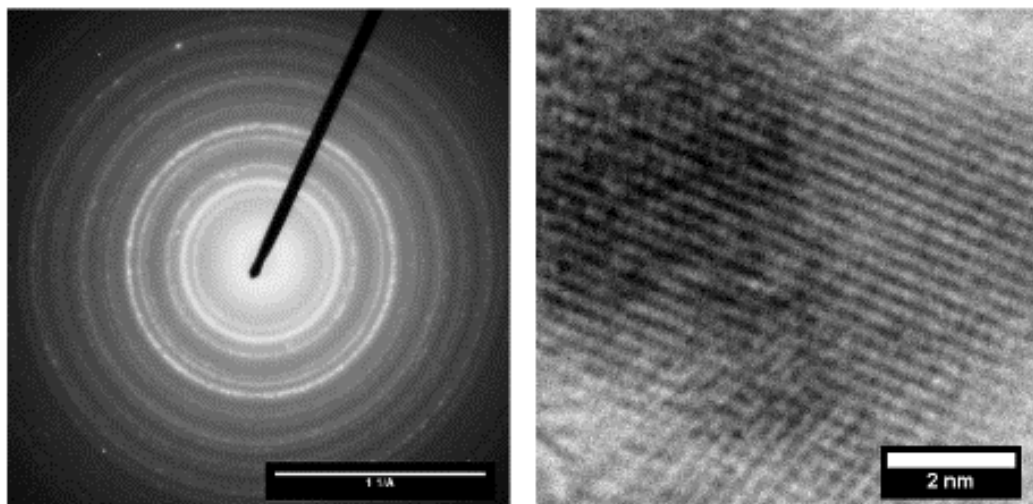
Figure 11: TEM diffraction pattern of the sample and an HRTEM image of the fringe plane (right)

These values suggest that either form is likely to be present, as database values are almost indistinguishable from one another, this is highlighted in Table 4The fringe plane was also

38

measured and averaged over 10 planes, a value of 2.57 Å, which corresponds to the (311) plane. The fringe plane intersecting this on the image above also corresponded to the (311) plane.
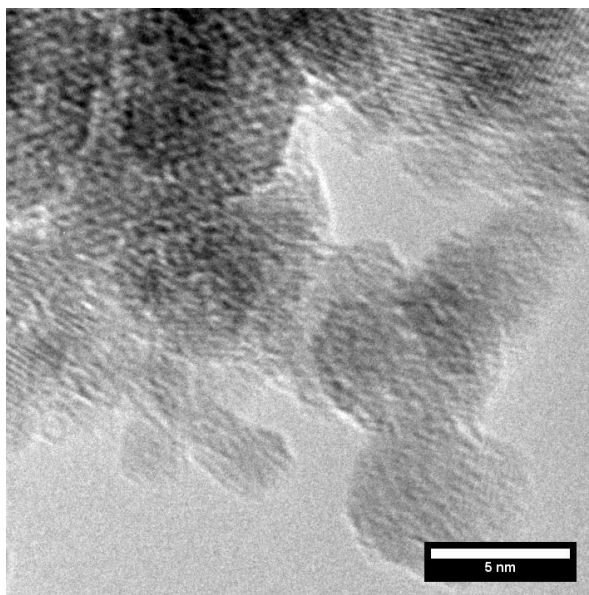
Figure 12: TEM image of magnetic nanoparticles, proposing the sizes are between 2-10 nm.

Table 4: Table below contains d-spacing values calculated from the diffraction pattern, and data for both magnetite and maghemite obtained from JCPDS file No. 19-629, and JCPDS file No. 39-1346, respectively [175]. The lattice constant of both oxides was obtained from the DIFFRAC.EVAcrystallography database.

Peak	d-spacing (Å)		
	Sample	Magnetite	Maghemite
(220)	3.13	2.9670	2.9530
(311)	2.66	2.5320	2.5177
(222)	2.22	-	-
(400)	1.83	2.0993	2.0866
(422)	1.72	1.7146	1.7045
(511)	1.57	1.6158	1.6073
(440)	1.36	1.4845	1.4758
a	8.822	8.3778	8.33

4.2.4. Thermogravimetric analysis (TGA)

Figure 13 shows the thermogravimetric analysis for the different soaking periods in each iron chloride-based solution and then NaOH; the soaking periods were done for up to 5 days. There are two clearly defined drops in mass occurring around the 115 – 200°C mark that is commonly down to water loss, which is free and absorbed – this was more than 80% up to 92% (Figure 13). Beyond this point, degradation of the pure poly-NIPAAM gel is observed in the approximate decrease of 5.6% mass of polymer gel is represent by the second decrease. The remaining mass can be partly be associated with metal oxide particles – which implies the loading is low between 3 and 6% of the total mass.
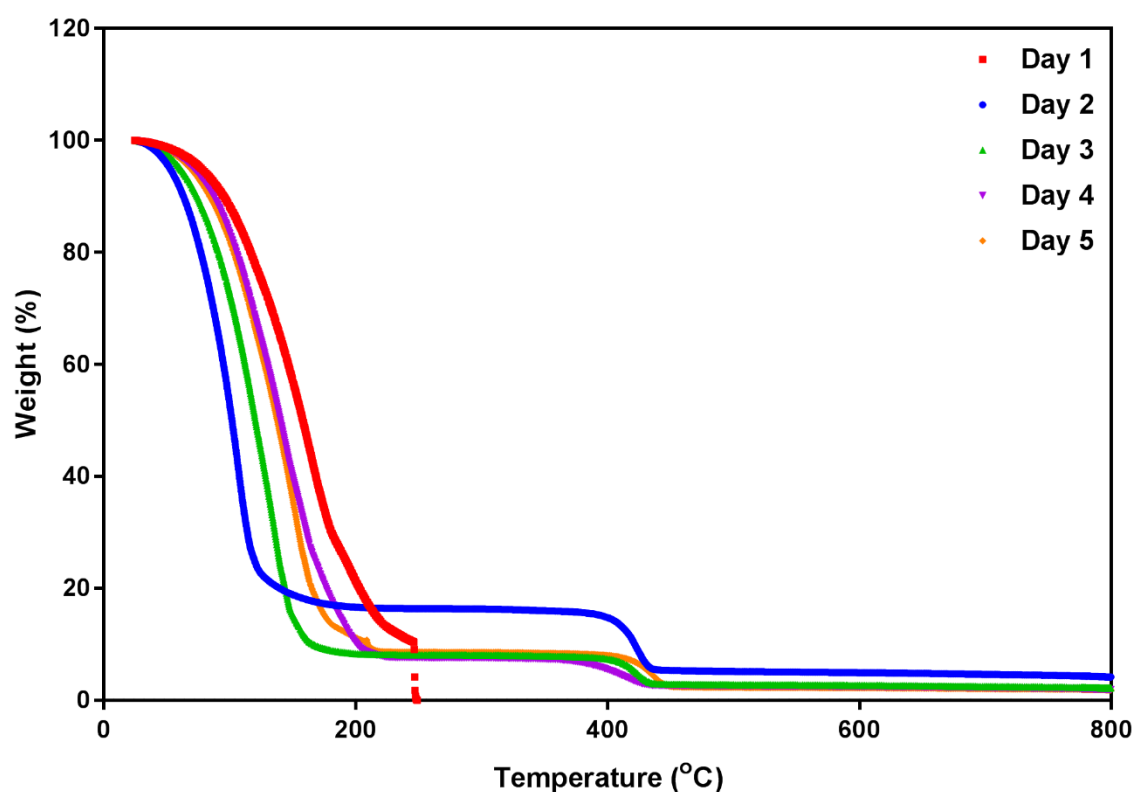
Figure 13: TGA curves for hydrogels soaked for different durations from 1 - 5 days.

4.2.5. Scanning Electron Microscopy (SEM) Images

Each gel after fabrication was soaked in a $FeCl_3$ and $FeCl_2$ solution, which was then decanted. The gels were transferred to a 0.5 M NaOH degassed vessel in order to precipitate the solid Fe_3O_4. Part of the black gels was freeze-dried and sectioned for scanning electron microscopy imaging.

SEM images show rough topography and high-intensity clusters, which can be associated with Fe_3O_4 nanoparticles (Figure 14). Measuring these high-intensity spots shows that they

are in the higher nano-range; however, this is most likely due to lack of control in the distribution of individual nanoparticles. Though a clear advantage seems to be the even coverage.
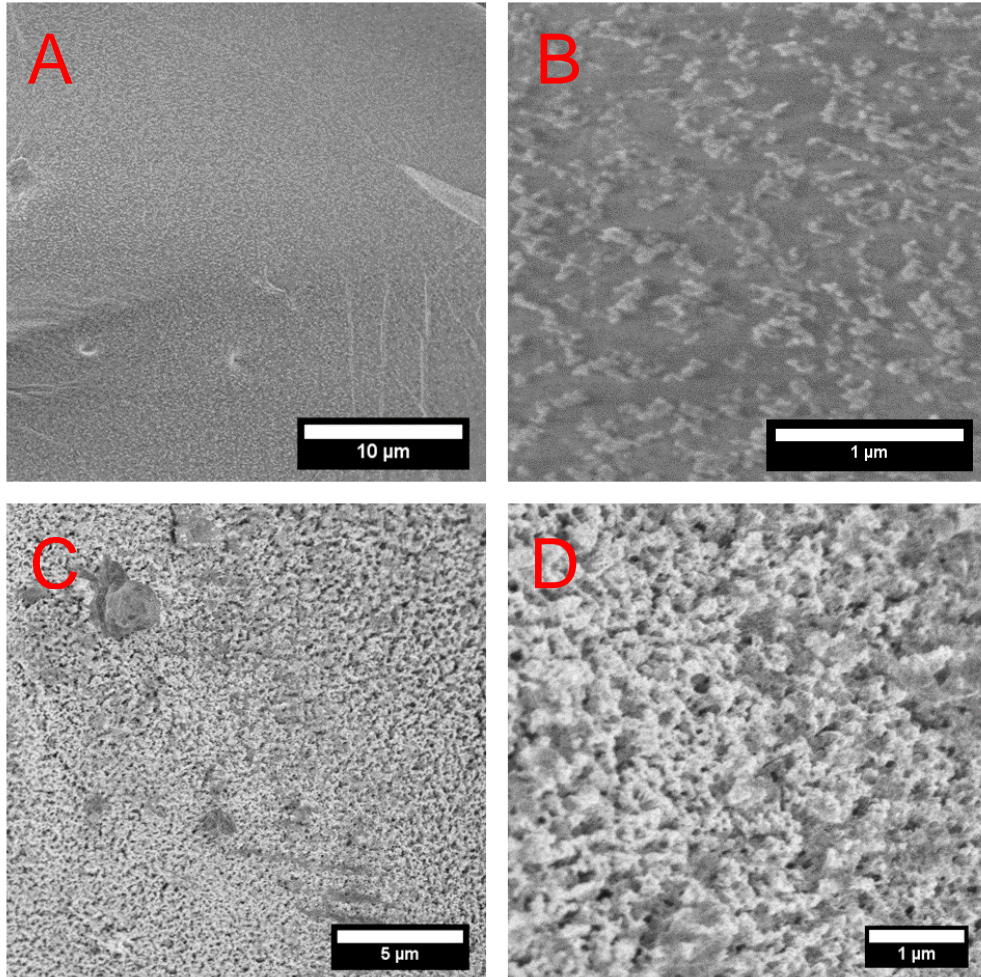
Figure 14: SEM images of in-situ precipitated ferrogels, A-B, show the even coverage on the surface, whereas the C-D show the rough surface in the cross-sectional images.

By soaking the nano-structured hydrogel in $FeCl_2$ and $FeCl_3$ solution, it was demonstrated from the cross-sections that Fe_3O_4 nanoparticles were directly embedded into the poly-NIPAAM matrix, and not just on the surface layer. It is observable in the images above (C and D).

4.2.6. Magnetic Characterisation Of Nanoparticles

Ferrogels displayed magnetic characteristics; this was demonstrated by placing a magnet close to the material – which responded by being attracted to it (Figure 15). Measurement of the magnetic properties of the samples was conducted for in-situ prepared samples using a benchtop setup that was calibrated for a known coil diameter and current (4.667 kA/m per Amp). By altering the current, the field intensity was varied, and the inductance was recorded, from which the B-H curve was plot (Figure 16). The residual magnetism was intercepted at the y-axis at approximately 0.02 T for both room temperature based gels, as well as heated to 45°C, and coercivity of the gels was found to be around -1.5 to1.9 kA/m. Interestingly, saturation was found to be 0.108 T, though no saturation was observed in the reverse field.

Figure 15: The image demonstrates the ferrogels magnetic properties using a neodymium magnet.
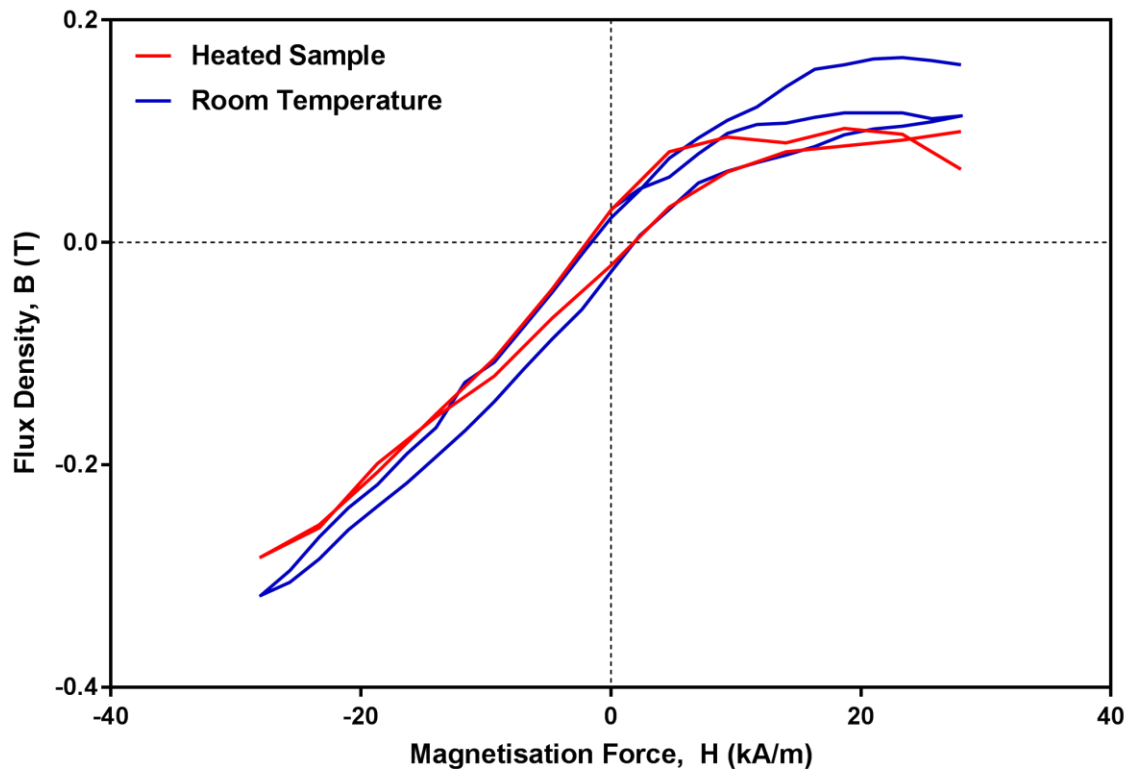
Figure 16: Magnetisation curve of in-situ prepared ferrogels, for a sample at room temperature and heated to ~ 45°C.

4.3. Microparticle Characterisation

The same characterisation techniques were applied to microparticles and gels that contained them. The driving force behind this section was to make the particles bigger, after analysis of their magnetic properties. In theory, this will lead to particles that are easily magnetisable under an applied field (See section 3.9).

4.3.1. SEM Imaging

Ferrogels produced using microparticles were imaged similarly and one immediate and notable difference is the lack of even coverage, often forming in clusters; this can be seen in Figure 17, highlighted by the red arrows. Furthermore, particles were embedded on the surface, as well as within the matrix, evidently present in the middle row (Fig 15 C-D. They can be seen protruding through the structure at different degrees, creating a rough surface texture.
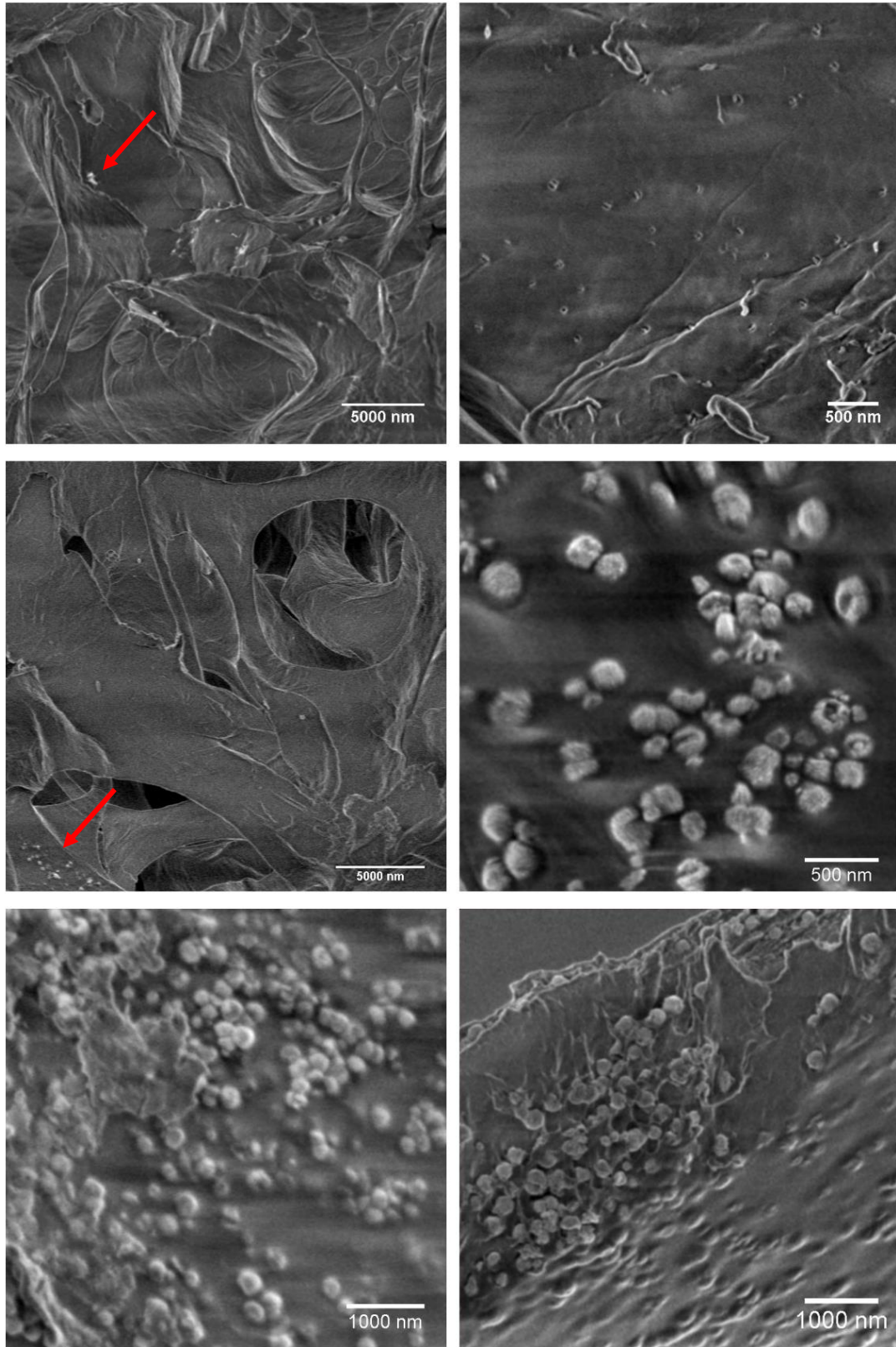
Figure 17: SEM images using a non-gold coating method to preserve the surface topography and artefacts. Ferrogels containing 0.2 mg/ml, 14 mg/ml and 100 mg/ml of iron oxide, top, middle and bottom, respectively [176] *. Arrows indicate regions that contain magnetite particles.*

4.3.2. Size

DLS results indicate a bimodal distribution, two regions around 150 – 200 nm and 375 - 475 nm are present. Sizes reaching up to 400 nm are still within the range as described by
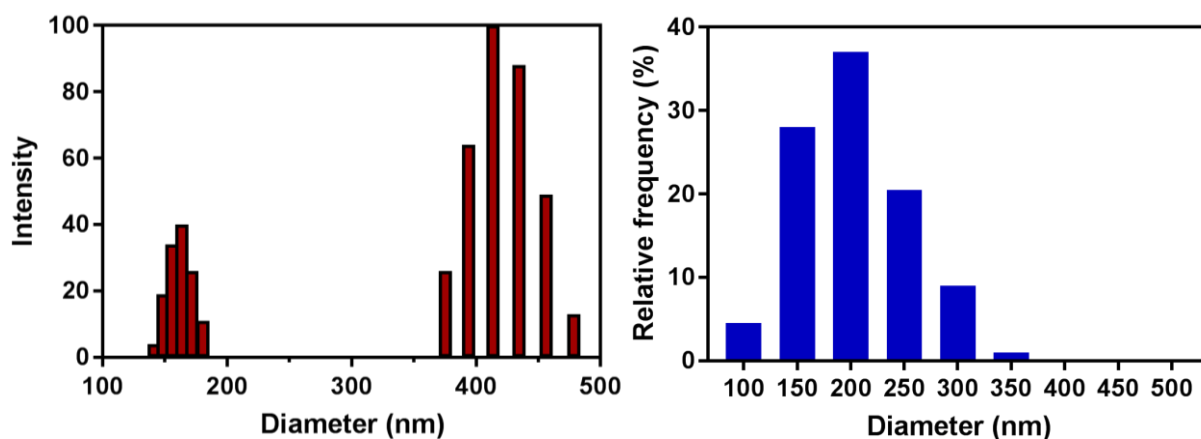
Figure 18: Size characterisation carried using DLS, and by analysing SEM images for 200 particles.

Qiufeng et al. [171]. However, the frequency distribution of the same particles measured within the matrix (Figure 19) show narrower distribution, highlighting the advantage of using the solvothermal method, the majority of which were between 140 – 240 nm.

4.3.3. XRD

XRD peaks show typical peaks expected from iron oxide particles and compared to the crystallographic open database (COD), which the peaks highly implies Fe_3O_4 as the primary phase. However, there is an absence of peaks around 37° (222) and 57° (331), the shoulder of the 222 peak is infered but not clearly defined due to the noisy region of the adjacent 311 peak. However, this spectrum still corresponded to a 96% match to the database (Figure 19). Other typical peaks around 30°, 35°, 43°, 53°, 57° and 62° were all present. The lattice parameter was calculated using the Bragg equation and using the Miller indices for each peak, the average lattice parameter was determined to be 8.39 Å, and is comparable to the lattice constant of 8.3778 Å of COD 9005812.
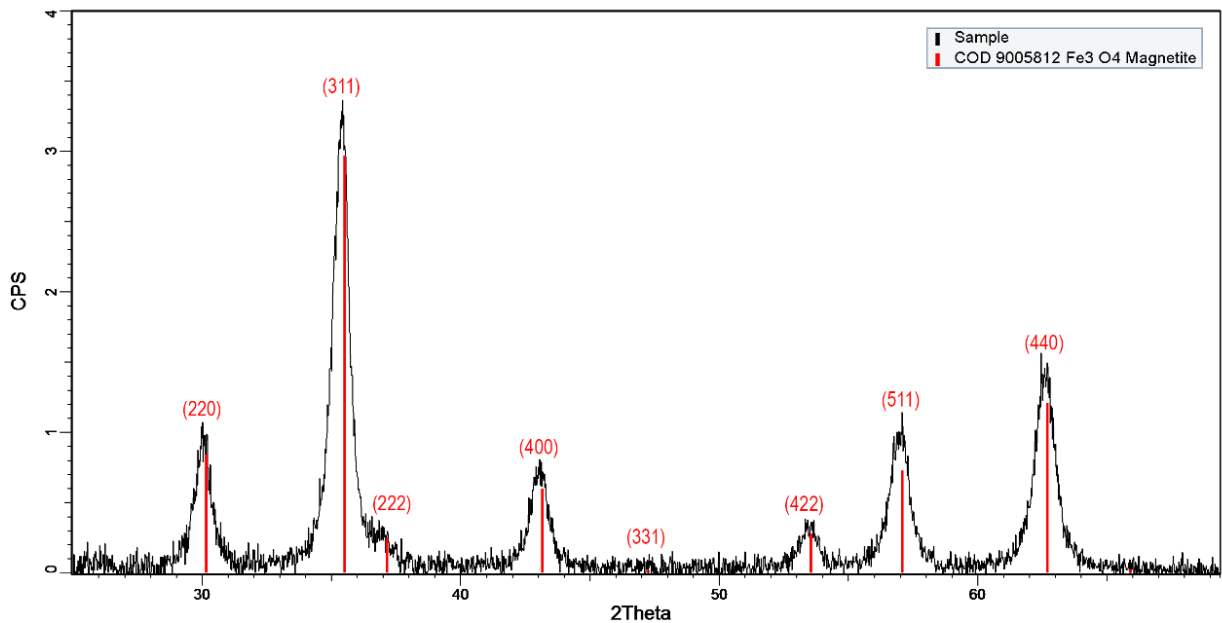
Figure 19: Comparison between the experimental peak positions and the theoretical Using Diffrac.Eva software; phase analysis shows respectable agreement to suggest the material is Fe_3O_4.

4.3.4. TGA

No significant losses are visible with TGA done on Iron-oxide microparticles as expected. A thorough drying stage beforehand meant not much water was lost around 100°C; a 2 wt% decrease is visible for both curves. There is a subtle, and gradual decomposition after this period to around 400°C due to any remaining water and TMAOH, estimated to be around 2.5%, after that TMAOH-coated particles stabilise. Interestingly, in the same region, an increase in mass is experienced for uncoated particles likely due to oxidation of the particles to Fe_2O_3, again stabilising at approximately 400°C. An unexpected decrease around 750°C occurs for both samples, which cannot be correlated with any material that may be present.
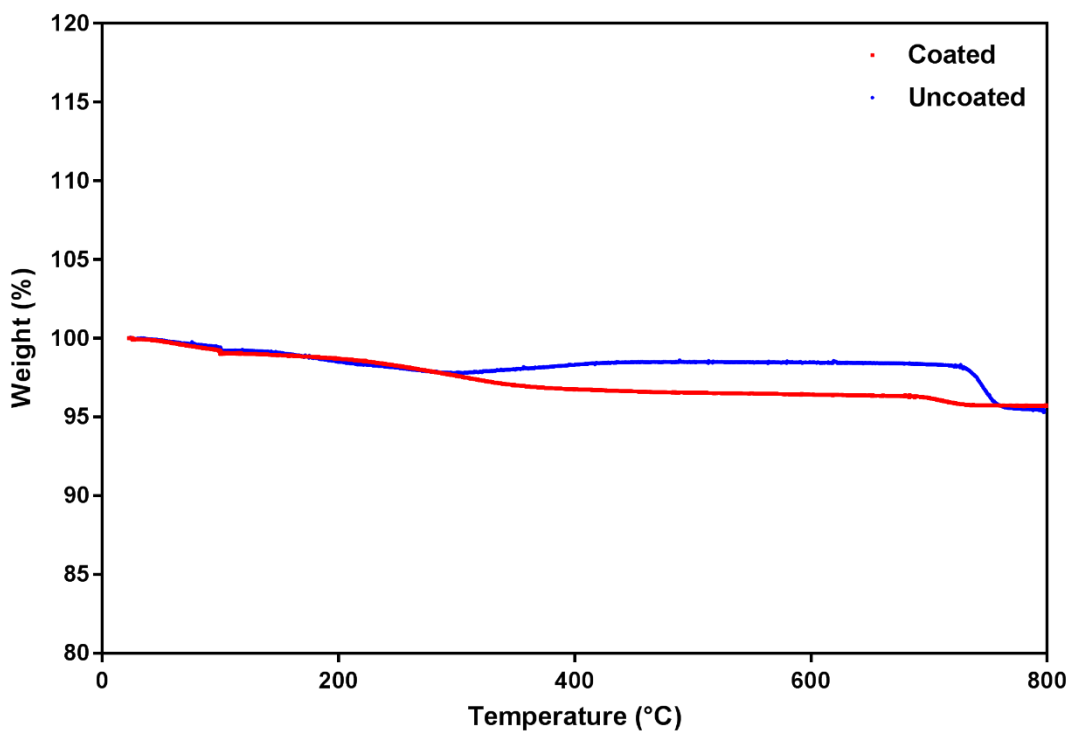
Figure 20: Mass losses observed of uncoated and TMAOH coated magnetite particles. Initial loss is at around a 100ºC, associated with water. A strange mass increase is observed at 300ºC.

4.3.5. Curing with micro-particles

Curing with and without surface coating show a notable difference in dispersion and stability of particles within the hydrogels. To coat, once the particles were washed of the ethylene glycol and unreacted species, they were bathed in 0.4 ml of TMAOH was added per millilitre of slurry, and then washed repeatedly with water. Figure 21 shows a gradient effect indicating the rapid sedimentation of iron oxide, even with a redox catalyst present – which is added for two reasons: to bring the reaction temperature down to approximately room temperature, which will prevent any destabilisation as a change in viscosity takes effect. Also, to accelerate the reaction to overcome the sedimentation effect until partial gelation has occurred. Addition of TMAOH counteracted this inadequacy due to the interaction of the particle surface and electrostatic double layer formed, increasing their stability [138]
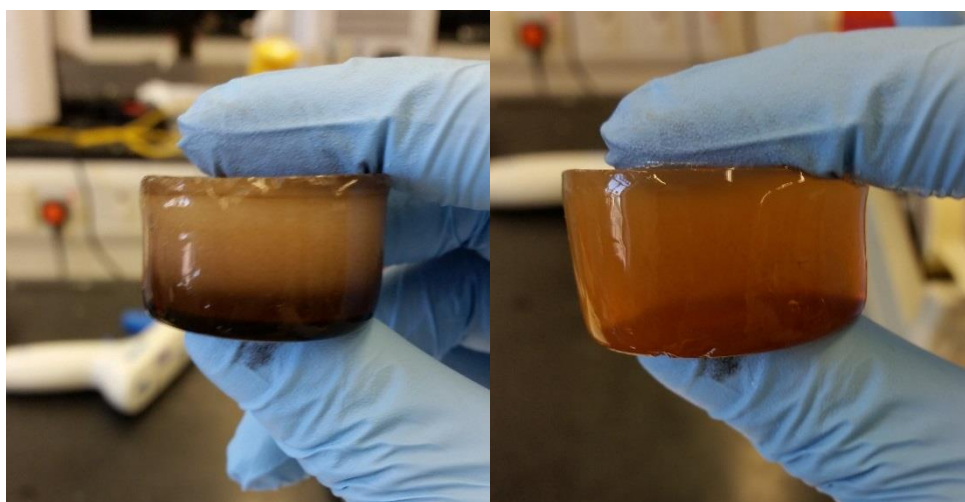
Figure 21: Images of hydrogels without (Left) and with TMAOH surface coating (Right).

4.4. Ferrogel Images
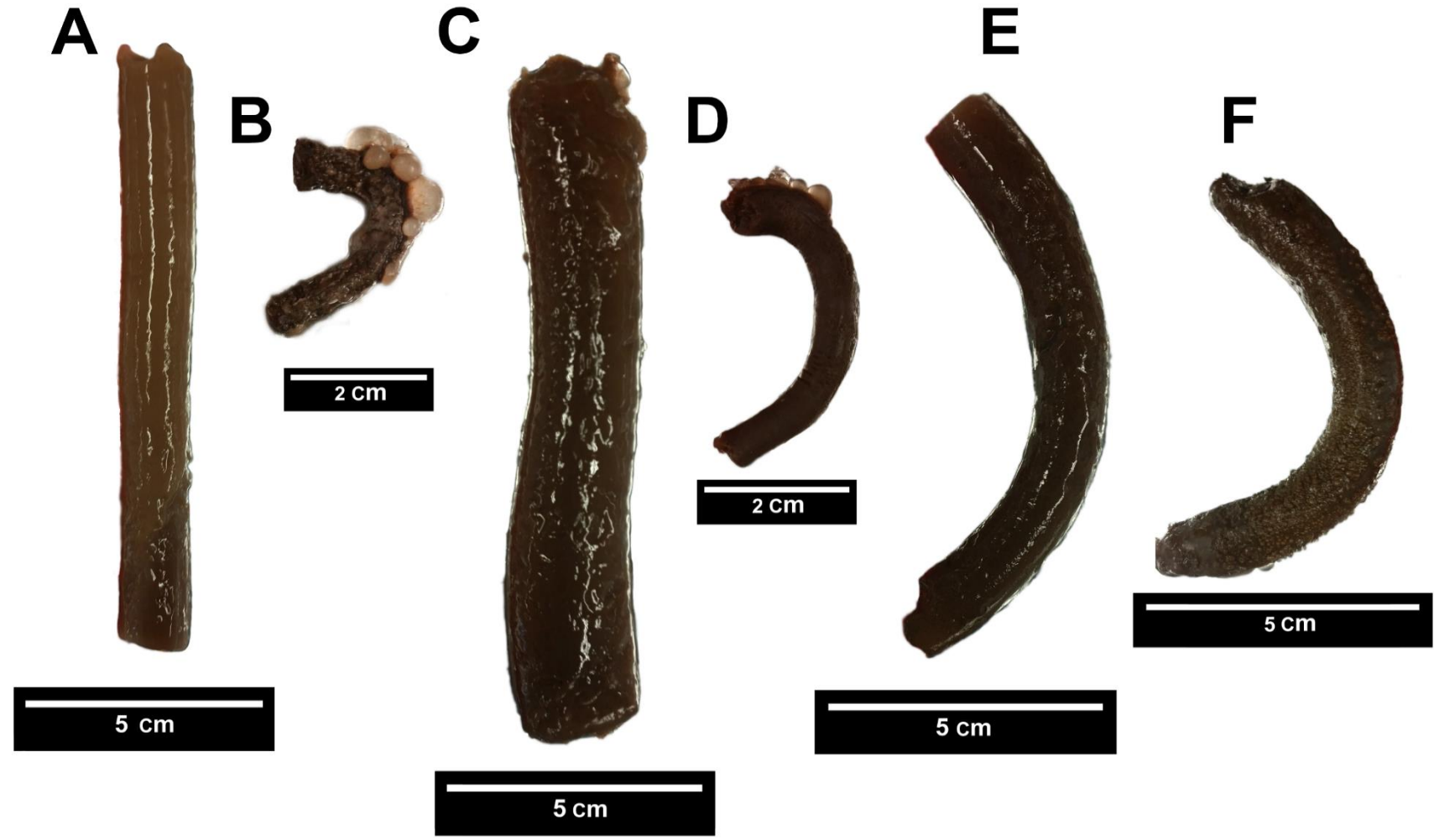
Figure 22: Ferrogels with different concentrations of iron oxide microparticles. A, C and E, corresponding to concentrations of 0.2 mg/ml, 14 mg/ml and 100 mg/ml, respectively. B, D and F are the heated states at approximately 45ºC in line with the same previous direction.

Figure 23: In situ developed ferrogels showing A, the fully hydrated state at room temperature and B, the collapsed state at approximately 45°C.

4.5. Ferrogel TGA

TGA was utilised to determine the percentage of total iron oxide within the polymeric structures. Figure 24 shows two key mass losses were around 100°C – which are associated with water removal. Then second mass loss was above 400°C due to the degradation of the Poly-NIPAAM matrix; the residual could thus be used to calculate the differences in iron oxide concentration. As expected the sample termed 100 mg/ml has 12.7 mg Fe_3O_4/ g wet hydrogel, an order of magnitude higher than 14 mg/ml and 0.01 g, that each have an estimated 1.7 and 0.58 mg/ g wet hydrogel, respectively.
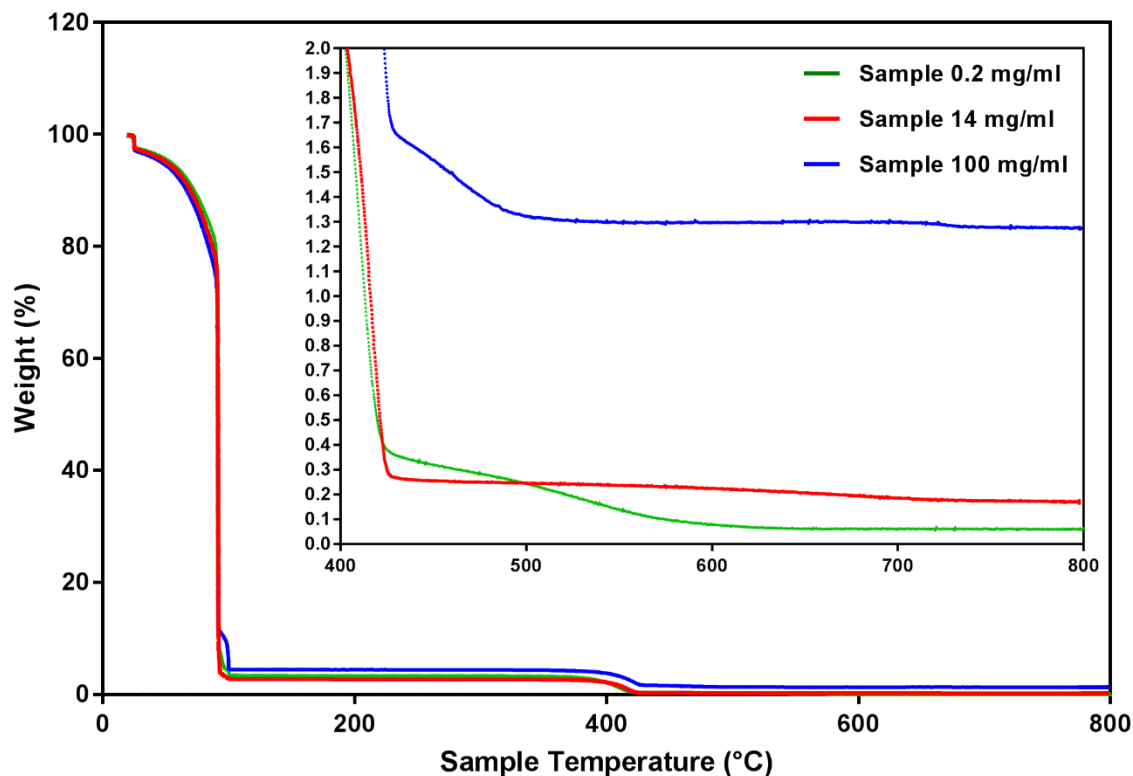
Figure 24: TGA of the three different ferrogels, to determine the concentration of iron oxide. An enhanced figure within to highlight the differences.

4.6. Swellability

The contracting of the in-situ ferrogel shown in Figure 23 is limited; as it is shown in the profile below, it reduced to 60% of its original volume. It also proposes that the LCST temperature is within 32°C. Comparing the images taken before and after heating, also show little change in terms of height and width.
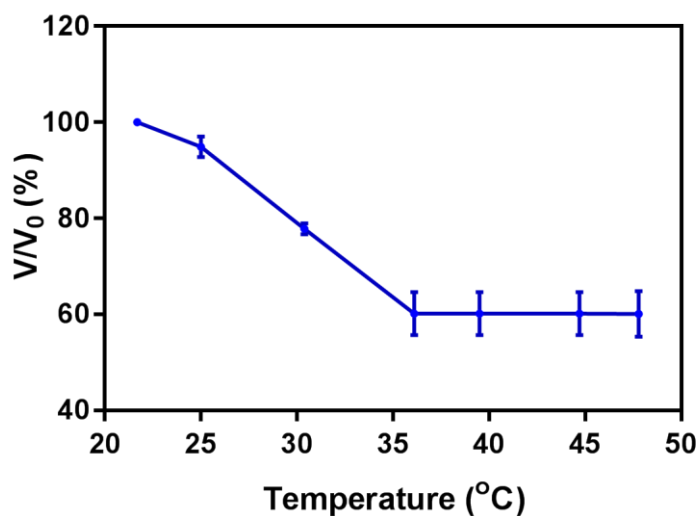
The same process was repeated with hydrogels of different concentrations of microparticles (Figure 22). Two of the concentrations used in images above (Figure 23) show a significant change in volume, the exception were gels with 100 mg/ml of iron oxide. This change in volume was consistent with all three gels measured; for the first two temperature points the standard deviation of the volume was at its highest value of 1.732 cm^3, and then improved at the contracted states where it was lower than or equal to 1 cm^3.
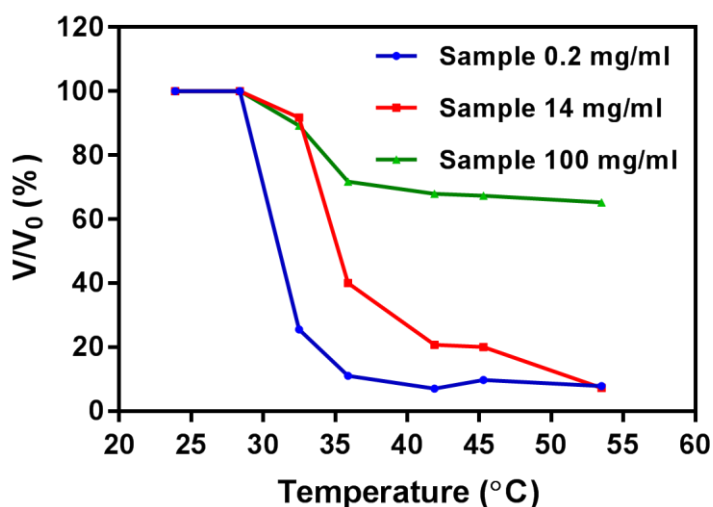
Figure 26: Change in volume concerning the temperature of several ferrogels loaded with different concentrations of Fe_3O_4.

Another interesting point that can be obtained from the graphs is the change in LCST temperatures with the concentration of particles. There is a definite shift in the temperature at which the volume phase transition occurs; this can be perceived from the transition of the curves in Figure 26, shifting to the right with increasing concentration. Also confirmed in Figure 27 and highlighted in more detail with their average changes and standard deviations (Table 5).
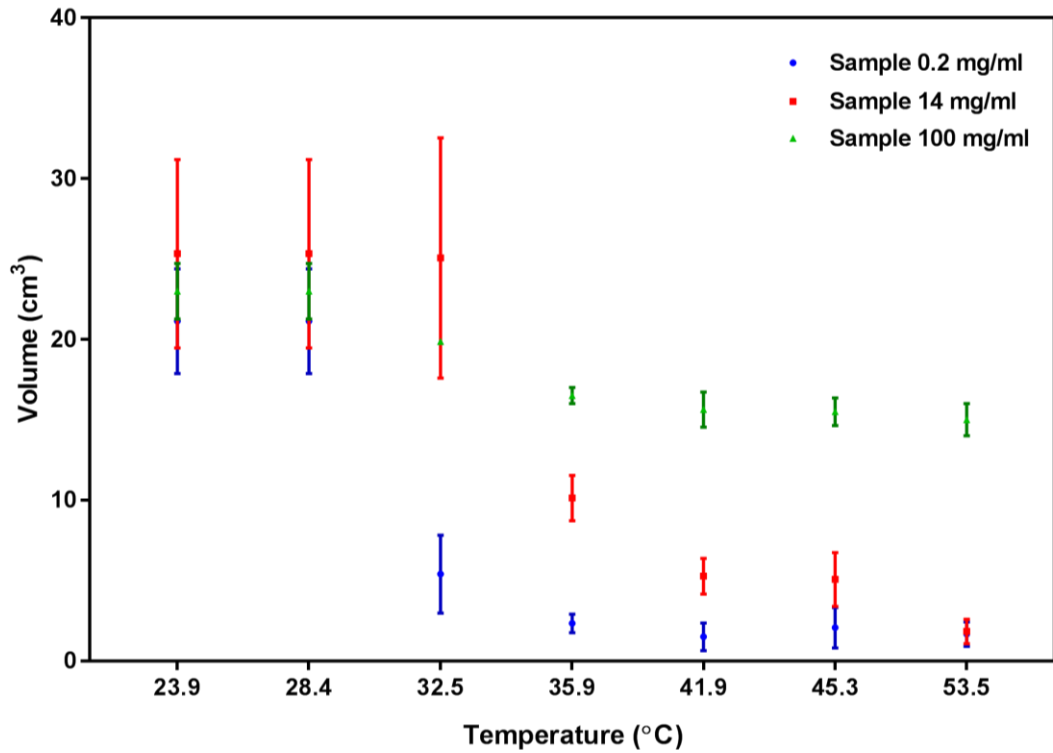
Figure 27: Volume distribution at each temperature measurement for all three concentrations of aerogels, done in triplicate.

Table 5: Average changes of three repeated measures for the different concentrations and temperatures. The averages are accompanied by the standard deviation, denoted SD.

	0.2 mg/ml		14 mg/ml		100 mg/ml	
Temp.	Mean (cm³)	SD (cm³)	Mean (cm³)	SD (cm³)	Mean (cm³)	SD (cm³)
23.9	21.1	3.3	25.3	5.9	23	1.7
28.4	21.1	3.3	25.3	5.9	23	1.7
32.5	5.4	2.4	25.1	7.5	19.9	0.1
35.9	2.3	0.58	10.1	1.4	16.5	0.5
41.9	1.5	0.87	5.3	1.1	15.6	1.1
45.3	2.1	1.3	5.1	1.7	15.5	0.87
53.5	1.7	0.8	1.8	0.7	15	1.0

Gels manufactured via the in-situ route, and those manufacture using the addition of different concentration of microparticles had different mechanical properties as a

Figure 28: Fluid-like nature of 14 mg/ml ferrogel, which had a tendency to leach out from both sides thinning the diameter as it did.

result. 100 mg/ml ferrogels, like In-situ gels, were more rigid and prone to breaking when suspended or handled as in Figure 15. Gels in general were more fluid like with 14 mg/ml of iron-oxide and able to extend multiple times its original length. An example of this is shown in Figure 28, where the gel tended to deform and gather on either side of the coil. By doing so, it was highly susceptible to fracture due to the reduction of the diameter. This formless gel had shape-memory properties, during contraction as shown in Figure 22; it regained its cylindrical shape – as it was originally moulded.

4.7.   Permeability

The change in permeability was averaged because all five gels were unaffected by soaking time. An average permeability change due to heat shrinkage was 1.15% and deviated by 0.0018%. The highest percentage change of 1.35% was attributed to 2-day soaking.

4.8.   Maxwell Inductance

Several field strengths were used corresponding to; 1 V, 2.37 V and 15 V. Results obtained from the inductance setup show marginal changes in effective permeability (U_{eff}), a ratio of the resistances before and after trimming summarised in Table 6. The same method was used for the heated samples, giving the overall change due to contraction.

Most considerable changes were for In-situ samples, 14 mg/ml and 100 mg/ml, these samples showed a definite increase in permeability by 0.29%, 0.15% and 0.57%, respectively. All these changes came from the same applied field at 1 V. No detectable change was noted for samples with the lowest concentration, most likely due to little magnetisable material present. Adverse changes are peculiar, as this is a

characteristic response of diamagnetic materials; they form magnetic moments opposing the applied field, the values perhaps highlight the limitations of the setup.

Table 6: Effective permeability of room temperature and warm samples for different concentrations and field strength.

Voltage (V)	U_{eff}	U_{eff}	Change (%)	Std. Dev. (%)
In-situ (Nanoparticles)				
1	0.9954	0.9982	0.29	0.7217
5	0.9999	0.9987	-0.12	0.0058
15	0.9980	0.9989	0.09	0.1274
Sample 0.2 mg/ml				
1	1	1	0	-
5	1	1	0	-
15	1	1	0	-
Sample 14 mg/ml				
1	0.9978	0.9993	0.15	1.0140
5	1.0000	0.9984	-0.16	0.0929
15	1.0005	0.9996	-0.09	0.1619
Sample 100 mg/ml				
1	0.9940	0.9996	0.57	0.3707
5	1.0460	0.9995	-0.06	0.1973
15	1.0010	0.9998	-0.12	0.0351

5. Discussion

5.1. Phase characterisation

The production of magnetic ferrogel composites heavily relied on the fabrication of the magnetic component, in this case, Fe_3O_4 nano- and microparticles. Phase characterisation was done to confirm the type of iron oxide using TEM and XRD spectra, and discovered the clear differentiation of phases between Fe_3O_4 and ɣ-Fe_2O_3 is difficult [112]. Although, most results obtained from standard methods such as XRD, diffraction pattern analysis seem to suggest the formation of Fe_3O_4. However, there is an ambiguity associated, due to the similar peak formation – this is due to a similar crystal structure.

The interplanar distance (d) and lattice parameter (a) to can be used to distinguish between the phases as done by Lemine *et al.*, according to the JCPDS file 19-0629 the values for the Fe_3O_4 lattice spacing are: d = 2.532 Å and a = 8.396 Å [177]. As an integrated software was used to obtain the XRD spectra Figure 10, an alternative compatible database was used (COD 9005812). Lattice constants from both databases compared well to those obtained using XRD, though the TEM diffraction pattern was 0.43 Å higher than the value of 8.39 Å stated in the database. This difference is most likely down to calibration and accuracy when measuring the ring diffractions.

Change in colour is also an initial indicator for purity; a black product is often associated with Fe_3O_4 and Fe_2O_3 has usually a brown-rust colour [109]. The brown-like appearance in the pictures above suggests the rapid oxidation of ferrogels from their original black state only after a few days seen.

A better-suited method according to various sources is to test their magnetic properties, as ɣ-Fe_2O_3 has a lower magnetic saturation value at room temperature than its counterpart [175]. Though, it is highly probable that the desired oxidation state was formed from the combination of XRD, original colour, and careful synthesis of both nano- and microparticle synthesis [171].

5.2. Size Characterisation

Size characterising such particles is difficult; their rapid tendency to agglomerate has to be controlled immediately after formation. Once dry, non-coated particles are difficult to re-disperse even through sonication – which was attempted during the initial phase of this project.

Two concentrations were initially tried; 10 µl and 1 µl of Ferro-solution per 1 ml of water, this concentration was repeated for both particle fabrication techniques, co-precipitation - expected to be within the nano-range and solvothermal, projected to be in the micron range. All concentration and size variations were sonicated for several minutes beforehand, as recommended.

Results by Qiufeng estimate the size of the microparticles to be around 365 - 407 nm, though the actual observed data shows a significant deviation from the adapted method [171]. Initial tests showed evidence of agglomeration; a decrease in average diameter from using a low concentration from 10 µl to 1 µl was observed, decreasing from 1499 nm and 1156 nm, yet still, higher than expected. Furthermore, this change in concentration negatively affected the polydispersity index (PDI) – which is a vital measure to assess the uniformity of the sample. The PDI value as recorded by the DLS is a relative polydispersity and measures the standard deviation divided by the mean. The relative polydispersity for a narrow polydisperse sample is less than 0.1, a moderate polydisperse sample is in between 0.1 and 0.4, and highly polydisperse samples are over 0.4. The PDI value indicated that the higher concentration was more homogeneous having a PDI value of 0.231, compared to 0.46. Nevertheless, both average diameter readings were too high. The process was repeated multiple times, and after further dilution, a multi-model distribution was obtained stating an average diameter of 347.6 nm (PDI: 0.117).

SEM analysis, in fact, showed that the particles were much smaller, proving the distortion is due to agglomeration. These particles were between 140 – 240 nm, significantly smaller than described in the literature, nevertheless, still within the accepted micron-range [171].

Magnetic nanoparticles were also characterised this way, again, both concentrations showed highly polydisperse distributions, 10 µl sample had the lowest PDI of 0.46, an average diameter of 2588 nm was observed. 1 µl of the sample had a PDI limit of 0.97,

typical for a broad distribution of sizes. They have indicated little effect from sonicating beforehand. However, further dilution had some positive effect, and after several attempts, the lowest average diameter was 79 nm with a PDI of 0.227. TEM results differ significantly from this assessment and indicate sizes anywhere between 1 – 10 nm, also by using the Scherer equation; the crystalline size was estimated to be 12.9 nm. The result suggests that severe agglomeration of particles has distorted the DLS reading, and is not a reliable indicator to assess individual particle size. Lim experienced flocculation of particles immediately without coating, so it is unsurprising that such an effect was observed for nanoparticles in this experiment, as they were not sonicated beforehand and with a sterically shielding layer [178]. Such layers contain groups that take up space, in order to prevent interaction from occurring - in this case, it is the particle-to-particle interaction leading to agglomeration.

DLS is highly dependent on the concentration, size and material; getting the balance right is crucial for reliable results [178]. Of the methods utilised, DLS is more suited to estimating the size of the agglomerates within the hydrogel. Numerous papers have suggested DLS to be a poor indicator of individual particle size for nano-materials due to the fast agglomeration tendencies [140]. TEM and XRD, however, are methods to estimate of the individual nanoparticles. XRD spectra for nanoparticles is noisy, and this could be the source for the small deviation of the estimated size. By adding a post-annealing step the crystallinity should improve the peak formation, another method involves refining the settings of the XRD to have longer run time and a longer duration of each step, such as the settings used by Mamani et al. [119,179].

5.3. Surface Coating

Encapsulating of iron oxide microparticles uniformly throughout the ferrogel was only possible after coating magnetic microparticles with the surface modifier, TMAOH. Before this, it can be seen gels cured displayed increased presence of magnetic material at the bottom. With the synergy of TEMED and TMAOH – one ensured fast gelation, and the latter decreased settling time of the particles, while also providing a steric repulsion layer, the particles were more uniformly distributed through the hydrogel. Even with the attempt at preventing agglomeration, results from size characterisation and images imply colloidal stability was improved, but not uniform.

TMAOH coating was used to also distribute the particles homogenously throughout the matrix, though; this does not look like it was a useful measure. SEM images show the irregular distribution of particles and some masses of agglomeration. Refining the concentration of TMAOH can be achieved via measuring the zeta potential of the particles for various concentrations to achieve greater stability [105]. In water, due to the hydroxyl ions, the potential of iron oxide particles coated with TMAOH is around - 45.0 mV [137]. Stability is dependent on pH of the solution, and due to the solution containing constituents from the manufacture of nanogels the pH is undoubtedly different when mixed with the nanogel solution, and could be the reason for this result in instability [136,180].

FTIR and TGA are a complimentary combination to assess the successful surface coating of iron oxide particles and the efficacy by decomposition at high temperatures. Iron oxide particles produce spectra with a relatively small amount of peaks. The main peak is at 550 – 700 cm^{-1} of the Fe-O interaction are present. However, both spectra are similar [105]. There is a gradual mass loss from 100 to 400°C to suggest decomposition, though this is made ambiguous due to opposing increase in mass for the control sample, this could be due to oxidation of the uncoated sample. Combined with this and the ability to form uniformly on a large scale, it can be concluded that successful stabilisation in a colloidal solution has occurred.

5.4. Ferrogels

The report shows the successful preparation of dual responsive hydrogels, that respond to magnetic and temperature stimuli. Two alternative manufacturing methods are employed: in situ co-precipitation, and a method which involved ex situ precipitation via a solvothermal step, followed by surface treatment then the immobilisation within the gel structure during polymerisation.

The main disadvantage with the in situ process is the lack of control during the precipitation phase. There was no increase in iron oxide concentration within the hydrogels by increasing soaking time after one day when the maximum concentration is achieved. This result is in agreement with findings in other studies, for example, Hernandez report on a protocol where their chitosan hydrogels are immersed in iron chloride solutions for 1 hour and up to 1 hour in NaOH [126]. Since the diffusion of iron

ions into the matrix is the primary driving process, a method to increase the iron concentration further is via increasing the swelling ability of the gel [123].

The alternate method used is to stabilise the particles in a colloidal solution (peptize) and form the hydrogel in this solution. This method allows for intricate control over concentration, morphology, crystallinity and method of synthesis – all of which are highly influential in the final magnetic properties of iron oxide. A difficulty with this method is ensuring even distribution of the nanoparticles within the material [181]. The SEM images we have been able to collect from the samples show that the iron oxide particle distribution is not entirely homogeneous and that there are regions that are sparsely populated with nanoparticles together with regions of densely packed particles within the hydrogel. This observation opens up interesting questions on the driving force for this clumping from a stable colloidal solution, but for our application, the particle distribution was of minor concern since the signal is dependent on the average density of the particles.

Addition of nanocomposite materials can aid the mechanical properties of the material in terms of swelling as well as mechanical properties – this was the primary motive of avoiding the standard construction of a hydrogel. The method adapted utilised equal volumes of 1.5 mol L^{-1} of Poly-NIPAAM nanogels cured for 40 minutes and water (2.5 ml). It was selected based on the mechanical robustness and high swelling ability as highlighted by Xia et al. [75]. There is an evident influence added particles have in its mechanical properties [82]. For example, in situ manufactured gels have a saturated matrix; this resulted in a small reduction of just 35% of its initial volume. A similar value was noted with the introduction of 100 mg/ml of microparticles; these gels also contracted by 35 - 40% of their initial value, when heated above the LSCT temperature. The behaviour suggests 100 mg/ml is almost at saturation point due to its similar properties with in situ gels. The concentration of loaded particles governed properties of ferrogels with microparticles in; from the different concentrations used the optimum for suitable mechanical properties is between the ranges of 14 – 100 mg/ml.

These findings are in agreement with other studies on nanocomposites. There is an optimum concentration for these nanocomposites, where a too low concentration of nanoparticles does not elicit the correct magnetic properties, and a too high concentration can negatively affect mechanical properties, swelling and deswelling

ability. At high concentrations of nanoparticles, it is expected that the structure will become more dense, brittle and the volume phase transition of the poly-NIPAAM matrix will become unnoticeable, similar to the effects of increasing cross-linker concentration [81,84].

Even though surface functionalisation was a preventative measure, a rapid change in colour occurred due to oxidation of the nanoparticles, indicating that the nanoparticles undergo a level of oxidation. Although this was not confirmed through characterisation methods. What is interesting to note is that the gels made with uncoated particles before the investigation into steric stabilisation remained an unvarying black colour. According to Hernandez et al., polymeric structures can act as a barrier to prevent oxidation, and particles that are on the surface can be oxidised more readily than those enclosed within the polymer [123]. In this case, the surfaces of the particles within the gel were brown, which is commonly associated with maghemite. It would be beneficial to compare the magnetic properties of both gels in order to establish if a phase change had occurred.

5.5. Magnetic Characterisation

Magnetic particles in the nano-scale achieve saturation at a slower degree and also require stronger magnetic fields for saturation to be achieved. Nano-particles studied by Santoyo et al. around 12 – 15 nm experienced similar coercivity of 1.5 – 1.9 kA/m as those produced via the in-situ route measured to be around 1.6 – 2 kA/m [98]. Saturation magnetisation was observed for both conditions between 0.9 and 0.11 T, this is similar than values found for similar sizes that can be anywhere between 0.3 – 0.43 T, for sizes between 4 – 15 nm [102]. Both heated and room temperature samples have similar remanence, coercivity and magnetic saturation properties, confirming there was little effect due to heat. As the samples show little retention of magnetic properties, according to Figure 4, it can be deduced that these ferrogels contain nanoparticles that are single-domain structures, and the size is approaching the superparamagnetic range [96].

The difference in magnetic properties can be due to the manufacturing method - low-temperature co-precipitation often results in poor crystallinity; hence, a post-annealing process is employed to improve the quality of the magnetic particles [119,182]. Kolhatkar et al. found that magnetic properties of nanocube exceeded nanosphere

structures, a higher degree of crystallinity had also higher magnetic saturation [183] - this could help explain the lower values found for magnetic saturation.

This was repeated for a sample containing 14 mg/ml of Fe_3O_4 microparticles, which was unsuccessful; little to no variation was visible in the inductance measurements when the current was altered. Undoubtedly due to the small amount of magnetic material present in the hydrogel, thus requiring either more material or generation of a stronger magnetic field.

The method employed in this project was an in-house method. It was limited to a small application of current to prevent the coil from overheating. For every 0.5 Amp increase in current, the magnetic field strength was measured. 6 A was the maximum current applied for measuring the inductance of in-situ prepared ferrogels, and for gels with microparticles, the current was extended to about 7 A before the coil started to heat up. Ability to generate a high field strength is the main limitation of the current setup. In this case, a magnetic field strength of up to 25 kA/m was achieved whereas, in literature strengths of 560 kA/m [184], 800 kA/m [117,140], and 1,400 kA/m [98] have been utilised.

5.6. Magnetic Sensing

A detectable change in permeability is notable for the small voltage applied (1 V), even though the change is around 1%. 2-day soaking showed the higher change of 1.35%, this interestingly correlates with the apparent increase in nanoparticles – as calculated through TGA analysis. The limitations of which are due to the single-domain characteristics of the nanoparticles, and the small applied field strength. Using the same material in a Maxwell-inductance bridge, however, resulted in a small change in signal of 0.29%, with the lowest voltage applied (0.47 V). At 15 V this was reduced to a change of 0.09%.

No apparent change was visible for any applied field with 2 mg/ml of particles, more likely due to the low concentration of particles. For higher concentration materials, the most considerable change was for 100 mg/ml (0.57%), and 14 mg/ml gave a 0.15% change in signal. No relationship can be drawn from increasing size of the particles as well as increasing the concentration of particles, even though a sample containing 100 mg/ml of microparticles had the highest reported change. The result conflicts what is reported by Tamanaha et al., the output signal from a Maxwell bridge is proportional

to the concentration of magnetic material [165], which somewhat agrees with the response with 100 mg/ml of Fe_3O_4 during contraction, but it was not consistently observed. A similar conclusion can be made for increased voltage, as the several positively registered values were for the lowest voltage tested (1 V). The spread of triplicate datasets is averaged with negative values, reducing the overall change, hence changes in permeability overall were lower than those obtained for in situ gels using the permeability test. By omitting the negative results as erroneous it increases the values to 0.58 and 1.74%, for 14 mg/ml and 100 mg/ml.

The magnitude of negative values outweighed any positive values that were calculated, distorting the readings. Relative permeability less than 1 is associated with diamagnetic materials [185], as the material within has been characterised as an iron-oxide variety – known to be ferrimagnetic. Of the naturally occurring minerals, it produces the most substantial magnetic response [96,109]. The fact that the standard deviations are also higher than the recorded values implies the problem is more to do with the sensitivity of the setup. Another theory is that the negative values are due to the incomplete balancing of the bridge; nevertheless, more work is needed to confirm these statements.

There is some optimism that the chosen method can be successful considering the setup registers detectable changes with the in situ manufactured samples. The inductance setup will have to be modified to overcome the current hurdles and limitations.

.

6. Conclusion

Magnetic hydrogels were created using two different methods; in-situ co-precipitation, and by surface coating microparticles produced via a solvothermal route, before embedding them into a poly-NIPAAM matrix. To achieve homogenous suspension of iron oxide, surface coating with tetramethylammonium hydroxide was vital. The functional groups increased the time in suspension, as well as providing a repulsion layer to prevent agglomeration in the ferrofluid.

Characterisation using XRD of both sizes produced suggest the material is Fe3O4, the distinguishing black colour also confirms this. Size analysis confirmed in-situ particles were on average 12 nm, whereas solvothermal particles were in the micron-range around 200 nm.

In-situ prepared ferrogels and gels that contained 100 mg/ml of the polymer of Fe_3O_4 displayed similar contracting characteristics. Those that contained 2 mg/ml and 100 mg/ml showed similar traits as well, decreasing by 93% of their original volume. Swelling studies also imply an increase in the natural LCST temperature of Poly-NIPAAM, normally reported around 32°C. For 14 mg/ml it was between 28.4 – 32.5°C and between 32.5 – 41.9°C, for 100 mg/ml. The work is in agreement that particle concentration has some influence on the LSCT temperature of hydrogels.

Varying soaking time did not affect iron oxide concentration. Hence the permeability of each in-situ gel was similar; a 1.15% change was detected. Using the inductance bridge, however, resulted in an average 0.09% change. Gels formed using magnetic microparticles resulted in inconclusive results, though with optimising of the setup there is enough to suggest that using a Maxwell inductance setup to sense the volumetric changes of environmentally responsive ferrogels is possible.

7. Further work

Work presented in this project provides a set of instructions on how to manufacture dual responsive hydrogels for future work. The success of this sensing method now lies in acquiring a detectable concentration of magnetic material and optimising the setup to measure this change.

7.1. Material

The concentration of magnetic particles currently utilised suggest an optimum range that balances both mechanical properties and swelling ability. Iron oxide loaded between 14 mg/ml and 100 mg/ml should be investigated, due to the highly fluid nature of samples with 14 mg/ml and almost rigid with 100 mg/ml. Furthermore, this will also provide more insight into the reduced swelling ability that was experienced with the last sample. It would be interesting to characterise the mechanical properties of all the hydrogels tested to reinforce the physical observations empirically.

Currently, the material in question – NIPAAM is an on-off responsive polymer. Complex polymers that display gradual transitions would be the ideal goal for further research.

Another issue that requires attention is the apparent oxidation of iron oxide, and this readily occurred in-situ and via surface coating. Optimisation of TEMED should be investigated, or consider the use of a polymeric layer to stabilise the chemical and magnetic properties.

It is suspected that the lack of response in the inductance bridge is down to the low quantity of magnetic material, increasing the nanocomposite material should result in more notable changes or using a material with higher magnetisation properties.

7.2. Setup

Another hurdle was adapting the setup to experiment using different coil sizes as inductance is dependent on several factors: Number of turns, coil length and area, as well as permeability of the magnetic core, optimising this could improve the output signal.

8. Appendix

8.1.   Initial PolyHIPE

Picking emulsions were the initial focus, with the goal to eventually create an oil-in-water emulsion stabilised with magnetic particles, and the water-soluble PNIAAM as the monomer.

Initially, work was done with poly-high internal phase emulsions, optimising the synthesis process using an oil-in-water emulsion and utilising the same combination of NIPAAM, MBAM, KPS and mineral oil. The images below show the development during this period; what is most apparent is the inconsistency of the final product (Figure 29).

The washing & drying procedure played an essential part as it led to Inconsistencies in the final samples as shown below. The images depict varying degrees of visual discrepancies. These differences were due to not using the Soxhlet apparatus, as they were instead left to soak in DCM for a whole day by stirring and replacing the solvent - this was carried out up to 4 times. One of the later attempts, which was washed with a soxhlet (*left*) displayed an opaque, spongey - yet brittle nature, which appeared to have no oil present. On the contrary, the rest were translucent to some degree – which was generally experienced when the sample contained oil.

Changing the solvent from DCM to hexane improved the quality of the final product further, removing oil from the core.

Figure 29: variation of quality during the initial phases of the project. The appearance on the right-hand side shows an oil retaining Poly-HIPE after several attempts of washing. Other parameters such as changing the oil and using a solvent, which was highly miscible in the oil later, improved the quality.

Fumed silica was used to form the composite material, in order to grasp and understand the concept of a picking poly-HIPE (Figure 30). The SEM shows no visible indication of the silica nanoparticles, as the sizes are less than 10 nm.
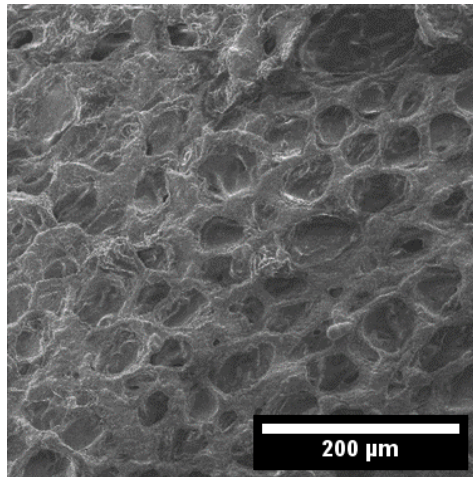
Figure 30: Pickering poly-HIPE, formulated using NIPAAM as temperature responsive polymer template from an oil-in-water emulsion. The collapsed structure indicates the material initially had a porous architecture.

The difficulty in formulating and drying iron-oxide nanoparticles lead to other methods being tested and for example, adding Sodium 4-vinylbenzenesulfonate (Na4VBS) into the matrix so that the positive Fe ions exchange with the sodium ions when the structures are soaked in an iron chloride solution. After in situ co-precipitation was carried out by the addition of NaOH, a brown magnetic structure was left, evident of Fe_2O_3 formation (Figure 31).

Poly-HIPEs were determined not to be the best option due to the poor mechanical properties and difficulty formulating a consistently oil-free poly-HIPE structure; hence, the attention was turned to hydrogels
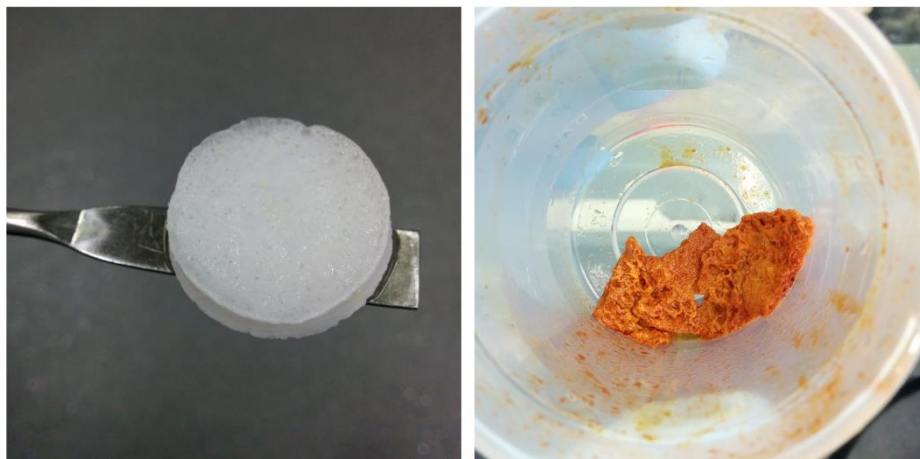
Figure 31: Poly-NIPAAM HIPE with added Na4VBS, before (Right) and after in situ co-precipitation was carried out.

9. FTIR

Figure 37 shows photoacoustic spectra of uncoated particles – which was used as a control sample, and the TMAOH surface-coated samples, attached to the hydroxyl groups on the iron oxide surface. The sharp peak around the fingerprint region corresponds to the Fe-O band around the 570 - 600 cm^{-1}. Peaks generally above the 3000 cm^{-1} mark are associated with O-H stretching vibration. Additionally there is also a weak -OH around the 1622 - 1640 cm^{-1} peak due to bending vibration. Whereas, Cheng et al., attributed the 1649 cm^{-1} peak to the C-N stretching of the $N(CH_3)_4OH$ [186]. The presence of clearly defined peaks between 2200 – 2400 cm^{-1} indicates the presence in the chamber of CO_2 [187]. The spectrum matches up with other reports of FTIR spectra of Fe_3O_4 [104,139,188]
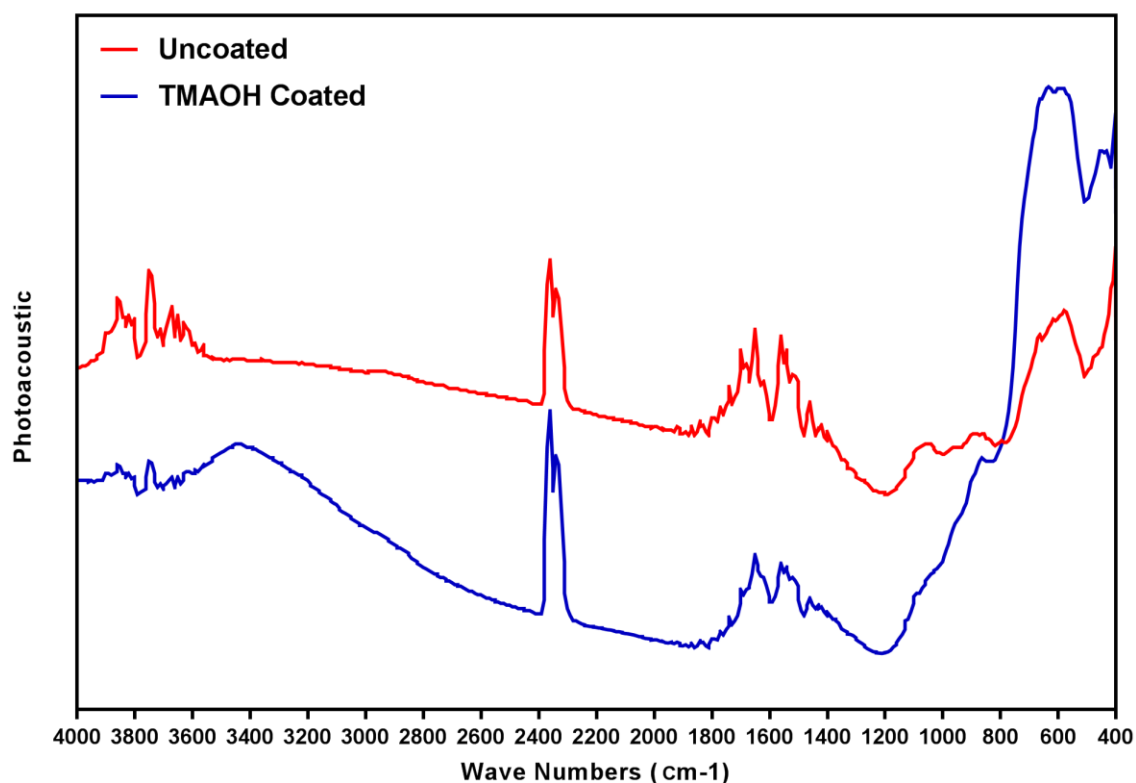
Figure 32: FTIR-PA spectra of uncoated Fe_3O_4 microparticles and with the surface modifier TMAOH.

10. References

1. Silverstein, M. S. Emulsion-templated porous polymers: A retrospective perspective. *Polymer (Guildf).* **55,** 304–320 (2014).

2. Alotaibi, S. S. & Riffat, S. Vacuum insulated panels for sustainable buildings: A review of research and applications. *International Journal of Energy Research* **38,** 1–19 (2014).

3. Chen, G., Qiao, C., Wang, Y. & Yao, J. Synthesis of magnetic gelatin and its adsorption property for Cr(VI). *Ind. Eng. Chem. Res.* **53,** 15576–15581 (2014).

4. Schattling, P., Jochum, F. D. & Theato, P. Multi-stimuli responsive polymers – the all-in-one talents. *Polym. Chem.* **5,** 25–36 (2014).

5. Bruvera, I. J., Hernández, R., Mijangos, C. & Goya, G. F. An integrated device for magnetically-driven drug release and in situ quantitative measurements: Design, fabrication and testing. *J. Magn. Magn. Mater.* **377,** 446–451 (2015).

6. Reddy, N. N. *et al.* Temperature responsive hydrogel magnetic nanocomposites for hyperthermia and metal extraction applications. *J. Magn. Magn. Mater.* **394,** 237–244 (2015).

7. Alexeev, V. L., Das, S., Finegold, D. N. & Asher, S. A. Photonic crystal glucose-sensing material for noninvasive monitoring of glucose in tear fluid. *Clin. Chem.* **50,** 2353–2360 (2004).

8. Zhang, N. *et al.* Facile Preparation of Magnetic Poly(styrene-divinylbenzene) Foam and Its Application as an Oil Absorbent. *Ind. Eng. Chem. Res.* **54,** 11033–11039 (2015).

9. Boyaci, T. & Orakdogen, N. pH-responsive poly(N,N-dimethylaminoethyl methacrylate-co-2-acrylamido-2-methyl-propanosulfonic acid) cryogels: swelling, elasticity and diffusive properties. *RSC Adv.* **5,** 77235–77247 (2015).

10. Matanović, M. R., Kristl, J. & Grabnar, P. A. Thermoresponsive polymers: Insights into decisive hydrogel characteristics, mechanisms of gelation, and promising biomedical applications. *International Journal of Pharmaceutics* **472,** 262–275 (2014).

11. Caló, E. & Khutoryanskiy, V. V. Biomedical applications of hydrogels: A review of patents and commercial products. *European Polymer Journal* **65,** 252–267 (2015).

12. Bazban-Shotorbani, S. *et al.* Revisiting structure-property relationship of pH-responsive polymers for drug delivery applications. *Journal of Controlled Release* **253,** 46–63 (2017).

13. Lue, S. J., Chen, C. & Shih, C. Tuning of Lower Critical Solution Temperature (LCST) of Poly(N-Isopropylacrylamide-co-Acrylic acid) Hydrogels. *J. Macromol. Sci. Part B* **50,** 563–579 (2011).

14. Getachew, B. A., Kim, S. R. & Kim, J. H. Self-Healing Hydrogel Pore-Filled Water Filtration Membranes. *Environ. Sci. Technol.* **51,** 905–913 (2017).

15. Song, S. H., Park, J. H., Chitnis, G., Siegel, R. A. & Ziaie, B. A wireless chemical sensor featuring iron oxidenanoparticle-embedded hydrogels. *Sensors Actuators, B Chem.* **193,** 925–930 (2014).

16. Beebe, D. J. *et al.* Functional hydrogel structures for autonomous flow control inside microfluidic channels : Abstract : Nature. *Nature* **404,** 588–590 (2000).

17. Lee, Y.-J. & Braun, P. V. Tunable Inverse Opal Hydrogel pH Sensors. *Adv. Mater.* **15,** 563–566 (2003).

18. Shibata, H. *et al.* Injectable hydrogel microbeads for fluorescence-based in vivo continuous glucose monitoring. *Proc. Natl. Acad. Sci.* **107,** 17894–17898 (2010).

19. van Berkum, S., Dee, J., Philipse, A. & Erné, B. Frequency-Dependent Magnetic Susceptibility of Magnetite and Cobalt Ferrite Nanoparticles Embedded in PAA Hydrogel. *Int. J. Mol. Sci.* **14,** 10162–10177 (2013).

20. Okay, O. General Properties of Hydrogels. in 1–14 (2009). doi:10.1007/978-3-540-75645-3_1

21. Richter, A. *et al.* Review on Hydrogel-based pH Sensors and Microsensors. *Sensors* **8,** 561–581 (2008).

22. Ashraful Alam, M., Takafuji, M. & Ihara, H. Thermosensitive hybrid hydrogels

with silica nanoparticle-cross-linked polymer networks. *J. Colloid Interface Sci.* **405,** 109–117 (2013).

23. Qiu, Y. & Park, K. Environment-sensitive hydrogels for drug delivery. *Adv. Drug Deliv. Rev.* **64,** 49–60 (2012).

24. Zhao, Z. B., Xie, H. J., Li, Y. L. & Jiang, Y. A multi-responsive multicomponent hydrogel with micro-phase separation structure: Synthesis and special drug release. *J. Drug Deliv. Sci. Technol.* **35,** 184–189 (2016).

25. Wang, J., Li, Q., Yi, S. & Chen, X. Visible-light/temperature dual-responsive hydrogel constructed by α-cyclodextrin and an azobenzene linked surfactant. *Soft Matter* **13,** 8 (2017).

26. Magnusson, J. P. *et al.* Ion-sensitive 'isothermal' responsive polymers prepared in water. *J. Am. Chem. Soc.* **130,** 10852–10853 (2008).

27. Heller, A. Electron-conducting redox hydrogels: design, characteristics and synthesis. *Current Opinion in Chemical Biology* **10,** 664–672 (2006).

28. Gökçeören, A. T., Şenkal, B. F. & Erbil, C. Effect of crosslinker structure and crosslinker/monomer ratio on network parameters and thermodynamic properties of Poly (N-isopropylacrylamide) hydrogels. *J. Polym. Res.* **21,** 370 (2014).

29. Sun, X., Shi, J., Xu, X. & Cao, S. Chitosan coated alginate/poly(N-isopropylacrylamide) beads for dual responsive drug delivery. *Int. J. Biol. Macromol.* **59,** 273–281 (2013).

30. Patel, N. G. & Zhang, G. Responsive systems for cell sheet detachment. *Organogenesis* **9,** 93–100 (2013).

31. Zhang, J. *et al.* Thermo-responsive microcarriers based on poly(N-isopropylacrylamide). *Eur. Polym. J.* **67,** 346–364 (2015).

32. Wang, Y. Q., Zhang, Y. Y., Wu, X. G., He, X. W. & Li, W. Y. Rapid facile in situ synthesis of the Au/Poly(N-isopropylacrylamide) thermosensitive gels as temperature sensors. *Mater. Lett.* **143,** 326–329 (2015).

33. Islam, M. R., Xie, S., Huang, D., Smyth, K. & Serpe, M. J. Poly (N-

Isopropylacrylamide) microgel-based optical devices for humidity sensing. *Anal. Chim. Acta* **898,** 101–108 (2015).

34. Hilmi, B., Hamid, Z. A. A., Akil, H. M. & Yahaya, B. H. The Characteristics of the Smart Polymeras Temperature or pH-responsive Hydrogel. *Procedia Chem.* **19,** 406–409 (2016).

35. Kim, S., Lee, K. & Cha, C. Refined control of thermoresponsive swelling/deswelling and drug release properties of poly(N-isopropylacrylamide) hydrogels using hydrophilic polymer crosslinkers. *J. Biomater. Sci. Polym. Ed.* **27,** 1698–1711 (2016).

36. Katono, H. *et al.* Thermo-responsive swelling and drug release switching of interpenetrating polymer networks composed of poly (acrylamide-co-butyl methacrylate) and poly (acrylic acid). *J. Control. Release* **16,** 215–228 (1991).

37. Aoki, T. *et al.* Temperature-Responsive Interpenetrating Polymer Networks Constructed with Poly (acry1ic acid) and. *Macromolecules* **27,** 947–952 (1994).

38. Gandhi, A., Paul, A., Sen, S. O. & Sen, K. K. Studies on thermoresponsive polymers: Phase behaviour, drug delivery and biomedical applications. *Asian Journal of Pharmaceutical Sciences* **10,** 99–107 (2015).

39. Roy, D., Brooks, W. L. A. & Sumerlin, B. S. New directions in thermoresponsive polymers. *Chem. Soc. Rev.* **42,** 7214 (2013).

40. Yin, X., Hoffman, A. S. & Stayton, P. S. Poly(N-isopropylacrylamide-co-propylacrylic acid) copolymers that respond sharply to temperature and pH. *Biomacromolecules* **7,** 1381–1385 (2006).

41. Bearat, H. H., Lee, B. H., Valdez, J. & Vernon, B. L. Synthesis, characterization and properties of a physically and chemically gelling polymer system using poly (NIPAAm-co-HEMA-acrylate) and poly (NIPAAm-co-cysteamine). *J. Biomater. Sci. Polym. Ed.* **22,** 1299–1318 (2011).

42. Hellweg, T., Dewhurst, C. D., Eimer, W. & Kratz, K. PNIPAM-co-polystyrene core-shell microgels: Structure, swelling behavior, and crystallization. *Langmuir* **20,** 4330–4335 (2004).

43. De, K. S. *et al.* Equilibrium swelling and kinetics of pH-responsive hydrogels:

Models, experiments, and simulations. *J. Microelectromechanical Syst.* **11,** 544–555 (2002).

44. Horkay, F., Han, M. H., Han, I. S., Bang, I. S. & Magda, J. J. Separation of the effects of pH and polymer concentration on the swelling pressure and elastic modulus of a pH-responsive hydrogel. *Polymer (Guildf).* **47,** 7335–7338 (2006).

45. Schmaljohann, D. Thermo- and pH-responsive polymers in drug delivery. *Advanced Drug Delivery Reviews* **58,** 1655–1670 (2006).

46. Swift, T., Swanson, L., Geoghegan, M. & Rimmer, S. The pH-responsive behaviour of poly(acrylic acid) in aqueous solution is dependent on molar mass. *Soft Matter* **12,** 2542–2549 (2016).

47. Nesrinne, S. & Djamel, A. Synthesis, characterization and rheological behavior of pH sensitive poly(acrylamide-co-acrylic acid) hydrogels. *Arab. J. Chem.* **10,** 539–547 (2017).

48. Lee, E. & Kim, B. Preparation and characterization of pH-sensitive hydrogel microparticles as a biological on-off switch. *Polym. Bull.* **67,** 67–76 (2011).

49. Arizaga, A., Ibarz, G., Piñol, R. & Urtizberea, A. Encapsulation of magnetic nanoparticles in a pH-sensitive poly(4-vinyl pyridine) polymer: A step forward to a multi-responsive system. *J. Exp. Nanosci.* **9,** 561–569 (2014).

50. Risbud, M. V, Hardikar, A. A., Bhat, S. V & Bhonde, R. R. pH-sensitive freeze-dried chitosan-polyvinyl pyrrolidone hydrogels as controlled release system for antibiotic delivery. *J. Control. Release* **68,** 23–30 (2000).

51. Emileh, A., Vasheghani-Farahani, E. & Imani, M. Preparation and characterization of pH-sensitive microgels of poly((2-dimethylamino) ethyl methacrylate). in *Macromolecular Symposia* **255,** 1–7 (2007).

52. Sacrista, J. & Asi, L. Magnetic Hydrogels Derived from Polysaccharides with Improved Specific Power Absorption : Potential Devices for Remotely Triggered Drug Delivery. 12002–12007 (2010).

53. Emi, T. T. *et al.* Pulsatile Chemotherapeutic Delivery Pro fi les Using Magnetically Responsive Hydrogels. *ACS Biomater. Sci. Eng.* (2018). doi:10.1021/acsbiomaterials.8b00348

54. Fuhrer, R., Athanassiou, E. K., Luechinger, N. A. & Stark, W. J. Crosslinking metal nanoparticles into the polymer backbone of hydrogels enables preparation of soft, magnetic field-driven actuators with muscle-like flexibility. *Small* **5,** 383–8 (2009).

55. Tang, S. C. N., Yan, D. Y. S. & Lo, I. M. C. Sustainable wastewater treatment using microsized magnetic hydrogel with magnetic separation technology. *Ind. Eng. Chem. Res.* **53,** 15718–15724 (2014).

56. Mody, V. V *et al.* Magnetic nanoparticle drug delivery systems for targeting tumor. *Appl. Nanosci.* **4,** 385–392 (2013).

57. Jalili, N. A., Muscarello, M. & Gaharwar, A. K. Nanoengineered thermoresponsive magnetic hydrogels for biomedical applications. *Bioeng. Transl. Med.* **1,** 297–305 (2016).

58. Crippa, F. *et al.* Dynamic and biocompatible thermo-responsive magnetic hydrogels that respond to an alternating magnetic field. *J. Magn. Magn. Mater.* **427,** 212–219 (2017).

59. Satarkar, N. S. & Hilt, J. Z. Magnetic hydrogel nanocomposites for remote controlled pulsatile drug release. *J. Control. Release* **130,** 246–251 (2008).

60. Qin, J. *et al.* Fabrication of intelligent photonic crystal hydrogel sensors for selective detection of trace mercury ions in seawater. *J. Mater. Chem. C* **5,** 8482–8488 (2017).

61. Wang, X., Ye, G. & Wang, X. Hydrogel diffraction gratings functionalized with crown ether for heavy metal ion detection. *Sensors Actuators B* **193,** 413–419 (2014).

62. Asher, S. A., Sharma, A. C., Goponenko, A. V & Ward, M. M. Photonic crystal aqueous metal cation sensing materials. *Anal. Chem.* **75,** 1676–1683 (2003).

63. Heo, Y. J., Shibata, H., Okitsu, T., Kawanishi, T. & Takeuchi, S. Fluorescent hydrogel fibers for long-term in vivo glucose monitoring. in *2011 16th International Solid-State Sensors, Actuators and Microsystems Conference, TRANSDUCERS'11* 2140–2143 (2011). doi:10.1109/TRANSDUCERS.2011.5969342

64.   Rein V. Ulijn *et al.* Bioresponsive hydrogels. *Mater. Today* **10,** 40–48 (2007).

65.   Hu, X., Li, G., Huang, J., Zhang, D. & Qiu, Y. Construction of self-reporting specific chemical sensors with high sensitivity. *Adv. Mater.* **19,** 4327–4332 (2007).

66.   Miyata, T., Asami, N. & Uragami, T. A reversibly antigen-responsive hydrogel. *Nature* 766–769 (1998).

67.   Plunkett, K. N., Berkowski, K. L. & Moore, J. S. Chymotrypsin responsive hydrogel: Application of a disulfide exchange protocol for the preparation of methacrylamide containing peptides. *Biomacromolecules* **6,** 632–637 (2005).

68.   Cameron, N. R. High internal phase emulsion templating as a route to well-defined porous polymers. *Polymer (Guildf).* **46,** 1439–1449 (2005).

69.   Liu, C. *et al.* Molecular Imprinting in Fluorescent Particle Stabilized Pickering Emulsion for Selective and Sensitive Optosensing of λ‑Cyhalothrin. (2013).

70.   Efthimiadou, E. K., Tapeinos, C., Tziveleka, L.-A., Boukos, N. & Kordas, G. pH-and thermo-responsive microcontainers as potential drug delivery systems: Morphological characteristic, release and cytotoxicity studies. *Mater. Sci. Eng. C. Mater. Biol. Appl.* **37,** 271–7 (2014).

71.   Si, T. *et al.* Effect of acrylic acid weight percentage on the pore size in poly(N-Isopropyl acrylamide-co-acrylic acid) microspheres. *React. Funct. Polym.* **71,** 728–735 (2011).

72.   Garcia, A. *et al.* Photo-, thermally, and pH-responsive microgels. *Langmuir* **23,** 224–229 (2007).

73.   Guragain, S., Bastakoti, B. P., Ito, M., Yusa, S.-I. & Nakashima, K. Aqueous polymeric micelles of poly[N-isopropylacrylamide-b-sodium 2-(acrylamido)-2-methylpropanesulfonate] with a spiropyran dimer pendant: quadruple stimuli-responsiveness. *Soft Matter* **8,** 9628 (2012).

74.   Mou, C.-L. *et al.* Monodisperse and fast-responsive poly(N-isopropylacrylamide) microgels with open-celled porous structure. *Langmuir* **30,** 1455–64 (2014).

75.   Xia, L.-W. *et al.* Nano-structured smart hydrogels with rapid response and high

elasticity. *Nat. Commun.* **4,** 2226 (2013).

76. Wan, T. *et al.* Crosslinker effects on swelling and gel properties of pH- and temperature-responsive poly (NIPAM/IA/AM) hydrogels. *Polym. Bull.* **73,** 1447–1458 (2016).

77. Lee, W. F. & Lin, Y. H. Swelling behavior and drug release of NIPAAm/PEGMEA copolymeric hydrogels with different crosslinkers. *J. Mater. Sci.* **41,** 7333–7340 (2006).

78. Obeso-Vera, C., Cornejo-Bravo, J. M., Serrano-Medina, A. & Licea-Claverie, A. Effect of crosslinkers on size and temperature sensitivity of poly(N-isopropylacrylamide) microgels. *Polym. Bull.* **70,** 653–664 (2013).

79. Kratz, K., Hellweg, T. & Eimer, W. Influence of charge density on the swelling of colloidal poly(N-isopropylacrylamide-co-acrylic acid) microgels. *Colloids Surfaces A Physicochem. Eng. Asp.* **170,** 137–149 (2000).

80. Korotych, O. *et al.* N-isopropylacrylamide-based fine-dispersed thermosensitive ferrogels obtained via in-situ technique. *Mater. Sci. Eng. C* **33,** 892–900 (2013).

81. Bin Imran, A., Seki, T., Takeoka, Y. & Imran, A. Bin. Recent advances in hydrogels in terms of fast stimuli responsiveness and superior mechanical performance. *Polym. J.* **42,** 839–851 (2010).

82. Du, Z., Hu, Y., Gu, X., Hu, M. & Wang, C. Poly(acrylamide) microgel-reinforced poly(acrylamide)/hectorite nanocomposite hydrogels. *Colloids Surfaces A Physicochem. Eng. Asp.* **489,** 1–8 (2016).

83. Petter Jelle, B. Traditional, state-of-the-art and future thermal building insulation materials and solutions â€" Properties, requirements and possibilities. *Energy Build.* **43,** 2549–2563 (2011).

84. Mathesan, S., Rath, A. & Ghosh, P. Molecular mechanisms in deformation of cross-linked hydrogel nanocomposite. *Mater. Sci. Eng. C* **59,** 157–167 (2016).

85. Haraguchi, K., Takehisa, T. & Fan, S. Effects of clay content on the properties of nanocomposite hydrogels composed of poly(N-isopropylacrylamide) and clay. *Macromolecules* **35,** 10162–10171 (2002).

86. Takafuji, M., Alam, M. A., Goto, H. & Ihara, H. Microspherical hydrogel particles based on silica nanoparticle-webbed polymer networks. *J. Colloid Interface Sci.* **455,** 32–38 (2015).

87. Gaharwar, A. K., Rivera, C. P., Wu, C. J. & Schmidt, G. Transparent, elastomeric and tough hydrogels from poly(ethylene glycol) and silicate nanoparticles. *Acta Biomater.* **7,** 4139–4148 (2011).

88. Zheng, C. & Huang, Z. Microgel reinforced composite hydrogels with pH-responsive, self-healing properties. *Colloids Surfaces A Physicochem. Eng. Asp.* **468,** 327–332 (2015).

89. Manchanda, K. Magnetic Susceptibility. *Britannica* (2006). doi:10.1016/j.ces.2008.07.028

90. Issa, B., Obaidat, I. M., Albiss, B. A. & Haik, Y. Magnetic nanoparticles: Surface effects and properties related to biomedicine applications. *International Journal of Molecular Sciences* **14,** 21266–21305 (2013).

91. Stoker, M. R. Electricity and magnetism. *Anaesth. Intensive Care Med.* **10,** 62–64 (2009).

92. Williams, D. Electricity and magnetism. *Anaesth. Intensive Care Med.* **18,** 360–363 (2017).

93. Spaldin, N. 1. Review of Basic Magnetostatics. in *Magnetic Materials: Fundamentals and Applications* 3–13 (2010).

94. J. M. D. Coey. *Magnetism and Magnetic Materials Covering. Cambridge University Press* (Cambridge University Press, 2010). doi:10.1016/0304-8853(84)90352-4

95. Lopez, J. A., González, F., Bonilla, F. A., Zambrano, G. & Gómez, M. E. SYNTHESIS AND CHARACTERIZATION OF Fe 3 O 4 MAGNETIC NANOFLUID. *Rev. Latinoam. Metal. y Mater.* **30,** 60–66 (2010).

96. Akbarzadeh, A., Samiei, M. & Davaran, S. Magnetic nanoparticles: preparation, physical properties, and applications in biomedicine. *Nanoscale Res. Lett.* **7,** 1–13 (2012).

97. Teja, A. S. & Koh, P.-Y. Synthesis, properties, and applications of magnetic iron oxide nanoparticles. *Prog. Cryst. Growth Charact. Mater.* **55,** 22–45 (2009).

98. Santoyo Salazar, J. *et al.* Magnetic iron oxide nanoparticles in 10-40 nm range: Composition in terms of magnetite/maghemite ratio and effect on the magnetic properties. *Chem. Mater.* **23,** 1379–1386 (2011).

99. Mahmoudi, M., Sant, S., Wang, B., Laurent, S. & Sen, T. Superparamagnetic iron oxide nanoparticles (SPIONs): Development, surface modification and applications in chemotherapy. *Advanced Drug Delivery Reviews* **63,** 24–46 (2011).

100. Ström, V., Olsson, R. T. & Rao, K. V. Real-time monitoring of the evolution of magnetism during precipitation of superparamagnetic nanoparticles for bioscience applications. *J. Mater. Chem.* **20,** 4168 (2010).

101. Fang, M., Ström, V., Olsson, R. T., Belova, L. & Rao, K. V. Rapid mixing: A route to synthesize magnetite nanoparticles with high moment Synthesis and aging effect of spherical magnetite nanoparticles for biosensor applications Rapid mixing: A route to synthesize magnetite nanoparticles with high moment. *Cit. Appl. Phys. Lett. J. Appl. Phys. J. Appl. Phys.* **99,** (2011).

102. Iwasaki, T., Mizutani, N., Watano, S., Yanagida, T. & Kawai, T. Size control of magnetite nanoparticles by organic solvent-free chemical coprecipitation at room temperature. *J. Exp. Nanosci.* **5,** 251–262 (2010).

103. Unsoy, G. *et al.* Magnetite: From Synthesis to Applications. *Curr. Top. Med. Chem.* **15,** 1622–1640 (2015).

104. Xuan, S., Wang, Y.-X. J., Yu, J. C. & Cham-Fai Leung, K. Tuning the Grain Size and Particle Size of Superparamagnetic Fe 3 O 4 Microparticles. *Chem. Mater* **21,** 5079–5087 (2009).

105. Andrade, Â. L., Fabris, J. D., Ardisson, J. D., Valente, M. A. & Ferreira, J. M. F. Effect of Tetramethylammonium Hydroxide on Nucleation, Surface Modification and Growth of Magnetic Nanoparticles. *J. Nanomater.* **2012,** (2012).

106. Shen, L. *et al.* Facile co-precipitation synthesis of shape-controlled magnetite nanoparticles. *Ceram. Int.* **40,** 1519–1524 (2014).

107. Wei, Y. *et al.* Procedia Engineering Synthesis of Fe 3 O 4 nanoparticles and their magnetic properties. *Procedia Eng.* **27,** 632–637 (2012).

108. Kirillov, V. L., Balaev, D. A., Semenov, S. V, Shaikhutdinov, K. A. & Martyanov, O. N. Size control in the formation of magnetite nanoparticles in the presence of citrate ions. *Mater. Chem. Phys.* **145,** 75–81 (2014).

109. Blaney, L. Magnetite (Fe3O4): Properties, Synthesis, and Applications. *Lehigh Rev.* **15,** 33–81 (2007).

110. Ramadan, W., Kareem, M., Hannoyer, B. & Saha, S. Effect of pH on the Structural and Magnetic Properties of Magnetite Nanoparticles Synthesised by Co-Precipitation. *Adv. Mater. Res.* **324,** 129–132 (2011).

111. Yusoff, A. H. M., Salimi, M. N., Jamlos, M. F. & Yusoff, A. Synthesis and characterization of biocompatible Fe 3 O 4 nanoparticles at different pH. *AIP Conf. Proc.* **1835,** 20010–20045 (2017).

112. Fang, M., Ström, V., Olsson, R. T., Belova, L. & Rao, K. V. Particle size and magnetic properties dependence on growth temperature for rapid mixed co-precipitated magnetite nanoparticles. *Nanotechnology* **23,** 145601 (2012).

113. Andrade, Â. L., Valente, M. A., Ferreira, J. M. F. & Fabris, J. D. Preparation of size-controlled nanoparticles of magnetite. *Journal of Magnetism and Magnetic Materials* **324,** 1753–1757 (2012).

114. Wu, W., Wu, Z., Yu, T., Jiang, C. & Kim, W.-S. Recent progress on magnetic iron oxide nanoparticles: synthesis, surface functional strategies and biomedical applications. *Sci. Technol. Adv. Mater.* **16,** 023501 (2015).

115. Wang, X. *et al.* Hydrothermal synthesis of 3D hollow porous Fe3O4 microspheres towards catalytic removal of organic pollutants. *Nanoscale Res. Lett.* **9,** 648 (2014).

116. Deng, H. *et al.* Monodisperse magnetic single-crystal ferrite microspheres. *Angew. Chemie - Int. Ed.* **44,** 2782–2785 (2005).

117. Liu, Y. *et al.* One-pot hydrothermal synthesis of highly monodisperse water-dispersible hollow magnetic microspheres and construction of photonic crystals. *Chem. Eng. J.* **259,** 779–786 (2015).

118. Yan, A. *et al.* Solvothermal synthesis and characterization of size-controlled Fe3O4 nanoparticles. *J. Alloys Compd.* **458,** 487–491 (2008).

119. Hufschmid, R. *et al.* Synthesis of phase-pure and monodisperse iron oxide nanoparticles by thermal decomposition. *Nanoscale* **7,** 11142–11154 (2015).

120. Hufschmid, R. *et al.* Synthesis of phase-pure and monodisperse iron oxide nanoparticles by thermal decomposition. *Nanoscale* **7,** 11142–11154 (2015).

121. Maity, D., Choo, S. G., Yi, J., Ding, J. & Xue, J. M. Synthesis of magnetite nanoparticles via a solvent-free thermal decomposition route. *J. Magn. Magn. Mater.* **321,** 1256–1259 (2009).

122. Mahmoudi, M., Sant, S., Wang, B., Laurent, S. & Sen, T. Superparamagnetic iron oxide nanoparticles (SPIONs): development, surface modification and applications in chemotherapy. *Adv. Drug Deliv. Rev.* **63,** 24–46 (2011).

123. Hernández, R. *et al.* Structure and viscoelastic properties of hybrid ferrogels with iron oxide nanoparticles synthesized in situ. *Soft Matter* **6,** 3910 (2010).

124. Helminger, M. *et al.* Synthesis and characterization of gelatin-based magnetic hydrogels. *Adv. Funct. Mater.* **24,** 3187–3196 (2014).

125. Wang, Y., Li, B., Zhou, Y. & Jia, D. Chitosan-induced synthesis of magnetite nanoparticles via iron ions assembly. *Polym. Adv. Technol.* **19,** 1256–1261 (2008).

126. Hernández, R. *et al.* Influence of iron oxide nanoparticles on the rheological properties of hybrid chitosan ferrogels. *J. Colloid Interface Sci.* **339,** 53–59 (2009).

127. Sahiner, N. In situ metal particle preparation in cross-linked poly (2-acrylamido-2-methyl-1-propansulfonic acid) hydrogel networks. *Colloid Polym. Sci.* **285,** 283–292 (2006).

128. Sairam, M., Naidu, B. V. K., Nataraj, S. K., Sreedhar, B. & Aminabhavi, T. M. Poly(vinyl alcohol)-iron oxide nanocomposite membranes for pervaporation dehydration of isopropanol, 1,4-dioxane and tetrahydrofuran. *J. Memb. Sci.* **283,** 65–73 (2006).

129. Ilg, P. Stimuli-responsive hydrogels cross-linked by magnetic nanoparticles. *Soft Matter* **9,** 3465 (2013).

130. Bonini, M., Lenz, S., Giorgi, R. & Baglioni, P. Nanomagnetic sponges for the cleaning of works of art. *Langmuir* **23,** 8681–8685 (2007).

131. Dallas, P. *et al.* Synthesis, characterization and thermal properties of polymer/magnetite nanocomposites. *Nanotechnology* **17,** 2046–2053 (2006).

132. Gonzalez, J. S. *et al.* Simple and efficient procedure for the synthesis of ferrogels based on physically cross-linked PVA. *Ind. Eng. Chem. Res.* **53,** 214–221 (2014).

133. Feldgitscher, C., Peterlik, H., Puchberger, M. & Kickelbick, G. Structural investigations on hybrid polymers suitable as a nanoparticle precipitation environment. *Chem. Mater.* **21,** 695–705 (2009).

134. Schoth, A., Keith, A. D., Landfester, K. & Muñoz-Espí, R. Silanization as a versatile functionalization method for the synthesis of polymer/magnetite hybrid nanoparticles with controlled structure. *RSC Adv.* **6,** 53903–53911 (2016).

135. Str, I. R. Revealing Fe 3 O 4 nanoparticles aggregation dynamics using dynamic light scattering. **3,** 1299–1305 (2009).

136. Xiao, L. *et al.* Water-soluble superparamagnetic magnetite nanoparticles with biocompatible coating for enhanced magnetic resonance imaging. *ACS Nano* **5,** 6315–6324 (2011).

137. Dani, R. K., Schumann, C., Taratula, O. & Taratula, O. Temperature-Tunable Iron Oxide Nanoparticles for Remote-Controlled Drug Release. *AAPS PharmSciTech* **15,** 963–972 (2014).

138. Euliss, L. E. *et al.* Cooperative Assembly of Magnetic Nanoparticles and Block Copolypeptides in Aqueous Media. *Nano Lett.* **3,** 1489–1493 (2003).

139. Wang, L., Li, J., Jiang, Q. & Zhao, L. Dalton Transactions Water-soluble Fe 3 O 4 nanoparticles with high solubility for removal of heavy-metal ions from waste water. **41,** (2012).

140. Wu, L. *et al.* Facile one-pot synthesis of different surfactant-functionalized water-

soluble Fe 3 O 4 nanoparticles as magnetic resonance imaging contrast agents for melanoma tumors. *RSC Adv.* **5,** 50557–50564 (2015).

141. Lu, X., Niu, M., Qiao, R. & Gao, M. Superdispersible PVP-coated Fe3O4nanocrystals prepared by a 'one-pot' reaction. *J. Phys. Chem. B* **112,** 14390–14394 (2008).

142. Kumar, S. R. *et al.* Hydrophilic polymer coated monodispersed Fe 3 O 4 nanostructures and their cytotoxicity. *Mater. Res. Express* **1,** 015015 (2014).

143. Boyer, C., Whittaker, M. R., Bulmus, V., Liu, J. & Davis, T. P. The design and utility of polymer-stabilized iron-oxide nanoparticles for nanomedicine applications. *NPG Asia Materials* **2,** 23–30 (2010).

144. Pinna, N. *et al.* Magnetite Nanocrystals: Nonaqueous Synthesis, Characterization, and Solubility. (2015). doi:10.1021/cm050060+

145. Li, Z., Chen, H., Bao, H. & Gao, M. One-Pot Reaction to Synthesize Water-Soluble Magnetite Nanocrystals. *Chem. Soc. J. Colloid Interface Sci Int. J. Pharm. J. Magn. Magn. Mater. Sci. Angew. Chem., Int. Ed. J. W. M.; Brooks, R. A. Sci. Clin. Appl. Magn. Carriers Chem. Mater* **31,** 118–215 (2002).

146. Theppaleak, T., Tumcharern, G., Wichai, U. & Rutnakornpituk, M. Synthesis of water dispersible magnetite nanoparticles in the presence of hydrophilic polymers. *Polym. Bull.* **63,** 79–90 (2009).

147. van Berkum, S., Dee, J. T., Philipse, A. P. & Erné, B. H. Frequency-dependent magnetic susceptibility of magnetite and cobalt ferrite nanoparticles embedded in PAA hydrogel. *Int. J. Mol. Sci.* **14,** 10162–77 (2013).

148. Oktay, B., Demir, S. & Kayaman-Apohan, N. Magnetic nanoparticle containing thiol-ene crosslinked hydrogels for controlled and targeted release of hydrophobic drugs. *Polymer Composites* (2016). doi:10.1002/pc.24144

149. Messing, R. *et al.* Cobalt ferrite nanoparticles as multifunctional cross-linkers in PAAm ferrohydrogels. *Macromolecules* **44,** 2990–2999 (2011).

150. Maurizi, L., Claveau, A. & Hofmann, H. Polymer adsorption on iron oxide nanoparticles for one-step amino-functionalized silica encapsulation. *J. Nanomater.* **2015,** 1–6 (2015).

151. Kydralieva, K. A., Dzhardimalieva, G. I., Yurishcheva, A. A. & Jorobekova, S. J. Nanoparticles of Magnetite in Polymer Matrices: Synthesis and Properties. *J. Inorg. Organomet. Polym. Mater.* **26,** 1212–1230 (2016).

152. Chen, H. *et al.* Photonic crystal materials and their application in biomedicine. *Drug Delivery* **24,** 775–780 (2017).

153. Jia, X. *et al.* Full-color photonic hydrogels for pH and ionic strength sensing. *Eur. Polym. J.* **83,** 60–66 (2016).

154. Holtz, J. H. & Asher, S. a. Polymerized colloidal crystal hydrogel films as intelligent chemical sensing materials. *Nature* **389,** 829–32 (1997).

155. Ozay, H. & Ozay, O. Reusable naked-eye hydrogel sensor. *Chem. Eng. J.* **232,** 364–371 (2013).

156. Dumitrescu, A. M. *et al.* Ni ferrite highly organized as humidity sensors. *Mater. Chem. Phys.* **156,** 170–179 (2015).

157. Rivero, R. E., Molina, M. A., Rivarola, C. R. & Barbero, C. A. Pressure and microwave sensors/actuators based on smart hydrogel/conductive polymer nanocomposite. *Sensors Actuators, B Chem.* **190,** 270–278 (2014).

158. Naficy, S., Razal, J. M., Spinks, G. M., Wallace, G. G. & Whitten, P. G. Electrically conductive, tough hydrogels with pH sensitivity. *Chem. Mater.* **24,** 3425–3433 (2012).

159. Deng, K., Gerlach, G. & Guenther, M. Force-compensated hydrogel-based pH sensor. in 943112 (2015). doi:10.1117/12.2084171

160. Lei, M., Baldi, A., Nuxoll, E., Siegel, R. A. & Ziaie, B. Hydrogel-based microsensors for wireless chemical monitoring. *Biomed. Microdevices* **11,** 529–538 (2009).

161. Zhang, Y., Kim, H. H., Kwon, B. H. & Go, J. S. Polymeric cantilever sensors functionalized with multiamine supramolecular hydrogel. *Sensors Actuators, B Chem.* **178,** 47–52 (2013).

162. Abu-Lail, N. I., Kaholek, M., LaMattina, B., Clark, R. L. & Zauscher, S. Micro-cantilevers with end-grafted stimulus-responsive polymer brushes for actuation

and sensing. *Sensors Actuators, B Chem.* **114,** 371–378 (2006).

163. Ruan, C., Zeng, K. & Grimes, C. A. A mass-sensitive pH sensor based on a stimuli-responsive polymer. *Anal. Chim. Acta* **497,** 123–131 (2003).

164. Kumar, P., George, B. & Kumar, J. A Simple Signal Conditioning Scheme for Inductive Sensors. *Seventh Int. Conf. Sens. Technol.* 516–519 (2013).

165. Tamanaha, C. R., Mulvaney, S. P., Rife, J. C. & Whitman, L. J. Magnetic labeling, detection, and system integration. *Biosensors and Bioelectronics* **24,** 1–13 (2008).

166. van Bruggen, M. P. B. & van Zon, J. B. A. Theoretical description of a responsive magneto-hydrogel transduction principle. *Sensors Actuators, A Phys.* **158,** 240–248 (2010).

167. Ennen, I., Kappe, D., Rempel, T., Glenske, C. & Hütten, A. Giant Magnetoresistance: Basic Concepts, Microstructure, Magnetic Interactions and Applications. *Sensors* **16,** 904 (2016).

168. Kim, D. & Wang, S. X. A Magneto-Nanosensor Immunoassay for Sensitive Detection of Aspergillus Fumigatus Allergen Asp f 1. **48,** 3266–3268 (2012).

169. Kim, D., Lee, J.-R., Shen, E. & Wang, S. X. Modeling and experiments of magneto-nanosensors for diagnostics of radiation exposure and cancer. *Biomed. Microdevices* **15,** 665–71 (2013).

170. Park, J. H., Kim, A. & Ziaie, B. Batch-fabricated hydrogel/polymeric-magnet bilayer for wireless chemical sensing. in *Proceedings of the IEEE International Conference on Micro Electro Mechanical Systems (MEMS)* **2015–Febru,** 585–588 (IEEE, 2015).

171. Qiufeng, Y., Zhao, D., Yang, K. & Li, Y. Preparation of Magnetic Fe3O4 Microspheres Using Different Surfactant and Silica-coated Magnetic Particles. *IEA* **466,** 47–51 (2015).

172. Bucatariu, S. *et al.* Synthesis and characterization of thermosensitive poly(N-isopropylacrylamide-co-hydroxyethylacrylamide) microgels as potential carriers for drug delivery. *J. Polym. Res.* **21,** (2014).

173. Haider, I., Siddiq, M., Mujtaba Shah, S. & ur Rehman, S. Synthesis and characterization of multi-responsive poly (NIPAm-co-AAc) microgels. in *IOP Conf. Series: Materials Science and Engineering* (2014).

174. Chatterjee, S., Salaün, F. & Campagne, C. The Influence of 1-Butanol and Trisodium Citrate Ion on Morphology and Chemical Properties of Chitosan-Based Microcapsules during Rigidification by Alkali Treatment. *Mar. Drugs* **12,** 5801–5816 (2014).

175. Zhao, S. & Asuha, S. One-pot synthesis of magnetite nanopowder and their magnetic properties. *Powder Technol.* **197,** 295–297 (2010).

176. Wan, Q. *et al.* Mapping Nanostructural Variations in Silk by Secondary Electron Hyperspectral Imaging. *Adv. Mater.* **29,** 1703510 (2017).

177. Lemine, O. M. *et al.* Sol–gel synthesis of 8nm magnetite (Fe3O4) nanoparticles and their magnetic properties. *Superlattices Microstruct.* **52,** 793–799 (2012).

178. Lim, J., Yeap, S., Che, H. & Low, S. Characterization of magnetic nanoparticle by dynamic light scattering. *Nanoscale Res. Lett.* **8,** 381 (2013).

179. Mamani, J. B., Costa-Filho, A. J., Cornejo, D. R., Vieira, E. D. & Gamarra, L. F. Synthesis and characterization of magnetite nanoparticles coated with lauric acid. *Mater. Charact.* **81,** 28–36 (2013).

180. Feng, X. & Lou, X. The effect of surfactants-bound magnetite (Fe3O4) on the photocatalytic properties of the heterogeneous magnetic zinc oxides nanoparticles. *Sep. Purif. Technol.* **147,** 266–275 (2015).

181. Dar, M. I. & Shivashankar, S. A. Single crystalline magnetite, maghemite, and hematite nanoparticles with rich coercivity. *RSC Adv.* **4,** 4105–4113 (2014).

182. Unni, M. *et al.* Thermal Decomposition Synthesis of Iron Oxide Nanoparticles with Diminished Magnetic Dead Layer by Controlled Addition of Oxygen. *ACS Nano* **11,** 2284–2303 (2017).

183. Kolhatkar, A. G. *et al.* Magnetic Sensing Potential of Fe 3 O 4 Nanocubes Exceeds That of Fe 3 O 4 Nanospheres. *ACS Omega* **2,** 8010–8019 (2017).

184. Ghandoor, H. El, Zidan, H. M., Khalil, M. M. H. & Ismail, M. I. M. Synthesis and

Some Physical Properties of Magnetite (Fe 3 O 4) Nanoparticles. *Int. J. Electrochem. Sci* **7,** 5734–5745 (2012).

185. Spaldin, N. *Basics. In Magnetic Materials: Fundamentals and Applications. Cambridge University Press* (2010). doi:10.1017/CBO9780511781599.002

186. Cheng, F. Y. *et al.* Characterization of aqueous dispersions of Fe3O4 nanoparticles and their biomedical applications. *Biomaterials* **26,** 729–738 (2005).

187. Shimanouchi, T. Carbon dioxide. *Tables of Molecular Vibrational Frequencies Consolidated Volume I* (2016). Available at: http://webbook.nist.gov/cgi/cbook.cgi?ID=C124389&Type=IR-SPEC&Index=1. (Accessed: 23rd November 2017)

188. Chaki, S. H., Malek, T. J., Chaudhary, M. D., Tailor, J. P. & Deshpande, M. P. Magnetite Fe 3 O 4 nanoparticles synthesis by wet chemical reduction and their characterization. *Adv. Nat. Sci. Nanosci. Nanotechnol.* **6,** 035009 (2015).

Chapter 2 Porous Magnetic Microcarriers For Dynamic Cell Culture

1. Aims and Objectives

The aim of this chapter is to develop porous magnetic microcarriers via the emulsion templating route for cell culture applications. As well as, to study the impact of the fluid shear stress in terms of the osteogenic response once the carriers have been inoculated with hMSCs. The following steps will contribute to the objectives:

1. Manufacture porous magnetic microcarriers using EHA and IBOA to form the polymer matrix.
2. Determine suitability for the culture of hMSCs, human fibroblast cells.
3. Use a method to manipulate the movement of microcarriers within the flasks to create fluid shear stress.
4. Assess viability and osteogenic response of cells over the culture period by studying DNA, ALP, calcium and collagen.

2. Introduction

Cell-based therapies are seen as an area that could potentially result in the lifestyle improvement of many. Inherent Limitations of self-healing, or ineffective methods currently employed clinically mean there is always an insatiable demand for efficient and innovative treatments. Although, there are current drawbacks; an effective method for therapeutic cell-based product delivery is yet to be defined [1], the limited availability of cells required for individual treatments also hinder development.

An improvement in the quality of life is possible for cases that involve impairment or regeneration exceeding the body's natural ability, such as bone defects from trauma, infection, skeletal abnormalities, or scenarios in which the regenerative process has deteriorated [2]. Allogenic and autologous therapies that aim to correct such issues, or treat trauma, depend on the individual requirements of each patient but are estimated to require cells into the billions. These vast numbers can be put into perspective by realising the whole human body on average contains 37.2 trillion cells, and the heart alone contains an estimated 2 -3 billion heart muscle cells [3,4]. Cases such as; osteogenesis imperfecta require 3 to 6 billion cells [5]; Myocardial infarction, 35 – 350 million [6]; Ma et al. estimated clinical applications require doses of 1 – 5 million cells/kg [7]. The lower range is relatively simple to attain via 2-dimensional conventional cell culture. However, if for the moment you start to visualise beyond the

magnitude of a few million cells, then time, labour intensity, space, sourcing such a high number and ensuring they are of high quality have to be considered. Current laborious methods of growing and expanding on planar culture become inadequate. Hence there is a requirement for a more industrial-style autonomous process, utilising either batch or continuous reactors.

Cells for the majority are anchorage-dependent; hence, a biocompatible substrate is often required for cells to adhere. This is the central role microcarriers have; they act as a substrate and provide a large surface for cells to grow and expand. Such a concept is still in its embryonic state; it, therefore, presents new challenges and opportunities compared to established culture techniques. Also, with more research and novel design aspects considered, they have the potential to supersede monolayer culture.

3. Literature Review

3.1. Human Mesenchymal Stem Cells (hMSCs)

The potent and self-renewal nature of stem cells has had people long interested due to their inherent ability to develop into various lineages. Of these various stem cells, the multipotent human mesenchymal stem cells (hMSCs) have gathered much interest due to several of their traits. Their therapeutic and anti-inflammatory properties [8–10]; homing ability to damaged tissue [11]; in one example in vivo imaging of mice tracked the intense migration of injected MSCs to the tibia fracture site over the period of 14 days [12]. Moreover, as it will be discussed later, their intrinsic ability to respond to changes in their microenvironment [7].

hMSCs are typically isolated from bone marrow, adipose tissues, umbilical cords, amniotic membrane, and cord blood samples – although the latter is usually of lower extracted yield compared to the previously mentioned sources [1]. By providing the right conditions, they can form osteoblasts, adipocytes, chondrocytes, tenocytes, and myocytes (See Figure 33) [13,14].

Most well-known therapies have involved MSCs, and a majority of these trials are focused on allogeneic therapies [15]. A simple search on the clinicaltrials.gov website as of 2017 displays 88 currently open hMSC trials investigating a broad range of problems or diseases such as; Alzheimer's, cystic fibrosis, treatment-resistant depression, ovarian cancer to cartilage and bone tissue engineering (ClinicalTrials.org, 2017).

To achieve bone morphology MSCs progress into osteoprogenitors, which then, in turn, become pre-osteoblasts, eventually, maturing [16]. Osteoblasts form a bone matrix which results in mineralisation of bone [17]. This structure undergoes constant modelling and remodelling working in unison with osteoclasts, which are derived from the myeloid lineage [18]. Working synergistically they remove old mineralised bone as osteoblasts deposit new matrix, eventually terminally differentiate and embed into the cortical bone as osteocytes - which end up regulating the formation and reabsorption [19,20]. Huang et al. observed three stages using osteoprogenitors: Proliferation was marked with increasing DNA experienced within the first 4 days; signs of differentiation were present from day 5 – 14 where markers such as ALP were expressed. And finally,

and maturation between day 15 to 28, where mineralisation deposition was present [21].
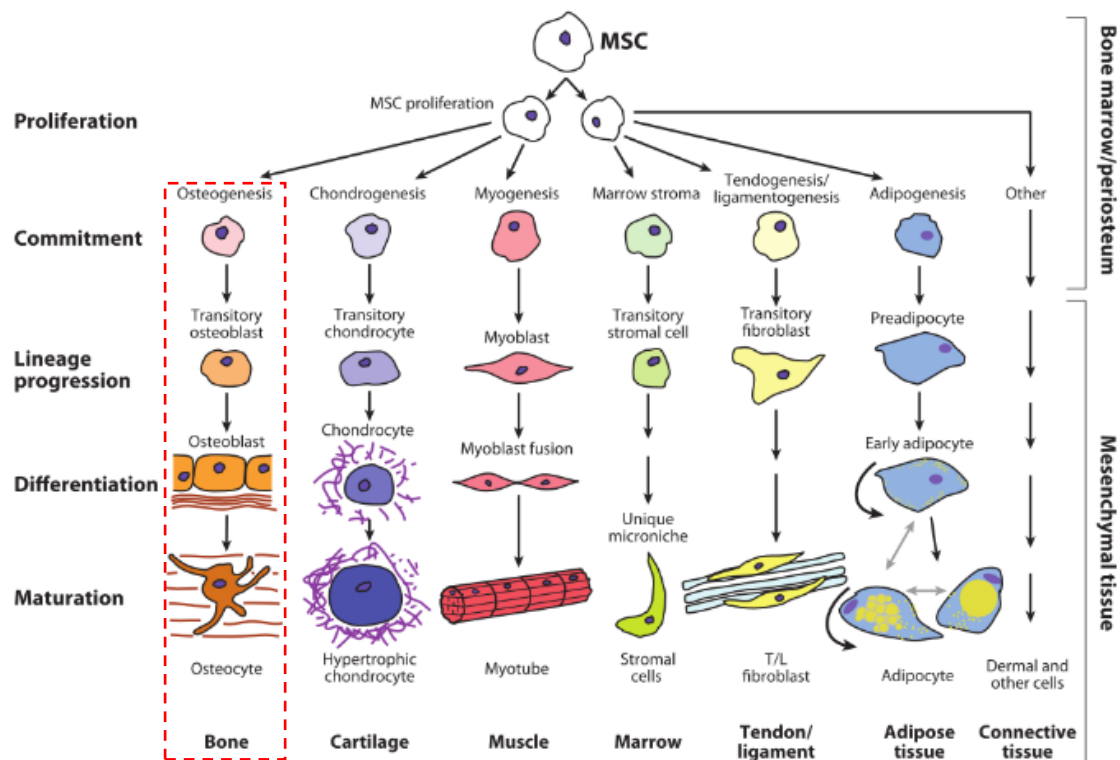
Figure 33: Basic Schematic of the various lineages human mesenchymal stem cells can take; adapted from Singer & Caplan, (2011).

Clinical trials using hMSCs have also shown potential in the enhancement of bone regeneration [22]. Early studies of osteogenesis imperfecta, for example, show that cell-based therapy can be useful. In a trial reported by Horwitz et al., 3 children underwent bone marrow transplant, and during the 6 months showed accelerated growth rates and overall bone function [23]. Horwitz et al. again studied 6 children who were dosed with 1 x10^6 - 5x10^6 cells/kg of BMSCs; the results showed successful engraftment and differentiation into osteoblasts [24]. Furthermore, growth before and after hMSC treatment was found to increase for five out of six patients.

hMSCs or variations of them have also been shown to be effective when seeded on scaffolds and then transplanted into the body. A porous scaffold was seeded with bone marrow mesenchymal stem cells (BMSCs) and implanted to repair large bone defects of four patients. No problems or complications were reported during, or after implantation; successful fusion between the scaffold was achieved with follow-ups after 6 – 7 years confirming this [25]. A study using an injection of autologous cells to

treat a bone fracture of the tibia using a more differentiated form of hMSCs. Callus formation was used as a marker to assess the rate of recovery, after two months the average formation was deemed greater and statistically significant, with no patient complications [26].

3.1.1. Human Embryonic Stem Cell-derived Mesenchymal Progenitors (hE-SMPs)

hE-SMP cells are similar to hMSCs, but are an advanced form derived from hESCs, also according to Maria De Peppo et al. they have a higher proliferation rate [13]. The author compared the osteogenic potential of hMSCs and hES-MPs and found that there was faster mineralisation with progenitor cells under osteogenic conditions.

3.1.2. hSMC Concerns

Although hMSCs have been shown to be effective in the treatment of diseases and injuries the administrating routes that present the most effective outcome remain unclear [27]. Presently long-term culture is required from hMSCs in order to achieve larger numbers that satisfy expected demands for these treatments. MSCs cultured to higher passage numbers experience senescence as well as a risk of malignant transformation from serum, and other growth factors [28]. The addition of foetal bovine/calf serum (FBS/FCS) due to its ill-defined nature, variations in quality and additional agents, could cause an immunological response in patients [29]. MSCs can also retain some FCS proteins, that could induce malignant transformation [30]. As a result, Chen et al. and Mao et al. looked into expanding culture serum free [30,31]. Both authors' successfully sustained culture and morphology of hMSCs derived from umbilical cord and human bone marrow, respectively. Chen et al. studied up to 25 passages, concluding that no chromosomal abnormalities were evidently indicating a stable karyotype [30]. Mao et al. used an alternate approach by using various concentrations of the growth factors: bFGF, TGF-b1 and PDGF-BB [31]. When several of these were combined, they showed competitive relative growth to 10% FBS, suggesting a synergetic effect, but individually were not as effective.

Human mesenchymal stem cells (hMSCs) in particular have been employed in clinical trials to treat numerous defects or diseases, which demonstrates their diverse applications. The increase of their use in trials also suggests that a reality where cell-based therapies can be accessible in the not so distant future. Although, the complexity of stem cells means there is an uncertainty associated with them due to

their self-renewal ability which could potentially lead to tumours, severe immune reactions, or growth of unwanted tissue [32]. Furthermore, the above-mentioned inconsistencies in serum constituents is another contributor which restrict the potential demands for hMSC therapies [33]. Also, according to the same author, another argument that cannot be overlooked is that primary hMSCs, irrespective of the source are short in supply for clinical and research purposes; which is just one of the reasons why scale-up processes are necessary.

3.2. Environmentally Induced Effects

It has become well established that environmental conditions for culture can encourage differentiation, proliferation, cell migration and cell alignment. The addition of various combinations of commonly used media constituents and growth factors is a well understood and a conventional method to influence mesenchymal stem cells differentiation into several lineages, which have been mentioned previously. For example, the addition of dexamethasone (DEX) and bone morphogenetic proteins (BMPs) favours osteogenesis; whereas, cells in serum-free medium and transforming growth factor ß (TGF-ß) are more likely to undergo chondrogenesis; and DEX, insulin, and 3-isobutyl-1-methylxanthine favour adipogenic differentiation [34,35]. The addition of 1 ng/ ml fibroblast growth factor (FGF) has also shown to be an effective way to maintain their osteogenic potential while increasing proliferation rates [36,37].

The addition of chemicals for lineage-specific media may enhance differentiation potential, but they can also limit proliferation rates; as a comparison with and without DEX has shown [38]. The sudden addition promotes differentiation, which means proliferation rates are reduced. Lower concentrations of DEX lead to higher proliferation rates in BMSCs, this was done with 10^{-6}, 10^{-7} and 10^{-8} M DEX concentrations [39]. The proliferation rates with no DEX; however, competitively increased with 10^{-8} M, but this was until day 20, and after that it decreased in comparison. Though a combination of DEX (10 nM) and FGF (1 ng/ml) was more effective than DEX alone, this was equivalent in terms of increased proliferation experienced with just FGF [37].

More interestingly, however, this has also given rise to various novel approaches to achieve differentiation such as; compression [40], fluid shear stress [41,42], magnetic [43] and electrical fields [44], vibrations [45] can all be influential factors. Mainly such

work has been carried out with MSCs as they are highly sensitive to their microenvironments [7].

By applying 0.1 V/cm to hMSCs using a current amplifier for 30 min/day for 10 days in osteogenic medium, Sun et al. found cell proliferation increased by a factor of three. ALP and calcium deposition were also significantly higher than their control counterparts [46]. Whereas Zhang et al. applied low-magnitude, high-frequency vibrations to human periodontal ligament stem cells for 30 min/daily between 10 – 180 Hz, it was established a frequency between 40 and 90 Hz was more favourable for osteogenic differentiation, however cell proliferation decreased[46]. The loading of three-dimensional culture under static tension upregulated scleraxis in human MSCs; a factor expressed during tendon and ligament development. Cyclic loading (1 Hz, 30 mins/day) was required to maintain scleraxis expression with time, demonstrating the need for dynamic mechanical stimulation for tenogenic differentiation of MSCs [47].

3.2.1. Methods to determine Osteogenesis

As hMSCs progress down the differentiation route into specialised bone cells various markers are used as indicators to determine how far along this lineage they have progressed. The enzyme Alkaline phosphate activity (ALP) for example, is described as an intermediate marker, and one of several commonly analysed indicators when assessing osteogenesis [17]. Earlier ones include core binding factor 1, Runt-related transcription factor 2 (RUNX2), which according to Ullah et al. is particularly significant; Osterix (Sp7) and collagen type I are also expressed during the pre-osteoblast stage [17,48]. From the pre-osteoblast stage till maturation higher amounts of bone matrix proteins are expressed for example: Bone sialoprotein (BSP) I and II and collagen type I [49]. Osteopontin and Osteocalcin are also markers developed near maturity [17].

The degree of mineralisation and collagen deposition are also common methods and can be determined by staining with either alizarin red or von Kossa stain, and Sirius red, respectively. Other quantitive methods include the use of PCR.

3.2.2. Fluid Shear Stress

Dynamic systems have reported an increase in proliferation rates. Boo et al. used a spinner flask and compared the effects to static culture, and reported a ~ 5-fold increase in cell density [41]. Tang et al. reported a similar finding with BMSCs; cell numbers also increased for Kanda et al. using rat-MSCs, this was with both expansion

media, and media with fibroblast growth factor [42,50]. There are apparently also cases where there has been no change between static culture, and a detrimental one. Perfusion culture showed indifference to static culture after 14 days of culture, though, a more strenuous setting was inferior to both [38]. Conditions and effects on proliferation and osteogenic activity from other sources are summarised in Table 7.

As the scope of this chapter is specific to bone tissue engineering, the more common and novel way to encourage hMSCs to favour bone-lineages is by providing mechanical stimulus in the form of fluid shear stress (FSS). Such a response is possible due to the simulation of their natural in vivo environment; where constant loading and unloading of bone causes FSS in the interstitial spaces around bone cells[51][52]. The internal fluid stress can vary depending on physical activity, but it has been estimated to be in the region of $8 - 30$ dynes/cm^2 within the lacunar-canalicular spaces [51]. In an in vitro environment, however, it has been shown be far less; FSS as low as 0.01 dynes/cm^2 on 3D scaffolds can trigger osteogenic response, whereas higher stress of 0.3 dynes/cm^2 was required for a planar surface [7]. This response from fluid stress continues along the lineage to osteoblasts and osteocytes, though their preferences to the amount of shear required for a positive response vary [19].

A study by Hofmann et al. cultured hMSCs dynamically by spinner flask method they showed there were increased levels of ALP and calcium content over a 3 and 5 week period when evaluated against static conditions [52]. Although static culture resulted in higher cell densities, no mineralisation was observed over this period. Other work by Woloszyk et al., used human dental pulp stem cells (hDPSCs) grown in osteogenic media suggests it is possible to influence the homogenous formation of mineralised structures, and calcium deposition by growing cells in a dynamically cultured environment [53]. Again, showing ALP was significantly higher in the dynamic culture at 120 rpm with osteogenic medium. BM-MSCs cultured on 3D scaffolds in a spinner flask operated continuously showed higher levels of DNA – and early markers of osteogenic differentiation; ALP, collagen type I α-1, BMP2, osteonectin, runt-related transcription factor-2 (RUNX2) and osterix compared to control counter-parts [54].

Although a majority of reports suggest there is an increase in ALP, there are conflicting reports, which suggest otherwise. Human embryonic stem cell-derived mesodermal progenitors and MSCs were studied in dynamic and static conditions over a 35 day

period. The progenitor cell line cultured in dynamic conditions showed significant increases in DNA and protein content. ALP activity, however, remained higher in static progenitor culture until day 35 [55].

The body is often active for periods and relatively inactive for others which makes the duration of stress applied challenging to establish; It has been noted that frequent application of FSS is more effective than stress continuously applied [51]. Upregulation of ALP and mineralisation with the intermittent oscillatory flow was still possible for a variety of scaffolds [34]. By comparing intermittent and continuous fluid flow in osteogenic-free medium, Liu et al. established an intermittent flow for 1 hour, showed significantly higher levels of ALP. In the later stages of the experiment, ALP levels using osteogenic medium were equivalent but expressed by a much lower at continuous flow rate. A similar trend for up-regulation of RUNx2. COL Iα, where both environments showed increased levels compared to their control counterparts. Furthermore, using perfusion culture of BM-MSCs under static, continuous and intermittent continuous flow resulted in similar levels of bone matrix proteins (OPN, OCN, BSP and col-1 α1) after 24 hours although a higher detachment of cells was observed in continuous FSS within this period [56].

Starch-based scaffolds, comprising of either ethylene vinyl alcohol or polycaprolactone, both were cultured using rat bone marrow cells and placed under dynamic conditions [57]. ALP production in both material types varied, normalised values with the caprolactone-based scaffolds was similar to static (~5 pmol/cell), in the case of ethylene vinyl alcohol-based scaffolds - both dynamic and static cultures were 3 - 4x higher. However, the dynamic regime excelled and was significantly different and 15 pmol/cell higher in ALP production than the static control.

Table 7: Summary of dynamic culture and its effects on MSCs; there were two main objectives to this: To understand how dynamic culture interacts with cell viability and proliferation rates, also to see how the presence of the enzyme Alkaline phosphatase (ALP) fluctuates with various parameters.

Cells	Type	Speed/Stress	Frequency	Duration	Summary	Ref.
hDPSCS	Spinner Flask	120 rpm	Continuous	47 days	Dynamic culture showed homogenous mineralisation Calcium deposition almost doubled Proliferation activity reduced	[53]
rMSCs	LMHF	60 hz	Intermittent 1 hr	6 days	Proliferation rate was not significantly different No significant difference in ALP between non-vibrated and vibrated.	[58]
hMSCs	Parallel Plate Flow	9 dynes/cm^2	Continuous	3 days	Osteogenic culture showed significantly lower ALP activity	[59]
hMSCs	Perfusion	4.2 dynes/cm^2	Continuous/ Intermittent 2x Daily	14 days	Cell viability was higher than continuous flow OM media control increased ALP greatly on day 7 Continuous flow had much lower ALP values Intermittent flow, with no OM media, was comparatively high as osteoinduced media control on day 7, lower on 21	[51]
hES-MPs	Rocker	45 cycles/ hr	Intermittent 1 hr	21 days	No noticeable effect on DNA content There was little to no difference using normal media, from day 7 through to 21. OM culture: Significant difference in ALP content on day 14 little variance after day 21	[60]
hMSCs	Spinner Flask	30 rpm	Continuous	21 days	Day 21 DNA results were not significantly higher Again, ALP rapidly increased during the first 7 days Not Significant after 21 days Calcium almost twelve times higher in dynamic culture	[61]
MSCs	Fluid Flow Chip	Various $10^{-5} - 10^{-2}$ dynes/cm^2	Continuous	7 days	ALP activity was higher for 10^{-2} dynes/cm^2 after 7 days Osteogenic induced media resulted in improved ALP activity	[62]

hMSCs	Flow perfusion	0.1 ml/min	Continuous	21 days	DNA increased at all time points, up to day 21 ALP was lower on day 2 Higher on days 7, 14 Decrease at the final time point – but it was higher still than static culture	[63]
hMSCs	Bioreactor	3 ml/min	Continuous	14 days	Significant difference in cell numbers in both general media and OM media (7 and 14 days) Significant difference observed in ALP with OM media at day 14 Otherwise insignificant with both media variations and time points	[64]
HfMSCs	Biaxial Rotating Perfusion Spinner Flask Rotating Wall	5 RPM 2 ml/min 20 RPM Free floating	Continuous	28 days	Proliferation in Biaxial was rapid but saturated quickly Other three reactors By week 4 other three reactors had similar DNA content, but lower than biaxial ALP higher in biaxial. Whereas similar in others Calcium levels similar on weeks one and two, biaxial had significantly high deposition by the fourth week Perfusion and Spinner flask similar by week 4	[65]
rBMC	Bioreactor	3 ml/min	Continuous	7 days	In all three media variations, dynamic cell count was greater than static ALP in both static and dynamic culture was significantly higher than the two other media variants ALP significantly better than static in osteogenic media	[50]
MSCs	Spinner Flask	30 RPM	Continuous	21 days	Approximately same number of cells at day 21 ALP was 2.4 times higher on day 14, then dropped to 1.4 times higher than static (Day 21) Spinner Flask had significantly higher calcium deposition Static culture outperformed rotating wall vessel	[66]

Studies such as those by Nishimura et al. and Maria de Peppo et al. have also expressed another benefit of employing such an environment, which is the increased proliferation rates - this could reduce incubation time from culturing to patient [50,55,64]. Results showed that mechanical strain could promote MSC proliferation, increase ALP activity and up-regulate the expression of Cbfa1 and Ets-1 [67]. Finally, another noteworthy point is that the introduction of FSS to the environment also promotes nutrient transfer to cells, due to the transport of medium in and out of the scaffold [34]. If the samples are porous, this will help significantly by refreshing the media, and oxygen concentration locally.

Table 7, summarises numerous recent studies that have reported on dynamic culture and its effects on the osteogenic behaviour, predominantly of MSCs.

From this short review, it can be understood that there are numerous variables to consider; duration, frequency, media constituents all have a vital role in the differentiation capability of hMSCs. The advantages of dynamic culture are not without consequence, and it often results in a decreased DNA count, which is most likely a result of applied stress. Though increasing for example speed may have this effect, and a decrease in the amount of DNA is the result [65]. Obviously as highlighted there are cases where DNA or cell count has been reported to stay similar to static conditions too. It is perhaps another reason why dynamic environments are generally preferred at short and frequent bursts [68]. Another compelling argument is that shorter dynamic conditions act as a "trigger" response If left for prolonged periods cells can adapt to their environment to some degree resulting in ineffective responses under continuously applied fluid shear stress [51].

In terms of evaluating osteogenic response there is a consensus for increasing ALP production because of dynamic culture; however even with the abundance of literature, it appears to be an ambiguous measure. Other common indicators such as; collagen type I α-1, ON, RUNX2 and osterix seem to be more consistent, even more so in the case of calcium staining, which typically is a result of higher levels of mineralisation in dynamic cultures.

3.3.   Microcarriers

Microcarriers have the potential to overcome the current limitations experienced in 2D cell culture, which become evident when the vast quantity of cells required for therapeutic treatments are considered [5]. Their 3-dimensional and frequently bead-like nature provide an increased surface area available for cell anchorage. These are made of either solid or porous beads, which can enhance the available growing area a manifold of times. This is due to their high surface to volume ratio. To put this into perspective, a single T-75 flask has a surface area of 75 cm^2; compared to Cytodex 1 beads by GE which have a surface area of 4,400 cm^2/ g dry weight; this is equivalent to ~ 59 standard T-75 flasks. These are solid spheroidal particles. The surface area is further increased when the particles are made porous; for example, Cytopore 1 has a surface area of 11,000 cm^2/ g dry weight. Equivalent to ~147 T75 flasks. The numbers demonstrate a clear advantage of using microcarriers to population multiply cells, as 1 gram of Cytopore 1 presents the same surface area for cells to proliferate on as almost 250 T75 flasks.

Using microcarriers presents various other qualities, which have also contributed to their rising success. They provide a framework for cells to adhere to, which permits the transfer of particles and cells together to ease transferring, an attractive trait for bioreactor technology. Also, porous microcarriers allow for good nutrient and oxygen transport [69], which is a crucial factor for the long-term cell culture, as there is evidence to suggest a low oxygen environment can act as an inhibitor during bone formation and in vitro osteogenesis [70]. 3D environments also aid the role of differentiation, showing a more effective response when compared to MSC monolayer culture [71].

3.3.1. Design

Scaffold design is crucial for optimal growth; mimicking structural and mechanical properties of native cells are factors that should be considered. It plays a significant role, in this case particularly for bone, as they are required to reflect the in-vivo arrangement of bone and its tissue [53].

3.3.1.1.   Choice of material

Extracellular matrix (ECM) produced by cells has a multifunctional role, not only does it guide development and regeneration; it also provides physical support for cells [72].

The feedback system present is capable of detecting small and subtle changes in ECM resulting in various responses, which as a result means certain cell types can be mechanosensitive [73]. Since they physically interact; crawl over, and through solid supports [74]. As a result density, stiffness and architecture, as well as other intrinsic factors, mean the choice of materials is logically the first point to consider; especially if the scaffolds are to be applied in vivo [75].

Fibroblasts, Endothelial cells and MSCs attached, spread and proliferated better on stiffer materials [72]. Altering surface roughness using nanoparticles has shown to increase attachment efficiency and increased proliferation rates of MSCs [76].

Such material properties can also affect their differentiation in different lineages; hMSCs cultured in identical serum conditions demonstrated preferential differentiation based on material stiffness. Cells cultured on soft polyacrylamide surface substrates differentiated into neuronal cells, while markers for differentiation towards osteoblast were present when the cells were cultured on a stiffer surface [77]. Similarly, Murphy et al. in the absence of any differentiation supplements, noted cells on a more flexible material were more inclined to chondrogenic lineage [72]. Material stiffness can be altered by changing the cross-linking density, polymer molecular weight or concentration [74].

Synthetic or natural polymers can present attractive traits for each side. Synthetic, unlike natural polymers, are not hindered by batch variation, poor mechanical properties and manufacturing challenges [75]. Most natural polymers used as scaffolds for tissue engineering, e.g. collagen, gelatine, alginate and chitosan are hydrogels and can be used as bulk materials or as coatings to make synthetic materials more cell adhesive. These natural hydrogels have the correct surface moieties for cells to attach to and grow on. Synthetic polymers often need additional surface functionalisation treatment to make their surfaces more cell adhesive. These treatments (e.g. plasma polymerisation and etching) are aimed to make surfaces more hydrophilic and adhesive to proteins. Once an initial layer of protein is formed on the surface cells can recognise the binding domains on these proteins to adhere and grow.

3.3.1.2. Pore Size and Porosity

Pore size and porosity can increase the area for cells to grow on, by providing a network for cells to anchor inside the structure. However, the migration of cells must

be taken into account as this is hindered if pore sizes are too small, whereas larger pores result in a lower surface area [73]. For tissue engineering, in particular, biodegradable microcarriers hold the potential to be directly transferred to the site of treatment. For this to be possible the pore size has to be large enough to allow vascularisation through the implanted carriers; since microcarriers are not connected to each other, the blood vessels will branch through each bead, eventually linking together [25].

Bone itself is an inhomogeneous porous structure as Cowin et al. summarised, there are three hierarchies of pore sizes in cortical bone [78]. They are ranging from the largest pores, which is estimated to be around the order of 20 μm, found in the Volkmann and Haversian canals which provide vasculature and enervation to the bone, around 0.1 μm in the lacunar-canalicular system and the smallest, which is around 0.01 μm around hydroxyapatite crystallites and collagen fibres (Numbers quoted as radii). Cancellous bone has a different structure, which resembles a sponge where the pore sizes can range between 300 - 600 μm in diameter [79].

As mentioned previously, the environment and mechanical properties of the native material are influential, thus for bone tissue engineering porous structures should be considered. To clarify, studies have also confirmed that cells respond to pore sizes. Pore sizes between 50 – 1000 μm have been experimented with, but it is generally accepted for bone tissue engineering greater than 100 μm are more favourable to promote osteogenesis [80]. Huri et al used 1000 - 1500 μm particles. For porogen leaching, they showed higher ALP and calcium content per DNA than < 500 μm and 500 – 1000 μm after 3 weeks of culture [81]. Pore homogeneity can also have an impact. Two distinct methods were applied to manufacture a porous silk-based scaffold; salt leaching results in inhomogeneous pore sizes, whereas, the inverse opal method provided a monodisperse structure [82]. By the end of week 6, any difference between the two structures was non-existent in terms of DNA and ALP; however, there was 46% more calcium on inverse opal structures. In an in vivo study, large uniform pores of 400 μm of hydroxyapatite-coated scaffolds resulted in 30 mm^3 more bone regeneration than a bilayer scaffold, which consisted of two different mean sizes: 200 μm for the inner; and 450 μm for the outer [80].

The important of pore size influence on the osteo-ability of cells has been documented; there is moreover, an argument to suggest pore size can also have some influence on culturing and growth. Murphy et al. pore sizes of 325 µm had over 60% attachment efficiency and greater cell number at the end of 7 days compared to pore sizes between 85 and 190 µm [83]. After 24 hours freeze-dried and salt-leached scaffolds with 85 µm and 345 µm, average pore sizes were 2 – 3 times higher than 520 µm salt-leached scaffolds. Larger pores are more beneficial for cell penetration within the scaffolds, especially in dynamic conditions [83,84]. After 15 days scaffolds with the smallest performed contrary to static results; 85 µm had 0.6×10^6 cell number/scaffold, and 520 µm had over 1.2 cell number/scaffold [85].

3.3.1.3.   Surface Treatment

Carrier design is not solely limited to intrinsic material characteristics, surface roughness or topology, as post-processing options are available to enhance or provide more favourable conditions for growth. In some cases, it is essential as cellular compatibility is also affected by wettability and chemical nature of the substrate. Surface modifications can be tailored using plasma enhanced chemical vapour deposition, UV induced Ozone treatment, and chemical treatments (e.g. surface polymer grafting) [86]. Such techniques are frequently used in the biomaterials industry for orthopaedic implants such as hip replacements to make them biocompatible and increase the rate of osteointegration [87].

Wettability, or surface hydrophilicity of a polymer, is often an indicator of their suitability for biological interactions. The deposition of polar functional groups (–OH, -COOH, C=O) on to the surface increases its interaction with water. For a higher success of cell adhesion wettability within the region of $40 – 70^\circ$ is recommended [88]. Air plasma etching for 15 mins reduced the water surface contact angle by 30° of hydrophobic PMMA particles [86]. Affinity to cell attachment of Polylactic acid and poly(D,L-lactic acid-co-glycolic acid) was also improved with air plasma, both polymers were more hydrophilic after treatment, due to their reductions in contact angles from 85° and 74.5° to 10° and 37°, respectively [89]. Owen et al. found that air or acrylic acid plasma coating was mandatory for the attachment of hES-MPs to 2-ethylhexyl acrylate (EHA) scaffolds [90]. The coating also influenced the production of ALP, and over 15 days was higher in samples coated with acrylic acid in osteogenic media than air plasma coated samples. Plasma introduction can be through grafting or deposition, the former

introduces species onto reactive groups in the polymer, whereas the latter does not interact with the bonds, but instead covers the scaffold surface [91,92]. The presence of nitrogen determined coverage due to the surface coating monomer used, allylamine; a higher concentration was present on the surface and within, compared to grafting, which was found mainly on the exterior [92].

Coating with ECM proteins, like collagen, laminin, fibronectin is another approach to enhance cell compatibility with synthetic materials. For example, Shekaran et al. highlighted that inherently hydrophobic polycaprolactone-carriers carriers (PCL), required ECM coatings for attachment and growth of MSCs [93]. Additionally, this study showed that the combination of poly-l-lysine and fibronectin outperformed the experiments where these proteins were used individually. In particular, a three-layer combination of fibronectin-poly-l-lysine fibronectin was more effective than combinations of dual and individual coating. In addition, when compared with Cytodex 3 carriers, they were equivalent in both attachment and growth performance.

Cell attachment is dependent on the surface chemistry of scaffolds. To further highlight this Chen et al. found that the choice of ECM-like coating influenced hESC attachment and expansion. Without the addition of Matrigel hESC concentrations were lower than 1×10^6 cells/ml on day 7 of culture, whereas with the additional Matrigel coating, for example, resulted in improved yields, 7 out of 11 culture surfaces tested exceeded the initial cell concentration by up to 70%. Of the 7 other ECM coatings tested (e.g. Fibronectin, Vitronectin) Matrigel and laminin had higher concentrations, both were deemed suitable for long term culture [94].

A review by Rashidi et al., suggests that the properties of the bulk material can be affected as a result of surface engineering [95]. Ozone, UV- treatment, and Wet-chemical processes could affect degradation rates and in some cases could change the mechanical properties of the materials [283]. Whereas, the introduction of functional groups via plasma treatment does not present such problems. It does, however, require samples sizes to be of a relatively small thickness to provide a homogenous coating though the small pore sizes of microcarriers could restrict coating within the centre [90].

3.3.2. Other Design Considerations

3.3.2.1. Biodegradability

Developing of microcarriers continues to provide novel ways to ensure maximum yield of cells such as scaffolds that are biodegradable, or carriers that degrade through enzymatic addition leaving a skeletal network of cells. Several companies offer degradable options, as in the case with gelatine-based Percell microcarriers, which can be dissolved with a proteolytic enzyme. The main benefit is the direct transfer of agglomerated cell-particles, or only cells directly into the patient, reducing the need for additional processes, for example, harvesting cells with a proteolytic enzyme.

3.3.2.2. Magnetic Microcarriers

The polymer particles can be made magnetic by incorporating smaller micro- to nanoparticles into the polymer matrix, these can be mixed in before curing, or can be combined post-curing by chemically cross-linking into the polymer network. The ways this can be achieved have been described in more depth (Chapter 1 – Section 2.11).

Magnetic microcarriers to be used in combination MRI imaging have been reported for targeted drug delivery [96], and biomarking. In these experiments, an MRI scanner is used to deliver a therapeutic magnetic microparticle (which incorporates magnetic microparticles to a particular site within the body. Which can then be used for targeted drug delivery, in particular for cancer treatment. However, there is little information available on the application of these particles in cell culture. Currently, only a single type of magnetically responsive microcarriers are on the market - which is alginate-based, and sold by Global Cell Solutions (The GEM). The leading purpose of the magnetic-responsive ability is for easy collection when harvesting, during manual or automated media change (Global Cell Solutions, 2016). Yet, could their ability to respond to external magnetic fields be more than just limited to easier processing and handling. Coupling this with the ability of hMSCs to respond to fluid shear stress, could cells inoculated on such a substrate be encouraged to differentiate through external manipulation. This is the focus of part of this chapter.

3.3.3. Culturing

A multitude of methods have been used to inoculate microcarriers, some involving agitation from a small duration to constant, and others entirely by bathing microparticles in cell-laden media. There does not seem to be a coherent protocol for culturing based on associated cell type, although, numerous successful methods have shown that agitation is a common factor in all seeding procedures involving commercial carriers [102, 103, 94]. The different seeding protocols are highlighted in Table 8, which intends to summarise culturing procedures various studies have undertaken.

In an earlier optimisation study, Ng et al. showed little difference between continuous stirring at 40 rpm and high-frequency intermittent stirring [97]. However, at the same impeller speed, but lower frequency showed a significant increase in cellular adhesion. The effectiveness of cell-to-bead attachment decreased again when the stirring speed increased but at the same lower frequency, though less cell agglomeration was seen. Hofmann et al., also compared dynamic and static culture as part of a larger experiment and found while dynamic culture had 50% lower DNA content over a 24 hour period, it did, however, have better distribution on the scaffold [52].

A study by Strathearn et al. suggests that serum can influence attachment. After a 2-hour period of monitoring, human embryonic kidney cells without FBS resulted in 90% attachment; compared to 20% when 5% serum was used. It was concluded that cells attached efficiently and more uniformly; this trend continued to a 144 hour period [98]. Comparing this a different cell line; Vero cells, again, showed a higher attachment efficacy under serum-free conditions; however; it was only 33% more effective than the 5% serum enriched media. Other studies have corroborated this Schop et al. for example, established there is a clear difference in seeding efficiency which decreases with increasing serum concentration (0, 5, 10 and 15%) [99]. Moreover, Mukhopadhyay et al., also found the rates of attachment with and without serum differed [100]. This same conclusion was found to be true with non-porous plastic microcarriers which were more effective at attachment and growth over 3 and 6 days of culture using hMSCs and serum-free media [101].

A number of studies have highlighted continuous and intermittent regimes of dynamic culture can increase cell numbers and homogeneity of inoculation short and long-term

[53,63,69]. Important to note is that that most commercially used carriers are surface functionalised. Thus, dramatically increasing their effectiveness for cell adhesion.

Another interesting point is the effect of serum on cell attachment; it is evident that there is a relationship present. Due to its importance in expansion, the addition of serum to microcarrier culture after the attachment phase should be considered, especially if the attachment is ineffective with serum added to the media [99].

Table 8: Summary of microcarrier seeding conditions from various research publications.

Cell type	Microcarrier	Seeding Density	Method	Additional Comments	Ref.
Fibroblasts	CultiSpher-GL	17.6×10^6 g^{-1}	Intermittent agitation 20 rpm, 5 mins, every hour	Media adjusted to 100 ml	[102]
hMSCs	Cytodex1, Cytodex3, Cultispher GL, HyQspheres	3 cells/ bead	Agitated 24 hours, 25 rpm	50 ml medium added	[103]
hMSCs	Synthermax II	$5000 – 6000$/ cm^2	No agitation for 18-20 hours		[112]
hESCs	Hellix II	$12000 – 16000$/ cm^2	No agitation for 24 hours	Media adjusted to 3 ml in each well plate.	[105]
hESCs	DE53, DE52, QA52, CM52,	40000 - 50000 cells/mg	110 rpm Orbital Shaker, 2 hours	Final volume 5 ml	[94]
hESCs	TSKgel Tresyl-5PW	$1.6 – 2 \times 10^6$	110 rpm Orbital Shaker, 2 hours	Final volume 5 ml	[94]
hESCs	Cytodex 1, 3, Cultispher G and Cytopore 2,	$1.6 – 2 \times 10^5$	110 rpm Orbital Shaker, 2 hours	Final volume 5 ml	[94]
Vero	Cytodex3	$\sim 1.8 \times 10^5$ /ml	Agitate for 5 min and keep static for 25 min) at about 60 rpm in the first 2 hr after inoculation	Agitation speed was at 80 rpm after that.	[104]
CHO	CultiSpher G	2×10^5 /ml	Inoculated at 25 ml with 5 min of stirring at 40 rpm followed by 15 min rest. Repeated 3 times.	Working volume increased to 50 ml, and 40 rpm of agitation.	[105]
CHO	Cytodex 3	1×10^5 /ml	Gentle agitation 20 – 60 rpm in 30 ml of Medium.	Medium increased to 50 ml, with constant agitation.	[106]

Vero	Cytodex-1 Cultispher-G	$0.03 - 1.0 \times 10^6$ cells/mL	Intermittent & continuous, at 40 rpm	100 ml working volume	[97]
hMSCs	non-porous Plastic P-102L	6000 /cm^2	Static for 1 hour	30 rpm constantly after	[101]
hMSCs	non-porous Plastic P-102L	6000 /cm^2	Static 18 hours	75 rpm (Bioreactor), 30 rpm (Spinner Flask) both constant	[107]

3.3.4. Expansion & Harvesting

Typically, once a flask is 80 – 90% confluent, anchored cells are split through the addition of a proteolytic enzyme in order to expand culture. A similar technique is recommended by commercial suppliers of microcarriers, who often provide guidelines highlighting methods that can ensure an efficient culturing process by applying it to 3-dimensional scaffolds. However, Nienow et al. found that the harvesting strategy designed by Solohill was inadequate for primary hMSCs; the original strategy involved 15 minutes in dissociation solution at static incubation conditions. A more effective method was changing the stagnant environment to short-term intense agitation in the same enzymatic solution; this resulted in > 95% yield [108]. The addition of agitation is particularly useful to detach cells from the cavities of porous structures.

The established method of dividing cell densities up and distributing smaller quantities on to newer growing is not unique to 3D culture. Bead-to-bead transfer provides an alternative and less intrusive technique of expanding culture. The mechanism encourages cell expansion by introducing additional microcarriers that provide a fresh growing surface; quite often cells proliferate and spread over the suitable surfaces as the beads adhere to the ECM. This technique is particularly interesting for cell-lines that are sensitive to chelating agents such as EDTA or collagenase. Numerous studies have highlighted the feasibility of achieving expansion in such a way, and various cell-lines have been successfully expanded by such means: CHO, HMSCs, Vero. HESCs [109].

CHO cells were cultured onto CultiSpher G and S and were successfully expanded using bead-to-bead, as well as transferring the beads to a new reactor environment [105]. hMSCs cultured onto modified polystyrene showed evidence of bead-to-bead migration of cells, as only the replenishment of new growing surface area allowed for long-term expansion for up to 40 days [110]. Based on the same report the formation of aggregated microcarriers is crucial for cell migration, hence should not be prevented, but can be controlled via the addition of new surface area.

Expansion through bead-to-bead migration is clearly feasible, the process and conditions for this to occur however seem to be vaguely understood. According to Schnitzler et al. and Wang et al., it could be influenced by the type of cell, the properties of the microcarrier surface or the media composition [104,111]. The visible

sign of aggregation or clumping maybe a good indication of "bead-to-bead" transfer capability, the cellular matrix produced may act like an adhesive, entrapping new carriers and consequently providing new surface area to migrate to and grow on.

A way achieving or encouraging agglomeration is through high cell density as Phillips et al. found, by doing so there was increased aggregation [109]. Another environmental trait as Hervy et al. described was shifting to intermittent bursts of agitation during seeding, which limited and controlled clump formation [112]. Chen et al. established that the size and shape of the microcarriers have an effect on aggregate formation [94]. Primarily due to the variation of cell-microcarrier aggregates forming with 10 different microcarriers. Positively charged cylindrical carriers (130 μm x 35 μm) generated more compact aggregates than 190 μm spherical Cytodex carriers. Whereas, a reduction of microcarrier size from 65 μm (Tosoh65 PR) to 10 μm (Tosoh10 PR) resulted in a denser cell network, but lower yield. Since the cells were larger, the latter acted as a linker for the cells, rather than a carrier.

Harvesting from 3D scaffolds is a two-stage process: detachment of cells, followed by separation of cells from microcarriers [113]. For microporous, structures bathing in a dissociation reagent does not yield an effective detachment of cells. Like the culturing phase, the detachment phase requires agitation to obtain >90% yields.

Careful design considerations and testing carried out early on could result in the direct transfer of cell-laden particles directly to the treatment site. Combined with degradable properties, there is then no need for cell harvesting steps like dissociating and cell filtration, as they are ready for delivery. Due to the tunable nature of the polymer matrix, this could leave a mesh of cells within days or months.

Table 9: List of commercially available microcarriers

Range	Manufacturer	Material	Av. Diameter (um)	Surface area (cm²/gram)	Charge	Additional Notes
The gem™	Global Cell Solutions	alginate-based	75 – 150	360 - 500		Dissolves and magnetically responsive
Cytodex Range	GE Healthcare	dextran-based	190*	4400	+	
Cultispher®	Percell	gelatin-based	130 – 380			Can be dissolved with proteolytic enzymes
Hillex®CT	Pall	polystyrene-based	160 - 200	257	+	
Various	Corning®	polystyrene-based	125-212	360		
Sigma-solohill	Sigma-Solohill	polystyrene beads	125-212	257-480		

4. Materials & Method

4.1. Curing Setup

Figure 34 below, is a rudimentary illustration of the setup that was utilised, only omitting the recirculation from the beaker, done using a peristaltic pump kept constant at a rate of 300 rpm. The syringe pump has been replaced with just a syringe containing the emulsion for illustration purposes only; having such a pump controlled the rate of extrusion of the emulsion, regularly kept at 0.02 ml/min. By changing the speed of the pumps, the sizes could be finely controlled and altered if necessary. The black rectangle was the elevated position of the 100 W UV lamp; the particles were irradiated constantly until the emulsion had cured in the syringe, or was empty – typically up to 1-2 hours.
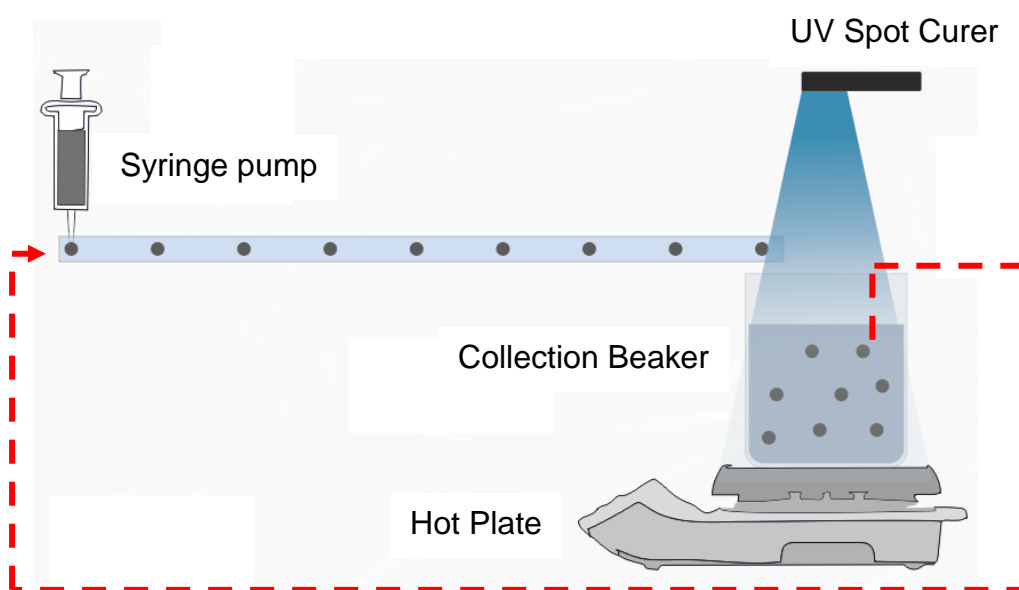

Figure 34: microfluidics setup utilising a hot plate and UV-lamp to cure spherical microcarriers containing magnetic carbonyl iron particles. The dashed red line represents recirculation feed.

4.2. Materials for Poly-HIPE and Assays

Manufacturing of Poly-HIPE:

Diphenyl(2,4,6-trimethylbenzoyl)phosphine oxide/2-hydroxy-2-methylpropiophenone (Photoinitiator), 2-Ehtyhexyl acrylate (EHA), isobornyl acrylate (IBOA), Trimethyllolpropane triacrylate (Cross-linker), Hypermer B246-SO-(MV) (Surfactant), , N,N,N′,N′-Tetramethylethylenediamine (TEMED) Potassium persulphate (KPS). All chemicals purchased from Sigma-Aldrich, unless stated otherwise.

Assays:

Tris-HCl, Zinc Chloride ($ZnCl_2$), Magnesium Chloride ($MgCl_2$), Deionised Water, Sodium Hydroxide (NaOH), Triton X-100, PBS, PNPP Phosphate Substrate Kit, resazurin blue salt, L-Glutamine, Fungizone, Penicillin-Streptomycin, Fetal Calf Serum, DMEM Medium, αMEM, dexamethasone, ascorbic acid. All chemicals purchased from Sigma-Aldrich, unless stated otherwise.

4.3. Preparing micro-particle scaffolds

The following procedure describes how micro-particle scaffolds were produced from an emulsion templating route; more information about this technique can be found in Chapter 3, section 2.6.

A solution consisting of EHA (3.9 g), IBOA (1.3 g), Cross-linker (1.4 g) and surfactant (0.198 g) was prepared, which formed the Oil phase. It was scaled up if necessary to make a stock solution. The solution was kept sealed, and wrapped in foil to avoid exposure to light.

Before usage, a certain quantity of stock (Oil phase) was weighed and between 10 - 60 wt% of carbonyl-iron, 0.126 g photo-initiator, and 0.126 g KPS was added, before being mixed thoroughly using a paddle stirrer – which was set to 400 rpm. Once a homogeneous colour was achieved, water (4x oil phase) was added – dropwise, under constant stirring to emulsify it. Separately, approximately 500 ml of water/glycerol (70 % glycerol) solution was made; and thoroughly mixed. The solution was pre-heated to 40°C and recirculated. Pumps were also pre-configured: The Peristaltic pump was set to 300 rpm; and Syringe Pump to 0.08 ml/min.

0.05 g TEMED was then added and stirred for a few seconds to disperse it into the emulsion. The Oil-in-water (O/W) emulsion was poured into a syringe and then

mounted on to a syringe pump. The syringe tube was covered in a cold jacket, to reduce the risk of the emulsion curing inside the tube, or needle.

Note: The curing time after the addition of TEMED is significantly reduced, which is why the pumps, water baths and ice packs must be prepared in advance.

Once the emulsion had all been pushed through, the particles were allowed to sit in warm water to ensure they were fully cured. They were then encouraged to settle by placing the beaker on top of a strong magnet. The solution was decanted, and the particles were washed multiple times with water and then stored in methanol.

4.4. Plasma Polymerisation – Acrylic Acid

IBOA-EHA porous beads were dried and transferred to a plasma rig and coated using acrylic acid, making the surfaces more hydrophilic. Acrylic acid was coated for 15 minutes. Using a 70% ethanol-water solution they were transferred for further processing.

4.5. Particle Preparation

A common problem experienced was pockets of trapped air inside the pores causing them to float, to overcome this problem, particles were left in a vacuum oven to allow any that were floating to sink, this was anywhere between a few hours to overnight. They were then sterilised using a strict procedure in a biological hood. Initially washed in 100% ethanol, then centrifuged for several minutes a gradual solvent exchange process was carried out with 70% ethanol and PBS, followed by centrifuging again, and this process was repeated for 50%, 25% ethanol-PBS, before a 100% PBS was added. Following this by two washes in media each with a centrifuging step in-between. The particles were stored in cell medium in the fridge to be used when required.

4.6. Actuator Setup

To stimulate the magnetic particles a linear actuator (L16 Linear Actuator 140mm, 35:1, 12V with Potentiometer Feedback) was modified so an arm of neodymium magnets with (0.8 kg of pull) could be attached perpendicular to it (See Figure 35). The cable was connected to a linear actuator control board (Firgelli Automations), and a 12 V power supply. Thus, by using the provided software the speed and frequency could be controlled to a high degree. The construction was rudimentary; the flasks were held by a bar clamp, and taped to a box – used to elevate the flasks above the movement of the actuator. The actuator itself was held down using several cable ties onto a test-tube rack, and a Blu Tack counterbalance to level the magnetic arm. To test the setup, microcarriers in water were moved using the arm. It was found that depending on the distance between the magnets and particles, they could move the greater distances of the flasks when close and little when further away. 3 mm was the maximum distance that demonstrated any displacement of the particles (Figure 36).

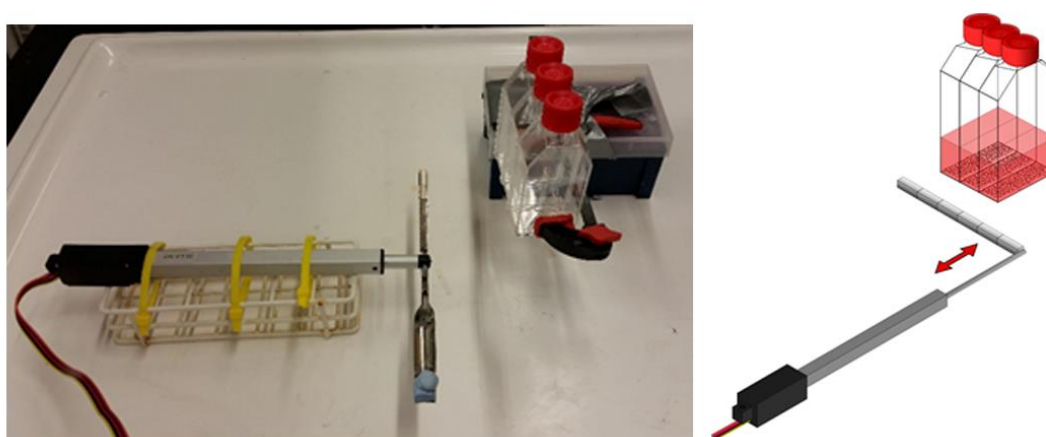*Figure 35: Image showing the modified linear actuator setup, and three T-25 flasks coupled using a G-clamp. The illustration on the right is for clarity is an isometric drawing of the critical components of the setup.*
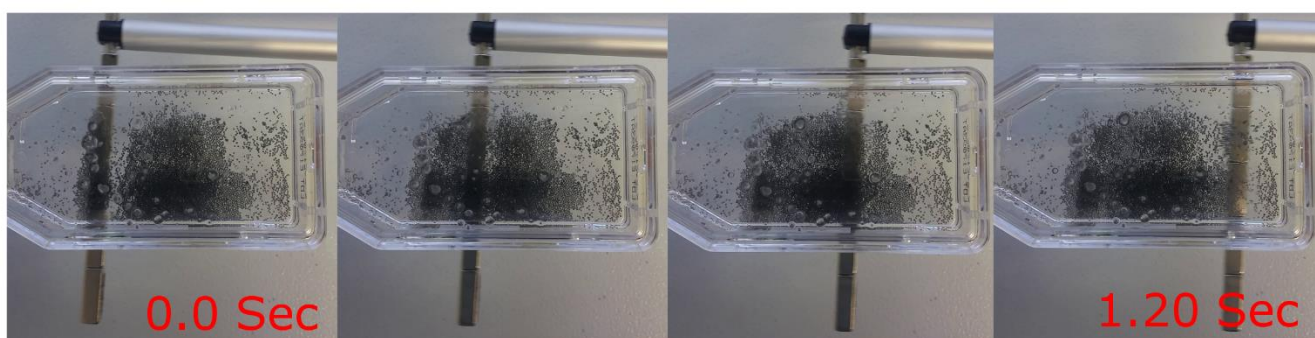

Figure 36: Timelapse of moving particles at a maximum speed of 3.2 cm/s, what can be seen is the movement of the magnetic particles to the left of the T-25 flask as the magnets pass beneath the surface.

117

4.7. Cell Culture

4.7.1. Fibroblasts

DMEM Medium containing: L-Glutamine, 200 mM; Fungizone, Penicillin-Streptomycin and Fetal Calf Serum was mixed. A T-75 containing fibroblasts (patient: 298) was cultured in 15 ml of medium until they were 70 – 80% confluent, at passage 2.

4.7.2. HESMPs

4.7.2.1.   Media Preparation

Expansion medium: Alpha-MEM (α-MEM), Foetal Bovine Serum (FBS), Penicillin (10,000 units)-Streptomycin, (10 mg/mL), L-Glutamine (200mM).

Passage Medium: Expansion medium, Fibroblastic Growth Factor Basic Recombinant Human Protein (hFGF) (10 µg/mL)

Osteogenic Medium: Expansion medium, 0.5 M beta-glycerolphosphate solution (βGP) 5 mg/mL Ascorbic Acid 2-Phosphate solution (AA2P), 10 µM Dexamethasone solution (Dex).

4.7.2.2.   Cell culture

A T-75 flask was coated with 2.5 mL of gelatin solution (0.1 w/v% gelatine solution) and left for 30 minutes. The cells were defrosted by holding the frozen vial until it thawed; it was then transferred with 12 ml of warm expansion medium. The vial was rinsed into the same medium to ensure most of the cells were transferred. After centrifuging at 1,000 rpm for 5 minutes, the supernatant was carefully removed. The cells were carefully aspirated in 12 ml of fresh expansion medium which was supplemented with hFGF, and transferred into the gelatine coated T-75 flask, and left to incubate. The cells were passaged using the supplemented medium and were used inoculated when they were 70 – 80% confluent.

4.7.3. Cell Counting

The medium was removed from the flask, and 5-6 ml of Trypsin-EDTA was added to the T-75 flask in order to detach the cells, they were then incubated for 5 minutes. The cells were checked under a microscope to see if they had detached; if not, they were encouraged to do so by knocking the side of the flask against a firm surface. The now cell suspension was swiftly diluted with approximately 10 ml of medium to neutralise the trypsin and transferred into a universal tube. It was centrifuged, for approximately

~ 5 mins at 10,000 rpm. The medium was decanted, while ensuring the pellet of cells remained stationary in the universal tube. A concentrated cell suspension was created by gently aspirating and purging 1 ml of medium until the pellet had re-dispersed.

A Neubauer haemocytometer was used to estimate the number of cells in the suspension; this along with a glass coverslip was prepared by cleaning with 70% IMS solution and then drying. Moisture was applied to the coverslip, to help it fix to the surface of the haemocytometer (Flip upside down to check it has stuck down properly). 10 µl of the concentrated suspension was pipetted between the coverslip and haemocytometer. The grid was focused using a microscope (10x objective) so that the cells within the squares can be counted. Cells were calculated by $Total\ No.\ cells = Average\ no.\ of\ cells\ x\ 10^4$ to get cells per millilitre.

4.8. Cell Seeding

The particles were firstly prepared in a biological hood at all times to ensure they remained sterile, by stirring and pipetting 1-2 ml into each T-25 flask used. The medium in each T-25 was replaced by an expansion medium and left in an incubator for up to an hour. This period was adequate to prepare and count the cells, ready for culture.

Cells were counted, and 250,000 cells were seeded randomly into each area of the flask, before being put back into the incubator. The medium was changed three days later, by removing 3 ml and adding 3 ml of fresh medium back in, this was done for a week to allow the cells to proliferate and form clumps. After 7 days the cells were carefully transferred into, new flasks using Pasteur pipettes, the medium was also replaced with osteogenic medium (See above). The experiment was started a day after transfer.

4.9. Cell Stimulation

Two different methods of stimulation were employed, the first to demonstrate the idea, and the second utilised the magnetic response.

4.9.1. Orbital Shaker

EHA-IBOA particles containing no iron were used to demonstrate the initial concept of shear stress-induced differentiation. Cells were seeded in six T-25 flasks; 3 static controls and 3 dynamic culture flasks. They were left for 3 days allowing the

aggregation of particles, before the first media change. They were shaken 30 mins a day at 50 rpm, for 7 days. Fresh media was replenished every 3 days by firstly removing 3 ml, and then adding 3 ml, keeping the total volume at 5 ml.

4.9.2. Modified Linear Actuator

The culturing process remained the same as before. Iron embedded microcarriers were stimulated at 100, 50 and 10 % speed for 30 mins daily for 6 days, and the experiment was stopped on day 7. Refer to Table 10 for settings.

Table 10: Actuator settings programmed into the Firgelli actuator software, include settings for all experiments done.

Speed (cm/s)	Accuracy (%)	Retract Limit (%)	Extend Limit (%)	Cycle/ Minute
3.2 (100%)	96	10	80	13
1.6 (50%)	96	10	80	10
0.3 (10%)	96	10	80	4

4.10. Resazurin Assay Protocol

A stock solution was prepared by adding 12.6 mg of resazurin sodium salt in 50 ml of distilled water, which was then filter sterilised. The stock was stored in a light free environment, and a working solution was prepared from this when required. To prepare the working solution; the stock was diluted 1:10 with culture medium.

The culture medium from the wells was drained and replaced with resazurin blue working solution, and left in an incubator for 4 hours. After 4 hours, 200 µl from each well was transferred in triplicate from each well to a 96-well plate. The pipetting was done in a staggered pattern and then read on a plate reader at λ_{ex}: 540 nm and λ_{em}: 590 nm.

4.11. Cell fixing

Culture medium was drained off and washed several times with PBS before being replaced with 3.7% formaldehyde solution for up to an hour. The formaldehyde solution was then removed from the samples and stored PBS.

4.12. H&E Staining

Optimal cutting temperature compound (OCT Media) was to mount the particles into blocks ready for histology. OCT Media was poured into moulds then frozen by rapid cooling using liquid nitrogen. The particles were transferred on top and distributed

before fresh OCT media filled up the remaining free volume of the mould. And again frozen in the same manner.

Thin Films (7- 10 µm) were processed on to glass slides using a cryostat. All sectioned slides were left on a warm (~ 40ºC) hot plate for a day.

Soaking of the slides was kept to a minimum to prevent thin slices of particles from detaching from the slides. The following protocol was followed: The slides were soaked in xylene (3 mins), followed by soaks in 100% IMS (1 min), and 70 % IMS (30 secs). Wash glass slides individually by carefully pipetting drops of distilled water down them. The slides were collectively immersed in filtered haematoxylin to stain the cell nuclei (1.5 mins; filtered) and then washed again via pipetting drops along the slides until the water begins to run clear. To stain the cytoplasm, the slides were introduced into Eosin for 5 minutes then briefly washed as previously mentioned. They were then sequentially immersed in 70 and 100% IMS, and finally, they were quickly immersed in Xylene. A glass coverslip was mounted on top, using DPX mounting solution and left to dry before being analysed using a microscope.

4.13. Staining with Phalloidin - TRITC/DAPI

Before staining, the cells were fixed following the protocol mentioned above. A solution of 0.1 % Triton X-100 in PBS was prepared and incubated in a light-free environment (20 mins). After the prescribed time it was decanted, and the samples were gently washed with PBS.

Dilute phalloidin-TRITC to a concentration of 1:1000 in PBS, add an aliquot of DAPI for every 10ml of phalloidin solution (Add enough to cover the samples), then incubate for 30 mins (no light).

The same process was followed for staining complete particles. Microcarriers were immersed in PBS, which contained both TRITC and DAPI stains at the desired concentrations.

4.14. ALP protocol

ALP protocol was split into multiple parts, as this required breaking up the cells, harvesting the lysate using a cell digestion buffer. The protocols for each step is outlined below in chronological order.

4.14.1. Cell Assay Buffer

Tris-HCl was diluted to 1.5 M, and $ZnCl_2$ and $MgCl_2$ were diluted to 1 mM, which was adjusted to pH 8 if required using NaOH. This was then kept as a stock reagent for all ALP protocols.

4.14.2. Cell Digestion Buffer

Cell assay buffer was diluted using deionized water by 10 vol% (9 dH_2O, 1 ml CAB), and to this 1% of Triton X-100 was added, which was mixed until the solution became clear. The protocol required freshly made cell digestion buffer.

4.14.3. Cell Digestion

Once the medium had been removed from the wells, the scaffolds were washed twice with PBS. Enough cell digestion buffer was added to submerge the scaffolds ensuring the same volume was used throughout. They were then left incubate for 30 mins. The lysate and scaffolds were transferred into 1.5 ml tubes, and were vortexed before being refrigerated overnight, or frozen in – 80ºC until they were analysed. A freeze-thaw procedure was carried out before analysis. Three cycles were done at – 80ºC for 10 minutes, and 37ºC for 15 minutes, then immediately centrifuged at 10,000 rpm for 5 minutes. Each tube was vigorously shaken, to ensure the lysate was mixed before analysis.

4.14.4. ALP Reading

The total volume of the substrate was calculated for each run (180 µl per well), depending on the total volume required: one tablet was dissolved into 1 ml of buffer, and 4 ml of water. 180 µl was pipetted into each well, of a 96 well plate. Using a Gilson pipette 20 µl of lysate was added to each well, so for one particular condition, it was done in triplicate (60 µl per condition). Upon addition of the lysates, we left the plate at room temperature until a faint colour change was change to yellow was observed, or 30 minutes passed. It was immediately transferred to a plate reader, which was configured to measure absorbance at 405 nm, every minute for 30 minutes.

4.14.5. DNA Assay

Quant-iT High Sensitivity DNA Assay Kit was used: Quant-iT DNA Assay Reagent, Quant-iT DNA Assay Buffer. The total volume required was calculated beforehand, based on each condition and for triplicate readings. Dilute the assay reagent in the assay buffer (1:200) and wrap the container in foil to create a light free environment.

Add 90 µL (270 µL for each condition) of working solution to each well, of a black 96-well plate. Into the same well plates add 10 µL of lysate (See 4.14.3) in triplicate. Inset the plate into the plate reader and utilise the shaking function for 10 seconds to mix the constituents, wait a further 10 minutes and shaking for another 10 seconds before reading. The plate was read at λ_{ex}: 485 nm, λ_{em}: 535 nm.

4.14.6. Alizarin Red S Stain Assay

Alizarin Red S was dissolved in deionised water at 1% w/v, and it was then warmed in a water bath to aid the dissolution before being filtered to remove any remaining particles.

Wash microcarriers several times using distilled water, then add the same volume of alizarin red solution to each sample. Allow the samples to sit for 30 mins so the solution can diffuse into the porous structure can occur. Remove alizarin red solution and wash repeatedly using distilled water, place on the shaker at a low setting for several minutes to help. Repeat until there are no visible signs of excess stain leeching out.

Add 5% of perchloric acid to destain releasing the calcium bound alizarin red. The samples were left on an orbital shaker for gentle agitation for 15 minutes. 150 µL of the released solution was transferred to a 96-well plate in triplicate for analysis using a plate reader at an absorbance wavelength of 405 nm.

4.14.7. Sirius Red

Direct red 80 was dissolved in saturated picric acid 1% w/v to form Sirius red solution. Again, filter to remove particles.

The samples were rewashed several times to get rid of any alizarin red S destain currently in the well plates, and repeated until it was all clear. The same volume of Sirius red was added to each well plate and left for 18 hours on an orbital shaker, at a low rpm. Remove solution and wash with deionised water, gentle shaking to speed up the removal process – this was repeated until the water was clear.

A known volume of 0.2 M NaOH:MeOH (1:1) was used to destain. The samples were placed on an orbital shaker for 20 minutes at a low setting again. 150 µL of the destain was transferred in triplicate to a 96 well plate. As before, the plate was read at an absorbance of 405 nm.

5. Results

5.1. Characterising Magnetic Particles

5.1.1. FTIR

Fe-O interaction peaks occur around the 400 – 600 cm^{-1} region (Figure 37). There are also some minor features of O-H stretching at higher end of the spectra (3600 – 4000 cm^{-1}), which is usually a strong indication of water presence, that can either be free or absorbed, a peak is also observed around the 1600 cm^{-1} mark that can be attributed to the same water interaction [114]. The main distinctive peaks in this spectra are situated in between 2300 – 2400 cm^{-1} – this is associated to carbon dioxide exposure from the environment as the sample holder even though it is purged with nitrogen, it is however still open to the atmosphere.
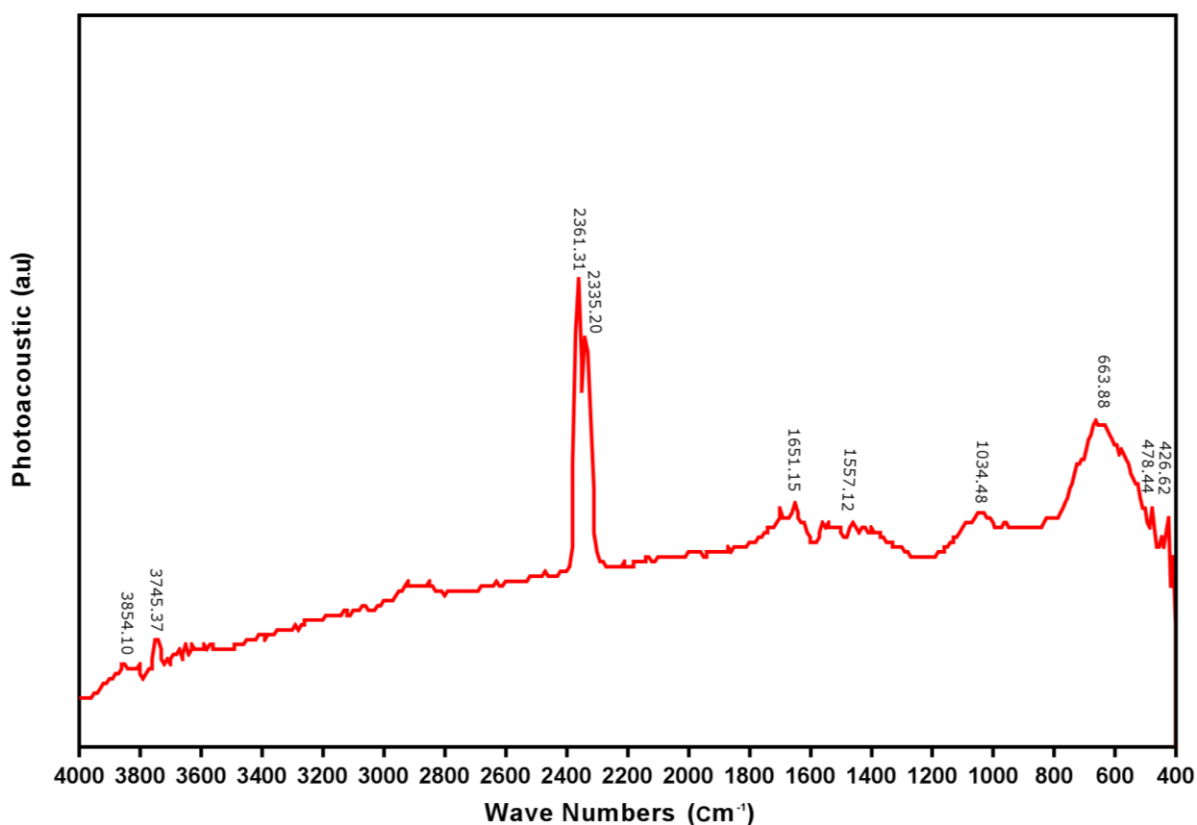
Figure 37: FTIR-PS spectrum of carbonyl iron powder used as the magnetic filler to the poly-HIPE matrix. The most notable interaction is the Fe-O bond in the region of 400 – 600 cm^{-1}.

5.1.2. Size distribution measured by particle size analyser

The distribution was bimodal, suggesting two defined regions between 0.001 - 0.12 and 0.14 – 40 µm; sizes of 0.1 and 8 µm contributed the highest percentage volume. A median of 3.27 µm and a span of 4.45 µm suggests that the variation in size is not a narrow distribution. Sonication was used beforehand to help break up any particle agglomerates, though volume distribution of particles around the 1-10 µm range is more intense, suggesting agglomeration. The reason behind this is that if a number distribution were considered, the peak with the primary peak would be more intense due to a higher number of particles contributing to the same volume density. Hence, it can be concluded that a higher number of particles are within the region of 0.001 to 0.12 µm.
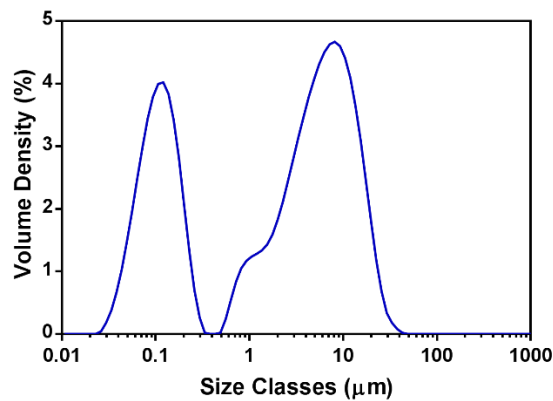
Figure 38: Volume percentage of bimodal size distribution for carbonyl iron powder obtained using laser diffraction.

5.2. Monolith Study

Photo-curing emulsions to create polymerised-HIPEs containing carbonyl iron particles showed early promise, but only remained possible for low concentrations of magnetic particles between 10 -20 wt% (Figure 39).

Figure 39: Image of 50:50 EHA:IBOA poly-HIPE with 9 wt% carbonyl Iron particles and 75% water content (Left) and 90% (Right).

With increased water concentration, UV-curing alone was sufficient, though, upon further inspection emulsion leaking from a fracture on the surface resulted in the understanding that the core of the structure remained a liquid emulsion. A cross-section of this shows an internal cavity with a distinct separation of the top and bottom layer, both of which were exposed to 30 seconds of UV. This trend continued for high concentrations of the particle, though increasing the water content improved the ability to cure the material as the concentration of particles became more diluted.

Figure 40: A sectioned cross-section of 50:50 EHA:IBOA, with 9 wt% carbonyl iron particles and 75 wt% water content, showing how the inner section remained uncured.

Thermal curing was used as a method to overcome this, by the addition of the water-soluble thermal initiator, potassium persulphate 2- 4 wt% (KPS) and the catalyst N,N,N',N'-tetramethylethylenediamine (TEMED). Addition of TEMED allowed the reaction to take place as low as room temperature and a quicker rate compared to the usual 60 - 70ºC. Though, this resulted in rapid gelation within a few minutes.

Closed cells were observed using the thermal initiator and displayed non-spherical boundaries at the interface, in combination with a UV-initiator however, an opened structure with highly-interconnected windows was formed (Figure 41, B-D). The benefit of using a dual-curing system also allowed for the inclusion of up to 60 wt% of particles.
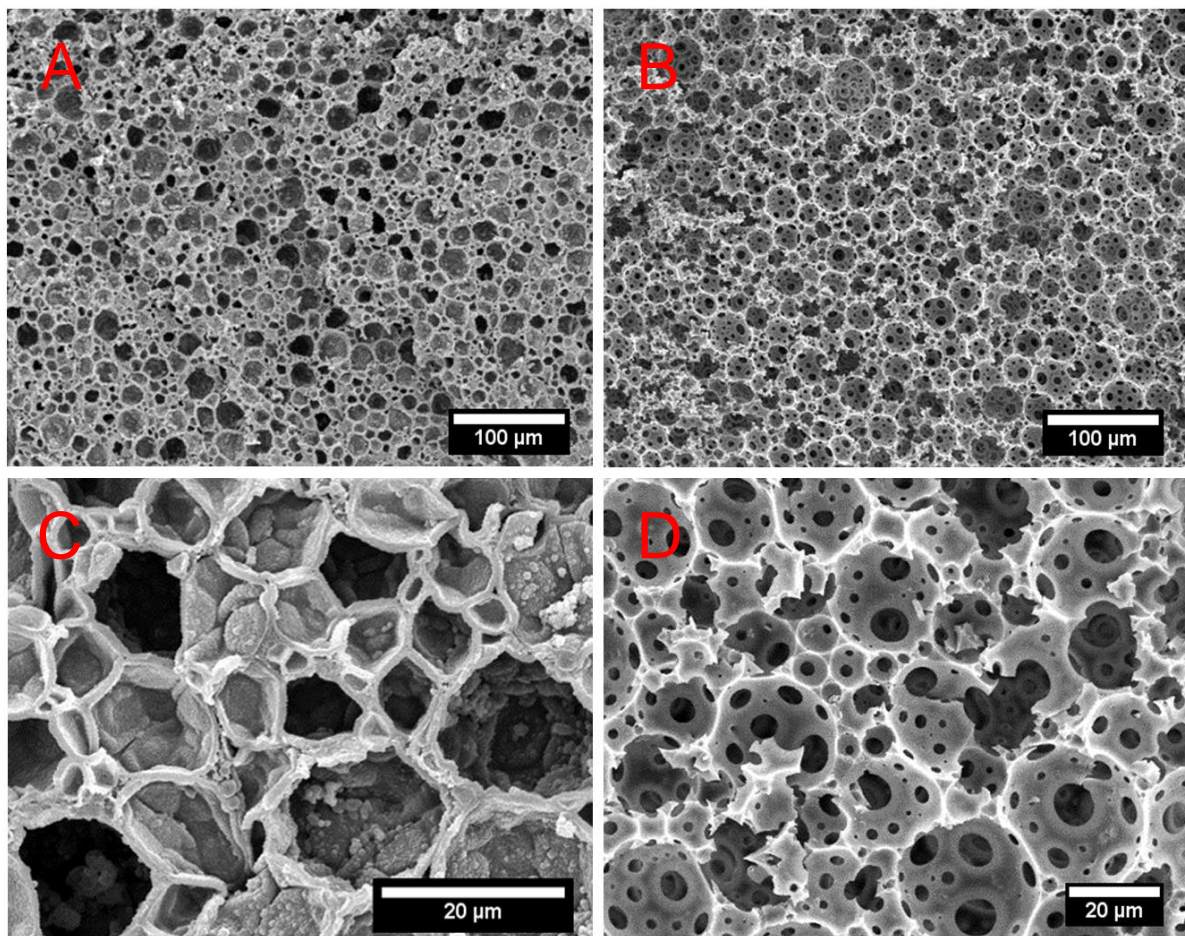
Figure 41: SEM images of room temperature cured poly-HIPE (A-C) and UV + temperature cured (B-D) variations. The enhanced version of each method along the bottom row shows the improved interconnectivity, unlike the closed pored structure experienced when using room temperature alone (Bottom left).

Often with the addition of micron- or nano-sized materials agglomeration is unavoidable without pre-surface the surfaces of the particles. Micro-CT was employed to determine the distribution of magnetic particles within the monolith structure (Figure 42). The images highlight without any particle introduction the image remains clean, with no key features. Addition of 9 wt% particles displays a greater contrast due to the dense nature of the iron-based particles, highlighting the even distribution within the monolith structure without the need for any surface treatment due to their inherent hydrophobic nature.
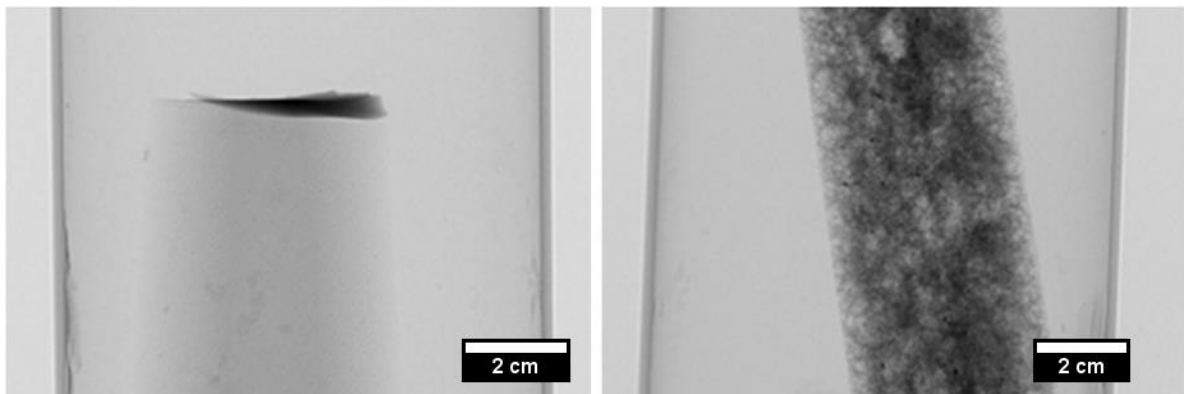
Figure 42: Micro-CT images of poly-HIPEs containing no carbonyl iron particles (Left) and 9 wt% (Right), the increased contrast highlight the well-dispersed nature of iron-based material.

5.3. Setup Optimisation

5.3.1. Microfluidics optimisation

In order to progress the project, findings from the monolith study above were utilised in order to develop a in order to develop a microfluidics setup suitable to create porous beads. The table below highlights the evolution below highlights the evolution of the microfluidics setup over the time of this project.

Figure 34 is the final iteration that was found to be most effective.

Table 11: Evolution of the microfluidics setup throughout the project, providing a summary of each iteration.

	Pros	**Cons**	**Image**	**Comments**
Original (plastic tubing coiled)	Simple and quick to use	Only UV Some UV lost through absorption		Was not possible to cure particles containing carbonyl Iron particles
Glass Coil	Heat and UV	Pressure Build up due to blockages at inlet and outlet Low duration of exposure to UV Inconsistent particle formation		Particles exposed to 10 sec per pass at 300 rpm
Water Bath	Heat and UV Increased time of exposure to UV No blockage formation Produces spherical particles	-		Majority of particles did not recirculate

5.3.2. Pore size optimisation

The first batch produced a fruitful result; the porous nature was confirmed using SEM imaging, as can be seen in Figure 44; the magnetic response was established using a strong magnet (Figure 43). The images show surface porosity and highly connected pores. The first set of experiments were carried out with a standard IBOA/EHA emulsion (as highlighted by Owen et al.) that incorporated 10-60% carbonyl iron particles Figure 44A to D[90]. The images show surface porosity and highly connected pores. The pore size distribution was measured from the SEM images, taking into the statistical correction factor $2/\sqrt{3}$ [115] in Figure 45 and the spread of the pore size distribution was highlighted in Figure 46. The addition of 10 wt% produced a narrower size distribution 1050 – 1250 µm, whereas smaller particles were more common with 60 wt%. Furthermore, there was a broader range possible; between 300 – 1300 µm.

The trend remained true for both 10 and 60 wt% carbonyl iron addition. Though the average pore size was smaller than 10 wt% addition, 28.1 µm and 36.5 µm, respectively, this spread of data can be visualised in Figure 46; it shows that the spread of data is lower with 60 wt% of particles, than it is with 10 wt%. Though, there is some influence with higher concentrations the range of data remains the same (60 µm).

However, results of more recent attempts in Figure 44E and F show that the SEM images show a more closed surface skin layer, with the inconsistent distribution of pores; despite the fact that they have retained their porous core structure. These striking changes were attributed to numerous factors such as reduction of power of the UV lamp, and chemical composition. A bespoke glass coil was commissioned to improve the setup, and reduce the UV absorption from the initial plastic tubing. In addition, the chemical compositions of the photo- and redox initiator were altered to reduce the curing ability of the water phase to improve surface porosity, as well as delay the curing time to increase the throughput.

Figure 43: Microcarriers displayed strong attraction when a magnet was placed in close vicinity of them.
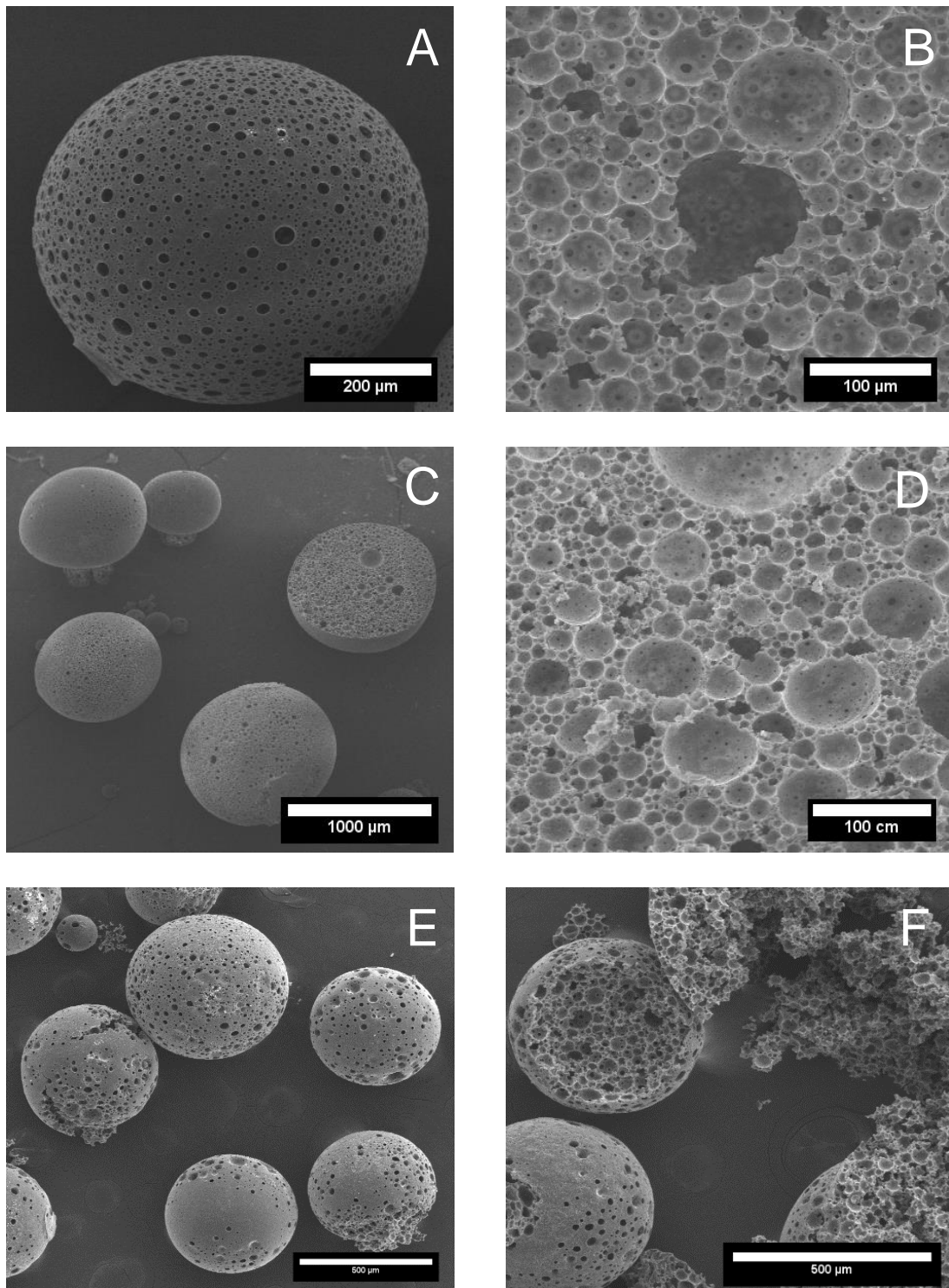
Figure 44: Microparticles manufactured with 10 wt% carbonyl Iron (A-B), Image A is of the general surface, and image B is the corresponding cross-section. This is the same with 60 wt % carbonyl Iron (C-D), where C is an overview, and D is the cross-section. Attempts made after that did not provide the same structural consistency. Image E shows some porous features, but inhomogeneous around the spheres. Though image F suggests they were still porous and interconnected within.
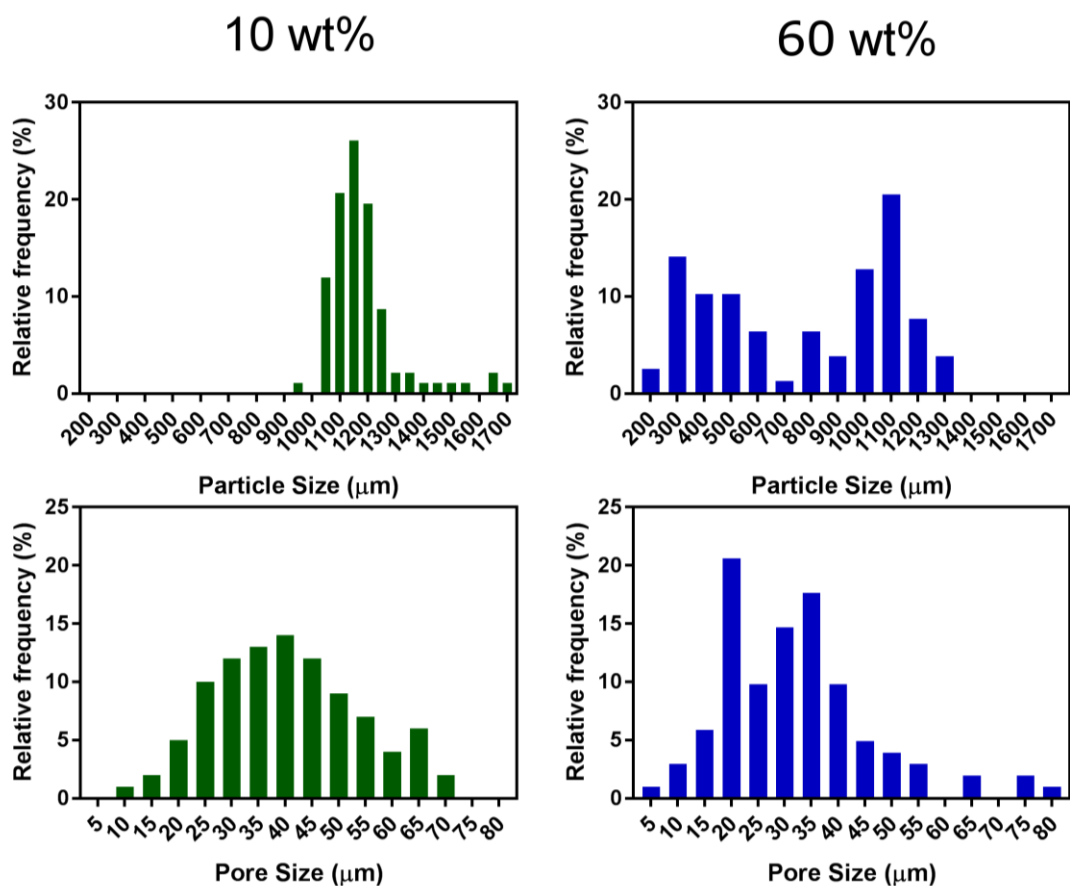
Figure 45: Particle (Top Row) and Pore size (Bottom Row) variation with 10 and 60 wt% of carbonyl-Iron particles. Addition of 10 wt% shows a consistent generation of particle size, whereas 60 wt% tends to broaden the distribution.
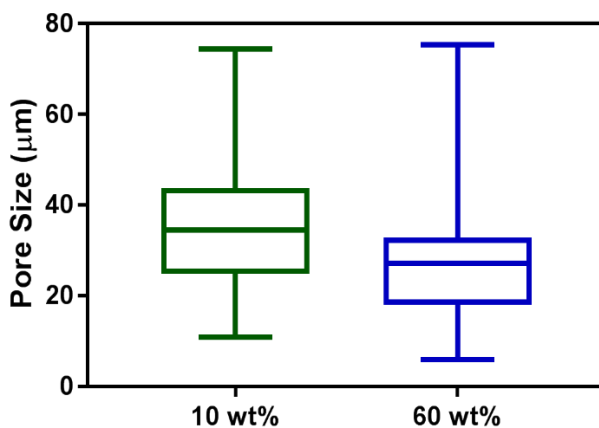
Figure 46: Shows the pore size variation between the two samples of 10 wt% and 60 wt% carbonyl iron, for example; the increase in magnetic particles results in an overall reduction of sizes as 75th percentile is lower than the average with 10 wt% of particles.

5.3.3. Glass Coil vs No Glass Coil

The effects of manufacturing particles with and without the glass coil were investigated. Introduction of the coil investigated. Introduction of the coil was a small modification to the existing setup; which involved submerging a

133

Figure 34). The no coil method required letting the particles settle in a bath, in order to increase their exposure to UV. The setup variations have been summarised in Table 11.

Figure 47 shows more pore coverage along the surface; this is evident in the images below - though, this is only an observation and has not been proven quantitatively. According to the distribution data, pore sizes were generally smaller without using a glass coil. It also shows better formation of independent spherical particles compared to the glass coil system. A consequence of the narrow inlet and outlet of the coil tubing, which causes an accumulation of particles due to the reduced area. The outlet diameter also presents a risk of pressure build up due to blockages forming at the inlet and outlet connectors.
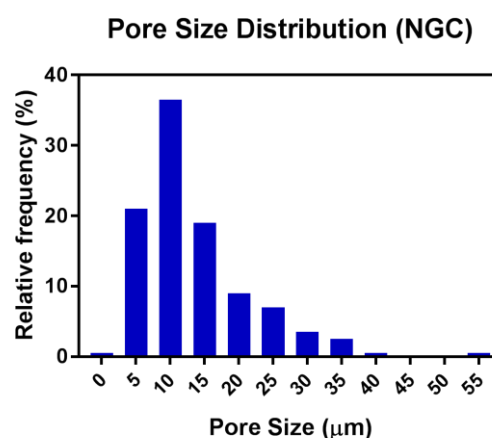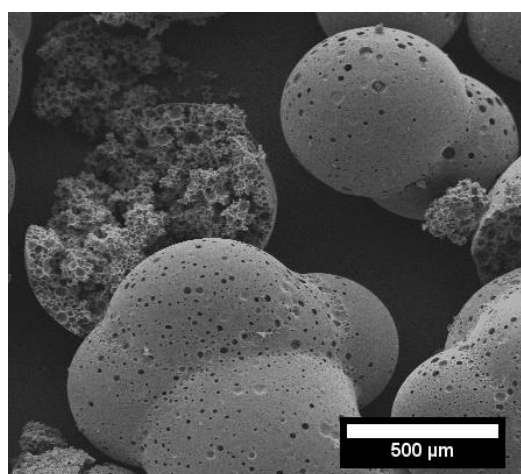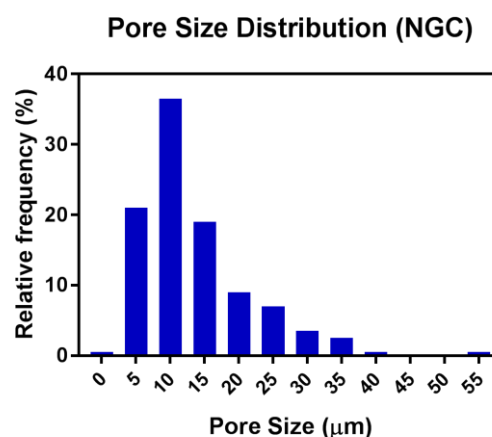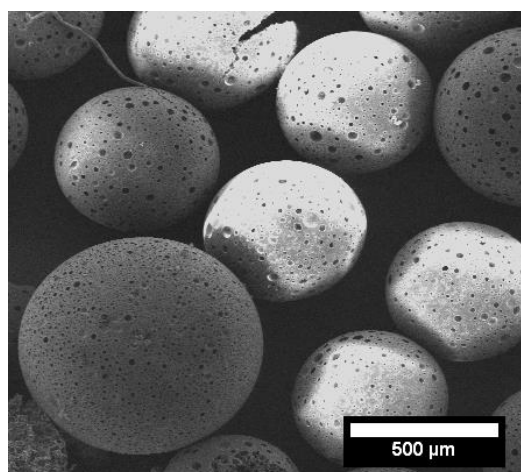
Figure 47: The disadvantage of using a glass coil (GC) is evident, high throughput and a narrow tubing have resulted in non-uniform deformity, while, a reservoir method ensures this phenomenon is limited. There are also more pores available; the data suggests there may be some influence on structure too.

134

5.4. Effects of redox initiator and a photoinitiator

The addition of the redox initiator was utilised to lower the reaction temperature of KPS from the usual 60 - 70ºC to room temperature. However the temperature of the recirculation water was still heated to 40ºC to ensure the reaction progressed quicker. AIBN was also tested as it is often used as a conventional thermal initiator for water-in-oil emulsions, due to its reaction temperature of 60-70ºC it was unsuitable. A lower viscosity at increased temperatures results in smudging of the emulsion within the tube and non-spherical shaped structures; hence, AIBN and KPS alone were not sufficient, and it was only KPS plus a redox initiator that was deemed more suitable due to the reduction in reaction temperature, essential to maintaining consistent particle extrusions. As a result, the emulsion polymerised within 30 minutes resulting in a small yield, to counteract this process it was reduced to half its original value from 0.7 wt% to 0.35 wt% of the Oil phase. As can be seen from Figure 48 (Left) the particles did not display the high degree of surface porosity compared to the original attempts.

The photo-initiator was doubled from 1.9 wt% to 3.8 wt% of the Oil phase to preserve the porous nature on the surface quicker, but even with this increase in hydrophobic based initiator the microcarriers still do not possess the same surface coverage of pores (Figure 48, Right)
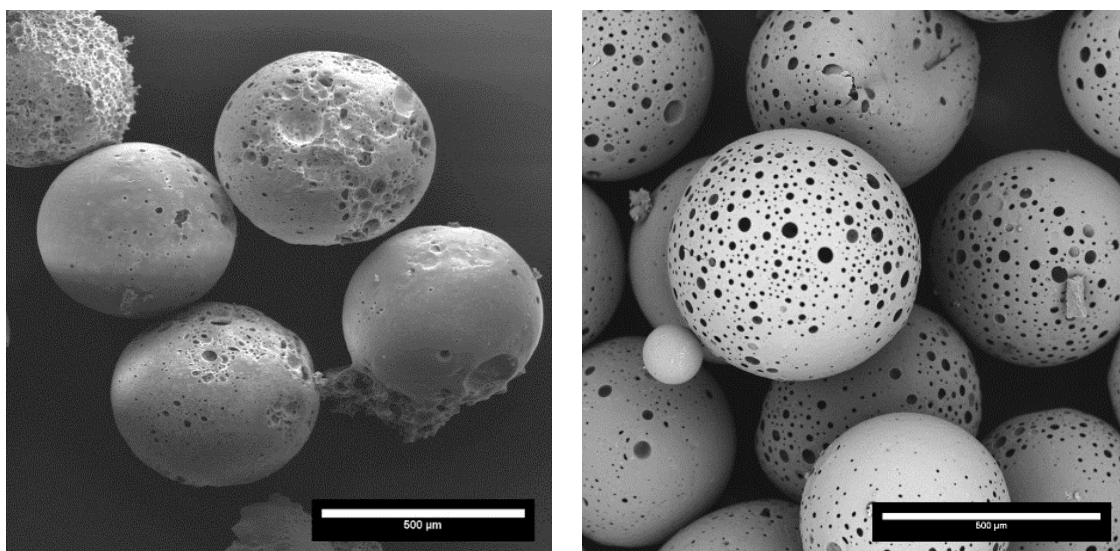
Figure 48: SEM images of half the redox initiator (Left) and double photo-initiator (Right).

Microstructures confirm a porous shell with a highly interconnected network inside, though not as effective as the first attempts. After numerous tests it was not possible to replicate the initial structures; however, doubling the photo-initiator and omitting the

glass coil from the set-up improved surface porosity. A particle-size analysis was conducted on at least 50 sample beads to determine the final characteristics. Both results below show consistent particle size formation around 500 µm as well as pore-size, at around 25 µm. These particles were carried forward as substrates for cell culture.
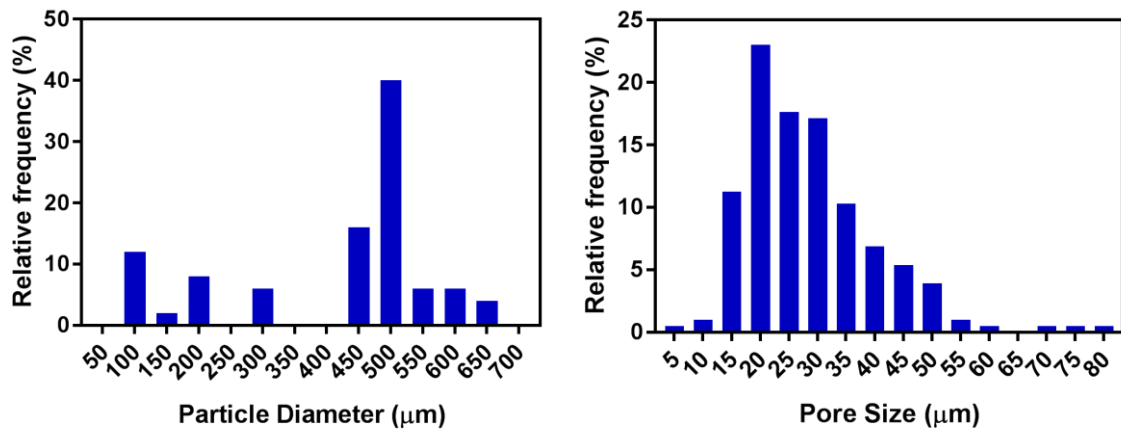
Figure 49: Distributions of particles and pore size diameter for the final microcarriers utilised during the culturing phase, both narrow show distributions.

5.5. Orbital Shaker Study

5.5.1. Fibroblasts

To assess the feasibility of the study fibroblasts were first seeded onto the particles and stimulated for a total of 7 days. Initially cultured through gentle stirring using an orbital shaker at its lowest setting (50 rpm). Although, there is a slight increase in proliferation, however, a statistical analysis conducted using a Mann-Whitney t-test shows that the data is not significant ($P > 0.05$). Nevertheless, it is a proof of concept that cells seeded on to the lab-manufactured carriers are able to sustain short-term culture.
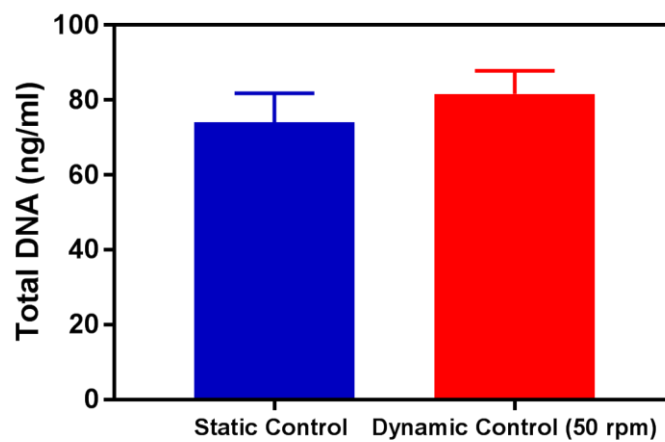
Figure 50: Static and dynamic control of approximately 250,000 human fibroblast cells seeded and after 10 days of culture and with 7 days of stimulation.

5.5.2. Human embryonic stem cell derived mesenchymal progenitors (hES-MPs)

The attention was then turned to a more popular responsive cell line. The cells, in this case, were cultured for one week before being transferred to new T-25s; and stimulated using the same protocol as above.

The DNA and ALP response produced per DNA content using a t-test showed that both sets of results were non-significant data (P > 0.05).
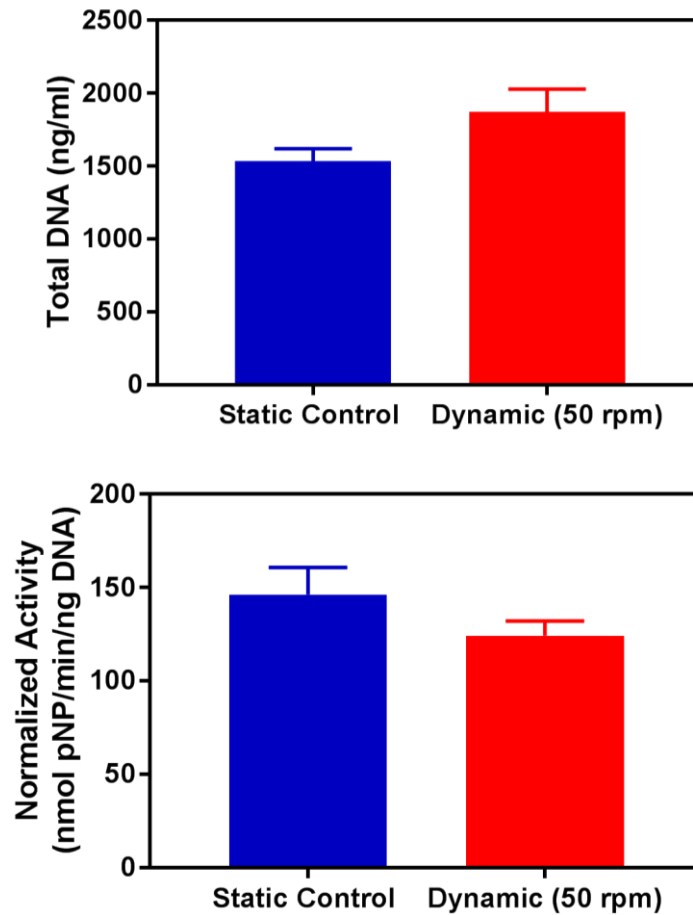
Figure 51: Approximately 250,000 human embryonic stem-cell derived mesenchymal progenitors were cultured in osteogenic media; results above are from a week of stimulating using an orbital shaker at 50 rpm every 30 minutes.

5.6. Preliminary Run

The previous results showed it was possible to culture using dynamic culture; however at this point, the magnetic response was yet to be tried. This preliminary experiment with the actuator was carried on samples within well plates, keeping the same 30-minute regime, but choosing a maximum speed of 3.2 cm/s. A planar control was used to see how DNA and ALP were influenced by 3D culture. All wells, in this case, were seeded with the same number of cells (80, 000).

Interestingly, monolayer culture on day three was already significantly higher than both attempts to inoculate 3D scaffolds (Figure 52). As this was done in a 12-well plate, it was presumed that planar culture would achieve a confluent state quicker, hence the loss of activity on day 6, followed by the sharp decline on day 13. Even with the significant loss of metabolic activity, the ALP production was 1.7% higher than static 3D culture and statistically significant compared to dynamic culture.

The proliferation of cells on 3D scaffolds by day three was similar and decreased slightly at day 6. However, due to intense stimulating a sharp decrease at day 13 for dynamic culture was observed. Whereas, the proliferation of static 3D scaffolds on day 13 was significantly higher than both monolayer and dynamic regime (P-value < 0.05, using one-way ANOVA) (Figure 52 Figure 53). Dynamic ALP presence was inadequate, and this was also reflected by a low DNA content, monolayer in comparison was expressively higher, analysed using a one-way ANOVA method (P < 0.05).
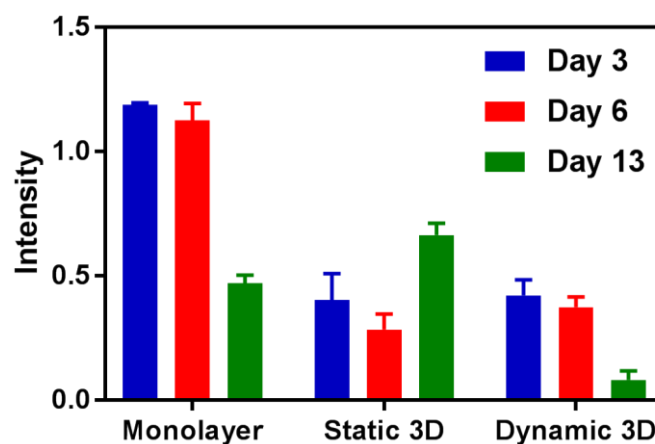
Figure 52: Resazurin results of hES-MPs cells in three different culture cultured environments: monolayer with static conditions; the other two variations were of the same cells on 3D magnetic particles also under a static and a dynamic environment. The study was carried out over 13 days.
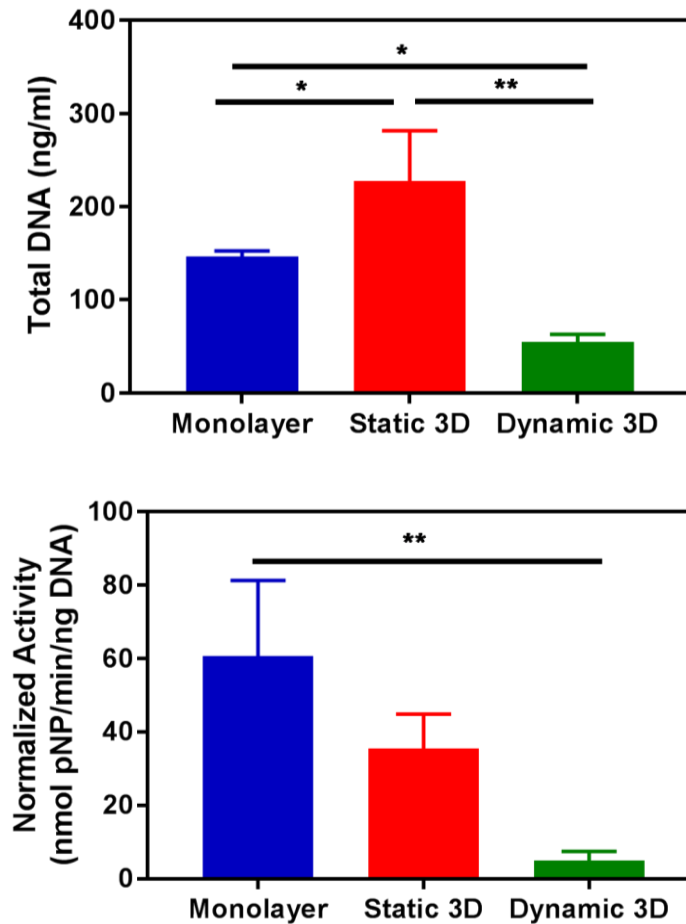
Figure 53: Initial experiment was done using a 12-well plate, consisting of ~80,000 hES-MPs cells under conventional monolayer culture and 3D culture (static and dynamic). Results

5.7. Optimising Speed

The next logical solution was to conduct a test to optimise the speed. The distance of the magnets was also adjusted to the limit of where the response was noticeable; by doing so, it allowed the particles to float along the surface instead of being intensely dragged along it. The experiment was carried out after a week of static incubation to allow cells to proliferate before being transferred to new flasks. After a day of incubation formations of agglomerated particles held together by cells, gave a good indication that seeding with 250,000 cells was successful.

Using a maximum speed (3.2 cm/s) as before, but moving the magnets away from the surface (~3 mm) improved their longevity in culture, though the DNA was lower than other regimes (Figure 54). Although by visually looking at the graphs there appear to be some differences, nevertheless, statistically no apparent significance was highlighted. Using one-way ANOVA, a comparison of environments where the

particles were manipulated with different dynamic speed to each other had no significance on the results; this applies for both DNA and ALP enzyme production.
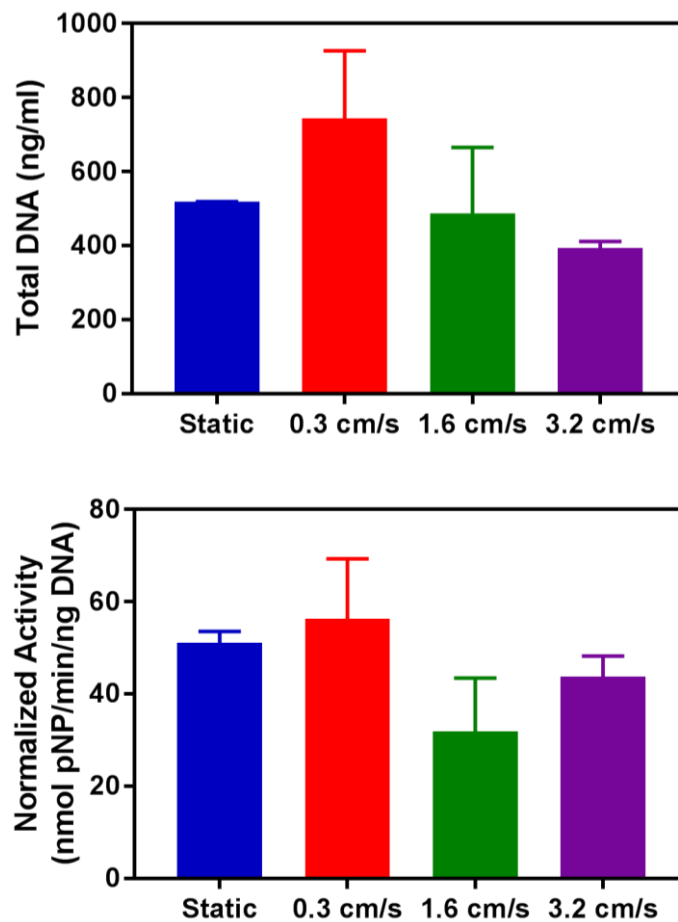
Figure 54: DNA and ALP results from maximum speed of 3.2 cm/s as before, 1.6 cm/s, 0.3 cm/s.

5.8. Stimulating For 21 And 31 Days

A more extended experiment at 10% speed was conducted, but in this case, Alizarin red S was used to detect calcium deposits, and Sirius red for collagen. As before, clumping of the particles was noticed after a day of incubation and increase over the incubation week.

Results show no apparent difference statistically in terms of metabolic activity, calcium and collagen production for static and dynamic cultures (Figure 55, Row A). Interestingly a decrease for both was observed for the additional 10 days of culture. Static and dynamic remained indifferent between the two different conditions (Row B). Though, by comparing both alizarin red of days 21 and 31 together a decrease of 40% and 16% for both static and dynamic cultures is notable. Staining using Sirius red showed higher levels of depreciation in collagen for both conditions, a drop of

approximately 78% was observed. All results were statistically analysed using Mann-Whitney T-Tests and were found to be not statistically significant (P > 0.05).

A point to note is during the destaining of Alizarin Red; it was noted that carbonyl iron particles underwent a dissolution process from the addition of 5% of perchloric acid.
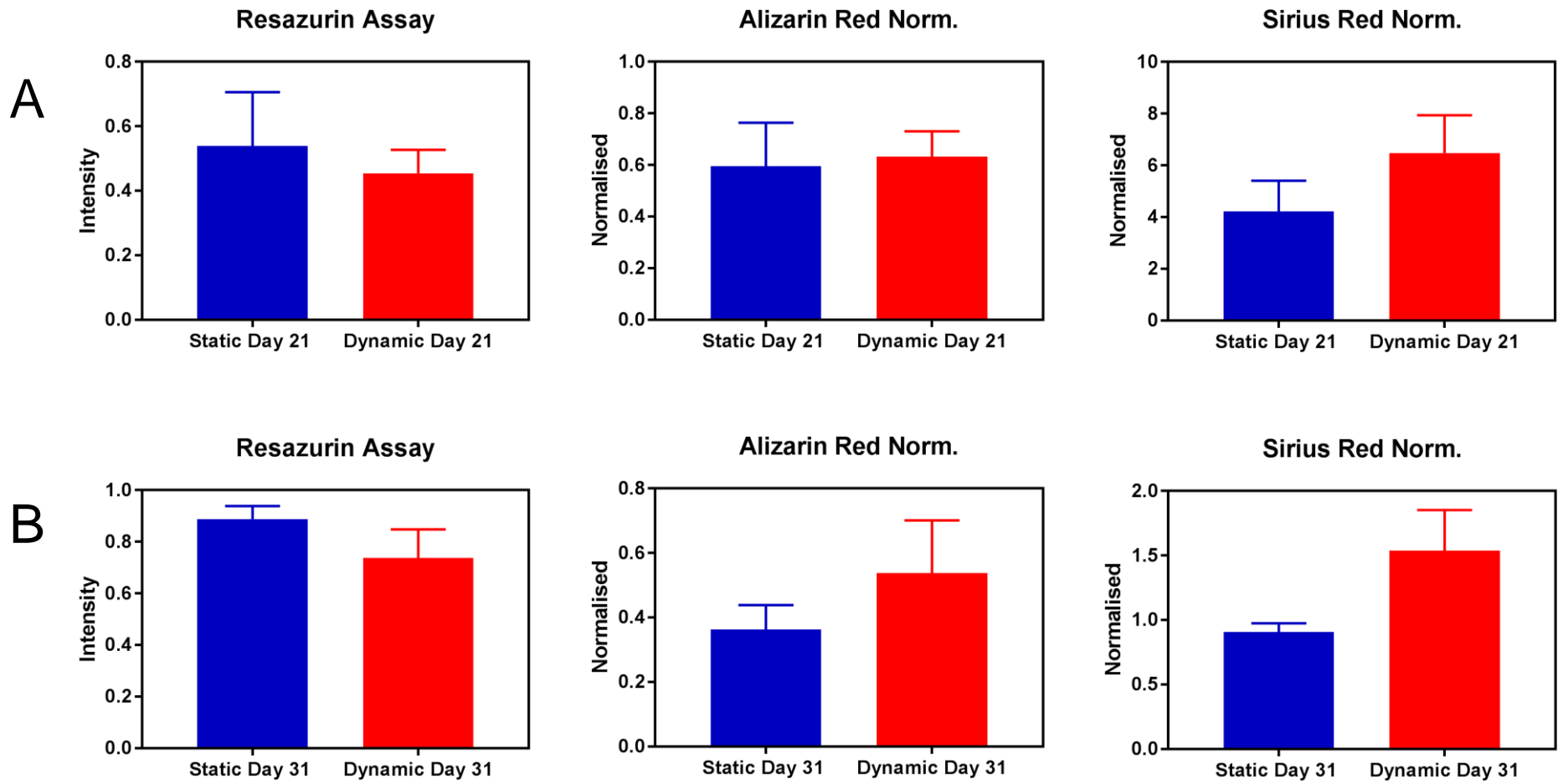
Figure 55: Assays conducted for 21 days (Row A) and 31 days (Row B) each include Resazurin assay results which were used to normalise Alizarin red S and Sirius Red data, which stain for calcium deposition and collagen, respectively.

5.9. Staining

Particle staining was carried out after 13 days of culture, with TRITC - phalloidin and DAPI, the procedure for which is highlighted in Section 4.13 of this chapter. Imaging with an upright fluorescence microscope shows the cell interaction with the magnetic microcarrier surfaces, evident by the scattered blue dots due to the DAPI penetrating the cell membrane. Besides, it shows evidence of agglomeration, held together by a network of the extracellular matrix, depicted by the pink-like stain. Growth was not only limited to the particle surface; there is adherence of cells along an ECM pathway as seen in Figure 56 below (Left).
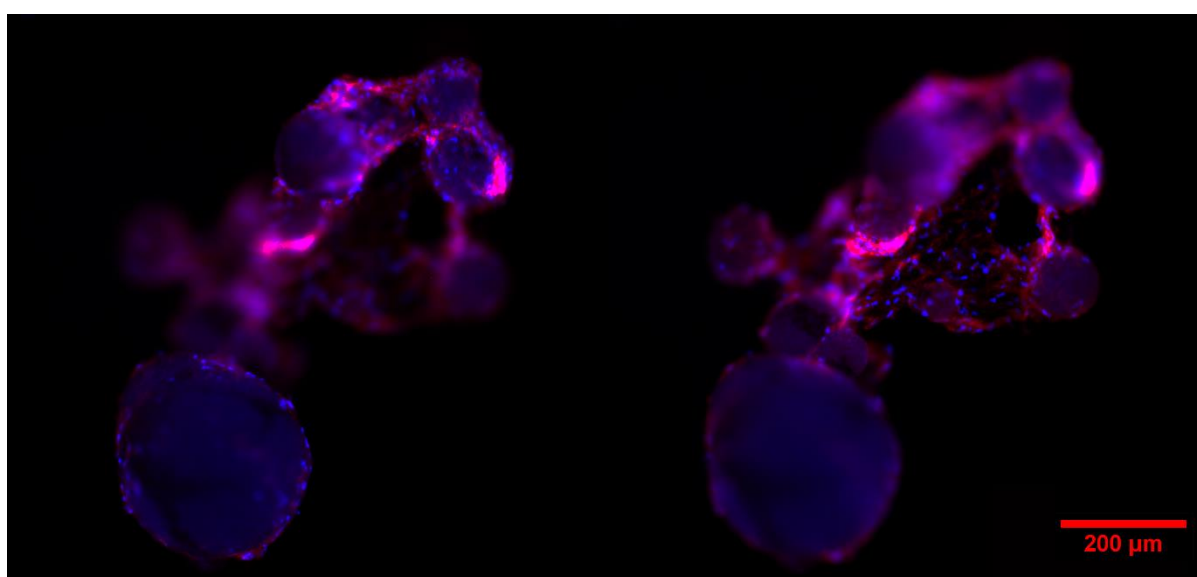
Figure 56: Phalloidin – TRITC and DAPI staining, showing depths of field; the image on the left showing the closest region, and the right showing the furthest region. Imaging was carried out using samples incubated for 13 days specifically for imaging, therefore experienced no dynamic stimulation.

The samples were embedded into wax, and 10-7 μm slices were mounted onto glass slides using a tissue slicer. H&E staining was carried out; the image on the right is a single ~ 7 μm slice of a microcarrier. Histology gave a good indication of the internal pore size of the particles and the distribution of the Micro-particles within the microcarrier. The presence of black clusters sporadically located around the scaffold, which appear to reside within the polymer matrix, the sizes range from as low as 2 μm to approximately 10 μm that is in line with the size distribution of carbonyl iron particles. Though it is difficult to accurately predict individual size using an upright microscope, it does, however, confirm agglomeration of the carbonyl-iron powder.

Furthermore, there are no visible indicators of cell growth, and this was a common theme for several other attempts. The absence of cells could be because the steps required during the staining process were too harsh, and often the polymer slices detach. To counteract this process staining intensity was reduced. As a result, it may not have been enough to highlight any cell deposits.

Figure 57: Histological slice of a microcarrier, with what appear to be randomly distributed magnetically responsive particles.
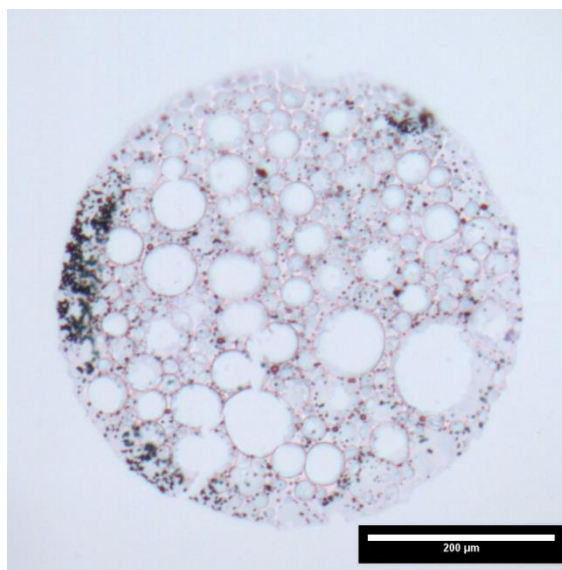
6. Discussion

Open, interconnected structures using EHA-IBOA HIPEs with the same UV-blend have been achieved in works previously [90]. In this case, the inability to cure the polymer was due to the addition of iron oxide. According to Salem, this is the case with other dark pigmented materials like carbon black – that are known to absorb UV effectively hence their application as UV-stabilisers [116]. It was theorised that UV light was also absorbed in this case; mainly on the surface and then not able to penetrate the core region. Thus the particles remained intact on the outer edges, but remained an emulsion at the core, as discovered during the monolith study. An alternative method using a water-soluble thermal curing agent resulted in a closed structure, with non-spherical pores. However, when used in unison with a UV-initiator it had both open interconnected pores, which were also spherical.

During the microfluidics stage, the absorption of UV was not expected to be a problem due to the micron-sized particles required. Initially, the curing setup consisted of water flowing at 300 rpm along coiled transparent tubing, while simultaneously exposing the particles to UV light (Table 11). Similarly, like the monolith structure when handling the beads, a small amount of pressure applied to the particles would result in the collapse of the whole structure – it became apparent that they were also cured on the surface.

To accommodate this requirement the curing setup was modified to improve its rudimentary form, this included recirculation of warm water using a hot plate and the introduction of a glass coil, to reduce the absorption from the plastic tubing. As can be

seen in the images, open porous structures were obtained, and the addition of up to 60 wt% iron-based particles was possible. The addition of 0.126 g of each initiator, thermal, photo- and 0.05 g of TEMED resulted in a fast curing emulsion within the syringe, reducing the throughput. In order to increase the time the emulsion remained a liquid the values of the thermally triggered components were halved, therefore increasing the yield.

During the culturing phase; microcarrier surfaces were modified by plasma coating with acrylic acid to increase their biocompatibility. In the early stages, it was unsuccessful; this was after particles had undergone plasma coating with acrylic acid to make the surfaces more hydrophilic. Results from resazurin assays were indifferent to their controls (particles and media) and visual checks did not show any indication of cellular attachment. More samples were manufactured; the newer samples also resulted in unsuccessful attempts, after further analysis SEM images showed the structure had changed to a closed-surface (Figure 44).

Structural differences are dependent on the emulsion type, whether it is oil-in-water or water-in-oil and the phase from which the reaction is initiated, either organic or aqueous – this ultimately determines the openness of the polymer structure [117]. In this particular case by applying the theory proposed by Robinson et al. in the water-oil emulsion utilised, KPS reacts from the aqueous-phase, crosslinking to form a closed pored structure. Addition of the blended UV initiator also contributes to this problem, as it consists of two parts - 2-Hydroxy-2-methylpropiophenone and Diphenyl(2,4,6-trimethylbenzoyl)phosphine oxide; the former is highly soluble in water (13.3 g/L) and the latter, slightly (0.0001 g/L). Curing from the oil phase would lead to better interconnectivity and more suited to preserving the integrity of surface pores, this can be read in more detail in chapter 3, section 2.8.2 and the following references cited in that section [305] [118]. Preservation of a porous structure will be more suited to having a single mixture of Diphenyl(2,4,6-trimethylbenzoyl)phosphine oxide, or an alternative hydrophobic photo-initiator. A hydrophobic thermal initiator can also be beneficial and was used to test this theory; AIBN, however, due to the reaction temperatures decreasing the viscosity of both the water phase and the emulsion, it was not possible to create consistent micro-spherical scaffolds at temperatures great than 60ºC with this particular microfluidics set up. AIBN and KPS react at the same

temperatures 60 - 70ºC, thermal curing with the latter was only possible at lower temperatures after the addition of the redox reagent.

As photo-polymerisation is regarded as a much quicker process, the shrinkage of the continuous phase after polymerisation will take effect earlier than the effects of thermal curing; the oil-water interface ruptures forming the plethora of open and interconnecting windows of the pores [119]. The inclusion of a glass coil in which microcarriers were transported along a closed-loop circuit, exposure to UV is limited to approximately 10 seconds per pass. The circuit, in fact, gave more precedence to the effects of thermal curing as the particles come back along the system for another dose of UV, but are continuously exposed to heat. Whereas, having a beaker in an open circuit regularly exposes the particles to equal amounts of UV and heat. To aid the preservation of pores the photo-initiator was also doubled to 3.8 wt% of the oil-phase, this improved the surface porosity (Figure 48) and increased cellular attachment.

6.1. Culturing

Numerous unsuccessful attempts were made to inoculate particles with hES-MPs, in one of these initial methods, no surface modification was used. Consequently, no cells were supported on these samples – which is the case due to the hydrophobicity of 2-Ethylhexyl acrylate and isobornyl acrylate poly-HIPEs [90]. The progression to air etching also yielded similar results, for low seeding densities of 40,000 – 80,000. Cells failed to show signs of adherence until plasma coating using acrylic acid was utilised.

Dynamic seeding was also attempted, from 30 minutes to up to 2 hours and contrary to what has been proposed in literature this was not effective. Most sources that have experimented with dynamic culture tend to have done so with commercial microcarriers that often have more specialised surfaces for example collagen and fibronectin [120]. The process of plasma coating was apparently effective, hence the increased affinity to the substrate surface.

To establish an accurate reading from any future assays seeded particles were separated from their original seeding wells or flasks to prevent any surface-attached cells providing ambiguity. Several different methods of transfer were tested, in order to establish a method that was least disruptive.

Firstly, wells were lined with Agarose, which is often used due to its non-adhesive surface properties as a means to prevent cell attachment to the surfaces - this would then require no transferring of particles on to clean surfaces [121]. However, the control – which consisted of cells and agarose, suggested that cells were still present within the wells. Resazurin assay values were 40 % higher from wells that contained cells and agarose than it was with particles, plus cells and agarose. The results imply hMSCs were attached to the agarose surface; this was also confirmed visually using an upright microscope.

Another method utilised sterile magnets wrapped in foil sleeves. The particles were gathered by submerging the foil-coated magnets into the media, and then transferred to a new culture area by sliding the foil off; this allowed the mass of particles to drop naturally. The process was repeated until the old wells were empty. The degree of constant and close contact required when using the dipping technique gathering the particles was deemed unsuitable after several bouts of infection were realised (Figure 58).

Finally, it was established that Pasteur pipettes were the superior option to transfer particles into new wells. Although it is also an inefficient method due to the repeated aspiration of particles, undoubtedly resulting in some detachment of cells - but it also produced better results than the other methods. An immediate change in media allowed for the removal of detached cells, and the inclusion of an incubation period allowed for recovery of any cellular losses.

Figure 58: Magnets wrapped in a sterile foil sleeve, which can be easily removed using a sliding motion. Any particles attached drop on to new culture surface.

In combination with the transferring method, success was eventually found with, acrylic acid coating, and high seeding densities of 150,000 – 250,000 cells. To improve cell attachment groups have found increase cellular adhesion by utilising serum-free media for the attachment phase, then subsequently replaced with serum containing media for the growing phase [99,100]. In the case of the cytodex carriers used by Mukhopadhyay et al. addition of serum resulted in charge neutralisation due to FCS absorbed proteins. As a measure to counteract this low serum concentrations between 0 – 15% are recommended for the attachment phase, then 10 – 15% for the expansion regime [99].

An early indicator of successful attachment was the observation of cluster formation with the inoculation of 250,000 hES-MPs cells, proposed to be a consequence of using a high density of cells as confirmed by Ferrari et al.; in this case, the formation was visible after a day of incubation [122]. Furthermore, since it is also dependent on the interplay between the cells and substrate, studies have indicated this is suggestive the material properties are compatible for bead-to-bead expansion - an attractive property for any future scale-up via an enzymatic free route as discussed previously [112]. Although cell-bead agglomerates are beneficial for the expansion and survival of cells according to Phillips et al., they can also be a limitation [109]. Clumping could result in restricted nutrient and oxygen transfer, reduced cell growth and death, though the effects the phenomenon has on cells is not fully understood [123]. Limiting the growth of the aggregates can be managed by adding new substrate, breakage and even agitation intensity can act as an encouraging method to redistribute cells to prevent large microcarrier-cell-aggregates [124].

6.2. Setup Development

It was noticed that the proximity of the magnets to the T-25s made a significant difference in cell survival and growth (Figure 52). Figure 59 demonstrates two main factors that affected the stimulation of the particles. Firstly, the distance of the magnets from the T-25 flasks (Image A), a smaller distance resulted in a more vigorous dragging motion of the microcarriers along the inner surface. The low DNA content in section 5.6 was concluded to be a result of this; cell death/detachment due to intense dragging. When the same speed was used at the threshold distance of 3.8 mm there was an increase of DNA. Also ALP increased by 88%.

There was also a variation of height, which, due to the improvised nature of the setup meant the arm holding the magnets was not perfectly horizontal. In the contracted form, the arm magnets furthest away were 3.8 mm, but when extended this increased to 4.2 mm – out of the range of movement by approximately 10%. As a result, the degree of movement or stimulation was not consistent - the flask furthest along the arm experienced little, whereas the one closer to the pivot experienced the most (Image B).
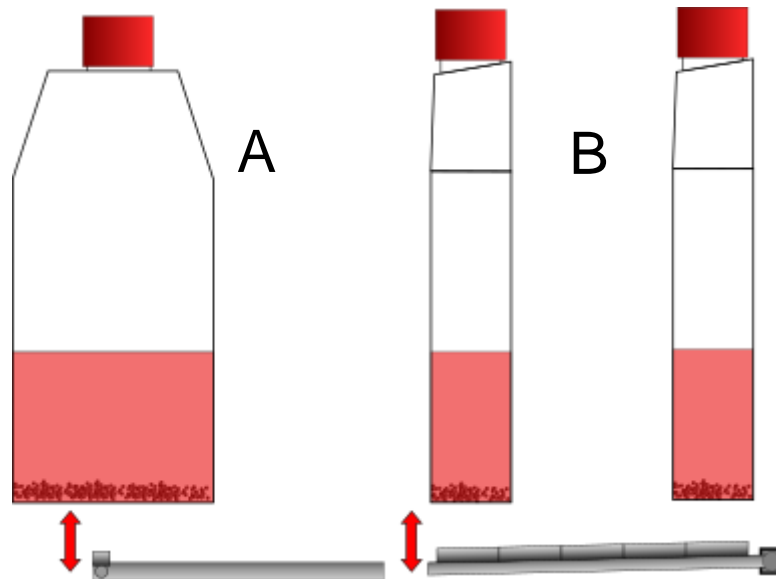
Figure 59: Image A is a side on (Arm perpendicular to the length of the T25), highlighting the distance between the magnets and the bottom of the flask. Image B, the frontal view (Arm parallel to the T25s), showing how there is a variation of height due to the actuator arm.

6.3. Orbital Shaker Study

Two sets of experiments were conducted using different cell lines: human fibroblasts and human mesenchymal stem cell-derived progenitors (hES-MPs), both were conducted at the lowest speed of 50 rpm.

Fluid stress generated in an orbital shear depends on the distance from the centre point of motion; the outer regions experience a higher degree compared to the centre. Lim et al. calculated the shear stress for different points and found at 40 rpm the stress at the centre can be as low as 0.86 and the outer region 1.50 dyne/cm^2 [125] although these values are dependent on viscosity, turning diameter, scaffold properties. It does, however; provide some idea of the shear stress generated using an orbital shaker at the same speed. Though it is difficult to translate the comparison directly, due to the 3D porous nature. Pore size is deemed an important characteristic; cells migrating into the centre of carriers compared to the outside surfaces experience different wall shear

stress environments [126]. It does suggest the stress generated is adequate surface cells, since fluid stress as low as 0.01 dynes/cm^2 on 3D scaffolds has proven to induce differentiation in MSCs [7].

Fibroblasts were found to be not significantly responsive to the shear stress-induced environment. Furthermore, there were no indications of cell-bead agglomerates after 10 days in culture, as done so with hES-MPs, which showed clumping after the first day. There are not many reports to suggest fibroblasts respond fluid shear stress in terms of proliferation; however, they seem to be more influenced by migrating, alignment and expression of various factors. When improved proliferation is experienced it occurs even at low fluid flow rates, in spinner flask culture at 40 rpm, perfusion culture between 1.0 ml hr^{-1} and 0.01 – 0.1 ml hr^{-1}, which was estimated to be around 10 - 20 mPa [127–129].

HES-MPs cells showed no significant differences in DNA content and a decrease in ALP production after a 7-day stimulation period, in total the cells had been in culture for 14 days. A similar result was found using a rocker at 45 pm for an hour a day showed there was no significant difference between static and dynamic culture at day 14 and 21 [130].

6.4. Linear Actuator Study

Before the stimulation phase, an incubation time of one week was given to allow hES-MP cells to proliferate. At the start of this period, passage medium was switched to the Osteogenic inducing variety. Addition of the right combination of factors can enhance both proliferation and preserve the differentiation potential of MSCs [37,131]. Fibroblast growth factor has been known to increase proliferation rates as well as maintain differentiation potential, and it may have been more beneficial to defer the introduction of differentiation-inducing media [31,36,50,132]. Kanda et al. found that DNA count was higher in medium with bFGF than osteogenic inducing supplements [50].

Dynamic particles showed very low DNA in the initial run; it was assumed the reason for this was the combination of the actuator speed, which was set to 3.2 cm/s and the fact the magnets were placed as close as possible to the plate. DNA content improved when the experiment was repeated in the optimisation study, but with the magnets now 3.8 mm further away from the bottom of the flasks. All regimes except the lowest

speed of were similar in terms of DNA; the individual setting resulted in a 43% increase compared to the static environment, which implied that the cells were not confluent on the substrates. Relative to static culture, a decrease was noticed at maximum speed (3.2 cm/s), and no difference was noticed at 1.6 cm/s. These variations are not unusual during optimisation; an effective speed is required such that it produces a large enough FSS environment to promote nutrient transfer, while minimising reduced cell viability. Optimising is a necessary step as the effects of proliferation are complex; interaction is dependent on flow rate, bioreactor type, cell line, scaffold and medium [64,65].

There were no notable differences in ALP between static and dynamic culture, the speed of stimulation also had no drastic effect after 14 days - seven of which were under dynamic regimes. The result is contrary to the study by Delaine-Smith et al. where at day 14 there was a 2-fold difference between static and rocked culture (Delaine-Smith, MacNeil, et al., 2012). A 2-fold increase was also noticed between static and dynamic after 14 days by Nishimura et al. [64]. Bjerre et al. noted that the peak expression of dynamically cultured MSCs occurs before day 21 [63]. These reports imply peak expression occurs around day 14 of culture, which could well remain true in this case as well, though reading on day 7 or 21 would be ideal for confirming this. After several weeks of culture static and dynamic regimes can be similar, and in some cases decrease; Stiehler et al. noticed an ~ 80% reduction [34,61,63].

In this study, several underlying factors could have affected the negligible differences in ALP and insignificant increases in DNA compared to the static environment. For one, agglomeration of cells is a debated topic; clearly, it is beneficial for expansion, but in this scenario, it could also create shear stress gradients, limiting the individual stress cells experience dependent on their location. Cells that have proliferated within the web-like ECM and inside the porous structure are potentially guarded against the stress experienced in the outer regions. Furthermore, a culturing phase for a week in osteogenic media also provides the right cues for differentiation to occur.

As ALP is an early marker for osteogenic differentiation; dramatic increases in ALP could have been overlooked since the first reading is taken after 14 days [130]. Finally, pore sizes were determined to be in the region of 10 - 40 μm, which is smaller than the recommended sizes to promote osteogenic differentiation, though clearly

acceptable within the regions of cortical bone; components are between 20 and 0.01 µm and more substantial in cancellous areas (300 - 600 µm) [19,79].

6.5.   Resazurin, Alizarin & Sirius Results

Metabolic assay of long-term culture showed a positive sign as the results indicate continuous proliferation from day 21 to 31; however, this showed no significant improvement, statistically.

Studies have shown that mineralisation of calcium is highly upregulated after stimulation in oscillatory fluid flow; more so with the addition of osteogenic induced media. In this case, the study conducted at day 21 and 31 of stimulation shows no real difference compared to the static counterpart. Comparatively, stimulated counterparts frequently exhibit considerable signs of mineralisation over the same period. This phenomenon has been reported by Lima et al., who cultured for 21 days [133]. The same cell-line was used by Delaine-Smith et al. in dynamic culture for 21 days, signs of mineralisation were present only with the introduction of OM media, though OM-dynamic environments were greater than static (Delaine-Smith, MacNeil, et al., 2012), other authors noted similar findings [61,134].

The staining intensity of samples at day 31 show a pronounced difference of calcium mineralisation, even though there is, in fact, an overall decrease in staining intensity from day 21; both static and dynamic cultures reduced by ~ 40 and 16 %, respectively. In a study by Huang et al. matrix mineralisation of osteoprogenitors occurs at day 15 as they begin to mature, and by day 28 maximum intensity is observed, as they reach a terminal state. Further differentiation into osteocytes leads to inactivity and a decrease in the production of the matrix [21].

There was a reasonable doubt to suggest the dissolution of magnetic particles due to the acid used. Perchloric acid, like sulphuric or nitric acid, is regarded as a strong acid; the dissolution of magnetite and carbonyl iron has been reported [135,136]. A control sample showed the same yellow intensity with no culture; when exposed to 5% of perchloric acid as stated in the alizarin red protocol, this could have also caused a knock-on effect when analysing for calcium and collagen. Assessing the UV-vis spectra of $FeCl_3$ implies no conflicting readings, since the absorption peak is around 300 - 350 nm [137].

An alternative method using alizarin red, with cetylpyridinium chloride might be a better alternative for future research that involves iron-based materials as a precautionary measure.

Collagen is an integral part of the differentiation step and forms the dense highly-cross-linked matrix; studies also show an increase under stress driven conditions [134]. The staining intensity in this case, however, showed a drop of 78% from day 21 to 31, a reason for which has not been fully understood. Most studies end around the 21-day period; the total incubation time at day-31 is 38 days; it is difficult to assess whether this is ordinary behaviour. As cells reach maturity, osteoblasts produce more type 1 collagen essential for matrix deposition [138]. Beyond this point, osteoblasts mature and begin to transition to old-osteocyte, osteoblastic markers for example collagen type 1 and ALP begin downregulating [17,49].

7. Conclusion

Microcarriers using emulsion templating were successfully formed with magnetically responsive particles embedded within the poly-HIPE matrix. In this case, it was only possible with photo- and thermally-initiated polymerisation working in unison; otherwise, photocuring itself was not sufficient to maintain the porous structure.

Cell culture was only supported after plasma coating the surfaces with acrylic acid and using static seeding. It was possible to preserve long-term culture for up to 38 days even when subjected to an intermittent-dynamic environment.

Fluid shear stress was created in two ways; the first with an orbital shaker, which showed no significant change induced by the dynamic environment at 50 rpm for human fibroblasts. A similar result was observed for human mesenchymal derived progenitors, even with the ~ 20% increase in DNA, counter to this the alkaline phosphatase activity reduced by 15%.

The second dynamic environment was created using an actuator modified with magnets. Fluid shear stress was created in the cultured environments through the transient dragging of the responsive microcarriers. Survival rates seemed to depend on the distance of the magnets from the surface, as an initial attempt with magnets as close as possible to the cultured surface resulted in considerably lower cell viability.

A combination of optimising actuator speed and distance from the particles improved cell durability – culturing up to 31 days was eventually possible under intermittent stimulation. 0.3 cm/s was found to be the most effective speed of the three tested.

Dynamic culture up to day 21 and 31 was analysed with several assays to determine cell viability. The results of which showed that calcium deposition and collagen also exhibited no substantial differences. The de-staining process using 5% perchloric acid resulted in the dissolution of magnetic particles. The resulting solution, however, does not conflict with the UV-absorption at 405 nm for Alizarin Red assay.

In summary, the outcomes of this study have shown that scaffolds doped with magnetic particles are suitable for long-term culture. In principle, these particles could be used to explore the effect of mechanical stimulation on the differentiation of MSCs. However, further work is required to determine the optimum environmental conditions to favour markers that are typically associated with advanced bone cell lines.

8. Future Work

Work done in this report has set the grounds for a type of microcarrier that is easy to handle due to its magnetic properties, also due to its ability to for particle-cell agglomerates a feature for easy expansion. Furthermore, providing the ability to control fluid stress externally – which could be utilised for bone tissue engineering. However, several areas require particular attention for further development in terms of material, and possible experiments:

It remains to be determined what influenced the impressive and uniform formation of pores over the microcarrier surface beforehand. The initial hypothesis is an optimum concentration of thermal and photoinitiators exist, or this was directly down to the deterioration of the UV-lamp. A better-suited initiator is required to preserve an open and interconnected one, preferably initiating from the continuous phase.

The surface can be functionalised via surface alteration using chemical treatment using fibronectin, laminin or collagen can be implemented to make cell adhesion more successful, especially if inoculation is carried out at lower cell densities. Moreover, potentially more uniform compared to plasma treatment, thus providing more surface area for attachment.

Other Poly-HIPE based materials such as polystyrene could be investigated with magnetic particle integration to determine how the change in a material affects expressions associated with bone development, as osteogenic differentiation is possible without the chemical cues of OM medium [139]. An advantage of using emulsion templating is the highly tuneable characteristics possible, by doing so porous architecture could be tuned to favour more bone architectures.

Surface area is a valuable parameter when manufacturing microcarriers; it would be interesting to compare the surface areas to commercial products. The different methods that could be considered are BET surface analysis or mercury porosimetry.

It would also be of interest to optimise the method in terms of stimulation duration, as this is a factor that can also produce better results. An extended run is ideally required for ALP measurements for completeness of days 21 and 31; furthermore, it will be interesting to characterise the ALP production before the stimulation phase in order to assess its evolution.

9. References

1. Motaln, H., Schichor, C. & Lah, T. T. Human mesenchymal stem cells and their use in cell-based therapies. *Cancer* **116,** 2519–2530 (2010).

2. Dimitriou, R., Jones, E., McGonagle, D. & Giannoudis, P. V. Bone regeneration: current concepts and future directions. *BMC Med.* **9,** 66 (2011).

3. Tirziu, D., Giordano, F. J. & Simons, M. Cell communications in the heart. *Circulation* **122,** 928–937 (2010).

4. Bianconi, E. *et al.* An estimation of the number of cells in the human body. *Ann. Hum. Biol.* **40,** 463–471 (2013).

5. Chen, A., Reuveny, S. & Oh, S. Application of human mesenchymal and pluripotent stem cell microcarrier cultures in cellular therapy: Achievements and future direction. *Biotechnol. Adv.* **31,** 1032–1046 (2013).

6. Heathman, T. R. J. *et al.* The Translation of Cell-Based Therapies: Clinical Landscape and Manufacturing Challenges. *Regen. Med.* **10,** 49–64 (2015).

7. Ma, T., Tsai, A.-C. & Liu, Y. Biomanufacturing of human mesenchymal stem cells in cell therapy: Influence of microenvironment on scalable expansion in bioreactors. *Biochemical Engineering Journal* **108,** 44–50 (2016).

8. Trounson, A. & McDonald, C. Stem Cell Therapies in Clinical Trials: Progress and Challenges. *Cell Stem Cell* **17,** 11–22 (2015).

9. Singer, N. G. & Caplan, A. I. Mesenchymal stem cells: mechanisms of inflammation. *Annu Rev Pathol* **6,** 457–478 (2011).

10. Kim, N. & Cho, S.-G. Clinical applications of mesenchymal stem cells. *Korean J Intern Med* **28,** 387–402 (2013).

11. Lin, W. *et al.* Mesenchymal stem cells homing to improve bone healing. *J. Orthop. Transl.* **9,** 19–27 (2017).

12. Granero-Moltó, F. *et al.* Regenerative effects of transplanted mesenchymal stem cells in fracture healing. *Stem Cells* **27,** 1887–1898 (2009).

13. Maria De Peppo, G. *et al.* Osteogenic Potential of Human Mesenchymal Stem Cells and Human Embryonic Stem Cell-Derived Mesodermal Progenitors: A

Tissue Engineering Perspective. *TISSUE Eng. Part A* **16,** 3413–3426 (2010).

14. Maxson, S., Lopez, E. A., Yoo, D., Danilkovitch-Miagkova, A. & Leroux, M. A. Concise review: role of mesenchymal stem cells in wound repair. *Stem Cells Transl. Med.* **1,** 142–9 (2012).

15. Trounson, A. & DeWitt, N. D. Cell therapies are emerging as the next major development in human medicine. *Nat. Publ. Gr.* **17,** (2016).

16. James, A. W. & W., A. Review of Signaling Pathways Governing MSC Osteogenic and Adipogenic Differentiation. *Scientifica (Cairo).* **2013,** 684736 (2013).

17. Yamaguchi, D. T. " Ins " and " Outs " of mesenchymal stem cell osteogenesis in regenerative medicine. *World J Stem Cells* **6,** 94–110 (2014).

18. Lerner, U. H. Osteoblasts, Osteoclasts, and Osteocytes: Unveiling Their Intimate-Associated Responses to Applied Orthodontic Forces. *Semin. Orthod.* **18,** 237–248 (2012).

19. Wittkowske, C., Reilly, G. C., Lacroix, D. & Perrault, C. M. In Vitro Bone Cell Models: Impact of Fluid Shear Stress on Bone Formation. *Front. Bioeng. Biotechnol.* **4,** 3389–87 (2016).

20. Vijayan, V. & Gupta, S. Role of osteocytes in mediating bone mineralization during hyperhomocysteinemia. *J. Endocrinol.* **233,** 243–255 (2017).

21. Huang, Z., Nelson, E. R., Smith, R. L. & Goodman, S. B. The Sequential Expression Profiles of Growth Factors from Osteroprogenitors to Osteoblasts In Vitro. *Tissue Eng.* **13,** 2311–2320 (2007).

22. Lin, W. *et al.* Mesenchymal stem cells homing to improve bone healing. *J. Orthop. Transl.* **9,** 19–27 (2017).

23. Horwitz, E. M. *et al.* Clinical responses to bone marrow transplantation in children with severe osteogenesis imperfecta. *Blood* **97,** 1227–1231 (2001).

24. Horwitz, E. M. *et al.* Isolated Allogeneic Bone Marrow-Derived Mesenchymal Cells Engraft and Stimulate Growth in Children with Osteogenesis Imperfecta: Implications for Cell Therapy of Bone Isolated allogeneic bone mar

mesenchymal cells engraft ar growth in children with ostec . *Source Proc. Natl. Acad. Sci. United States Am.* **99,** 8932–8937 (2002).

25. Marcacci, M. *et al.* Stem cells associated with macroporous bioceramics for long bone repair: 6- to 7-year outcome of a pilot clinical study. *Tissue Eng.* **13,** 947–55 (2007).

26. Robertson, P. A. *et al.* Natural History of Posterior Iliac Crest Bone Graft Donation for Spinal Surgery. *Spine (Phila. Pa. 1976).* **26,** 1473–1476 (2001).

27. Wei, X. *et al.* Mesenchymal stem cells: a new trend for cell therapy. *Nat. Publ. Gr.* **34,** 747–754 (2013).

28. Ullah, I., Subbarao, R. B. & Rho, G. J. Human mesenchymal stem cells - current trends and future prospective. *Biosci. Rep.* **35,** (2015).

29. McLeod, M. C. *et al.* Transplantation of GABAergic Cells Derived From Bioreactor-Expanded Human Neural Precursor Cells Restores Motor and Cognitive Behavioral Deficits in a Rodent Model of Huntington's Disease. *Cell Transplant.* **22,** 2237–2256 (2013).

30. Chen, G. *et al.* Monitoring the biology stability of human umbilical cord-derived mesenchymal stem cells during long-term culture in serum-free medium. *Cell Tissue Bank.* **15,** 513–521 (2014).

31. Mao, H., Kim, S. M., Ueki, M. & Ito, Y. Serum-free culturing of human mesenchymal stem cells with immobilized growth factors. *J. Mater. Chem. B* **5,** 928–934 (2017).

32. Reisman, M. & Adams, K. T. Stem cell therapy: a look at current research, regulations, and remaining hurdles. *P T* **39,** 846–57 (2014).

33. Jung, S., Panchalingam, K. M., Wuerth, R. D., Rosenberg, L. & Behie, L. A. Large-scale production of human mesenchymal stem cells for clinical applications. *Biotechnol. Appl. Biochem.* **59,** 106–120 (2012).

34. Delaine-Smith, R. M. & Reilly, G. C. Mesenchymal stem cell responses to mechanical stimuli. *Muscles. Ligaments Tendons J.* **2,** 169–80 (2012).

35. Cai, R., Nakamoto, T., Hoshiba, T., Kawazoe, N. & Chen, G. Control of

Simultaneous Osteogenic and Adipogenic Differentiation of Mesenchymal Stem Cells. *J. Stem Cell Res. Ther.* **4,** 1000223 (2014).

36.   Coipeau, P. *et al.* Impaired differentiation potential of human trabecular bone mesenchymal stromal cells from elderly patients. *Cytotherapy* **11,** 584–594 (2009).

37.   Oh, J.-E. & Eom, Y. W. Maintenance of Proliferation and Adipogenic Differentiation by Fibroblast Growth Factor-2 and Dexamethasone Through Expression of Hepatocyte Growth Factor in Bone Marrow-derived Mesenchymal Stem Cells. *Biomed. Sci. Lett.* **22,** 1–8 (2016).

38.   Teng, S. *et al.* Influence of biomechanical and biochemical stimulation on the proliferation and differentiation of bone marrow stromal cells seeded on polyurethane scaffolds. *Exp. Ther. Med.* **11,** 2086–2094 (2016).

39.   Yuasa, M. *et al.* Dexamethasone Enhances Osteogenic Differentiation of Bone Marrow- and Muscle-Derived Stromal Cells and Augments Ectopic Bone Formation Induced by Bone Morphogenetic Protein-2. *PLoS One* **10,** e0116462 (2015).

40.   Kim, M. J. *et al.* MG-63 Cell Proliferation with Static or Dynamic Compressive Stimulation on an Auxetic PLGA Scaffold. *Int. J. Polym. Sci.* **2017,** 1–6 (2017).

41.   Boo, L., Selvaratnam, L., Tai, C. C., Ahmad, T. S. & Kamarul, T. Expansion and preservation of multipotentiality of rabbit bone-marrow derived mesenchymal stem cells in dextran-based microcarrier spin culture. *J. Mater. Sci. Mater. Med.* **22,** 1343–1356 (2011).

42.   Tang, Y. *et al.* The combination of three-dimensional and rotary cell culture system promotes the proliferation and maintains the differentiation potential of rat BMSCs. *Sci. Rep.* **7,** (2017).

43.   Junji, M. The review of cellular effects of a static magnetic field. *Sci. Technol. Adv. Mater.* **7,** 305 (2006).

44.   Song, S. *et al.* Collaborative effects of electric field and fluid shear stress on fibroblast migration. *Lab Chip* **13,** 1602 (2013).

45.   Zhang, C. *et al.* Effects of mechanical vibration on proliferation and osteogenic

differentiation of human periodontal ligament stem cells. *Arch. Oral Biol.* **57,** 1395–1407 (2012).

46.   Sun, S., Liu, Y., Lipsky, S. & Cho, M. Physical manipulation of calcium oscillations facilitates osteodifferentiation of human mesenchymal stem cells. *FASEB J.* **21,** 1472–80 (2007).

47.   Kuo, C. K. & Tuan, R. S. Mechanoactive Tenogenic Differentiation of Human Mesenchymal Stem Cells. *Tissue Eng. Part A* **14,** 1615–1627 (2008).

48.   Ullah, I., Subbarao, R. B. & Rho, G. J. Human mesenchymal stem cells -current trends and future prospective. *Biosci. Rep. Biosci. Reports* **35,** (2015).

49.   Capulli, M., Paone, R. & Rucci, N. Osteoblast and osteocyte: Games without frontiers. *Archives of Biochemistry and Biophysics* **561,** 3–12 (2014).

50.   Kanda, Y. *et al.* Dynamic cultivation with radial flow bioreactor enhances proliferation or differentiation of rat bone marrow cells by fibroblast growth factor or osteogenic differentiation factor. *Regen. Ther.* **5,** 17–24 (2016).

51.   Liu, L. *et al.* Different effects of intermittent and continuous fluid shear stresses on osteogenic differentiation of human mesenchymal stem cells. *Biomech. Model. Mechanobiol.* **11,** 391–401 (2012).

52.   Hofmann, S. *et al.* Control of in vitro tissue-engineered bone-like structures using human mesenchymal stem cells and porous silk scaffolds. *Biomaterials* **28,** 1152–1162 (2007).

53.   Woloszyk, A. *et al.* Influence of the mechanical environment on the engineering of mineralised tissues using human dental pulp stem cells and silk fibroin scaffolds. *PLoS One* **9,** e111010 (2014).

54.   Stiehler, M. *et al.* Effect of dynamic 3-D culture on proliferation, distribution, and osteogenic differentiation of human mesenchymal stem cells. *J. Biomed. Mater. Res. Part A* **89A,** 96–107 (2008).

55.   Maria de Peppo, G. *et al.* Human Embryonic Stem Cell-Derived Mesodermal Progenitors Display Substantially Increased Tissue Formation Compared to Human Mesenchymal Stem Cells Under Dynamic Culture Conditions in a Packed Bed/Column Bioreactor. *Tissue Eng. Part A* **19,** 175–187 (2013).

56. Kreke, M. R., Sharp, L. A., Lee, Y. W. & Goldstein, A. S. Effect of Intermittent Shear Stress on Mechanotransductive Signaling and Osteoblastic Differentiation of Bone Marrow Stromal Cells. *TISSUE Eng. Part A* **14,** 529–537 (2008).

57. Gomes, M. E., Sikavitsas, V. I., Behravesh, E., Reis, R. L. & Mikos, A. G. Effect of flow perfusion on the osteogenic differentiation of bone marrow stromal cells cultured on starch-based three-dimensional scaffolds. *J. Biomed. Mater. Res. A* **67,** 87–95 (2003).

58. Lau, E. *et al.* Effect of low-magnitude, high-frequency vibration on osteogenic differentiation of rat mesenchymal stromal cells. *J. Orthop. Res.* **29,** 1075–1080 (2011).

59. Yourek, G., McCormick, S. M., Mao, J. J. & Reilly, G. C. Shear stress induces osteogenic differentiation of human mesenchymal stem cells. *Regen. Med.* **5,** 713–24 (2010).

60. Delaine-Smith, R. M., MacNeil, S. & Reilly, G. C. Matrix production and collagen structure are enhanced in two types of osteogenic progenitor cells by a simple fluid shear stress stimulus. *Eur. Cells Mater.* **24,** 162–174 (2012).

61. Stiehler, M. *et al.* Effect of dynamic 3-D culture on proliferation, distribution, and osteogenic differentiation of human mesenchymal stem cells. *J. Biomed. Mater. Res. - Part A* **89,** 96–107 (2009).

62. Gao, X. *et al.* Regulation of cell migration and osteogenic differentiation in mesenchymal stem cells under extremely low fluidic shear stress. *Cit. Biomicrofluidics* **8,** (2014).

63. Bjerre, L., Bünger, C. E., Kassem, M. & Mygind, T. Flow perfusion culture of human mesenchymal stem cells on silicate-substituted tricalcium phosphate scaffolds. *Biomaterials* **29,** 2616–2627 (2008).

64. Nishimura, I. *et al.* Effect of osteogenic differentiation medium on proliferation and differentiation of human mesenchymal stem cells in three-dimensional culture with radial flow bioreactor. *Regen. Ther.* **2,** 24–31 (2015).

65. Zhang, Z. Y. *et al.* A comparison of bioreactors for culture of fetal mesenchymal

stem cells for bone tissue engineering. *Biomaterials* **31,** 8684–8695 (2010).

66. Sikavitsas, V. I., Bancroft, G. N. & Mikos, A. G. Formation of three-dimensional cell/polymer constructs for bone tissue engineering in a spinner flask and a rotating wall vessel bioreactor. *J. Biomed. Mater. Res.* **62,** 136–148 (2002).

67. Qi, M.-C. *et al.* Mechanical strain induces osteogenic differentiation: Cbfa1 and Ets-1 expression in stretched rat mesenchymal stem cells. *Int. J. Oral Maxillofac. Surg.* **37,** 453–458 (2008).

68. Kreke, M. R., Sharp, L. A., Lee, Y. W. & Goldstein, A. S. Effect of intermittent shear stress on mechanotransductive signaling and osteoblastic differentiation of bone marrow stromal cells. *Tissue Eng. Part A* **14,** 529–37 (2008).

69. Chen, K. G., Mallon, B. S., McKay, R. D. G. & Robey, P. G. Human Pluripotent Stem Cell Culture: Considerations for Maintenance, Expansion, and Therapeutics. *Cell Stem Cell* **14,** 13–26 (2014).

70. Yeatts, A. B., Geibel, E. M., Fears, F. F. & Fisher, J. P. Human mesenchymal stem cell position within scaffolds influences cell fate during dynamic culture. *Biotechnol. Bioeng.* **109,** 2381–2391 (2012).

71. Kwang-PohGoh, T. *et al.* Microcarrier Culture for Efficient Expansion and Osteogenic Differentiation of Human Fetal Mesenchymal Stem Cells. *Biores. Open Access* **2,** 84–97 (2013).

72. Murphy, C. M., Matsiko, A., Haugh, M. G., Gleeson, J. P. & O'Brien, F. J. Mesenchymal stem cell fate is regulated by the composition and mechanical properties of collagen-glycosaminoglycan scaffolds. *J. Mech. Behav. Biomed. Mater.* **11,** 53–62 (2012).

73. Murphy, C. M. & O'Brien, F. J. Understanding the effect of mean pore size on cell activity in collagen-glycosaminoglycan scaffolds. *Cell Adh. Migr.* **4,** 377–81 (2010).

74. Evans, N. D. & Gentleman, E. The role of material structure and mechanical properties in cell–matrix interactions. *J. Mater. Chem. B* **2,** 2345 (2014).

75. Borghi, F. F. *et al.* Emerging Stem Cell Controls: Nanomaterials and Plasma Effects. *J. Nanomater.* **2013,** 1–15 (2013).

76. Kommireddy, D. S., Sriram, S. M., Lvov, Y. M. & Mills, D. K. Stem cell attachment to layer-by-layer assembled TiO2 nanoparticle thin films. *Biomaterials* **27,** 4296–4303 (2006).

77. Engler, A. J., Sen, S., Sweeney, H. L. & Discher, D. E. Matrix Elasticity Directs Stem Cell Lineage Specification. *Cell* **126,** 677–689 (2006).

78. Cowin, S. C. & Cardoso, L. Blood and interstitial flow in the hierarchical pore space architecture of bone tissue. *J. Biomech.* **48,** 842–854 (2015).

79. Lee, S. *et al.* Potential Bone Replacement Materials Prepared by Two Methods. *MRS Proc.* **1418,** mrsf11-1418-mm06-02 (2012).

80. Guda, T. *et al.* Hydroxyapatite scaffold pore architecture effects in large bone defects in vivo. *J. Biomater. Appl.* **28,** 1016–1027 (2013).

81. Huri, P. Y., Ozilgen, B. A., Hutton, D. L. & Grayson, W. L. Scaffold pore size modulates in vitro osteogenesis of human adipose-derived stem/stromal cells. *Biomed. Mater.* **9,** 045003 (2014).

82. Sommer, M. R. *et al.* Silk fibroin scaffolds with inverse opal structure for bone tissue engineering. *J. Biomed. Mater. Res. - Part B Appl. Biomater.* **105,** 2074–2084 (2017).

83. Murphy, C. M., Haugh, M. G. & O'Brien, F. J. The effect of mean pore size on cell attachment, proliferation and migration in collagen-glycosaminoglycan scaffolds for bone tissue engineering. *Biomaterials* **31,** 461–466 (2010).

84. Wang, Y. *et al.* Influence of Pore Size of Silk Fibroin Scaffolds on Chondrocyte Differentiation in Static and Rotation Culture Conditions. *Cell Prolif.* 1321–1321 (2009).

85. Wang, Y. *et al.* The synergistic effects of 3-D porous silk fibroin matrix scaffold properties and hydrodynamic environment in cartilage tissue regeneration. *Biomaterials* **31,** 4672–4681 (2010).

86. Liu, C., Cui, N.-Y., Osbeck, S. & Liang, H. Air plasma processing of poly(methyl methacrylate) micro-beads: Surface characterisations. *Appl. Surf. Sci.* **259,** 840–846 (2012).

87. Goodman, S. B., Yao, Z., Keeney, M. & Yang, F. The future of biologic coatings for orthopaedic implants. *Biomaterials* **34,** 3174–83 (2013).

88. Alves, N. M., Pashkuleva, I., Reis, R. L. & Mano, J. F. Controlling cell behavior through the design of polymer surfaces. *Small* **6,** 2208–2220 (2010).

89. Khorasani, M. T., Mirzadeh, H. & Irani, S. Plasma surface modification of poly (l-lactic acid) and poly (lactic-co-glycolic acid) films for improvement of nerve cells adhesion. *Radiat. Phys. Chem.* **77,** 280–287 (2008).

90. Owen, R. *et al.* Emulsion templated scaffolds with tunable mechanical properties for bone tissue engineering. *J. Mech. Behav. Biomed. Mater.* **54,** 159–172 (2016).

91. Chu, P. Plasma-surface modification of biomaterials. *Mater. Sci. Eng. R Reports* **36,** 143–206 (2002).

92. Barry, J. J. A., Silva, M. M. C. G., Shakesheff, K. M., Howdle, S. M. & Alexander, M. R. Using Plasma Deposits to Promote Cell Population of the Porous Interior of Three-Dimensional Poly(D,L-Lactic Acid) Tissue-Engineering Scaffolds. *Adv. Funct. Mater.* **15,** 1134–1140 (2005).

93. Shekaran, A. *et al.* Biodegradable ECM-coated PCL microcarriers support scalable human early MSC expansion and in vivo bone formation. *Cytotherapy* **18,** 1332–1344 (2016).

94. Chen, A. K. L., Chen, X., Choo, A. B. H., Reuveny, S. & Oh, S. K. W. Critical microcarrier properties affecting the expansion of undifferentiated human embryonic stem cells. *Stem Cell Res.* **7,** 97–111 (2011).

95. Rashidi, H., Yang, J. & Shakesheff, K. M. Surface engineering of synthetic polymer materials for tissue engineering and regenerative medicine applications. *Biomater. Sci.* **2,** (2014).

96. Pouponneau, P., Leroux, J.-C., Soulez, G., Gaboury, L. & Martel, S. Co-encapsulation of magnetic nanoparticles and doxorubicin into biodegradable microcarriers for deep tissue targeting by vascular MRI navigation. *Biomaterials* **32,** 3481–3486 (2011).

97. Ng, Y. C., Berry, J. M. & Butler, M. Optimization of physical parameters for cell

attachment and growth on macroporous microcarriers. *Biotechnol. Bioeng.* **50,** 627–635 (1996).

98. Strathearn, K. E., Ph, D. & Pardo, A. M. P. Parameters to Consider When Expanding Cells on Corning ® Microcarriers Application Note. (2014).

99. Schop, D. *et al.* Expansion of human mesenchymal stromal cells on microcarriers: Growth and metabolism. *J. Tissue Eng. Regen. Med.* **4,** 131–140 (2010).

100. Mukhopadhyay, A., Mukhopadhyay, S. N. & Talwar, G. P. Influence of serum proteins on the kinetics of attachment of vero cells to cytodex microcarriers. *J. Chem. Technol. Biotechnol.* **56,** 369–374 (2007).

101. Heathman, T. R. J. *et al.* Expansion, harvest and cryopreservation of human mesenchymal stem cells in a serum-free microcarrier process. *Biotechnol. Bioeng.* **112,** 1696–1707 (2015).

102. Sommar, P. *et al.* Engineering three-dimensional cartilage-and bone- like tissues using human dermal fibroblasts and macroporous gelatine microcarriers. *Br. J. Plast. Surg.* **63,** 1036–1046

103. Kwang-Poh Goh, T. *et al.* Microcarrier Culture for Efficient Expansion and Osteogenic Differentiation of Human Fetal Mesenchymal Stem Cells. doi:10.1089/biores.2013.0001

104. Wang, Y. & Ouyang, F. Bead-to-bead transfer of Vero cells in microcarrier culture. *Cytotechnology* **31,** 221–224 (1999).

105. Ohlson, S., Branscomb, J. & Nilsson, K. Bead-to-bead transfer of Chinese hamster ovary cells using macroporous microcarriers. *Cytotechnology* **14,** 67–80 (1994).

106. Nam, J. H., Ermonval, M. & Sharfstein, S. T. The effects of microcarrier culture on recombinant CHO cells under biphasic hypothermic culture conditions. *Cytotechnology* **59,** 81–91 (2009).

107. Rafiq, Q. A., Brosnan, K. M., Coopman, K., Nienow, A. W. & Hewitt, C. J. Culture of human mesenchymal stem cells on microcarriers in a 5 l stirred-tank bioreactor. *Biotechnol. Lett.* **35,** 1233–1245 (2013).

108. Nienow, A. W., Rafiq, Q. A., Coopman, K. & Hewitt, C. J. A potentially scalable method for the harvesting of hMSCs from microcarriers. *Biochem. Eng. J.* **85,** 79–88 (2014).

109. Phillips, B. W. *et al.* Attachment and growth of human embryonic stem cells on microcarriers. *J. Biotechnol.* **138,** 24–32 (2008).

110. Hervy, M. *et al.* Long term expansion of bone marrow-derived hMSCs on novel synthetic microcarriers in xeno-free, defined conditions. *PLoS One* **9,** 1–7 (2014).

111. Schnitzler, A. C. *et al.* Bioprocessing of human mesenchymal stem/stromal cells for therapeutic use: Current technologies and challenges. *Biochem. Eng. J.* **108,** 3–13 (2016).

112. Hervy, M. *et al.* Long Term Expansion of Bone Marrow-Derived hMSCs on Novel Synthetic Microcarriers in Xeno-Free, Defined Conditions. *PLoS One* **9,** (2014).

113. Nienow, A. W. *et al.* Agitation conditions for the culture and detachment of hMSCs from microcarriers in multiple bioreactor platforms. *Biochem. Eng. J.* **108,** 24–29 (2016).

114. Chen, D., Yu, M., Zhu, M., Qi, S. & Fu, J. Carbonyl iron powder surface modification of magnetorheological elastomers for vibration absorbing application. *Smart Mater. Struct.* **25,** (2016).

115. Carnachan, R. J., Bokhari, M., Przyborski, S. A. & Cameron, N. R. Tailoring the morphology of emulsion-templated porous polymers. *Soft Matter* **2,** 608 (2006).

116. Salem, M. A. Mechanical Properties of UV-Irradiated Low-Density Polyethylene Films Formulated With Carbon Black and Titanium Dioxide. *Egypt. J. Sol* **24,** 141–150 (2001).

117. Robinson, J. L., Moglia, R. S., Stuebben, M. C., McEnery, M. A. P. & Cosgriff-Hernandez, E. Achieving Interconnected Pore Architecture in Injectable PolyHIPEs for Bone Tissue Engineering. *Tissue Eng. Part A* **20,** 1103–1112 (2014).

118. Quell, A., De Bergolis, B., Drenckhan, W. & Stubenrauch, C. How the Locus of Initiation Influences the Morphology and the Pore Connectivity of a

Monodisperse Polymer Foam. *Macromolecules* **49,** 5059–5067 (2016).

119. Huš, S. & Krajnc, P. PolyHIPEs from Methyl methacrylate: Hierarchically structured microcellular polymers with exceptional mechanical properties. *Polym. (United Kingdom)* **55,** 4420–4424 (2014).

120. Datta, N. *et al.* In vitro generated extracellular matrix and fluid shear stress synergistically enhance 3D osteoblastic differentiation. *Proc. Natl. Acad. Sci.* **103,** 2488–2493 (2006).

121. Napolitano, A. P. *et al.* Scaffold-free three-dimensional cell culture utilizing micromolded nonadhesive hydrogels. *Biotechniques* **43,** 494–500 (2007).

122. Ferrari, C. *et al.* Limiting cell aggregation during mesenchymal stem cell expansion on microcarriers. *Biotechnol. Prog.* **28,** 780–787 (2012).

123. Jossen, V. *et al.* Theoretical and Practical Issues That Are Relevant When Scaling Up hMSC Microcarrier Production Processes. *Stem Cells Int.* **2016,** 1–15 (2016).

124. Mei, Y. *et al.* Modulating and modeling aggregation of cell-seeded microcarriers in stirred culture system for macrotissue engineering. *J. Biotechnol.* **150,** 438–446 (2010).

125. Lim, K. T. *et al.* Synergistic effects of orbital shear stress on in vitro growth and osteogenic differentiation of human alveolar bone-derived mesenchymal stem cells. *Biomed Res. Int.* **2014,** 316803 (2014).

126. Zhao, F., Vaughan, T. J. & McNamara, L. M. Quantification of fluid shear stress in bone tissue engineering scaffolds with spherical and cubical pore architectures. *Biomech. Model. Mechanobiol.* **15,** 561–577 (2016).

127. Jarman-Smith, M. *et al.* Human fibroblast culture on a crosslinked dermal porcine collagen matrix. *Biochem. Eng. J.* **20,** 217–222 (2004).

128. Wang, H. J., Bertrand-De Haas, M., Riesle, J., Lamme, E. & Van Blitterswijk, C. A. Tissue engineering of dermal substitutes based on porous PEGT/PBT copolymer scaffolds: Comparison of culture conditions. *J. Mater. Sci. Mater. Med.* **14,** 235–240 (2003).

129. Korin, N., Bransky, A., Dinnar, U. & Levenberg, S. A parametric study of human fibroblasts culture in a microchannel bioreactor. *Lab Chip* **7,** 611 (2007).

130. Puwanun, S. *et al.* A simple rocker-induced mechanical stimulus upregulates mineralization by human osteoprogenitor cells in fibrous scaffolds. *J. Tissue Eng. Regen. Med.* (2017). doi:10.1002/term.2462

131. Lai, W.-T., Krishnappa, V. & Phinney, D. G. Fgf2 Inhibits Differentiation of Mesenchymal Stem Cells by Inducing Twist2 and Spry4, Blocking Extracellular Regulated Kinase Activation and Altering Fgfr Expression Levels. *Stem Cells* **29,** 1102–1111 (2011).

132. Gharibi, B. & Hughes, F. J. Effects of Medium Supplements on Proliferation, Differentiation Potential, and In Vitro Expansion of Mesenchymal Stem Cells. *Stem Cells Transl. Med.* **1,** 771–782 (2012).

133. Lima, J., Gonçalves, A. I., Rodrigues, M. T., Reis, R. L. & Gomes, M. E. The effect of magnetic stimulation on the osteogenic and chondrogenic differentiation of human stem cells derived from the adipose tissue (hASCs). *J. Magn. Magn. Mater.* **393,** 526–536 (2015).

134. Lim, K.-T. *et al.* Enhanced Osteogenesis of Human Alveolar Bone-Derived Mesenchymal Stem Cells for Tooth Tissue Engineering Using Fluid Shear Stress in a Rocking Culture Method. *Tissue Eng. Part C Methods* **19,** 128–145 (2013).

135. Salmimies, R., Mannila, M., Juha, J. & Häkkinen, A. Acidic Dissolution of Magnetite: Experimental Study on The Effects of Acid Concentration and Temperature. *Clays Clay Miner.* **59,** 136–146 (2011).

136. Hurrell, R. How to Ensure Adequate Iron Absorption from Iron-fortified Food. *Nutr. Rev.* **60,** S7–S15 (2002).

137. Jiang, Y. *et al.* Speciation and kinetic study of iron promoted sugar conversion to 5-hydroxymethylfurfural (HMF) and levulinic acid (LA). *Org. Chem. Front.* **2,** 1388–1396 (2015).

138. Blair, H. C. *et al.* Osteoblast Differentiation and Bone Matrix Formation In Vivo and In Vitro. *Tissue Eng. Part B Rev.* **23,** 268–280 (2017).

139. Tseng, P.-C. *et al.* Spontaneous osteogenesis of MSCs cultured on 3D microcarriers through alteration of cytoskeletal tension. *Biomaterials* **33,** 556–564 (2012).

Chapter 3| Characterising Poly-High Internal Phase Emulsions For Thermal Insulation Materials

10. Aims and Objectives

This chapter aims to investigate the thermal insulation properties of porous poly-high internal phase emulsions using a flux sensor, and how the property can be enhanced. Several steps will be taken to investigate this:

1. Investigate how the addition of natural fibre affects the thermal properties
2. Different volume fractions of the dispersed phase will be used to create samples of various porosities; they will be tested to determine if porosity can improve the conductivity.
3. Compare measurements using a well-established method, in this case, laser flash diffusivity.

11. Introduction

The recent amendment of the Energy performance of buildings directive aims to cut emissions by at least 40% by 2030 [1]. It further calls for the improvement of Europe's ageing buildings, with an estimated 35% are now older than 50 years, by also encouraging the use of "Smart technology" improve their energy efficiency. Moreover, the most cost-effective way of dealing with this is through efficient management of current strategies rather than alternative forms of energy supply [2].

The crux of energy loss from buildings is through the housing envelope and is experienced through the roof, windows and doors at 25%, but an estimated 30 % is through the walls alone. A Simple retrofit to older poorly insulated buildings could reduce the energy leaked through the building [3]. According to the European Commission, a total of 5 – 6% reduction in energy is possible by refining current energy efficiency methods; this would also see a reduction of a 150 Mt of CO_2 is possible by 2050 [4].

The primary job of insulating materials within a building envelope is to; minimise transfer of heat [5], allow the structure to "breathe", be resistant to moisture, and bacteria. Materials used for such applications are assessed by their thermal conductivity, which is a result of a combination of factors such as; density, porosity, moisture content, and mean temperature difference of the material [6]. Traditional thermal materials have thermal conductivities between 33 – 40 mW/(mK) [3], and this is true particularly for fibreglass (glass wool), which is still an industry standard in

housing developments even though it causes respiratory ailments and is not easy to handle [7]. There are also the potential superinsulators such as aerogels and gas-filled panels, which can replace such dated materials, but their mechanical properties and costs have restricted their widespread use in industry.

Poly-High Internal Phase Emulsions (Poly-HIPE) have been mentioned countless time for their potential role as thermal insulators, yet there is little information available on their thermal performance. Interestingly, their morphology contains the necessary characteristics insulators have, as polymers, they have an inherent property to resist heat, the small pores trap air also aid insulation. Additionally, various properties like pore size, porosity, and degree of openness can be tailored to a high degree – and these will be discussed in more detail in this chapter.

12. Literature Review

12.1. Thermal Insulation

Insulation is the inherent property of a material to restrict the transfer of heat that occurs in three forms: Conduction, Convection and Radiation.

Although conduction is highly dependent on the material itself, by altering the structure through the introduction of small pockets of air or other gases the property is enhanced further. Insulation materials are highly porous, sometimes up to 90 % to house gases within, which are logically poor conductors of heat due to the random movement and distribution of molecules, air, for example, has a conductivity value of 0.0271 $W\ m^{-1}\ K^{-1}$. By ensuring these voids are smaller than 4 mm the contribution from convection can be neglected in porous insulators, conduction and radiation become the primary sources of transfer [8,9]. The same relationship can be found with radiation conductivity, a property that also decreases with pore size [3]. As a result, the summation of all thermal resistance components increases, which is mostly why fibrous or porous materials excel as insulators.

12.1.1. Thermal Conductivity

Thermal conductivity (k, $W\ m^{-1}\ K^{-1}$) is the measure of how well a material conducts/insulates heat; in a one-dimensional case, Fourier's law gives the heat flow through each surface [10]. It is defined as the ratio of heat flux to the thermal gradient (See Equation 2) In applications that require heat loss to be small a lower value is

favoured and a higher value for when heat transfer is crucial. Q is the heat flux (W m^{-2}), L is the length of material (m), A is area (m^2), T_1 - T_2 (K) is the temperature difference created.

$$k = \frac{QL}{A(T_1 - T_2)}$$ *Equation 2*

12.1.2.   Characterising Thermal Conductivity

The characterisation of a material's thermal conductivity can be obtained using numerous methods, all using similar principles or techniques; these can either rely on a constant heat transfer applied by a constant temperature difference, i.e. Steady state, or non-steady state, which employ a transient regime.

Guarded hot plate method is a steady-state method used most commonly for building insulation materials. In its purest form, it is typically a sample of material between a hot and cold plate enclosed within guarded insulation.

Cp : Cold plate
Diff 1 : Imbalance sensing element 1
Diff 2 : Imbalance sensing element 2
Gpb : Back guard plate
Ht : Measurement zone heating element
Ht.Gpl : Lateral guard heatin element

Ins : Thermal insulation
Sp : Measurement zone surface plate
Sp.Gpl : Lateral guard surface plate
Temp 1 : Temperature sensor 1
Temp 2 : Temperature sensor 2
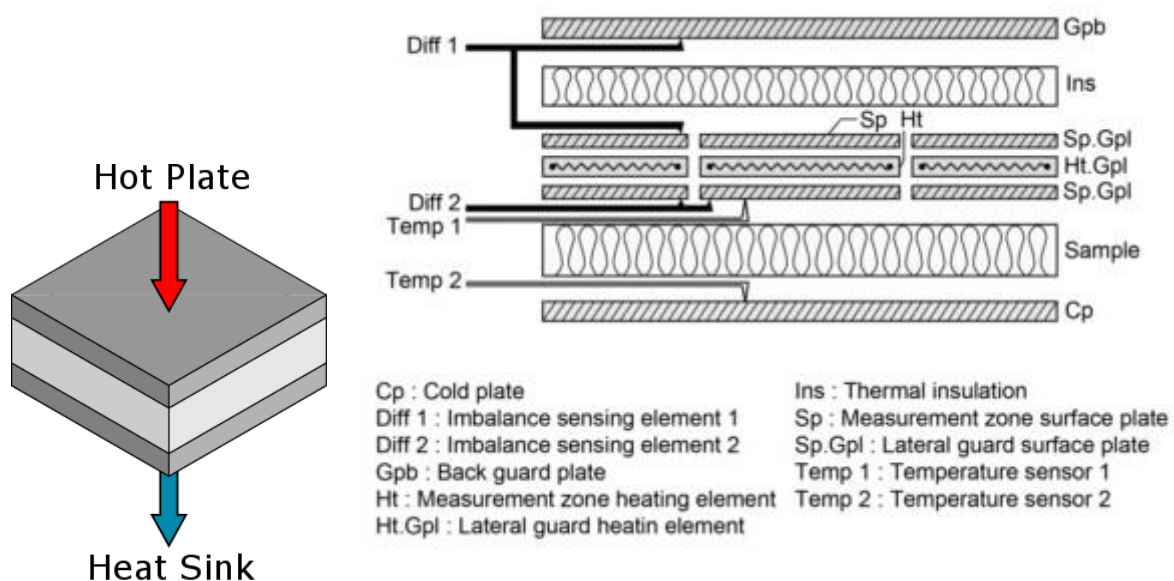
Figure 60: A guarded hot plate in its purest form, the sample of material to be measured sandwiched between heating and cooling plates (Left). The same concept is shown on the left but enclosed in insulation and guards to minimise heat loss adapted from [11].

For building materials, this method is also regulated by British standards - Thermal performance of building materials and products (BS EN 12667:2001).

The accuracy and reliability of a guarded hotplate as shown on the right of Figure 60 is well regarded with the uncertainty of data as low as 2-3% [9]. Steps are taken to

ensure heat lost laterally is minimal, with the outer guard plates equipped with individual heating elements to the main sample area. With the surrounding area the same temperature as the core, lateral and back fluxes are therefore negligible. This uniform heat profile creates a unidirectional flow of heat towards the cold plate through the sample [12]. By using Fourier's thermal conductivity equation above the conductivity can be determined.

Comparative cut bar method utilises the known conductivities of reference material, to determine the unknown conductivity of the sample in question. The cylindrical cut sample is placed between samples with known conductivities, which is heated at one end to create the thermal gradient. As the transfer of heat through the materials will be similar, the conductivity of the unknown sample can be calculated [13].

The principle remains similar to that of the guarded hotplate. By using the known thermal conductivities of the reference sample, the one-dimensional equation above can be utilised to solve for the unknown conductivity.

Laser Flash diffusivity method although typically utilised at high temperature for ceramics, metals and glass, it has been deemed suitable for polymers by Dos Santos et al. [14]. It is a non-steady state and non-contact method. Thermal diffusivity which is an essential factor in transient heat conduction [14] is defined as the passing rate of heat from the hot surface to the opposite (cold) surface; a material with higher diffusivity dissipates heat more readily and visa versa. Furthermore, it is regarded as an indirect method as the outcome from obtained diffusivity, specific heat and density are used to determine conductivity as described in Equation 3 below.
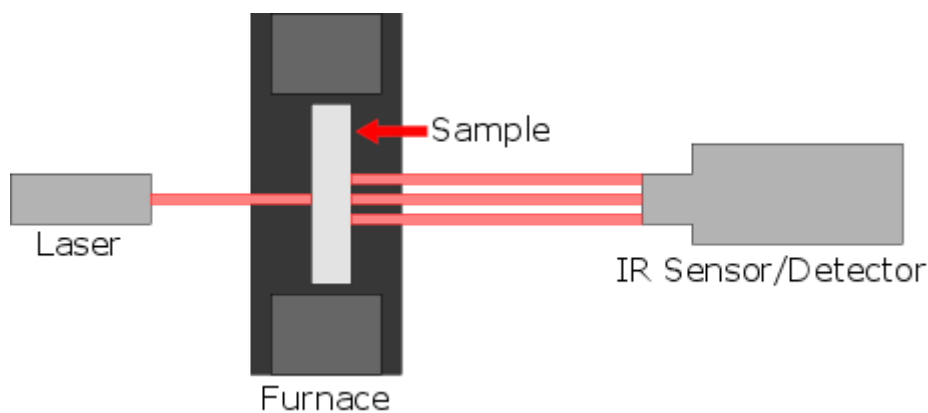

Figure 61: A simple depiction of the laser flash diffusivity method. The pulse laser is heating the sample in the furnace, while the IR/Detector records the change in temperature on the rear side.

There are specific requirements that need to be met with this technique: It requires materials to be opaque (In the visible and near-IR length), it must reflect light and must have good emission and absorption. More often than not further material processing is required to obtain quality data. Both sample and reference sample are coated in a fine layer of graphite, which increases the emissivity improving the signal-to-noise ratio [15].

Laser pulses are delivered to the sample to heat the near side, which then diffuses through the material. On the opposite end, a liquid nitrogen detector periodically measures the transient change in temperature [16].

The equation that is utilised thereafter concerns several factors, which are all dependent on heat and are usually characterised independently before flash diffusivity analysis. Where: k is conductivity in W m^{-1} K^{-1}, the diffusivity of the material which is measured value donated by the symbol α (m^2/s), C_p is the specific heat capacity of the sample (J/kg^{-1} K^{-1}), and ρ is the density in kg/m^3.

$$k = \alpha C_P \rho \qquad \text{\textit{Equation 3}}$$

12.2. Traditional Methods

The commercial market is saturated with conventional insulating materials, some of which have been in used for decades. Mineral wool remains a common choice in housing and accounts for 60% of the total insulation market [17]. Mineral wool is fibrous and irritant, it can be the cause of respiratory problems, its possible health impacts have been debated and remain inconclusive, and some variations are still suspected carcinogens. There is a high occurrence of lung cancer related mortality in workers in the slag wool industry, although the available data make it impossible to draw any reliable conclusions since the increase in lung cancer could be related to exposure to slag wool or any other chemical the workers are exposed to professionally [17].

Polyurethane (PU) is another common insulation material, which is used as either ready-made boards or sprays to fill cavities as the density of polystyrene increased, the thermal conductivity decreased [18]. Kuranska et al. combined PU with natural fibres and discovered that PU combined with flax and rapeseed derived fibres could

177

control the conductivity from 20.05 to 20.69 mW m^{-1} K^{-1}. The result was also dependent on the fibre length; 0.5 mm and 2 - 2.5 mm were found to be more effective [19]. An important consideration when using PU for insulation materials is its decomposition products during combustions, PU releases hydrogen cyanide (HCN) and isocyanates when combusting, which are poisonous [2].

Expanded Perlite and Vermiculite are typically investigated as a combination with other building materials, for example, hollow bricks filled with either mineral [20,21], mixed with lightweight concrete and production of composite panels [22,23]. Also, a review by Rashad summarised that addition of perlite to concrete, mortar, brick and plaster reduced the thermal conductivity of these materials [24]. Addition of 5, 10, 15 and 20 wt% of vermiculite gradually increased in thermal conductivity from 0.054 to 0.242 W m^{-1} K^{-1}. Whereas, the addition of perlite when used as fillers for PU, decreased the thermal conductivity up until 10 wt% to 0.052 W m^{-1} K^{-1}, but increased thereafter to 0.124 W m^{-1} K^{-1} [25]. Sutcu et al. showed that up to 10 wt% of vermiculite also showed better thermal insulation properties, which was a result of porosity and small pores of the mineral [26].

Cork contains naturally occurring cellular-like structure that makes it light and ideal for thermal and sound insulation. Unlike most natural materials, it is resistant to biological attack – which is another appealing property. Board density was found to be influential; natural cork has a thermal conductivity of 0.042 W m^{-1} K^{-1}, while increased compactness resulted in higher values from approximately 0.05 to almost 0.083 W m^{-1} K^{-1} [27,28].

A common aspect of all materials that are heavily relied upon in industry is their ability to trap air and hydrophobic characteristics for consistent thermal properties. A significant advantage with all conventional materials have over newer methods is the ease at which they can be machined on-site to specific dimensions. There is a belief that conventional systems have reached their limit in terms of insulating properties.

12.3. Insulation using natural materials

Natural materials such as by-products from various industries, chicken feathers, hemp, and recyclable materials suggest a shift to a more environmental friendly route to solve the insulation problem. Although it remains an attractive prospect as a way to minimise

waste streams, the thermal conductivities of such materials at best are similar to traditional materials (See Table 13).

Due to their natural based components, further processing is required, and without it, their inherent wettability could contribute to biological attacks. Additionally, their flammability is also a concern [29].

12.4. Advanced Methods

12.4.1. Aerogels

Aerogels are regarded as a super-insulating material, and typically have a conductivity of less than 0.02 W $m^{-1}K^{-1}$ [5]. The dramatic decrease is largely down to their combination of nano-sized pores and highly porous structure (80 – 99 %); therefore, excel as thermal and acoustic insulation. Furthermore, density is increasingly significant due to a rise in material conduction, and it was presumed that the optimum density was in the region between 100 – 160 kg m^{-3} at ambient temperature [8].

Due to the absence of the primary heat transfer mechanisms: convection and conduction, radiation becomes the dominant transfer method, more so, at elevated temperatures. By doping with particles such as carbon black, TiO_2 and ZnO, silica, the contribution made by radiation can also be limited [30]. Carbon aerogels outperformed a closed foam variation at extreme temperatures of up to 2000°C, where the aerogel had a total conductivity of 0.601 W m^{-1} K^{-1} and the closed-foam structure with carbon particles almost three times more [31]. Increasing the amount TiO_2 concentration from 0 – 20% confirmed this, as a decrease in thermal conductivity was observed from 0.041 to 0.030 W m^{-1} K^{-1}, respectively [30]. Wei et al. compared carbon doped aerogel with a regular specimen at elevated temperatures, they found the carbon-doped gels showed little variation in conductivity and remained under 0.03 W m^{-1} K^{-1} between 300 – 500 K, unlike their counterparts [8]. A paper by Eskandari et al. also demonstrated that a small addition of 3% silica aerogel to unplasticised Polyvinyl Chloride decreased the thermal conductivity by 54% to 0.091 W m^{-1} K^{-1} [32].

Aerogels can shrink during the processing stages, which can cause deformations in the mechanical structure, leading to brittleness; large scale production, for this reason, is difficult [33]. Their brittle nature can be associated with their low density and poor distribution of material that makes them incapable of withstanding pressure [34]. Granular variations of aerogels are not as effective as monolith structures but are more

prevalent in this form. However, in doing so, the thermal performance is sacrificed owed to the increased presence of air in the packing voidage, which has a higher conductivity than a monolith aerogel [34]. Compression was found to reduce the spacing around the granules, and a bed density of 150 – 165 kg/m^3 reached a minimum of 13 mW m^{-1} K^{-1}. Although over compaction leads to lower voidage, it destroys the granular-structures leading to more material contact, which increases the conductivity further [34].

There are several reasons for the limited introduction of aerogels into the industry: the main reason is due to the energy-intensive process used to manufacture them. Furthermore, due to the brittle nature, they are prone to dust production consisting of amorphous silica, although this is not considered to be hazardous it is a physical irritant [5]. Moreover, as mentioned, the variation of thermal conductivity in the granular state.

12.4.2.   Gas Filled (GIPs) and Vacuum Panels (VIPs)

Due to the process of hermetically sealing panels to maintain a vacuum or trap gas inside, such an option is expensive. VIPs start installed at around 3 – 4 mW m^{-1} K^{-1}, and after 25 years they can increase to around 7 - 10 mW m^{-1} K^{-1} due to air or moisture permeating into the panels [35,36].

GIP envelopes have low-emissivity barriers to reduce transfer via radiation. Air or Inert noble gases have low thermal conductivity values hence are ideal in such applications [37].

The main disadvantage with such panels is that they cannot be cut to size on site, therefore have bespoke size requirements; additionally any puncture or holes will increase the conductivity to around 20 mW m^{-1} K^{-1} [3].

Table 12: Summary of thermal conductivities from commercially available insulation materials. The ranges are between typical performance ranges depend on factors such as density, moisture content.

Traditional Insulation Materials		
Material	**Thermal Conductivities** (W m^{-1} K^{-1})	**Ref.**
Expanded Polystyrene (EPS)	0.037 – 0.055	[38]
Extruded Polystyrene (XPS)	0.033 – 0.042	[39]
Cork	0.042	[27]
Polyurethane (PU)	0.022 – 0.045	[40,41]
Perlite	0.04 – 0.06	[24]
Vermiculite	0.063	[26]
Mineral Wool	0.035 – 0.045	[17]

Table 13: Alternative insulation methods recycled either from products such as textiles, a by-product of various industries or from natural resources like wool.

Alternative Methods		
Material	**Thermal Conductivities** (W m⁻¹ K⁻¹)	**Ref.**
Hemp	0.04 - 0.082	[4]
Flax	0.035 - 0.075	[4]
Sheep Wool	0.034 - 0.05	[42]
Recycled polyester	0.033 – 0.035	[43]
Textile waste	0.044 - 0.103	[38]
Natural Polymer from Hydrangea macrophyll	0.0421	[35]
Basalt fibre panels	0.0305 - 0.0345	[44]

Table 14: Advanced methods of insulation, which are termed superinsulators. All of which are commercially available.

Advanced Methods		
Material	**Thermal Conductivities** (W m⁻¹ K⁻¹)	**Ref.**
Silica Aerogels	0.017 - 0.021	[45]
Vacuum insulation Panels	0.0043 - 0.0061	[46]
Gas-filled Panels	0.01 - 0.04	[35]

12.5. Fabricating Porous Architecture

Porous architecture is a crucial design factor not only in thermal insulation engineering but also biomaterials engineering – which was a requirement in chapter 2. For that matter, any applications that require high surface areas, or scaffolds that provide a network for structural support.

For polymers, there are numerous methods to do this, each with their advantages and disadvantages. A few common methods have been highlighted below; these were deemed suitable for the applications in this report; their pore size range can be found in Figure 62.

Solvent casting

Solvent casting process utilises porogens to aid the creation of porous defects, normally, salt or sugar. Dispersing insoluble particles into a monomer solution and then trapping them in place by polymerisation. The porogen-polymer materials are thoroughly washed using a solvent in which the particles dissolve readily.

The washing/leaching process is slow, making it suitable only for developmental stages, and for when the structures required are small [47]. Larger materials require the solvent to penetrate deeper into the scaffold, which increases the time required to wash. Porogen geometry is also something that requires consideration – since the shape of the pores can be influential in cell-based applications as mentioned earlier in chapter 2. If homogeneity is an essential factor, sieving has to be utilised beforehand – this may have to be repeated several times to ensure a narrow size distribution is achieved.

Its simplicity is a significant advantage; the straightforwardness of changing pore size and porosity can all simply be achieved by changing the particles used and concentration [48].

Freeze-drying (Lyophilisation)

It is a method used to create porous hydrogel structures. Phase separation is caused due to thermodynamic instability during rapid cooling [47]. Voids are formed where the separated solvent is removed through sublimation.

183

It is regarded as being suitable only for hydrogel materials. Due to the process involved, it is difficult to control pore size and porosity they mostly depend on the water-to-polymer ratio and varying the freezing temperature [49]. Sublimation can cause the outer regions of the polymer to collapse forming a surface skin; this is the result of the interfacial tension caused by solvent removal at the solvent-air interface. After the energy-intensive process, the outcome is often weak mechanically [47]. Although it requires a long time to process, no post-washing is necessary.

Gas Foaming

High-pressure CO_2 is passed through discs of material, which have been subjected to compression moulding. A high volume fraction of CO_2 is pushed through; this process occurs for several days before being brought back to atmospheric.

The limitations of this process arise, from the use of high temperatures, and the lack of control over pore size, interconnectivity and porosity [49].

These techniques were deemed more suitable for the current application and have their advantages and disadvantages, but what is common is the limitations of controlling pore size and interconnectivity – which are important for thermal applications and even cell culture. Their flexible nature is one of the reasons why there is a plethora of literature in numerous areas of research, and it remains true in this instance as well; they are suitable for biomaterials, thermal insulation, and even sensor-based applications. Emulsion techniques - will be discussed below in more detail.
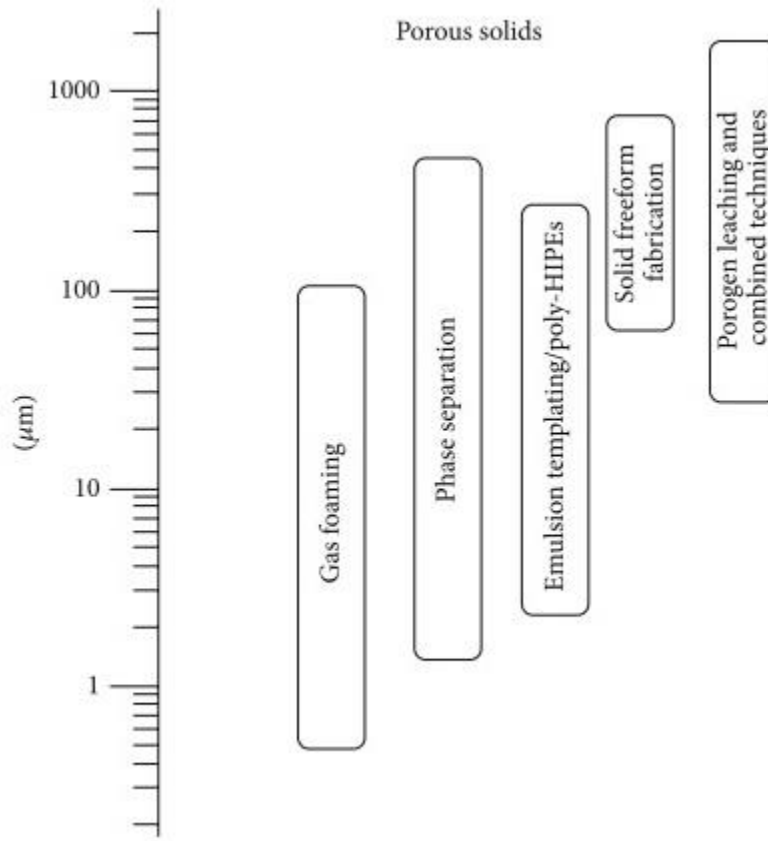
Figure 62: Pore sizes of various techniques available to produce porous materials, adapted Berro et al.[50].

12.6. Emulsions

Emulsions are formed through the addition of two immiscible liquids, one that resides as the water component and the other forming the oil phase. The dispersed phase or internal phase is added dropwise into the continuous phase (external phase), while under constant agitation or intermittent shaking. The type of emulsion determined by the liquid, which resides in the dispersed phase, Oil-in-water (O/W), or Water-in-Oil (W/O).

Above a critical value, however, phase inversion can occur. It is controlled by the volume ratio of the two immiscible liquids, whereby the continuous and dispersed phase reverse that causes an oil-in-water emulsion to become a water-in-oil emulsion [50].

On their own, however, if left standing as such, the natural tendency of each liquid to separate will take effect - each droplet will, by various processes form a larger liquid mass, until there is a clear differentiation between the two liquids. This is regarded as

thermodynamically driven, the free energy increases during the emulsification process. At this moment, the system will be thermodynamically driven to achieve an equilibrium state and the mechanisms to achieve lower interfacial area will happen readily by flocculation, creaming, sedimentation and Ostwald ripening; an illustrated representation of each process is shown in Figure 63 [51].

Agglomeration of randomised droplets is also a common observation. Although, during this flocculation stage they retain their individual shape, and no diffusion of mass between them occurs, however, if the droplets remain close for an extended period there is a tendency of Ostwald ripening, or coalescence to materialise [52].

Creaming is observed due to the difference in densities of the two immiscible-liquids, as this is more a separation process leading to the other forms of destabilising methods. The cream, consisting of higher concentrations of the dispersed phase as it is risen to the top, forming almost two different emulsions [51]

A gradient effect is also created during sedimentation; the dispersed phase gathering in an array at the bottom [53], this, like creaming, is a density-dependent process, causing denser droplets to settle at the bottom.

Smaller droplets often aid the growth of larger droplets (by disintegrating themselves and adding their mass to the large droplet), also known as Ostwald ripening – eventually leading to a broader size distribution as mass diffuses into larger droplets. Eventually, this chain leads to the total breakdown of an emulsion.

In all the above processes, the droplets retain their integrity; Thinning of the interfacial film around approaching particles must reach a critical thickness before coalescence can occur. Often, this is regarded as the final method of separation, and two distinct regions will be apparent.
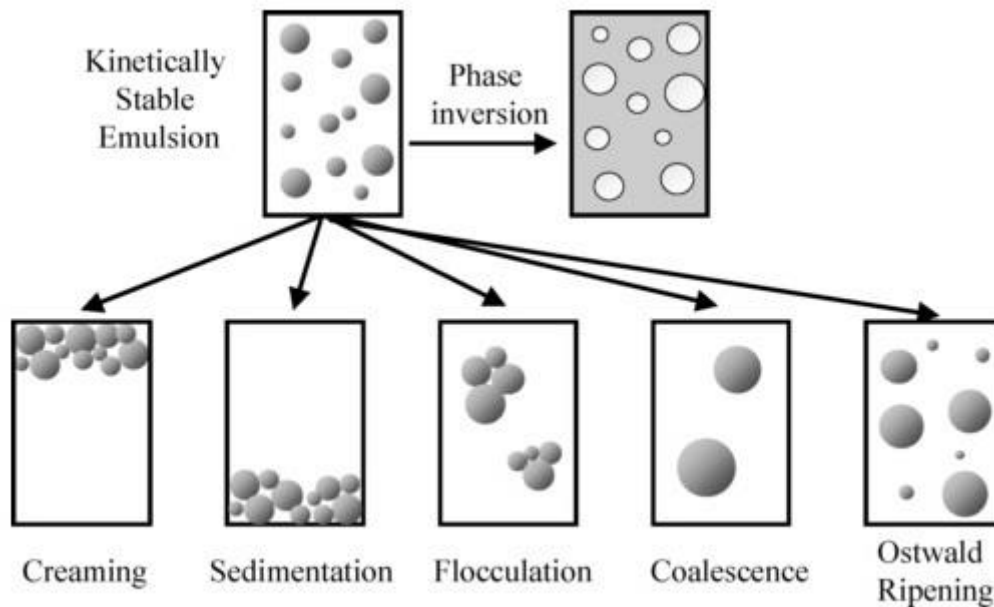
Figure 63: Simple schematic illustrates the mechanisms that lead to emulsions collapsing, image from McClements [52].

It is the ability of the system to resist these natural physiochemical changes, which is regarded as emulsion stability. Therefore, the need for surface-active species (Surfactants) arises, which help control or prevent such undesirable effects.

The amphipathic form of emulsifying agents aids the preservation of emulsion structure, allowing the inevitable deterioration to span months, or years – which is why they are so heavily relied upon in various industries (Cosmetic, Food and beverage to name a few).

12.7. Emulsion Templating

Emulsion science allows the fabrication of closed, or open-pored scaffolds with a high degree of freedom, to suit the required application.

The dispersed phase provides micron or nano-sized architecture to form a viscous solution. Pores are typically heterogeneous in size; a single emulsion can have all, or a combination of the following within the scaffold: microporous (less than 2 nm), mesoporous (between 2 - 50 nm), or macroporous (greater than 50 nm) [54].

A high internal phase emulsion or HIPE as they are commonly referred to as, are the classification of the emulsion due to the fraction of the dispersed phase. A dispersed

phase exceeding 74% is regarded as a HIPE, where anything below is considered a low or medium internal emulsion [54]. The fraction arises from the packing arrangement of droplets in the emulsion, regarded as the maximum volume of the droplet phase to preserve a uniform and spherical internal structure. Anything above is usually non-uniform, or a polyhedral variety [55].

Emulsion architecture can be controlled by varying components (surfactants, co-surfactants, oils and solvents) temperature and homogenisation conditions [56]. Below, various factors that affect different parameters of emulsions have been investigated.

12.7.1.   Dispersed Phase

The quantity of the dispersed phase has great consequence on the final structure as mentioned; the pore sizes, porosity and shape of the pores can all be controlled altering this alone. Furthermore, a low enough value can determine whether the monolith once cured is an open, or closed pored structure.

As a single drop is released, it is quickly surrounded by the continuous phase, and as another is added the spatially independent water droplets are kept apart by the continuous phase. At this stage, if the material is suddenly polymerised it will form a closed pored structure because the barrier between them is too thick for it to contract and form an interconnected window. If more and more droplets are added this barrier becomes thinner, with growing amounts of the continuous phase forming thinly around each droplet [57]. Natural contraction at this point due to polymerisation forms holes within the membrane at the thinnest parts of the interface creating windows, in other words, an open and interconnected network. Addition of a high volume of the dispersed phase lowers the density of the structure, as greater voids of air are available for the same volume of the continuous phase. Although increasing porosity greater than 95% is plausible, the thinning of the interfacial barrier can make the structure fragile, lowering its ability to withstand applied force.

12.7.2.   Surfactant – Emulsion Role

A general accepted rule of thumb states that the liquid in which the surfactant has higher solubility forms the continuous phase - Bancroft's rule. Surfactants largely depend on the application, the type of emulsion and properties required. A surfactant that dissolves entirely in one component, then the other, can prevent inversion for

example. Additionally, careful selection to suit the physiochemical properties of the two phases can lead to more stable emulsions.

12.7.2.1. HLB Scale

A more quantifiable system to aid the user on surfactant selection is the hydrophile-lipophile balance (HLB), which is a scale limited between the numbers 1-20, which takes into account the relative sizes of the hydrophilic and hydrophobic portion of the surfactant. The number is calculated by multiplying the ratio of molecular weight of the hydrophilic portion of the surfactant and the total molecular weight of the surfactant by 20. If a molecule is completely hydrophilic, it has an HLB number of 20, while entirely hydrophobic materials have an HLB number of 0. The incremental change in numbers is associated with a higher HLB number tends to be water-soluble, preferentially forming w/o emulsions - due to the increased presence of hydrophilic groups. At the lower end of the HLB scale they are Lipophilic, consequently favouring o/w emulsions – a result of having more hydrophobic groups present [58]. Emulsifying surfactants that have an HLB value from 3-6 are typically suited for w/o emulsifiers, while surfactants with an HLB value of 8-16 – are typically o/w emulsifiers. Emulsions made with surfactants with HLB values in the range of 8 – 11 are close to the phase inversion point according to Jiang et al., these, therefore, depend on other factors in determining the emulsion type, for example temperature, phase volume, additives and emulsification process [59].

12.7.2.2. Surfactant Stabilisation

Surfactants play an essential role in emulsion templating, as they help stabilise two immiscible liquids. The addition of a suitable surfactant helps lower the interfacial tension, and provide kinetic stability to a system, which is inherently unstable.

Surfactant concentration is therefore vital as Chen & Tao discovered, there exists a range in which concentration is insufficient and does not form an emulsion, and anything excessive leads to instability; determined by an increased amount of separation of the two phases in the emulsion [60]. Also in agreement with Wong et al., who found 0.75 w/vol% of Hypermer 2296 (An oil soluble emulsifier) was the lowest concentration that formed suitable homogenous emulsions for polymerising [61]. Blends of surfactants can be utilised to achieve greater emulsion stability [55]. Commonly, a mix of ionic and non-ionic surfactants is used which modify van der

Waals interaction and interfacial viscosity giving the overall emulsion highly stable properties [62].

Stability is essential, as the emulsion can then serve its required purpose, but it also serves a role in maintaining droplet size. Greater stability often leads to a decrease in droplet size due to the lower surface energy per unit area [63]. As a result, HIPEs can have pore sizes within the nano region of 1 μm up to 100 μm [64].

12.7.2.3. Particles as Surfactant

Emulsions can be stabilised using particles and referred to as Pickering emulsions. Though this topic will only be mentioned briefly since it was a focal point during the initial stages of the thesis, but none of the results have been reported in the thesis.

The use of particles, unlike surfactants, is not determined by an arbitrary scale, but by the hydrophobic or hydrophilic properties of the material. Particles can innately align themselves on the edges of the oil-and-water interface, wetting to a higher degree in the water phase if they are more hydrophilic, and more so in the oil phase if they are hydrophobic. The angle of the particle, relative to the droplet is often a good indicator of which emulsion type will take primacy over the other — angles greater than 90° form Water-in-Oil type, and less than, form the inverse [65]. The closer to 90° the angle is, the more stable an emulsion is considered to be [66]. These contact angle, if required can be altered by the surface chemistry of the particles - as discussed previously.

12.7.3.   Mechanical Effect

Breaking of droplets into smaller ones by agitation helps form more stable emulsions; Wong et al. showed that stirring duration affected the droplet sizes, HIPE stirred for 30 seconds showed a more considerable size distribution, compared to those stirred for 10 minutes [61]. Chen and Tao also showed that a higher stirring intensity led to more stable emulsions, which was characterised by the volume separated from the emulsion over 24 hours [60]. Hus & Krajnc compared the morphology of Poly-HIPEs and found that the variable – stirrer speed when altered from 500 to 25,000 rpm resulted in smaller pores and interconnected pores [67]. The use of high-speed stirring also formed a narrower size distribution compared to lower speed stirring.

12.7.4. Temperature

Carnachan et al. demonstrated increasing the temperature of the aqueous phase before emulsification from room temperature up to 80°C, directly increased average void diameter and interconnectivity of a divinylbenzene based HIPE [68]. The occurrence is a result of emulsion instability arising due to change in viscosity affecting the rate of coalescence; surfactant migration into the oil phase is also regarded to be a contributing factor.

12.7.5. Additives

Surfactants and their effects on stability have been discussed. However an additional method involves the use of electrolytes. The addition of even small amounts of salt, which is a common choice, resulted in improved stability of emulsions. Thickening of the aqueous, to which the electrolyte is added prevents the chain of de-stabilisation mechanisms to proceed [69]. The stability leads to the reduction of Ostwald ripening and coalescence. Often stability is determined by evaluating the change of the packing factor over a length of time. It is simply the amount of sediment emulsion compared to the separated upper phase; as the emulsion destabilises the differences in the phases becomes more significant, and the factor reduces. Jiang et al. showed that addition of NaCl concentration affected the packing factor; at lower concentrations it was higher than 0.75, increasing up to 5 M this decreased eventually stabilising around 0.65 at 20 and 30°C, but more consistency was observed at higher temperature [59].

Compounds with long chains can act as co-stabilisers, Li et al. showed that 2 wt% NaCl alone was not sufficient to maintain a stable emulsion when compared to the addition of 10 wt% of either hexadecane or hydroxyl terminated polybutadiene [70]. In the same study, optimising the divinyl-benzene and water content resulted in a further decrease in void size from the initial 99.2 μm with 5 wt% and 89%, to 8.2 μm with 10 wt% and 81% water. In comparison, hydroxyl terminated polybutadiene resulted in smaller pore sizes between 3.2 and 2.8 μm with the addition of 10 – 15 wt%.

12.8. Poly High Internal Phase Emulsions (Poly-HIPE)

The polymerisation of emulsions is achieved when the monomer phase resides in the continuous regime. Thus, forming a scaffold around the droplets of the dispersed droplets. HIPEs once polymerised are frequently a foam-like material with open and

interconnected pores quite similar to aerogels, or cork. They form highly porous materials with small-interconnected pores, often with low densities and large surface areas; this makes them a promising material for numerous fields. Research into poly-HIPE has been extensive due to their multi-purpose applications; in areas such as biomaterials for scaffolds, drug delivery; oil and gas industry for separating oil from water; as well as the food industry.

12.8.1. Surfactant – PolyHIPE Role

Earlier the vital role of surfactants in emulsions was highlighted; however, they also have an instrumental role in dictating Poly-HIPE interconnectivity and degree of openness.

Increasing surfactant concentration has been shown to lead to a more open structure, according to Carnachan et al., this is mainly due to the thinning barrier between the emulsion droplets [68]. Even subtle changes can have a substantial effect, in this particular case below 5% had a closed cell structure, and at 7% resulted in an open interconnected monolith [71]. Huš & Krajnc also showed that increasing the concentration of 5 – 15 Vol% led to decreasing void size with increasing interconnectivity [67].

Surfactant blends of Span80, cetyltrimetylammonium bromide (CTAB) and dodecylbenzenesulfonic acid sodium salt (DDBSS) and, Span20, CTAB and DDBSS decreased in void size. Though the difference between these two blends was small, it was, however, an improvement compared to using a single surfactant type. Again, this reduction of pore size is due to the stability achieved in the emulsion phase, and the creation of a stronger interfacial film which minimises Ostwald ripening [72].

The importance of the droplet phase has been mentioned earlier, even though the dispersed phase can tailor the porosity and packing of the polyHIPE, the surfactant is regarded to be more influential. It was reported that a combination of a low concentration of surfactant (5% w/w) combined with a high droplet phase (97%) still resulted in a closed structure[56].

Nevertheless, the cost of excessive surfactant concentrations can lead to poor mechanical properties. Styrene-Divinylbenzene PolyHIPE with 5 vol% surfactant showed significantly better mechanical properties than a polyHIPE stabilised with 20 vol% of the same porosity [61].

192

The surfactant type influences surfactant concentrations and depending on other constituents; the optimum concentrations will vary greatly. An optimisation procedure is required to achieve the desired results.

12.8.2. Thermal and Photo Curing

The more common sources of thermally triggered radicals are from water-soluble, potassium persulphate (KPS) and ammonium persulphate (APS), and oil soluble, AIBN (2,2′-Azobis(2-methylpropionitrile).

The low activation energy of redox initiators can often be used in conjunction with standard thermal initiators to supply radicals at lower temperatures 0 – 50°C [73]. TEMED (N,N,N′,N′-tetramethylethylenediamine) is well reported, coupled with either KPS or APS allowing the reaction to progress at room temperature.

Hus et al. discovered that by switching a combination of APS/TEMED to AIBN, the pore sizes became larger and more inhomogeneous, and with less interconnectivity[68]. A similar seemed to hold with Gurevitch & Silverstein; the average void diameter decreased from 20 to 10 μm with the changing from KPS to benzoyl peroxide (BPO) – which was soluble in the oil phase [74]. Kranjnc et al. also found that the initiator influenced pore and void size; a combination of APS and TEMED, compared to AIBN and APS produced smaller pores and voids [75].

Emulsions that utilise thermal initiators react at approximately 70°C, which is reported often, and require anywhere between a few hours to 24 hours to polymerise [76–78]. These elevated temperatures are enough to cause destabilisation and polymerisation in tandem, suggesting the final morphology does not necessarily reflect the 'true' emulsion droplets before curing [79].

Photo-polymerising HIPE material is a multitude of times quicker – occurring within the first few seconds of exposure to UV light. Nevertheless, the depth of penetration limits it to samples no more than a few millimetres thick. In such cases a combination of photo and thermal initiators can be used, the frontal UV initiated reaction provides a chain reaction of heat produced to the deeper regions of space [80].

12.8.2.1. Point Of Initiation

Closed or open-pored structures can be obtained by simply changing the phase the initiator dissolves in. Robinson et al. showed that by changing from the water-soluble

initiator, APS, to an organic soluble one (benzoyl peroxide) the interconnectivity was improved [64]. This is in agreement with work down by Quell et al., who used the initiators AIBN and KPS, they found that by initiating from the interface led to closed polyhedral voids, whereas, from the bulk led to open and interconnected voids [81].

Understanding the solubility of the initiator in the water or oil is, therefore, essential because this can determine interconnectivity. In a W/O emulsion for example, if the water interface contains the aqueous initiator the first point of initiation and cross-linking will be around each droplet forming a closed structure. Whereas, an organic-soluble initiator forms from the bulk material. The changing of monomer to polymer causes a chain of forces pulling molecules to the epicentre of the reaction (shrinkage of the continuous phase), in turn triggering a tear at the thinnest point in the interfacial barrier creating an open network [64,81]. Though the effect of thermal initiators has been considered, this assumption should remain true for photoinitiators as they also exhibit a higher affinity to certain solvents.

12.8.3.   Post Processing

After polymerisation, scaffolds generally go through a post-process washing stage. Any unreacted species such as; monomer, surfactant, porogenic solvent, or other additives remain within the porous structure. Washing can involve a simple solvent rinse, or in some cases, a more thorough approach is required using an automated and repetitive apparatus such as a Soxhlet. The inclusion of a condenser allows the extraction solvent to recycle through evaporation and then condensation, filling up the thimble. The extracted solvent is automatically syphoned as it reaches a particular height in the thimble chamber, purging into the extractor flask, for the process to repeat until desired.

It was found that solvent extraction time influenced the cellular morphology of poly-HIPE, increasing the surface area by 58 – 107%. At low duration - 1 – 3 hours was deemed ineffective, whereas a 6-hour wash was found to be optimum, resulting in a substantial increase in area and better mechanical properties. Both of these properties were found to decrease as a result of prolonged washing [72].

13.   Materials & Method

13.1. Materials for EHA Scaffolds

Diphenyl(2,4,6-trimethylbenzoyl)phosphine oxide/2-hydroxy-2-methylpropiophenone (Photoinitiator), 2-Ehtyhexyl acrylate (EHA), Isobornyl acrylate (IBOA), Trimethyllolpropane triacrylate (Cross-linker), Hypermer B246-SO-(MV) (Surfactant). All chemicals purchased from Sigma-Aldrich, unless stated otherwise.

13.2. Silicon Moulds

A 1:9 ratio of silicon elastomer and curing agent was poured into a pot and stirred vigorously for several minutes. By doing so air, bubbles were generated in the viscous liquids, to remove this place under vacuum to collate them to the surface, and by re-pressurising the oven the bubbles burst, leaving a homogenous liquid. Once all the bubbles had been removed, the oven was heated up to 70°C for 2 hours.

13.3. Preparing Scaffolds

A solution consisting of EHA (3.9 g), IBOA (1.3 g), Cross-linker (1.4 g) and surfactant (0.198 g) was prepared and scaled up if necessary to make a stock. The stock was kept sealed, and wrapped in foil to avoid exposure to light.

Before usage, a certain quantity of stock (Oil phase) was weighed and between 1 – 5% photo-initiator, and 1 – 5% KPS was added, before being mixed thoroughly using a paddle stirrer – which was set to 400 rpm. Water (4x oil phase) was added – dropwise, under constant stirring to emulsify it. Once a homogeneous white colour was achieved, the emulsion was poured into the moulds, and cured under a UV lamp for 30 seconds on each side. Cured samples were slowly pried off the surfaces, and washed with methanol, then dried to a constant weight in a vacuum oven.

The porosity of each sample was varied by altering the volume of water, which acts as the internal phase. Samples with 60, 70, 75, 80 and 90 were denoted with the expected porosity value and the letter P at the end. i.e. 60P.

13.4. Helium Pycnometry

Samples were prepared by stamping, using a 7 mm biopsy punch. The chamber was filled until it was beyond half the volume requirement. Typically, this meant three stamped samples in each run. The high porosity of polyHIPEs meant that filling the chamber requires more than the usual amount of material. Otherwise, an error does

occur during the run explaining the amount of sample is inadequate. The samples were weighed before starting the run.

Analysis conditions were specified; purge cycles and pressure were set to 20 cycles with 20 purges (Standard condition) and a pressure of 19.5 Psi. The chamber was sealed, and then the process was followed through using the setup wizard, ensuring the right chamber insert was selected (Important Step).

13.5. Measuring Conductivity

Two Thermocouples were attached to attached to voltmeters. Also, the flux sensor was connected to another voltmeter. The flux sensor SHF1010T (Sequoia) was used during these trials. A Greenteg sensor replaced this after that. The flux sensor was adhered to the sample using thermal conducting paste and pressed to make sure the presence of trapped air was minimised. The sample was placed in the partition, aligning the grooves, so the sample required no assistance sitting upright; this orientation made sure there were no gaps that air could freely pass through.

Two pots were in placed into each of the two chambers. One which had hot water (~70°C), and the other with ice. The thick polystyrene cover was immediately placed back, and readings from all three voltmeters were noted at 10-minute intervals. The process was carried out for 3 hours, for each sample and in triplicate. By the end of the 3 hours, there was approximately a 10°C difference between the two chambers.

13.6. Flash Line Diffusivity

Each variation of samples was cut to the appropriate standard required in triplicate; each one approximately a 10 mm x 10 mm square. They were gold coated before the graphite coating because of the translucent nature of the material.

Typically, a heat gun is used to post graphite coating, which helps the fine layer adhere to the sample and stops the layer smudging when being transferred in place. The polymer samples, however, were heated using a heat gun, then immediately coated. By doing so, the graphite adhered to the gold surface without clumping which it tended to do using the typical method.

Samples were placed into in the holders; with the reference sample at the back and the sample to test at the front. The heating chamber was sealed, and allowed to reach vacuum. Liquid nitrogen was added to the cooling system during the period when the

vacuum was established, and after 5 minutes of depressurising the chamber, it was sealed. The nitrogen flow rate was controlled using a rotameter, the float of which was set midway.

The recorded measurements of density and thickness were utilised in the software when setting up the measurement file. The programmed temperature was set at 34°C, and the limit was set to 40°C.

14.   Results

Poly-HIPE were created using standard moulds, a 10 mm x 10 mm square for testing thermal insulation properties. The opaque nature of the sample is due to the low volume of water present (60%); this amount usually classifies as a poly medium internal phase emulsion. Samples with 70% water phase and above were more translucent, and are regarded as the poly-HIPE variety; because of this, they required further preparation for laser flash diffusivity measurements.

Composite mixtures were also manufactured with different concentrations of wood fibres extracted from wooden insulation boards. Figure 65, shows the addition of 5 wt%, 15 wt% and 40 wt% of wood fibres. Due to the hydrophilic nature of the fibres thorough mixing was required. However, regions of clumping and tendency of the fibres to mesh were unavoidable. Hence, in the first two images, a blotchy surface is more apparent.
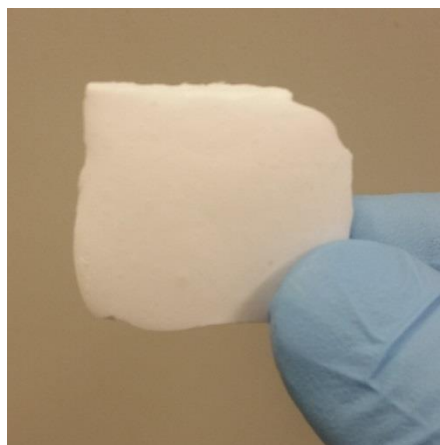

Figure 64: A typical sample utilised in the thermal measurement installation; this particular one is 60% porous (60P).

Figure 65: EHA-IBOA poly- high internal phase emulsions with added wood fibres (From left to right): 5 wt% and 70% water,

14.1. Helium Pycnometry and Porosimetry

Helium pycnometry was used to calculate porosities of all five samples. The porosity of all the samples was calculated using equation 4, and Table 15 shows how the values are close to the theoretical values. Calculated porosity values were all less than 5% different from their theoretical counterparts, the highest difference of ~ 3.8% for sample 80P. Additionally, the density of the sample follows a trend, decreasing as the porosity increases, sample 75P, however, shows a slight increase.

$$Porosity = \frac{Total\ Volume - Skeletal\ Volume}{Total\ Volume}$$

Equation 4

Table 15: Showing the calculated volumes based on material dimensions (Total Volume), and the skeletal volume as established by Helium Pycnometery, and the calculated porosities.

Sample	Total Volume (cm³)	Skeletal V (cm³)	Standard Dev. (cm³)	Density (g/cm³)	Standard Dev. (cm³)	Porosity
60P	0.0770	0.0304	0.0001	1.0279	0.002	0.61
70P	0.0652	0.0182	0.0002	0.9814	0.0084	0.72
75P	0.0618	0.0156	0.0002	0.9817	0.0151	0.74
80P	0.0638	0.0147	0.0001	0.9587	0.0088	0.77
90P	0.0728	0.0083	0.0001	0.9283	0.0149	0.89

Mercury Porosimetry was used on a single sample to cross-check the values obtained from Helium pycnometery. A 75P sample, estimated to be 75% porous, was 75.9% porous according to the results; this aligns well with the expected value and the value obtained by pycnometry. Comparing the difference between mercury porosimetry and

the theoretical value is 1.2%, which implies porosimetry aligns better with theoretical results, though more measurements will be required to conclude this. Nevertheless, it also confirms the use of helium pyconmetery as a reliable alternative as the difference between the two values differs by 2.5%.

14.2. Measuring Conductivity

Thermal conductivity was measured for various poly-HIPE with increasing dispersed volume fraction. Generally, from Figure 66 there is a trend to suggest increasing porosity leads to a proportional change in conductivity, except for porosity at 70%. 60P had the lowest average conductivity of 0.0499 W m^{-1} K^{-1}, whereas the highest was experienced at 90% porosity (0.1331 W m^{-1} K^{-1}). Percentage variation from the mean was determined for each sample, in the table below. The deviation for each sample was ± 20% from the mean, suggesting it not to be as reliable as most standard methods are. There was some significance in the results, but mainly at the two extremes, so 60P compared to and 80P and 90P for example.

The additional wood fibre was added to two samples: 60P and 90P to observe the effect on the thermal conductivity values. The mean increased by almost 47% from its initial value, conflictingly, 90P WF decreased by 25%. Standard deviation remained above 20% of the mean. Almost all comparisons with the addition of wood fibre showed a significant difference.

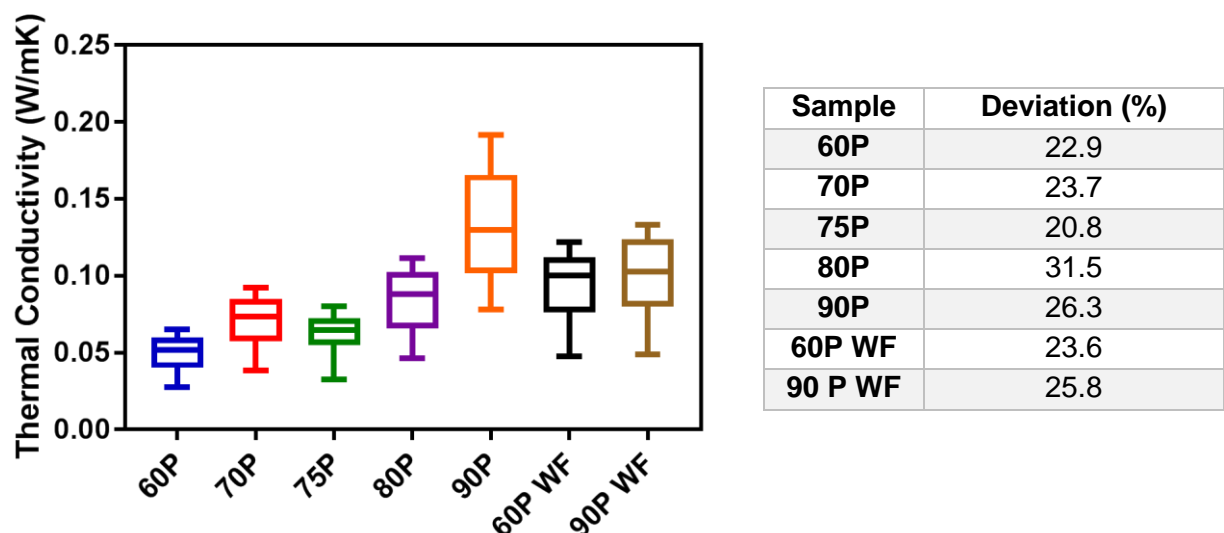| Sample	Deviation (%)
60P	22.9
70P	23.7
75P	20.8
80P	31.5
90P	26.3
60P WF	23.6
90 P WF	25.8

Figure 66: Thermal conductivity values as determined using the setup, with increasing porosity and with added wood fibres (WF).
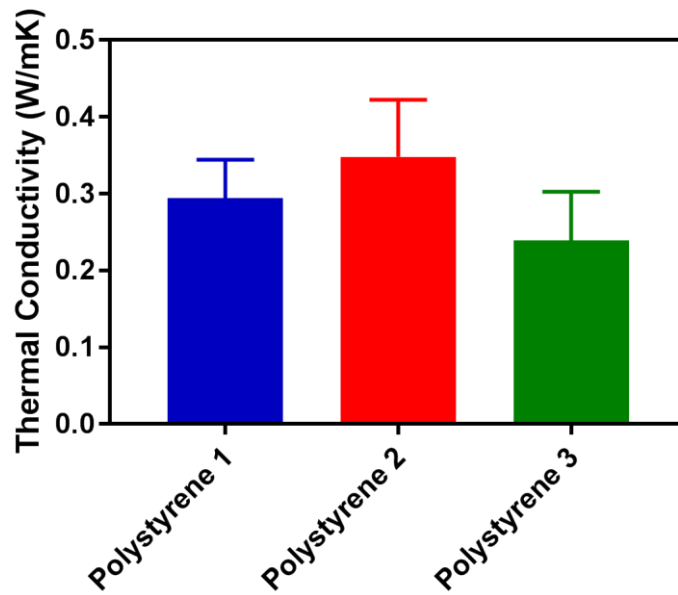
Figure 67: Thermal conductivity values of the known sample of polystyrene insulation.

A known sample of polystyrene polymer was used to determine the accuracy of the insulation setup. According to the setup after a 3-hour run, the average conductivity was found to be between 0.2 and 0.3 W m^{-1} K^{-1}. The actual value according to the sample was in the region of 0.035 W m^{-1} K^{-1}, which is a factor of 10 out from alleged value (Figure 67).

14.3. Flash Line Diffusivity

Using equation 3, conductivity values were calculated from the thermal diffusivity values obtained from the flashline equipment, thickness and density for each material – Table 16. Most values obtained using this method are high for an insulating material, thus can be considered erroneous. Samples with 70 % porosity are on average 0.135 W m^{-1} K^{-1}, an acceptable. Repeat measurements for this sample also suggest a high degree of reliability deviating by as little as 0.003 W m^{-1} K^{-1}.

Table 16: Results gained using Anter Flashline 3000; the densities were obtained using helium pycnometery.

Sample	Thickness (cm)	Density (kg/m³)	Heat Capacity J/(kg·K)	Diffusivity (m²/s)	Conductivity W/(m·K)	Conductivity REF (m²/s)
60P	0.211	1027.9	2064.8	3.45E-05	73	4.85E-05
70P1	0.179	981.4	1511.6	9.00E-08	0.134	3.03E-05
70P2	0.192	981.4	898.1	1.50E-07	0.132	4.02E-05
70P3	0.184	981.4	954.3	1.47E-07	0.138	3.52E-05
75P	0.248	981.7	1882.1	1.30E-03	2408	4.02E-05
80P	0.32	958.7	6022.7	2.07E-03	11935	4.04E-05
90P	0.377	928.3	1818.3	3.17E-03	5349	4.82E-05

15. Discussion

15.1. Laser Flash Diffusivity

Laser Flash diffusivity was utilised as a standard method to compare conductivity measurements from those obtained via the box method. Although polymers have been reported to be suitable for measurements using this technique, the porous nature of the sample was another hurdle to overcome, as this leaves the material translucent. The sample preparation requirements for almost all samples often require a thin coating of graphite to improve the signal-noise ratio, in this case, samples were coated in gold and graphite to overcome the translucent nature; as recommended for polymer materials [14]. Utilising both Gold and graphite have a negligible influence on the final conductivity values as highlighted in the same report.

Triplicate samples with 70 % porosity are the only credible results obtained via this route; an average value of 0.135 W m^{-1} K^{-1} suggests unimpressive insulation properties. Especially when compared to the traditional methods that can achieve between 0.02 – 0.04 W m^{-1} K^{-1}, though the low deviation suggests that it is a reliable method. This value can, however, improve through thorough optimisation of the material, and it is perhaps something to consider in the near future.

It is difficult to establish a specific reason behind the presence of extremely high conductivity values. Conventional sources of error according to the ASTM standard

E1461 are; sample, data acquisition, temperature measurements and performance of the detector[15]. According to Kempers et al. the samples also have to be uniform in thickness; in this particular case, uneven surfaces during sample preparation may be the more suspected source of error [83]. Room temperature measurements also require particular care due to noise via ambient radiation, a way to minimise this is through the combination of high laser power and an increase in the number of repeated measures [14].

Laser flash has been utilised with polymers; some authors recommend it for samples with <500 μm, which Poly-HIPEs typical consist of [84]. Conductivities of carbon aerogels and closed pore carbon foam, with 227 nm and 130 μm pore size were determined 0.108 W m^{-1} K^{-1}, and 0.225 W m^{-1} K^{-1}, respectively [31]. These values are in line with those obtained from sample 70P; it suggests if readings along the same magnitude are obtained for the rest of the samples, this may be an accurate reading of its insulation potential.

15.2. Conductivity Setup

The method utilised to calculate conductivity utilises Fourier's law of conduction. It was possible to neglect convection as a source of heat transfer mechanism within the material due to the pore-sizes within the micron-scale [85].

Material density is one of the influential factors that affect insulating properties. As the results from helium pycnometer state, density did follow the trend expected with increasing porosity. Between 72% and 74%, there was a slight increase, though marginal, the standard deviation suggests a material error, and could be reduced by repeating the readings.

A general, increasing trend is evident from 60P to 90P, increasing by 62% to ~ 0.133 W m^{-1} K^{-1}. For a foam structure, the increasing pore volume fraction leads to a decrease in the thermal conductivity values, at 95% it was reduced to 0.054 W m^{-1} K^{-1}, this is contrary to what was established in this report [86]. Although surfactant concentration dominates the degree of openness of Poly-HIPEs, volume-fraction has some influence; this usually amounts to a similar effect [87,88]. Poly-HIPEs at 60% porosity have more material between each adjacent pore; confirmed by the higher density of the material. Conductivity should be higher as a result at room temperature conditions, as was the case with PU and XPS foams [46,89]. It could be possible that

due to the higher porosity the material is more translucent, leading to an increased influence by radiative conduction [9,36]. A preventative measure could be through the use of an opacifier; materials such as carbon black, clay, TiO_2 are commonly used [30].

Incorporation of wood fibre doubled the conductivity from the initial 60P sample; however, 90P sample appeared to become more insulating, decreasing the conductivity of the reference sample by 25%. The improvement could be a result of the point made above, because of the reduction in material transparency, though more experiments will be required to clarify this. Wood fibre based insulations can be as low as 0.05 W m^{-1} K^{-1} [4]. However a delicate balance is required, an an increase in fibre density can be counter-productive, due to more material conducting heat and thermal bridging effects. Another concern, and one, which undoubtedly affected the results, is an inhomogeneous method used to distribute fibre that is prone to agglomerating in the polymer solution.

For readings obtained using this method, it was crucial to determine the accuracy of it. Known samples of insulating polystyrene were measured in triplicate; values of which were a factor 10 out from what was expected, between 0.025 – 0.04 W m^{-1} K^{-1} [90].

By comparing values of both methods, the flux sensor based method showed that all poly-HIPE variations were on average below the values of 0.1 W m^{-1} K^{-1}, whereas almost all laser flash values were extremely high to the point they can be dismissed as erroneous. However, the average conductivity for sample 70 P was 0.134 W m^{-1} K^{-1}, which is the same order of magnitude compared to some insulators, but still approximately 50% more than the value obtained using the setup described in this report.

It was assumed this method suffered from the non-steady state environment created, and this was addressed in the later stages of the project, but more tests are required to determine if this was beneficial for the polymer readings. Another source of error arises from the non-heated walls of the insulation box, whereas, methods like guarded hot plate use heated guards to minimise any variation of temperature from the centre.

Experimental results are ambiguous and surrounded by uncertainty until these can be confirmed using a reliable method like a guarded hotplate method; it is unclear whether the chosen process can determine the thermal conductivity of materials.

Poly-HIPEs present interesting and customisable traits that can make them an alternative form of insulation material. The inherent insulating properties of polymer materials and small pore sizes are attractive traits, for such applications. In chapter 2, emulsion templating of pores with 20 – 40 μm diameter were created using a variation of the same water-in-oil emulsion and with limited optimisation. Based on this there is an inclination to suggest that insulating properties can be tailored to suit a particular application, or closely match modern insulating materials.

16. Conclusion

A polymerised high internal emulsion was created with varying degrees of porosity. Its porosity was characterised using helium pycnometry, confirming that the theoretical method of calculating the volume fraction was accurate. Value of a single sample was confirmed by measuring the porosity using a mercury porosimetry.

Flash line diffusivity was found to be unpredictable and largely inaccurate when used to determine the conductivity of the material. Sample 70P was repeated three times to assess the reliability of the readings; the values deviated as little as 0.0029 W m^{-1} K^{-1} from the mean of 0.134 W m^{-1} K^{-1}.

There was a general trend to suggest that increasing porosity leads to an increase in thermal conductivity, with the exception being sample 75P. According to the setup, used EHA/IBOA poly-HIPEs with 60 % porosity had an average thermal conductivity value of 0.049 W m^{-1} K^{-1}, whereas, the highest was 0.13 W m^{-1} K^{-1} for 90 % porosity. These values are significantly higher than conventional insulation materials, for instance, mineral wool - which typically is in the region of 0.035 – 0.045 W m^{-1} K^{-1} [17]. However, a standard method is required to confirm that these values are accurate.

Thermal insulation potential of Poly-HIPEs have not been documented even though their properties are similar to aerogels, because of this they require further investigation. Due to their highly tunable nature - a property lacked by aerogels they make for an interesting material to examine. Furthermore, the addition of nanocomposite materials could yet enhance their thermal properties to compete with modern insulators.

17. Future Work

The main hindering point of this project has been the uncertainty associated with the experimental design, sensor, and a method to quantify results with a standard method; such as a guarded hot plate, or comparative bar method.

It is clear that a conductive plate design will be more accurate and reliable to determine the conductivity of highly porous poly-HIPE materials. Using the equipment that we already possess it is possible to fabricate a setup along the same appearance as depicted in several publications and BSC standards (BS EN 12667:2001). Qin used a simple setup of two aluminium plates one placed on a hotplate, followed by the flux sensor and sample, then by a cold aluminium plate – kept cool through natural radiation [91]. Furthermore, several authors have manufactured a guarded hot plate that can be obtained by using relatively inexpensive Peltier based heating [90,92].

Due to the results obtained for sample 70P, it will be interesting to do several repeats of other samples in order to determine if a reasonable value can be obtained.

The degree of control utilising Poly-HIPE material is extensive, there have been references to specific control measures that can be done to minimise pore size down to 1 μm. Minimising this factor is significant, as nano-sized pores are what make aerogels so effective as thermal and sound insulators. In the previous chapters the addition of nano- and micro-composites have improved the properties of standard materials, this can also be possible in this application, with the addition of for example nanoclay [93]. The addition of filler materials is something that was going to be investigated in this report, though due to other commitments and problems it was not possible.

Once conductivity has been determined, long-term performance should also be considered which would ultimately determine its suitability as an insulator [40]. Furthermore, for Poly-HIPEs to be considered as potential thermal insulators, an in-depth study is required to establish the optimum thickness. This variable should take in numerous cost factors such as material, energy, and potential savings compared to a conventionally insulated house.

Problems encountered in this project open the way for a seamless investigation to determine if Poly-HIPEs can indeed make suitable thermal insulators.

18. References

1.   European Commission. 2030 climate & energy framework. 1–2 (2015). Available at: https://ec.europa.eu/clima/policies/strategies/2030_en. (Accessed: 4th December 2017)

2.   Petter Jelle, B. Traditional, state-of-the-art and future thermal building insulation materials and solutions – Properties, requirements and possibilities. *Energy Build.* **43,** 2549–2563 (2011).

3.   Jelle, B. P., Gustavsen, A. & Baetens, R. The path to the high performance thermal building insulation materials and solutions of tomorrow. *J. Build. Phys.* **34,** 99–123 (2010).

4.   Kymäläinen, H. R. & Sjöberg, A. M. Flax and hemp fibres as raw materials for thermal insulations. *Build. Environ.* **43,** 1261–1269 (2008).

5.   Cuce, E., Cuce, P. M., Wood, C. J. & Riffat, S. B. Toward aerogel based thermal superinsulation in buildings: A comprehensive review. *Renewable and Sustainable Energy Reviews* **34,** 273–299 (2014).

6.   Kaynakli, O. A review of the economical and optimum thermal insulation thickness for building applications. *Renew. Sustain. Energy Rev.* **16,** 415–425 (2012).

7.   Sadineni, S. B., Madala, S. & Boehm, R. F. Passive building energy savings: A review of building envelope components. *Renew. Sustain. Energy Rev.* **15,** 3617–3631 (2011).

8.   Wei, G., Liu, Y., Zhang, X., Yu, F. & Du, X. Thermal conductivities study on silica aerogel and its composite insulation materials. *Int. J. Heat Mass Transf.* **54,** 2355–2366 (2011).

9.   Domínguez-M Noz, F., Anderson, B., Cejudo-López, J. M. & Carrillo-Andrés, A. Uncertainty in the thermal conductivity of insulation materials. *Energy Build.* **42,** 2159–2168 (2010).

10.   Hostler, S., Abramson, A., Bandi, S. & Schiraldi, D. Thermal conductivity of a clay-based aerogel. *Int. J. Heat Mass Transf.* **52,** 665–669 (2008).

11. Dubois, S. & Lebeau, F. Design, Construction and Validation of a Guarded Hot Plate Apparatus for Thermal Conductivity Measurement of High Thickness Crop-Based Specimens.

12. Dubois, S. & Lebeau, F. Design, construction and validation of a guarded hot plate apparatus for thermal conductivity measurement of high thickness crop-based specimens. *Mater. Struct. Constr.* **48,** 407–421 (2015).

13. Tong, X. C. *Advanced Materials for Thermal Management of Electronic Packaging. Advanced Materials* **30,** (2011).

14. Dos Santos, W. N., Mummery, P. & Wallwork, A. Thermal diffusivity of polymers by the laser flash technique. *Polym. Test.* **24,** 628–634 (2005).

15. E1461. *E1461. Standard test method for thermal diffusivity by the flash method. ASTM, West Conshohocken, PA* **i,** (2001).

16. Smith, D. S. *et al.* Thermal conductivity of porous materials. (2013). doi:10.1557/jmr.2013.179

17. Väntsi, O. & Kärki, T. Mineral wool waste in Europe: A review of mineral wool waste quantity, quality, and current recycling methods. *Journal of Material Cycles and Waste Management* **16,** 62–72 (2014).

18. Khoukhi, M., Fezzioui, N., Draoui, B. & Salah, L. The impact of changes in thermal conductivity of polystyrene insulation material under different operating temperatures on the heat transfer through the building envelope. (2016). doi:10.1016/j.applthermaleng.2016.03.065

19. Kuranska, M. & Prociak, A. Porous polyurethane composites with natural fibres. *Compos. Sci. Technol.* **72,** 299–304 (2012).

20. Zukowski, M. & Haese, G. Experimental and numerical investigation of a hollow brick filled with perlite insulation. *Energy and Buildings* **42,** 1402–1408 (2010).

21. Sutcu, M. Influence of expanded vermiculite on physical properties and thermal conductivity of clay bricks. *Ceram. Int.* **41,** 2819–2827 (2015).

22. Sengul, O., Azizi, S., Karaosmanoglu, F. & Tasdemir, M. A. Effect of expanded perlite on the mechanical properties and thermal conductivity of lightweight

concrete. *Energy Build.* **43,** 671–676 (2011).

23. Medri, V. *et al.* Production and characterization of lightweight vermiculite/geopolymer-based panels. *Mater. Des.* **85,** 266–274 (2015).

24. Rashad, A. M. A synopsis about perlite as building material - A best practice guide for Civil Engineer. *Construction and Building Materials* **121,** 338–353 (2016).

25. Li, T. T., Chuang, Y. C., Huang, C. H., Lou, C. W. & Lin, J. H. Applying vermiculite and perlite fillers to sound-absorbing/thermal-insulating resilient PU foam composites. *Fibers Polym.* **16,** 691–698 (2015).

26. Sutcu, M. Influence of expanded vermiculite on physical properties and thermal conductivity of clay bricks. *Ceram. Int.* **41,** 2819–2827 (2015).

27. Sierra-Pérez, J., Boschmonart-Rives, J., Dias, A. C. & Gabarrell, X. Environmental implications of the use of agglomerated cork as thermal insulation in buildings. *J. Clean. Prod.* **126,** 97–107 (2016).

28. Barreca, F. & Fichera, C. R. Thermal insulation performance assessment of agglomerated cork boards. *Wood Fiber Sci.* **48,** 1–8 (2016).

29. Zach, J., Hroudová, J., Brožovský, J., Krejza, Z. & Gailius E, A. Development of Thermal Insulating Materials on Natural Base for Thermal Insulation Systems. *Procedia Eng.* **57,** 1288–1294 (2013).

30. Yuan, B., Ding, S., Wang, D., Wang, G. & Li, H. Heat insulation properties of silica aerogel/glass fiber composites fabricated by press forming. *Mater. Lett.* **75,** 204–206 (2012).

31. Feng, J., Feng, J., Jiang, Y. & Zhang, C. Ultralow density carbon aerogels with low thermal conductivity up to 2000 °C. *Mater. Lett.* **65,** 3454–3456 (2011).

32. Eskandari, N., Motahari, S., Atoufi, Z., Hashemi Motlagh, G. & Najafi, M. Thermal, mechanical, and acoustic properties of silica-aerogel/UPVC composites. *J. Appl. Polym. Sci.* **134,** (2017).

33. Feng, J., Zhang, C. & Feng, J. Carbon fiber reinforced carbon aerogel composites for thermal insulation prepared by soft reinforcement. *Mater. Lett.*

67, 266–268 (2012).

34. Neugebauer, A. *et al.* Thermal conductivity and characterization of compacted, granular silica aerogel. *Energy Build.* **79,** 47–57 (2014).

35. Alotaibi, S. S. & Riffat, S. Vacuum insulated panels for sustainable buildings: A review of research and applications. *International Journal of Energy Research* **38,** 1–19 (2014).

36. Baetens, R., Petter Jelle, B. & Gustavsen, A. Aerogel insulation for building applications: A state-of-the-art review. *Energy Build.* **43,** 761–769 (2010).

37. Baetens, R., Jelle, B. P., Gustavsen, A. & Grynning, S. Gas-filled panels for building applications: A state-of-the-art review. *Energy Build.* **42,** 1969–1975 (2010).

38. Briga-Sá, A. *et al.* Textile waste as an alternative thermal insulation building material solution. (2013). doi:10.1016/j.conbuildmat.2012.08.037

39. Wei, G., Wang, L., Xu, C., Du, X. & Yang, Y. Thermal conductivity investigations of granular and powdered silica aerogels at different temperatures and pressures. *Energy Build.* **118,** 226–231 (2016).

40. Kotaji, S. *et al.* SUSTAINABILITY OF POLYURETHANE THERMAL INSULATION - PERFORMANCE ASSESSMENT AT BUILDING AND BUILDING COMPONENT LEVEL. *Cesb 10 Cent. Eur. Towar. Sustain. Build. - From Theory To Pract.* 399–402 (2010).

41. Tiberio Cardoso, G., Claro Neto, S. & Vecchia, F. Rigid foam polyurethane (PU) derived from castor oil (Ricinus communis) for thermal insulation in roof systems. *Front. Archit. Res.* **1,** 348–356 (2012).

42. Zach, J., Korjenic, A., Petránek, V., Hroudová, J. & Bednar, T. Performance evaluation and research of alternative thermal insulations based on sheep wool. *Energy Build.* **49,** 246–253 (2012).

43. Patnaik, A., Mvubu, M., Muniyasamy, S., Botha, A. & Anandjiwala, R. D. Thermal and sound insulation materials from waste wool and recycled polyester fibers and their biodegradation studies. *Energy Build.* **92,** 161–169 (2015).

44. Moretti, E., Belloni, E. & Agosti, F. Innovative mineral fiber insulation panels for buildings: Thermal and acoustic characterization. *Appl. Energy* **169,** 421–432 (2016).

45. Hüsing, N. & Schubert, U. Aerogels—Airy Materials: Chemistry, Structure, and Properties. *Angew. Chemie Int. Ed.* **37,** 22–45 (1998).

46. Lorenzati, A., Fantucci, S., Capozzoli, A. & Perino, M. VIPs thermal conductivity measurement: Test methods, limits and uncertainty. in *Energy Procedia* **78,** 418–423 (2015).

47. Annabi, N. *et al.* Controlling the porosity and microarchitecture of hydrogels for tissue engineering. *Tissue Eng. Part B. Rev.* **16,** 371–83 (2010).

48. Smita Mohanty, M. C. Effect of Different Solvents in Solvent Casting of Porous scaffolds – In Biomedical and Tissue Engineering Applications. *J. Tissue Sci. Eng.* **06,** 1–7 (2015).

49. Loh, Q. L. & Choong, C. Three-Dimensional Scaffolds for Tissue Engineering Applications: Role of Porosity and Pore Size. *Tissue Eng. Part B Rev.* **19,** 485–502 (2013).

50. Zhou, J. *et al.* Magnetic Pickering emulsions stabilized by Fe3O4 nanoparticles. *Langmuir* **27,** 3308–16 (2011).

51. Particle Sciences. Emulsion Stability and Testing. **2,** 1–2 (2011).

52. McClements, D. J. Critical review of techniques and methodologies for characterization of emulsion stability. *Crit. Rev. Food Sci. Nutr.* **47,** 611–649 (2007).

53. Tadros, T. F. Emulsion Formation, Stability, and Rheology. in *Emulsion Formation and Stability* 1–75 (Wiley-VCH Verlag GmbH & Co. KGaA, 2013). doi:10.1002/9783527647941.ch1

54. Silverstein, M. S. Emulsion-templated porous polymers: A retrospective perspective. *Polymer (Guildf).* **55,** 304–320 (2014).

55. Cameron, N. R. High internal phase emulsion templating as a route to well-defined porous polymers. *Polymer* **46,** 1439–1449 (2005).

56. Bai, L. & McClements, D. Extending Emulsion Functionality: Post-Homogenization Modification of Droplet Properties. *Processes* **4,** 17 (2016).

57. Kovačič, S., Štefanec, D. & Krajnc, P. Highly porous open-cellular monoliths from 2-hydroxyethyl methacrylate based high internal phase emulsions (HIPEs): Preparation and void size tuning. *Macromolecules* **40,** 8056–8060 (2007).

58. Aveyard, R., Binks, B. P. & Clint, J. H. Emulsions stabilised solely by colloidal particles. *Adv. Colloid Interface Sci.* **100–102,** 503–546 (2003).

59. Jiang, J., Mei, Z., Xu, J. & Sun, D. Effect of inorganic electrolytes on the formation and the stability of water-in-oil (W/O) emulsions. *Colloids Surfaces A Physicochem. Eng. Asp.* **429,** 82–90 (2013).

60. Chen, G. & Tao, D. An experimental study of stability of oil-water emulsion. *Fuel Process. Technol.* **86,** 499–508 (2005).

61. Wong, L. L. C., Baiz Villafranca, P. M., Menner, A. & Bismarck, A. Hierarchical polymerized high internal phase emulsions synthesized from surfactant-stabilized emulsion templates. *Langmuir* **29,** 5952–5961 (2013).

62. Vilasau, J. *et al.* Phase behaviour of a mixed ionic/nonionic surfactant system used to prepare stable oil-in-water paraffin emulsions. *Colloids Surfaces A Physicochem. Eng. Asp.* **384,** 473–481 (2011).

63. Barbetta, A., Cameron, N. R. & Cooper, S. J. High internal phase emulsions (HIPEs) containing divinylbenzene and 4-vinylbenzyl chloride and the morphology of the resulting PolyHIPE materials. *Chem. Commun.* 221–222 (2000). doi:10.1039/a909060f

64. Robinson, J. L., Moglia, R. S., Stuebben, M. C., McEnery, M. A. P. & Cosgriff-Hernandez, E. Achieving Interconnected Pore Architecture in Injectable PolyHIPEs for Bone Tissue Engineering. *Tissue Eng. Part A* **20,** 1103–1112 (2014).

65. Melle, S., Lask, M. & Fuller, G. G. Pickering emulsions with controllable stability. *Langmuir* **21,** 2158–62 (2005).

66. Vílchez, A., Rodríguez-Abreu, C., Esquena, J., Menner, A. & Bismarck, A. Macroporous polymers obtained in highly concentrated emulsions stabilized

solely with magnetic nanoparticles. *Langmuir* **27,** 13342–52 (2011).

67. Huš, S. & Krajnc, P. PolyHIPEs from Methyl methacrylate: Hierarchically structured microcellular polymers with exceptional mechanical properties. *Polym. (United Kingdom)* **55,** 4420–4424 (2014).

68. Carnachan, R. J., Bokhari, M., Przyborski, S. A. & Cameron, N. R. Tailoring the morphology of emulsion-templated porous polymers. *Soft Matter* **2,** 608 (2006).

69. Chevalier, Y. & Bolzinger, M.-A. Emulsions stabilized with solid nanoparticles: Pickering emulsions. *Colloids Surfaces A Physicochem. Eng. Asp.* **439,** 23–34 (2013).

70. Li, Z., Liu, H., Zeng, L., Liu, H. & Wang, Y. The facile synthesis of PMMA polyHIPEs with highly interconnected porous microstructures. *J. Mater. Sci.* **51,** 9005–9018 (2016).

71. Cameron, N. R. & Sherrington, D. C. High Internal Phase Emulsions (HIPEs) - Structure , Properties and Use in Polymer Preparation. in *Advances in Polymer Science* **126,** 163–214 (1996).

72. Pakeyangkoon, P., Magaraphan, R., Malakul, P. & Nithitanakul, M. Effect of soxhlet extraction and surfactant system on morphology and properties of Poly(DVB)PolyHIPE. in *Macromolecular Symposia* **264,** 149–156 (WILEY-VCH Verlag, 2008).

73. Huš, S., Kolar, M. & Krajnc, P. Tailoring morphological features of cross-linked emulsion-templated poly(glycidyl methacrylate). *Des. Monomers Polym.* **18,** 698–703 (2015).

74. Gurevitch, I. & Silverstein, M. S. Polymerized pickering HIPEs: Effects of synthesis parameters on porous structure. *J. Polym. Sci. Part A Polym. Chem.* **48,** 1516–1525 (2010).

75. Krajnc, P., Štefanec, D. & Pulko, I. Acrylic Acid "Reversed" PolyHIPEs. *Macromol. Rapid Commun.* **26,** 1289–1293 (2005).

76. Zou, S., Yang, Y., Liu, H. & Wang, C. Synergistic stabilization and tunable structures of Pickering high internal phase emulsions by nanoparticles and surfactants. *Colloids Surfaces A Physicochem. Eng. Asp.* **436,** 1–9 (2013).

77. Matsusaka, N., Suzuki, T. & Okubo, M. Effects of stirring prior to starting emulsion polymerization of styrene with nonionic emulsifier on particle formation and its incorporation. doi:10.1007/s00396-012-2593-2

78. Sergienko, A. Y., Tai, H., Narkis, M. & Silverstein, M. S. Polymerized high internal-phase emulsions: Properties and interaction with water. *J. Appl. Polym. Sci.* **84,** 2018–2027 (2002).

79. Gurevitch, I. & Silverstein, M. S. Polymerized pickering HIPEs: Effects of synthesis parameters on porous structure. *J. Polym. Sci. Part A Polym. Chem.* **48,** 1516–1525 (2010).

80. Lu, G. D., Yan, Q. Z. & Ge, C. C. Preparation of porous polyacrylamide hydrogels by frontal polymerization. *Polym. Int.* **56,** 1016–1020 (2007).

81. Quell, A., De Bergolis, B., Drenckhan, W. & Stubenrauch, C. How the Locus of Initiation Influences the Morphology and the Pore Connectivity of a Monodisperse Polymer Foam. *Macromolecules* **49,** 5059–5067 (2016).

82. Cameron, N. R. High internal phase emulsion templating as a route to well-defined porous polymers. *Polymer (Guildf).* **46,** 1439–1449 (2005).

83. Kempers, R., Kolodner, P., Lyons, A. & Robinson, A. J. A high-precision apparatus for the characterization of thermal interface materials. *Cit. Rev. Sci. Instruments* **80,** (2009).

84. Pennec, F. *et al.* A combined finite-discrete element method for calculating the effective thermal conductivity of bio-aggregates based materials. *Int. J. Heat Mass Transf.* **60,** 274–283 (2013).

85. Smith, D. S. *et al.* Thermal conductivity of porous materials. *J. Mater. Res.* **28,** 2260–2272 (2013).

86. Bourret, J. *et al.* Effect of the pore volume fraction on the thermal conductivity and mechanical properties of kaolin-based foams. *J. Eur. Ceram. Soc.* **33,** 1487–1495 (2013).

87. Menner, A. & Bismarck, A. New evidence for the mechanism of the pore formation in polymerising high internal phase emulsions or why polyHIPEs have an interconnected pore network structure. in *Macromolecular Symposia* **242,**

19–24 (WILEY-VCH Verlag, 2006).

88. Owen, R. *et al.* Emulsion templated scaffolds with tunable mechanical properties for bone tissue engineering. *J. Mech. Behav. Biomed. Mater.* **54,** 159–172 (2016).

89. Placido, E., Arduini-Schuster, M. C. & Kuhn, J. Thermal properties predictive model for insulating foams. *Infrared Phys. Technol.* **46,** 219–231 (2005).

90. Dubois, S. & Lebeau, F. Design, construction and validation of a guarded hot plate apparatus for thermal conductivity measurement of high thickness crop-based specimens. *Mater. Struct. Constr.* **48,** 407–421 (2015).

91. Qin, X. Chicken Feather Fibre Mat/PLA Composites for Thermal Insulation. (2015).

92. Kobari, T., Okajima, J., Komiya, A. & Maruyama, S. Development of guarded hot plate apparatus utilizing Peltier module for precise thermal conductivity measurement of insulation materials. *Int. J. Heat Mass Transf.* **91,** 1157–1166 (2015).

93. Uysal, O. *et al.* Eff ect of Nano-Clay Addition on Th ermal Conductivity of Rigid Polyurethane. *Int. Metall. Mater. Congr.* **18,** (2016).